Cover Page

Universiteit Leiden

The handle http://hdl.handle.net/1887/57416 holds various files of this Leiden University dissertation

Author: Segers, Marijke
Title: Galaxy formation traced by heavy element pollution
Date: 2017-11-28

Galaxy formation traced
by heavy element pollution

Proefschrift

ter verkrijging van
de graad van Doctor aan de Universiteit Leiden,
op gezag van Rector Magnificus prof. mr. C.J.J.M. Stolker,
volgens besluit van het College voor Promoties
te verdedigen op dinsdag 28 november 2017
klokke 12:30 uur

door

Marijke C. Segers
geboren te Leiden
in 1990

Promotiecommissie

Promotor: Prof. dr. J. Schaye

Overige leden: Dr. R. A. Crain   (Liverpool John Moores University)
                  Prof. dr. S. L. Ellison   (University of Victoria)
                  Dr. B. D. Oppenheimer   (University of Colorado Boulder)
                  Prof. dr. M. Franx
                  Prof. dr. H. J. A. Röttgering

Voor Jelmer

Contents

1

Introduction

Galaxies form inside extended haloes of dark matter, which correspond to the highest density peaks in the web of cosmic structures. Under the influence of gravity, the Universe has evolved from a roughly homogeneous state at early times to a highly structured state at the present day, where on large scales the baryonic matter closely traces the distribution of the dark matter. However, while dark matter stops its contraction once it reaches virial equilibrium, as it is only subject to gravity, baryonic matter can lose additional energy through radiative cooling, which allows it to form smaller structures like stars and galaxies.

When studying the formation of galaxies, it is important to realize that they are not closed systems. They form and evolve through interactions with their surroundings, involving the exchange of mass, energy and momentum. Fig. 1.1 gives an illustration of how baryons cycle in and out of galaxies, as they undergo processes like heating and cooling, star formation and expulsion by galactic winds. In this thesis, we concentrate on several aspects of this cycle of galaxy formation, such as the fuelling of star formation in the galaxy interstellar medium (ISM) and the abundance of 'metals'[1] in the gas around galaxies.

1.1 Gas accretion and star formation

Galaxies grow and build their stellar content as they accrete gas from the intergalactic medium (IGM). Gas accretion can happen either via the 'cold mode', where gas reaches the galaxy along cold, filamentary streams (e.g. Kereš et al., 2005; Dekel et al., 2009), or via the 'hot mode', where gas first gets shock-heated to the virial

---

[1]Following common practice in astronomy, we refer with 'metals' to all elements heavier than helium.
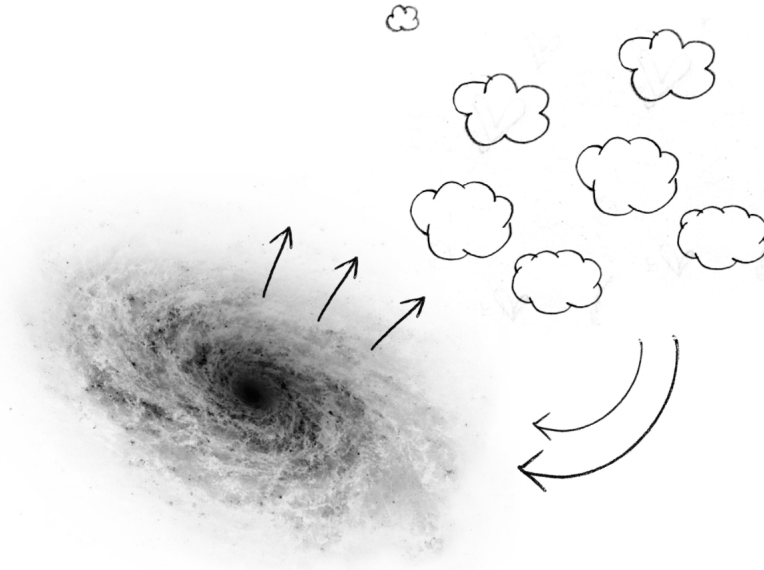
Figure 1.1: Galaxy formation illustrated by the cycle of baryons in and out of galaxies. Galaxies accrete gas from the intergalactic medium (IGM), which provides the fuel for star formation, in addition to the gas returned by evolved stars. While galaxies build up their stellar mass content, and black holes grow in their centres, they affect their surrounding medium through various forms of feedback. These include chemical feedback, as galactic winds enrich the circumgalactic medium (CGM) and IGM with metals. The energy feedback from star formation and active galactic nuclei is particularly important for quenching star formation, thereby providing a mechanism for regulating galaxy growth. The CGM, which is diffuse and therefore usually studied in absorption, is observed to contain a wide variety of metal ion species. [Galaxy image: original image by Hubble Heritage Team (AURA/STScI/NASA/ESA), colours inverted and converted to black and white by MCS]

temperature of the halo and subsequently cools out of a quasi-static equilibrium (Rees & Ostriker, 1977; Silk, 1977). The cold mode has been found to contribute substantially to the growth of galaxies across all mass-scales and redshifts, while the contribution from the hot mode increases with cosmic time and is, at a fixed epoch, higher for more massive galaxies (e.g. Birnboim & Dekel, 2003; Kereš et al., 2005, 2009; van de Voort et al., 2011b). Galaxies can acquire additional gas, particularly in the dense environments of galaxy groups and clusters, by stripping off gas from the envelopes of satellite galaxies (e.g. Sancisi et al., 2008) or through mergers with neighbouring galaxies.

Once the gas has become part of the ISM and locally reaches sufficiently high densities to become self-gravitating, stars are formed. The rate at which this happens is observed to be closely related to the gas surface density in the ISM (the Kennicutt-Schmidt relation; Kennicutt, 1998). Globally, observations show that the rate at which galaxies build up the stellar mass content of the Universe – the cosmic star formation rate (SFR) density – peaks at a redshift of $z \approx 2$: it steeply increases with cosmic time at high redshifts, and gradually decreases again at low redshifts (e.g. Behroozi et al., 2013). For individual galaxies, their SFR peaks, on average, at a higher redshift if their host halo mass is higher. Galaxies eventually stop forming stars – they *quench* – as they run out of fuel due to internal or external processes (see Section 1.2), which creates a bimodality in the observed properties of galaxies: while star-forming galaxies are generally found to have blue colours and a disc-like morphology, quenched galaxies are generally red and elliptical (e.g. Baldry et al., 2004).

As stars in the galaxy evolve, they experience phases of strong mass-loss, during their lives or when they ultimately explode as supernovae (SNe), thereby releasing a fraction of their mass back into the ISM. A stellar population, consisting of multiple stars with their masses distributed according to some initial mass function (IMF; e.g. Salpeter, 1955; Chabrier, 2003), loses up to 50% of its original mass. If this material is not expelled from the galaxy by galactic feedback, it adds to the galaxy gas reservoir, where it can be used to fuel subsequent generations of star formation (e.g. Mathews, 1990; Martin et al., 2007). We refer to this process as 'gas recycling'. Previous studies suggest that an internal supply of gas in the form of stellar ejecta is necessary to close the gas budget of star-forming galaxies (nearby disc galaxies: Leitner & Kravtsov 2011; central cluster galaxies: Voit & Donahue 2011), and that it can extend the gas consumption time-scale by a factor of $1.5 - 4$ (Kennicutt et al., 1994).

The elemental composition of the ejecta, and the time-scale on which they are released, depends on the mass of the star. Massive stars ($M_{\rm star} > 8\,{\rm M}_\odot$) evolve quickly, with main sequence lifetimes of ~ 10 Myr, and lose mass in stellar winds during the main sequence phase and, most importantly, in the form of a core collapse SN (Type II[2]) explosion at the end of their lives. Such an explosion is initiated when, through a series of nuclear fusion reactions, a stellar core of iron is created, after which nuclear fusion can no longer provide the energy to keep the star in thermal and hydrostatic equilibrium. The iron core then starts contracting rapidly, as also

---

[2]We use 'Type II' to refer to all core collapse SNe, including Type Ib and Ic.

the pressure from the degenerate electrons is not sufficient to counteract gravity. Due to the compression, the core eventually turns into a degenerate neutron core, which causes the infalling envelope of the star to bounce off and to be accelerated outwards (see e.g. Woosley et al. 2002 for a review on massive star evolution). SN Type II explosions mainly release α-elements, like oxygen, neon, magnesium and silicon, which are elements built from the repeated capture of α particles (helium nuclei).

Low- and intermediate-mass stars ($0.8 < M_{\text{star}} < 8\,\text{M}_\odot$) evolve more slowly, with main sequence lifetimes up to many Gyr, and experience strong stellar winds when they reach the asymptotic giant branch (AGB) during their post-main sequence evolution. This stage is characterized by a steep rise of the stellar luminosity and an expansion of the stellar envelope. Due to instabilities in the envelope as the star goes through a series of thermal pulses during hydrogen and helium fusion in shells around the core, the star loses mass at a high rate and eventually releases its entire envelope into the surrounding gas. AGB ejecta are particularly rich in metals like carbon and nitrogen, which have been synthesized in the central parts, but have been mixed with the outer stellar layers through convection during so called 'dredge-up' phases.

The stellar cores remaining after the AGB phase can form another enrichment channel when they explode as SN Type Ia. These remnants are white dwarfs mainly consisting of carbon and oxygen and in which degenerate electrons provide the pressure to oppose gravity. While the exact explosion mechanism is still unclear, the commonly adopted scenario is that when the white dwarf occurs in a close binary system with another carbon-oxygen white dwarf, it can accrete mass from the companion, causing the white dwarf to eventually exceed the Chandrasekhar mass limit ($\approx 1.4\,\text{M}_\odot$). Since the degenerate electron pressure is then no longer capable of opposing gravity, the white dwarf contracts, which leads to carbon ignition in the centre. However, the corresponding increase in the temperature does not affect the pressure in the degenerate material, so that the temperature keeps rising. This results in a thermonuclear runaway until the energy released is finally high enough to overcome the binding energy and the white dwarf explodes. SN Type Ia produce a wide range of elements, but they are particularly important sources of iron.

As the different enrichment mechanisms act on different time-scales and are characterised by different enrichment patterns, the elemental composition of galaxies (in the ISM and in stars) holds clues about their formation history. In particular, the stellar α-element-to-iron abundance ratio, $[\alpha/\text{Fe}]_*$ (referring to the difference in the logarithmic α/Fe abundance ratio with respect to the solar value: 'α-enhancement'), is a commonly observed quantity used to study the star formation history of local early-type galaxies (e.g. Trager et al., 2000; Thomas et al., 2010; Johansson et al., 2012; Conroy et al., 2014).

1.2 Galactic feedback

Feedback refers to all the processes originating in the galaxy itself that have an impact on its evolution. We discussed an example of this in the previous section,

namely the enrichment of galaxies (and their surroundings) with metals from stars ('chemical feedback'). Stellar ejecta not only provide fuel for star formation (in the form of hydrogen), but they also affect the gas cooling rates by increasing the metal abundance. These metals are efficient coolants due to the high number of bound electrons and the multitude of levels to which they can be excited (see e.g. Sutherland & Dopita, 1993; Wiersma et al., 2009a). The metallicity of the gas in the halo and the ISM therefore affects the rate at which gas is accreted on to the galaxy and the rate at which stars are formed.

Furthermore, the energy feedback from stars and active galactic nuclei (AGN) is an important mechanism for regulating star formation in galaxies, as it can suppress the gas accretion rate and SFR. Without feedback, these processes would happen too efficiently, resulting in galaxies that are too massive, too compact and too old. In models of galaxy formation, stellar and AGN feedback are necessary to regulate the growth of low- and high-mass galaxies, respectively (see e.g. Schaye et al., 2015). Energetic stellar feedback mainly comes from SN Type II explosions (releasing about 10^{51} erg per explosion) and the winds and radiation from massive stars, while AGN feedback is powered by the accretion of gas on to a central black hole (BH; e.g. Salpeter, 1964; Lynden-Bell, 1969). These sources provide the energy to remove mass from the ISM by driving galaxy-scale outflows, thereby removing potential star formation fuel from the ISM. While certain aspects of the driving mechanism are still unclear – such as the coupling efficiency of the wind to the ISM gas, the importance of radiation pressure on dust grains (e.g. Murray et al., 2005) and the role of collective energy injection from multiple SN explosions (e.g. Mac Low & McCray, 1988) –, galactic winds are a commonly observed phenomenon around star-forming galaxies over a wide range of redshifts (e.g. Pettini et al., 2001; Weiner et al., 2009; Steidel et al., 2010; Rubin et al., 2014). Additionally, shocks and radiation cause the ISM gas to heat up (for example through the creation of hot interstellar bubbles; see e.g. Weaver et al., 1977), which suppresses the conversion of gas into stars. Galactic feedback can also be preventative, as it heats and removes gas from the halo and thereby prevents the accretion of fresh gas on to the galaxy (e.g. van de Voort et al., 2011a).

While the cosmic growth of BHs and their host galaxies seems to go hand in hand (e.g. Boyle & Terlevich, 1998; Silverman et al., 2008; Mullaney et al., 2012b), possibly because they are fuelled from a shared cold gas reservoir (e.g. Hopkins & Quataert, 2010), BH growth becomes especially efficient in high-mass galaxies (with stellar masses exceeding $M_* \sim 10^{10.5}\,\mathrm{M_\odot}$), in which stellar feedback has become ineffective at driving galactic outflows (as opposed to low-mass galaxies, which exhibit efficient star formation-driven winds; e.g. Dubois et al., 2015; Bower et al., 2017). For these galaxies, stellar feedback no longer prevents high gas densities from building up in the central regions, so that gas can efficiently accrete on to the BH. The associated feedback from AGN therefore act as a regulation and quenching mechanism for star formation in massive galaxies, where it impacts upon more massive galaxies at earlier times, as they cross the characteristic mass-scale of $M_* \sim 10^{10.5}\,\mathrm{M_\odot}$ earlier. Hence, AGN feedback naturally gives rise to galactic 'downsizing', a galaxy formation scenario in which massive galaxies form the bulk of their stars earlier and over a shorter period of time than low-mass galaxies

(e.g. Cowie et al., 1996; Neistein et al., 2006). As we will show in Chapter 3, AGN feedback provides an explanation for the observed α-enhancement of massive, early-type galaxies, which is generally interpreted as evidence for the downsizing scenario: AGN feedback naturally leaves the stars of massive galaxies primarily enriched in α-elements, which are released by massive stars on short time-scales.

Being the most luminous objects in the Universe, AGN are important sources of radiative feedback in galaxies: in addition to photoheating and radiation pressure, their ionizing radiation can have a significant effect on the ionization state of the gas in and around the galaxy (e.g. Carswell et al., 1982; Gonçalves et al., 2008). However, both observations and theory suggest that the radiation output from AGN is not continuous. BH growth is predicted to happen through short, repeated accretion events (e.g. Hopkins & Quataert, 2010; Novak et al., 2011; Gabor & Bournaud, 2013), possibly due to instabilities in the BH accretion disc or the clumpiness of the accreting material, which causes the AGN activity to occur in episodic bursts. Observational evidence for AGN variability comes from various objects – gas clouds showing [O III] (e.g. Lintott et al., 2009; Keel et al., 2012; Schirmer et al., 2013) or Lyα emission (Schirmer et al., 2016), or the γ-ray emitting *Fermi* bubbles in the Milky Way (e.g Su et al., 2010; Zubovas et al., 2011) – that exhibit clear signs of photoionization from a nearby bright source, but seem to be associated with galaxies that do not show AGN activity at the time of the observation. Hence, AGN are generally believed to be transient phenomena, which can occur in all galaxies (as all galaxies seem to host BHs), but are in an active state for only a fraction of the time.

1.3   The circumgalactic and intergalactic medium

The IGM holds a large reservoir of gas that, on the one hand, replenishes the ISM of galaxies through accretion and, on the other hand, gets enriched with the products from stellar nucleosynthesis through galactic outflows. Observations suggest that, at the present day, a substantial fraction of the metals ever released by stars in winds and SN explosions may have been expelled into the IGM (Peeples et al., 2014). The close interplay between galaxies and their environment is particularly evident in the circumgalactic medium (CGM), typically defined as the medium residing within a few hundred kpc from galaxies. Studying its content and physical state gives insight into the formation history of galaxies and their past and present feedback efficiency.

As the gas in the IGM and CGM is generally diffuse, with typical hydrogen number densities of $n_H = 10^{-5} - 10^{-3}$ cm^{-3}, it is difficult to detect in emission. Hence, a common approach is to observe it in absorption against the light of a bright background source, which is usually a quasi-stellar object (QSO[3]; as, since the pioneering works by Gunn & Peterson 1965 and Bahcall & Spitzer 1969, done by many: see e.g. Petitjean & Bergeron, 1990; Chen et al., 2001; Tumlinson et al., 2013), but can also be the combined light from many galaxies (see e.g. Adelberger et al., 2005; Steidel et al., 2010; Bordoloi et al., 2011). As the light from the background source travels towards the observer, the intervening gas leaves an imprint by absorbing the continuum light at wavelengths that reflect the redshift and (elemental and ion)

---

[3]Note that we use the terms 'QSO' and 'AGN' interchangeably throughout this thesis.

composition of the gas. This enables us to measure the column density of neutral hydrogen (Hɪ; by examining the absorption in the Lyman series lines) and various metal ions along selected sightlines through the Universe. Studies employing this technique have been particularly successful in probing the absorption arising from doublet transitions like Mgɪɪ, Siɪᴠ, Cɪᴠ and Oᴠɪ, which are easily recognizable by their distinctive spectral pattern (e.g. Steidel & Sargent, 1992; Songaila, 1998; Tripp et al., 2008).

A crucial, but challenging, step when studying the galaxy CGM in absorption is associating the information from the QSO spectra to the galaxies. Two complementary approaches involve either selecting the galaxies that are closest (in terms of their projected distance and line-of-sight, LOS, velocity separation) to a sample of absorbers (e.g. Stocke et al., 2006; Burchett et al., 2016), or measuring the absorption around galaxies that have been selected to be close to a QSO sightline (e.g. Tumlinson et al., 2013; Turner et al., 2014). Both approaches often suffer from ambiguity in the absorber-galaxy association, and the first approach frequently results in galaxy non-detections. However, QSO absorption-line studies still provide us with useful information about the CGM of galaxies in a statistical sense: metal absorbers (and strong Hɪ absorbers) are generally found to be closely associated with galaxies, where the gas around low-redshift ($z < 1$) galaxies is observed to be metal-enriched – with ions like Siɪɪɪ, Cɪᴠ and Oᴠɪ – out to radial distances of a few hundred kpc, or distances comparable to the halo virial radius (e.g. Bordoloi et al., 2014; Liang & Chen, 2014; Prochaska et al., 2011). In contrast, weak Hɪ absorbers (i.e. the Lyα forest) more likely trace the sheets and filaments of the cosmic web.

Except for the highest column density absorbers observed in QSO spectra, the Damped Lymanα (DLA) systems, absorbers are always found to be significantly ionized. By examining the absorption in different ion transitions one can constrain the density and temperature of the absorbing gas. The two main ionization mechanisms are photoionization and collisional ionization: photoionization generally dominates throughout the diffuse IGM, where the gas is constantly subject to UV background (UVB) radiation from the cosmic population of QSOs and galaxies (see e.g. Faucher-Giguère et al., 2009; Haardt & Madau, 2012), while collisional ionization becomes important in hotter media. Observations show that low-ionization species like Mgɪɪ and Siɪɪɪ predominantly trace the photoionized gas at temperatures of $T \sim 10^4$ K. However, higher ionization species like Cɪᴠ and Oᴠɪ, which have ion fractions peaking at higher temperatures, can arise in both photoionized and collisionally ionized gas (e.g. Thom & Chen, 2008; Savage et al., 2014; Stocke et al., 2014).

In addition to providing constraints on the efficiency of energy feedback from galaxies, the CGM can also be used to gain insight into the strength of radiative feedback in the form of photoionization by AGN. Absorption arising within a few thousand km/s below the redshift of the QSO and close pairs of QSOs enable one to study the 'AGN proximity effect' in the LOS and transverse directions, respectively, with respect to the position of the (foreground) AGN host. Along the LOS, the column density of Hɪ is observed to be suppressed in the vicinity of an active AGN (e.g. Carswell et al., 1982; Scott et al., 2000; Dall'Aglio et al., 2008), consistent with enhanced photoionization relative to the UVB. In the transverse direction, however, observations of the different ions are less straightforward to interpret. While metal

ions do hint at a significant proximity effect (Gonçalves et al., 2008), the HI abundance seems to be unaffected (e.g. Schirber et al., 2004; Kirkman & Tytler, 2008). Furthermore, the fact that the radiation output from AGN fluctuates, implies that more galaxies are affected by proximity effects, not just the ones that harbour an active AGN at the time of the observation. As we will show in Chapter 4, the fact that the CGM does not instantaneously return to its equilibrium ionization state after the central AGN fades, has important consequences for the interpretation of CGM observations.

1.4   Cosmological simulations

Numerical simulations are a widely used tool in many areas of astronomy, from star and planet formation to hierarchical structure formation on cosmological scales. They can complement observations in two ways.

- Simulations can make predictions about processes and quantities that are not directly observable (yet), and can thereby assist the interpretation of observations. They are well suited to study the evolution of systems that evolve on time-scales much longer than a human lifetime. Simulations also allow us to examine the object of study at an earlier evolutionary stage. For example, in the study of galaxy formation, they can be used to study the origin of the ISM gas of a certain type of galaxy. Tracing matter back in time in this manner tells us whether the gas was accreted from the IGM, stripped from satellite galaxies or released by evolved stars. Other examples include quantities that are not directly probed by any observable, like the total metallicity of a QSO absorption-line system. A common approach is to simulate a gas pocket such that the metal ion column densities match the observed ones, and thereby derive constraints on the metallicity.

- Simulations enable us to do numerical 'lab' experiments, by running multiple simulations with slightly different input variables and comparing the outcomes. These comparisons can, for example, give insight into the role of physical processes like metal-line cooling and SN feedback in the formation of galaxies or their effect on the structure of the CGM.

Cosmological simulations aim to reproduce a representative volume of the Universe, discretizing its content by mass or volume elements, and follow its evolution over a certain period of cosmic time (see e.g. Vogelsberger et al., 2014; Schaye et al., 2015). An alternative approach is to follow only a small region, for instance containing only a single galaxy or a group of galaxies, that has been extracted from a larger, cosmological volume (i.e. a cosmological 'zoom-in' simulation; see e.g. Hopkins et al., 2014). This provides a way of compensating for the higher computational costs from simulating at a higher resolution or with a more detailed physical model.

For numerical simulations to be reliable tools for studying galaxy formation, however, it is essential that they produce relatively realistic galaxies. On the largest scales, where structure formation is only governed by gravity, simulations with only

dark matter have been very successful at reproducing the observed cosmic structures. On smaller (galactic) scales, however, baryonic physics becomes important, the numerical implementation of which is subject to a lot of uncertainties. The reason is that the processes relevant for galaxy formation span a huge dynamic range, from processes acting on the atomic level to processes on cosmological scales, such that it is not possible to simulate all processes in a self-consistent way. Cosmological simulations address this problem by invoking 'subgrid' routines, which simulate the effective impact of processes acting on scales below the resolution limit on resolved scales. Examples of processes implemented as subgrid routines are the formation and evolution of stellar populations (as individual stars are not resolved), the growth of BHs and the generation of galactic winds from stellar and AGN feedback. The implementation of galactic feedback in particular is a great source of uncertainty: small variations in the model details have been shown to have a large impact on the properties of simulated galaxies (e.g. Haas et al., 2013), and various aspects, like the coupling efficiency of the released energy to the ISM, are still unclear.

The simulations used in this thesis mainly come from the EAGLE simulation suite (Schaye et al., 2015; Crain et al., 2015), a set of cosmological hydrodynamical simulations created with the aim of producing a population of realistic galaxies by calibrating the parameters of subgrid routines to observations. More specifically, the parameters governing the efficiency of stellar and AGN feedback have been chosen such that the simulations reproduce the observed present-day galaxy stellar mass function and stellar mass - BH mass relation, with the additional constraint that the galaxies have reasonable sizes. EAGLE also successfully reproduces various observational galaxy properties that were not considered during the calibration. These include the evolution of the cosmic stellar mass density (Furlong et al., 2015), the distribution of galaxies in the colour-magnitude diagram (Trayford et al., 2015) and the metallicity of stars and ISM gas for galaxies with $M_* \gtrsim 10^{10} \, M_\odot$ (Schaye et al., 2015). In addition to the fiducial (or 'reference') simulation for which the subgrid parameters have been calibrated, the EAGLE suite includes a number of simulations in which a certain aspect of the subgrid physics has been varied with respect to the reference model, enabling the exploration of the impact of various physical processes on galaxy formation.

The IGM in EAGLE exhibits broad agreement with the observed cosmic mass densities and column density distribution functions of H$\textsc{i}$ and various metal ions (like C$\textsc{iv}$ and O$\textsc{vi}$) over a wide range range of redshifts (Rahmati et al., 2015, 2016). This implies that galactic winds in EAGLE are not only effective at transporting metals from the galaxies into the IGM, but that the metals are also roughly in the right ionization state. Ion abundances in EAGLE are computed by assuming that the gas is in ionization equilibrium and exposed to the Haardt & Madau (2001) UVB. Despite the broad agreement with the observations, however, there are some discrepancies, such as the incidence of high-column density ($N_{\mathrm{O\textsc{vi}}} \sim 10^{15} \, \mathrm{cm}^{-2}$) O$\textsc{vi}$ absorbers (Rahmati et al., 2016). This relates to a common issue of the CGM in simulations (including EAGLE): the predicted column density of O$\textsc{vi}$ around star-forming galaxies seems to be systematically lower, by a factor of $\approx 2-10$, than what is found by observations (e.g. Hummels et al., 2013; Ford et al., 2016; Oppenheimer et al., 2016; Suresh et al., 2017). As we will show in Chapter 4, the photoionizing

effect of fluctuating AGN strongly enhances the abundance of circumgalactic O$\textsc{vi}$, even after the AGN fade as a result of non-equilibrium effects, and thereby provides a potential way of reconciling the predicted and observed O$\textsc{vi}$ column densities (see also Oppenheimer et al., 2017).

Despite any discrepancies, as long as one is aware of them, cosmological simulations with a detailed chemical enrichment model are a good tool to study the metals in and around galaxies. Various studies have used such simulations to, for example, demonstrate the sensitivity of the CGM metal content to the properties of galactic winds (e.g. Aguirre et al., 2001b,a; Oppenheimer & Davé, 2006; Wiersma et al., 2011), or to track down the main source (i.e. galaxies of a certain mass) of cosmic metals and to estimate the time-scales on which they were expelled (e.g. Wiersma et al., 2010; Booth et al., 2012). Throughout this thesis, we also make extensive use of simulations to study the matter released by stars at various stages of the baryon cycle and explore the impact of different types of feedback. We investigate the role of stellar ejecta in fuelling star formation (Chapter 2), the effect of energy feedback from AGN on the α-enhancement of massive galaxies (Chapter 3) and the effect of photoionization by fluctuating AGN on the CGM abundance of O$\textsc{vi}$ (Chapter 4).

1.5   This thesis

In this thesis, we explore what metals can tell us about galaxy formation. Metals are the products of stellar nucleosynthesis, but they are found both inside and outside galaxies. They trace the gas returned by stars, while providing information on the time-scales and physical conditions characterizing various stages of galaxy evolution through their elemental composition and ionization state. We complement theoretical work using the EAGLE simulations, where we focus on the galaxies as well as the surrounding medium, with an observational study of the low-redshift ($z < 1$) CGM using the Multi Unit Spectroscopic Explorer (MUSE) on the Very Large Telescope (VLT).

In **Chapter 2**, we explore the significance of recycled stellar ejecta as fuel for star formation. We use the EAGLE simulations to calculate the fractional contribution of the gas from evolved stars to the SFR and stellar mass of present-day ($z = 0$) galaxies and find that these fractions are highest for galaxies with a stellar mass similar to that of the Milky Way ($M_* \approx 10^{10.5}\,\mathrm{M}_\odot$). For central galaxies of this mass, we estimate the fractions to be 35% and 20%, respectively, while for satellites, they can be much higher (up to $\gtrsim 90\%$) due to environmental effects. The importance of recycling decreases for galaxies with $M_* < 10^{10.5}\,\mathrm{M}_\odot$ and $M_* > 10^{10.5}\,\mathrm{M}_\odot$ as a result of the increasing efficiency of feedback from star formation and AGN, respectively. Exploiting the capabilities of EAGLE, we also assess the relative significance of the different stellar mass-loss channels (i.e. massive stars, AGB stars and SN Type Ia) and the dependence of gas recycling on galactocentric radius. Furthermore, we present relations that enable one to estimate the importance of gas recycling – both in dense ISM gas eligible for star formation and in the stars that have already formed – in present-day galaxies from two observational diagnostics: metallicity and α-enhancement.

The stellar α-enhancement, $[\alpha/\text{Fe}]_*$, is a commonly measured quantity in observations of massive early-type galaxies, as it provides insight into their formation history. The α-enhancement is generally found to increase with stellar mass (or stellar velocity dispersion) and stellar age, which is consistent with a galactic downsizing scenario, where more massive galaxies form the bulk of their stars earlier and over a shorter period of time, so that their stars are mainly formed from an ISM enriched with α-elements from quickly evolving massive stars. In **Chapter 3**, we show that the EAGLE simulations reproduce the trends observed for massive galaxies ($M_* > 10^{10.5}\,\text{M}_\odot$), but only if the energy feedback from AGN is included. We infer that AGN feedback is responsible for the observed trends, as it efficiently quenches star formation in massive galaxies, quenching more massive galaxies at earlier times. It thus prevents the iron from SN Type Ia (which originate from longer lived intermediate-mass stars) from being incorporated into younger stars.

In **Chapter 4,** we study another form of feedback from AGN, namely the photoionizing radiation they emit and its effect on the metal ion abundances in the CGM. We particularly focus on the impact of the fluctuating nature of this radiation, as AGN feedback is generally believed to occur in episodic bursts. We simulate the effect in post-processing in the following manner: we select four galaxies – with $M_* \sim 10^{10}\,\text{M}_\odot$ and $M_* \sim 10^{11}\,\text{M}_\odot$, at both $z = 0.1$ and $z = 3$ – from the fiducial EAGLE simulation, implement fluctuating central sources of ionizing radiation and follow the non-equilibrium behaviour of 133 ions in their CGM using the reaction network from Oppenheimer & Schaye (2013b). We find that, due to the fact that the recombination of metal ions is significantly delayed with respect to the time-scale on which the AGN fade, the CGM gas is left in an overionized state for several megayears, forming so called 'AGN proximity zone fossils' around all four galaxies. In these regions, there is an excess of high-ionization state ions like Ovi, Neviii and Mgx (and Civ at $z = 0.1$) and a lack of low-ionization state ions like Siiv (and Civ at $z = 3$). We find that the column density of Ovi can be enhanced by more than an order of magnitude, especially at small impact parameters and if the time in between two subsequent AGN-on phases is short. We predict that the CGM metal abundances around $M_* \sim 10^{10-11}\,\text{M}_\odot$ galaxies, as observed in QSO absorption-line studies, are significantly affected by AGN photoionization, even though most of these galaxies are not classified as active AGN hosts.

In **Chapter 5,** we carry out our own QSO absorption-line survey, probing the Hi and metal ion abundances in the CGM of 208 galaxies at $z < 1$. We employ the integral field spectrograph MUSE to search for galaxies in the fields centred on 16 bright QSOs that have archival spectra taken with the Cosmic Origins Spectrograph on the Hubble Space Telescope. MUSE enables us to detect galaxies and immediately measure their redshifts, without needing to carry out follow-up spectroscopy. The resulting sample consists of predominantly low-mass (median $M_* = 10^{8.9}\,\text{M}_\odot$) galaxies, which are interesting as they are thought to be an important source of metals in IGM. We measure the median pixel optical depth (from the COS spectra) as a function of LOS velocity (v_LOS) and projected distance (d_trans) from the galaxies, and find that the Hi absorption is significantly enhanced, with respect to the detection limit, out to $v_\text{LOS} \approx 260$ km/s (≈ 3.2 pMpc in the case of pure Hubble flow) and $d_\text{trans} \approx 300$ pkpc. For Ovi and Ciii, the absorption signal extends

to $v_{\mathrm{LOS}} \approx 115$ km/s (≈ 1.3 pMpc) and $d_{\mathrm{trans}} \approx 300$ pkpc and to $v_{\mathrm{LOS}} \approx 115$ km/s (≈ 1.3 pMpc) and $d_{\mathrm{trans}} \approx 120$ pkpc, respectively. Furthermore, we find that the O VI absorption strength increases as the stellar mass or SFR of the galaxies increases.

2

Recycled stellar ejecta as fuel for star formation and implications for the origin of the galaxy mass-metallicity relation

We use cosmological, hydrodynamical simulations from the Evolution and Assembly of GaLaxies and their Environments and OverWhelmingly Large Simulations projects to assess the significance of recycled stellar ejecta as fuel for star formation. The fractional contributions of stellar mass-loss to the cosmic star formation rate (SFR) and stellar mass densities increase with time, reaching 35% and 19%, respectively, at $z = 0$. The importance of recycling increases steeply with galaxy stellar mass for $M_* < 10^{10.5}$ $M_\odot$, and decreases mildly at higher mass. This trend arises from the mass dependence of feedback associated with star formation and AGN, which preferentially suppresses star formation fuelled by recycling. Recycling is more important for satellites than centrals and its contribution decreases with galactocentric radius. The relative contribution of asymptotic giant branch (AGB) stars increases with time and towards galaxy centres. This is a consequence of the more gradual release of AGB ejecta compared to that of massive stars, and the preferential removal of the latter by star formation-driven outflows and by lock up in stellar remnants. Recycling-fuelled star formation exhibits a tight, positive correlation with galaxy metallicity, with a secondary dependence on the relative abundance of alpha elements (which are predominantly synthesized in massive stars), that is insensitive to the subgrid models for feedback. Hence, our conclusions are directly relevant for the origin of the mass-metallicity relation and metallicity gradients. Applying the relation between recycling and metallicity to the observed mass-metallicity relation yields our best estimate of the mass-dependent contribution of recycling. For centrals with a mass similar to that of the Milky Way, we infer the contributions of recycled stellar ejecta to the SFR and stellar mass to be 35% and 20%, respectively.

Marijke C. Segers, Robert A. Crain, Joop Schaye, Richard G. Bower, Michelle Furlong, Matthieu Schaller and Tom Theuns

2.1   Introduction

The rate at which galaxies form stars is closely related to the amount of fuel that is available. Although we still lack a complete understanding of how galaxies obtain their gas, several potential sources of star formation fuel have been investigated in previous works, both observationally and using hydrodynamical simulations (e.g. Putman et al., 2009). Galaxies accrete gas from the intergalactic medium (IGM) along cold, dense, filamentary streams (e.g. Kereš et al., 2005; Dekel et al., 2009; Brooks et al., 2009; van de Voort & Schaye, 2012), which can extend far inside the halo virial radius, and through quasi-spherical infall from a diffuse hot halo, which contains gas that has been shock-heated to the halo virial temperature (Rees & Ostriker, 1977; Silk, 1977). Cosmological, hydrodynamical simulations give predictions for the relative importance of these two 'modes' of gas accretion, generally indicating a dominant role for the cold mode in the global build-up of galaxies, with the hot mode becoming increasingly important towards lower redshifts and in more massive systems (e.g. Birnboim & Dekel, 2003; Kereš et al., 2005, 2009; Crain et al., 2010; van de Voort et al., 2011b; Nelson et al., 2013). Galaxies can also acquire new fuel for star formation by stripping the gas-rich envelopes of merging galaxies as soon as these become satellites in a group or cluster environment (e.g. Sancisi et al., 2008; van de Voort et al., 2011b) or by re-accreting gas that has previously been ejected from the galaxy in an outflow and is raining back down in the form of a halo fountain (e.g. Oppenheimer & Davé, 2008; Oppenheimer et al., 2010).

In addition to the various channels of accreting gas from the IGM, every galaxy has an internal channel for replenishing the reservoir of gas in the interstellar medium (ISM), namely the shedding of mass by the stellar populations themselves. Stars lose a fraction of their mass in stellar winds before and while they go through the asymptotic giant branch (AGB) phase. Furthermore, a substantial amount of stellar material is released as stars end their lives in supernova (SN) explosions. Eventually, ~ 50% of the initial mass of a stellar population will be released. If this material is not ejected into the circumgalactic medium (CGM), where it can emerge as X-ray emitting gas in the hot circumgalactic corona (e.g. Parriott & Bregman, 2008; Crain et al., 2013), or entirely expelled from the galaxy into the IGM (e.g. Ciotti et al., 1991), but rather ends up in the cool ISM gas reservoir, then it can be 'recycled' to fuel subsequent generations of star formation (e.g. Mathews, 1990; Martin et al., 2007). Note that what we call 'gas recycling' here is different from the process considered in works on galactic outflow fountains, in which 'recycling' refers to the re-accretion of gas ejected from the ISM, regardless of whether it has ever been part of a star. In this work 'recycled gas' refers to the gas from evolved stars that is used to form new stars, regardless of whether it has been blown out of a galaxy.

Using observational constraints on the rates of gas infall and the history of star formation, Leitner & Kravtsov (2011) assessed the significance of recycled stellar evolution products in the gas budget of a number of nearby disc galaxies (including the Milky Way). They modelled the global mass-loss history of each galaxy from an empirically motivated distribution of stellar population ages and a set of stellar yields and lifetimes, and showed that the gas from stellar mass-loss can provide

most of the fuel required to sustain the current rates of star formation. They suggested that this internal supply of gas is important for fuelling star formation at late epochs, when the cosmological accretion rate drops or is suppressed by preventative feedback (e.g. Mo & Mao, 2002), hence falling short of the observed star formation rate (SFR) of the galaxies. Furthermore, Voit & Donahue (2011) argued that due to the high ambient pressures and the resulting short gas cooling times, central cluster galaxies are very efficient at recycling stellar ejecta into new stars. They showed that the stellar mass-loss rates are generally comparable to, or even higher than, the observed rates of star formation and emphasized the importance of including this form of internal gas supply in any assessment of the gas budget of such systems. These conclusions are consistent with the observation by Kennicutt et al. (1994) that recycling of stellar ejecta can extend the lifetimes of gaseous discs by factors of 1.5 – 4, enabling them to sustain their ongoing SFRs for periods comparable to the Hubble time (see also Roberts, 1963; Sandage, 1986). These studies suggest that recycled stellar mass-loss is an important part of the gas budget of star-forming galaxies, even hinting that it may be a necessary ingredient to reconcile the gas inflow and consumption rates of the Milky Way.

In this paper, we investigate the importance of gas recycling for fuelling star formation by explicitly calculating the contribution of stellar mass-loss to the SFR and stellar mass of present-day galaxies. We use cosmological simulations from the Evolution and Assembly of GaLaxies and their Environments (EAGLE) project (Schaye et al., 2015; Crain et al., 2015) to explore the recycling of stellar ejecta, as a cosmic average as a function of redshift and within individual (central and satellite) galaxies at $z = 0$, where we give quantitative predictions for recycling-fuelled star formation as a function of galaxy stellar mass and establish a connection with observational diagnostics by relating these predictions to gas-phase and stellar metallicities.

The EAGLE simulations explicitly follow the mass released by stellar populations in the form of stellar winds and SN explosions of Types Ia and II, enabling us to study the relative significance of these mass-loss channels for fuelling star formation. The subgrid parameters in the models for feedback associated with star formation and active galactic nuclei (AGN) have been calibrated to reproduce the $z \simeq 0$ observed galaxy stellar mass function (GSMF) and the relation between stellar mass, M_*, and the mass of the central supermassive black hole (BH), M_{BH}, with the additional constraint that the sizes of disc galaxies must be reasonable. The EAGLE simulations not only successfully reproduce these key observational diagnostics with unprecedented accuracy, but are also in good agreement with a large and representative set of low- and high-redshift observables that were not considered during the calibration (Crain et al., 2015; Furlong et al., 2015; Lagos et al., 2015; Rahmati et al., 2015; Sawala et al., 2015; Schaller et al., 2015b; Schaye et al., 2015; Trayford et al., 2015).

We consider the reproduction of a realistic galaxy population to be a prerequisite for this study, since its conclusions are sensitive to the detailed evolution of the gas 'participating' in galaxy formation, requiring that the simulations accurately model the evolving balance between the inflow of gas on to galaxies and the combined sinks of star formation and ejective feedback. That EAGLE satisfies this criterion

is particularly advantageous, since hydrodynamical simulations are not subject to several limiting approximations inherent to simpler techniques, for example semi-analytic models of galaxy formation. This, in addition to their inclusion of a detailed implementation of chemodynamics, makes the EAGLE simulations an ideal tool for establishing quantitative predictions concerning the role of gas recycling in fuelling star formation.

We also briefly explore the sensitivity of our results to the physical processes in the subgrid model. To do so, we use a suite of cosmological simulations from the OverWhelmingly Large Simulations (OWLS) project (Schaye et al., 2010). As the OWLS project aimed to explore the role of the different physical processes modelled in the simulations, it covers a wide range of subgrid implementations and parameter values, including extreme variations of the feedback model and variations of the stellar initial mass function (IMF). We will show that the efficiency of the feedback associated with star formation and AGN plays an important role in regulating the fuelling of star formation with recycled stellar ejecta.

We note that, because of the tight correlation we find between the contribution of stellar mass-loss to the SFR (stellar mass) and the ISM (stellar) metallicity, our characterization and explanation of the role of stellar mass-loss as a function of galaxy mass and type has important and direct implications for the origin of the mass-metallicity relation.

This paper is organized as follows. In Section 2.2, we present a brief overview of the simulation set-up and the subgrid modules implemented in EAGLE. In this section, we also introduce the two quantities we use to assess the importance of gas recycling, namely the fractional contributions of stellar mass-loss to the SFR and stellar mass. In Section 2.3, we present quantitative predictions from EAGLE for the evolution of the cosmic averages of these quantities and for their dependence on metallicity and galaxy stellar mass. We explore the sensitivity of these results using a set of OWLS simulations in Section 2.4. Finally, we summarize our findings in Section 2.5.

2.2   Simulations

The amount of gas that galaxies can recycle to form new generations of stars, depends fundamentally on the fraction of stellar mass that is returned to the ISM. How much of this mass is actually used to fuel star formation is not straightforward to calculate analytically, due to the variety of processes, such as cosmological infall, gas stripping of satellite galaxies, and feedback associated with star formation and AGN, that can have an effect on the star formation histories of individual galaxies. Hence, we use cosmological simulations from the EAGLE and OWLS projects to investigate this.

For the majority of this work we use the EAGLE simulations, which were run with a modified version of the smoothed particle hydrodynamics (SPH) code GADGET3 (last described by Springel, 2005) using a pressure-entropy formulation of SPH (Hopkins 2013; see Schaller et al. 2015a for a comparison between SPH flavours). The simulations adopt a Λ cold dark matter cosmology with pa-

rameters $[\Omega_m, \Omega_b, \Omega_\Lambda, \sigma_8, n_s, h] = [0.307, 0.04825, 0.693, 0.8288, 0.9611, 0.6777]$ (Planck Collaboration et al., 2014).

We will study primarily the largest EAGLE simulation, which we will refer to as *Ref-L100N1504* (as in Schaye et al., 2015) or as the 'fiducial' model. This simulation was run in a periodic volume of size $L = 100$ comoving Mpc (cMpc), containing $N = 1504^3$ dark matter particles and an equal number of baryonic particles. The gravitational softening length of these particles is 2.66 comoving kpc (ckpc), limited to a maximum physical scale of 0.7 proper kpc (pkpc). The particle masses for baryons and dark matter are initially $m_b = 1.8 \times 10^6$ $M_\odot$ and $m_{dm} = 9.7 \times 10^6$ $M_\odot$, respectively. However, during the course of the simulation the baryonic particle masses change as mass is transferred from star to gas particles, corresponding to the recycling of mass from stellar populations back into the gas reservoir.

2.2.1 Subgrid physics

The subgrid physics used in EAGLE is largely based on the set of subgrid recipes developed for OWLS, but includes a few important improvements. Star formation is modelled using a metallicity-dependent density threshold (given by Schaye, 2004), above which gas particles are assigned a pressure-dependent SFR (that by construction reproduces the observed Kennicutt-Schmidt star formation law; Schaye & Dalla Vecchia, 2008) and are converted stochastically into star particles. Each star particle represents a stellar population of a single age (simple stellar population; SSP) and inherits its mass and metallicity from its progenitor gas particle. The adopted IMF is a Chabrier (2003) IMF, spanning the mass range of $0.1 - 100$ $M_\odot$. Following the prescriptions of Wiersma et al. (2009b), an SSP loses mass through stellar winds and supernova explosions (SN Type II) from massive stars and through AGB winds and SN Type Ia explosions from intermediate-mass stars. The time-dependent mass-loss, which we show in Section 2.2.2, is calculated using the metallicity-dependent stellar lifetime tables of Portinari et al. (1998), in combination with the set of nucleosynthetic yields of Marigo (2001, for stars in the mass range $0.8 - 6$ $M_\odot$) and Portinari et al. (1998, for stars in the mass range $6 - 100$ $M_\odot$), all of which are based on the same Padova evolutionary tracks. For SN Type Ia, the yields are taken from the W7 model of Thielemann et al. (2003) and the distribution of progenitor lifetimes is modelled using an empirically motivated time-delay function that is calibrated to reproduce the observed cosmic SN Type Ia rate (see fig. 3 of Schaye et al., 2015). At every gravitational time step (every 10th time step for star particles older than 100 Myr), the ejecta are distributed over the neighbouring gas particles according to the SPH interpolation scheme[1]. The simulations follow the abundances of 11 individual elements, which are used to calculate the rates of radiative cooling and heating on an element-by-element basis and in the presence of Haardt & Madau (2001) UV and X-ray background radiation (Wiersma et al., 2009a). Energy feedback from star formation is implemented by stochastically injecting thermal energy

---

[1]As discussed in Schaye et al. (2015) and different from Wiersma et al. (2009b), EAGLE uses weights that are independent of the current gas particle mass for the distribution of stellar mass-loss. The reason for this is to avoid a runaway process, causing a small fraction of the particles to end up with very large masses compared to their neighbours, as particles that have grown massive due to enrichment, are also likely to become increasingly enriched in future time steps, if they carry more weight in the interpolation.
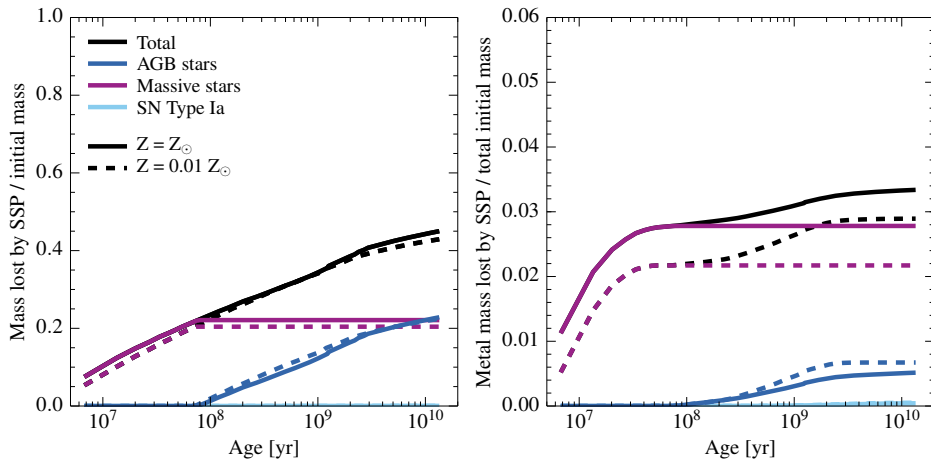
Figure 2.1: The cumulative fraction of the initial mass (total: left-hand panel; in the form of metals, i.e. elements heavier than helium: right-hand panel) that is released by an SSP as a function of its age, adopting a Chabrier (2003) IMF in the range $0.1 - 100$ $M_\odot$. The curves show the contributions from AGB stars (blue), massive stars (purple) and SN Type Ia (cyan), as well as the total (metal) mass ejected by the SSP (black), for two stellar metallicities: solar (solid) and 1 percent of solar (dashed). Initially, only massive stars contribute to the mass-loss, but for SSP ages $\gtrsim 10^8$ yr the contribution from AGB stars becomes increasingly significant. These AGB ejecta are, however, less metal-rich than the ejecta from massive stars. The contribution from SN Type Ia to the (metal) mass-loss remains insignificant at all times. Increasing the metallicity does not have a strong effect on the total mass-loss, but increases the total ejected metal mass as well as the relative contribution from massive stars.

into the gas surrounding newly-formed star particles as described by Dalla Vecchia & Schaye (2012). The fraction $f_{\rm th}$ of the total available feedback energy that is used to heat the gas, depends on the local gas metallicity and density, so as to account for increased thermal losses in higher metallicity gas and to compensate for the increased numerical radiative losses in higher density gas (Crain et al., 2015). The growth of BHs is modelled by inserting seed BHs into haloes more massive than $m_{\rm halo,min} = 10^{10}$ h^{-1} $M_\odot$, which can grow either through gas accretion, at a rate that depends on the angular momentum of the gas, or through mergers with other BHs (Booth & Schaye, 2009; Rosas-Guevara et al., 2015). AGN feedback is implemented as the stochastic injection of thermal energy into the gas surrounding the BH (Booth & Schaye, 2009; Dalla Vecchia & Schaye, 2012). The subgrid routines for stellar and AGN feedback have been calibrated to reproduce observations of the present-day GSMF, the $M_* - M_{\rm BH}$ relation and to yield reasonable galaxy sizes (Schaye et al., 2015; Crain et al., 2015).

2.2.2 Mass released by an SSP

Fig. 2.1 shows the total mass (left-hand panel) and metal mass (right-hand panel) released by an SSP as a function of its age as prescribed by the chemodynamics model. The curves show the total integrated mass ejected (black) and the integrated

mass sourced by AGB stars (blue), massive stars (i.e. stellar winds plus SN Type II; purple) and SN Type Ia (cyan) for two different SSP metallicities: solar (solid lines) and 1 percent of solar (dashed), using a solar value of $Z_\odot = 0.0127$. Both panels show that the ejected (metal) mass, which is expressed as a fraction of the total initial mass of the SSP, increases as the SSP ages. Initially only massive stars contribute, but for ages $\gtrsim 10^8$ yr the contribution from AGB stars becomes increasingly significant. Comparing, for each channel, the total to the metal mass-loss shows that the ejecta from massive stars are more metal-rich than those from AGB stars. The contribution from SN Type Ia to the (metal) mass-loss remains insignificant for all SSP ages[2]. Varying the metallicity over two orders of magnitude changes the total mass-loss by only a few percent, but changes the total ejected metal mass, as well as the relative contribution from massive stars, by $\sim 10 - 15\%$.

Since the choice of IMF determines the relative mass in intermediate-mass and massive stars per unit stellar mass formed, it affects the mass-loss from an SSP. Leitner & Kravtsov (2011) indeed show that the differences between alternative, reasonable choices of the IMF can be significant (see their fig. 1). In Appendix 2.A, we similarly conclude that the total and metal mass-loss is a factor of ~ 1.5 greater for a Chabrier IMF than for the more bottom-heavy Salpeter IMF (which is adopted by one of the OWLS model variations examined in Section 2.4).

2.2.3   Numerical convergence

In order to test for numerical convergence, we use a set of three simulations that were run in volumes of size $L = 25$ cMpc. This includes a high-resolution simulation (*Recal-L025N0752*), whose subgrid feedback parameters were recalibrated to improve the fit to the observed present-day GSMF (see table 3 of Schaye et al., 2015). We show a concise comparison between the fiducial simulation and *Recal-L025N0752* when we present results as a function of halo and stellar mass in Section 2.3.3, while a more detailed convergence test can be found in Appendix 2.B.1. In the rest of the results section (Section 2.3), we use only the fiducial simulation, which, due to its 64 times greater volume than *Recal-L025N0752*, provides a better statistical sample of the massive galaxy population, and models a more representative cosmic volume.

2.2.4   Identifying haloes and galaxies

Haloes are identified using a Friends-of-Friends (FoF) algorithm (Davis et al., 1985), linking dark matter particles that are separated by less than 0.2 times the mean interparticle separation. Gas and star particles are assigned to the same halo group as their nearest dark matter particle. The SUBFIND algorithm (Springel et al., 2001; Dolag et al., 2009) then searches for gravitationally bound substructures within the FoF haloes, which we label 'galaxies' if they contain stars. The galaxy position is

---

[2]Note that we only show the relative contributions from massive and intermediate-mass stars to the *total* ejected metal mass. These may be different from their contributions to the ejected mass of individual elements, as for example iron, which has a substantial fraction of its abundance sourced by SN Type Ia (see fig. 2 of Wiersma et al., 2009b).

defined to be the location of the particle with the minimum gravitational potential within the subhalo. The galaxy at the absolute minimum potential in the FoF halo (which is almost always the most massive galaxy) is classified as the 'central' galaxy, whereas the remaining subhaloes are classified as 'satellite' galaxies.

The mass of the main halo, M_{200}, is defined as the mass internal to a spherical shell centred on the minimum gravitational potential, within which the mean density equals 200 times the critical density of the Universe. The subhalo mass, M_{sub}, corresponds to all the mass bound to the substructure identified by SUBFIND. The stellar mass, M_*, refers to the total mass in stars that is bound to this substructure and that resides within a 3D spherical aperture of radius 30 pkpc. Other galaxy properties, such as the SFR and the stellar half-mass radius, are also computed considering only particles within this aperture, mimicking observational measurements of these quantities (as shown in fig. 6 of Schaye et al. 2015, the present-day GSMF using a 30 pkpc 3D aperture is nearly identical to the one using the 2D Petrosian aperture applied by SDSS). The aperture has negligible effects on stellar masses for $M_* < 10^{11}$ $M_\odot$ and galactic SFRs, as the vast majority of the star formation takes place within the central 30 pkpc. For the more massive galaxies, on the other hand, the stellar masses are somewhat reduced, as the aperture cuts out the diffuse stellar mass at large radii that would contribute to the intracluster light.

2.2.5 Measuring the star formation rate and stellar mass contributed by recycling

We explicitly track the contributions to the SFR and stellar mass from gas recycling. For a gas particle of mass $m_g^i(t)$ at time t, the total fraction of its mass contributed by released stellar material (in the form of hydrogen, helium and heavy elements) is given by

$$f_{g,rec}^i(t) = \frac{m_g^i(t) - m_b}{m_g^i(t)}, \tag{2.1}$$

where m_b is the initial gas mass of gas particles at the start of the simulation. Since a gas particle is the smallest quantum of mass we are able to consider, its recycled fraction is by construction assumed to be perfectly mixed. Therefore, if the gas particle is considered star forming, $f_{g,rec}^i(t)$ also indicates the fraction of its current SFR that is contributed by stellar ejecta. Then, summing up the contributions from all N_g^{gal} gas particles in a galaxy (within the 30 pkpc 3D aperture) yields the SFR contributed by recycling for this galaxy:

$$SFR_{rec}^{gal}(t) = \sum_{i=1}^{N_g^{gal}} \frac{m_g^i(t) - m_b}{m_g^i(t)} SFR^i(t), \tag{2.2}$$

where $SFR^i(t)$ is the SFR of gas particle i at time t. Similarly, summing up the contributions from all N_g^{cos} gas particles in the simulation volume yields the cosmic average of this quantity:

$$SFR_{rec}^{cos}(t) = \sum_{i=1}^{N_g^{cos}} \frac{m_g^i(t) - m_b}{m_g^i(t)} SFR^i(t). \tag{2.3}$$

Since a star particle inherits its mass and elemental abundances from its progenitor gas particle, the fraction of its mass contributed by recycling is

$$f^j_{*,\text{rec}}(t) = \frac{m^j_{*,\text{init}} - m_\text{b}}{m^j_{*,\text{init}}},$$ (2.4)

where $m^j_{*,\text{init}} = m^j_\text{g}(t_\text{birth})$ is the mass of star particle j at the time of its birth, t_birth. Note that equation (2.4) is valid for all $t \geq t_\text{birth}$, even though the star particle itself loses mass. This is again a consequence of the assumption of perfect mixing on the particle scale. Summing up the contributions from all N^gal_* star particles in a galaxy that are within the 3D aperture,

$$M^\text{gal}_{*,\text{rec}}(t) = \sum_{j=1}^{N^\text{gal}_*} \frac{m^j_{*,\text{init}} - m_\text{b}}{m^j_{*,\text{init}}} m^j_*(t),$$ (2.5)

and all N^cos_* star particles in the simulation volume,

$$M^\text{cos}_{*,\text{rec}}(t) = \sum_{j=1}^{N^\text{cos}_*} \frac{m^j_{*,\text{init}} - m_\text{b}}{m^j_{*,\text{init}}} m^j_*(t),$$ (2.6)

give the galaxy stellar mass and cosmic stellar mass, respectively, contributed by recycled gas.

While SFR_rec and $M_{*,\text{rec}}$ are related, it is still helpful to consider both: SFR_rec indicates the instantaneous impact of gas recycling, whereas $M_{*,\text{rec}}$ indicates the importance of recycling over the past history of star formation. In this work, we mainly focus on the *relative* contribution of gas recycled from stellar mass-loss to the total (cosmic or galactic) SFR and stellar mass. Normalizing SFR_rec and $M_{*,\text{rec}}$ by the respective total quantities, yields SFR_rec/SFR and $M_{*,\text{rec}}/M_*$, specifying the *fractions* of the SFR and the stellar mass that are due to stellar mass-loss.

In addition to the total amount of recycling, we will also consider the relative contributions from the different sources of stellar mass-loss that were included in the subgrid model (Section 2.2.2). As the transfer of mass from AGB stars, SN Type Ia and massive stars between star and gas particles is explicitly followed by the EAGLE simulations[3], we can calculate SFR_rec/SFR and $M_{*,\text{rec}}/M_*$ solely due to gas from AGB stars by simply replacing $m^i_\text{g}(t) - m_\text{b}$ in equations (2.2) and (2.3) by m^i_AGB and replacing $m^j_{*,\text{init}} - m_\text{b}$ in equations (2.5) and (2.6) by $m^j_\text{AGB,init}$, where m_AGB is the mass from AGB stars in the respective gas or star particle. The SFR_rec/SFR and $M_{*,\text{rec}}/M_*$ due to gas from SN Type Ia and massive stars are calculated analogously.

2.3 Recycled stellar mass-loss in EAGLE

In this section, we use the fiducial EAGLE simulation, *Ref-L100N1504*, to make quantitative predictions for the importance of gas recycling for fuelling ongoing star

---

[3]Note that these enrichment channels only refer to the *last* enrichment episode. Every stellar population releases mass via the different channels in a way that depends only on its age and metallicity (for a given IMF).
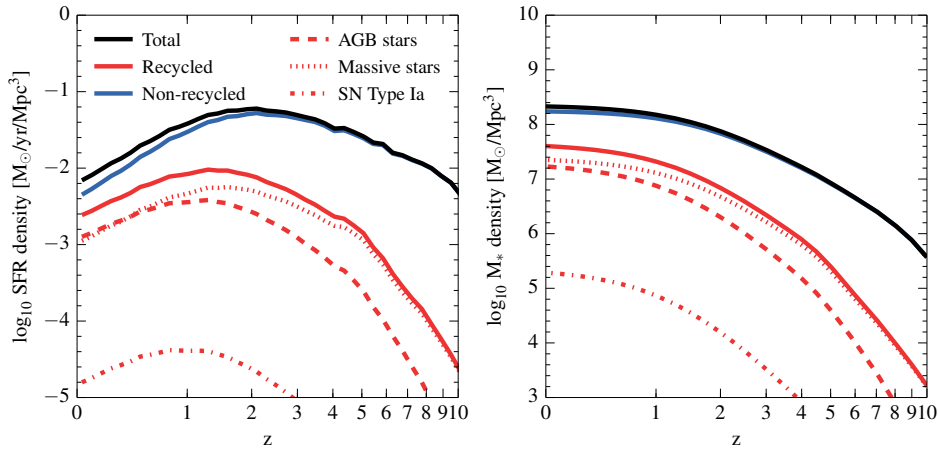
Figure 2.2: The evolution of the cosmic SFR density (left) and the cosmic stellar mass density (right) fuelled by recycled stellar mass-loss (red), as well as the SFR and stellar mass densities fuelled by all gas (black) and gas that has not been recycled (blue). The 'recycled' SFR and stellar mass densities are split according to the contributions from AGB stars (dashed), massive stars (dotted) and SN Type Ia (dot-dashed). Recycling of stellar mass-loss becomes increasingly important for fuelling star formation towards the present day. The gas from massive stars accounts for the majority of the cosmic SFR and stellar mass density from recycled gas at high redshift, but the contribution from AGB stars increases with time (accounting for the majority of the 'recycled' SFR density for $z \lesssim 0.4$).

formation in present-day galaxies over a wide range of galaxy masses. However, we start with a brief investigation of the evolution of recycling-fuelled star formation over cosmic history.

2.3.1   Evolution of the cosmic average

The left-hand panel of Fig. 2.2 shows the total cosmic SFR density (black), the cosmic SFR density fuelled by stellar mass-loss (red, solid: 'recycled') and the cosmic SFR density fuelled by unprocessed gas (blue: 'non-recycled') as a function of redshift. The red curve has been split into the contributions from the three mass-loss channels that are tracked by the simulation: AGB stars (dashed), massive stars (dotted) and SN Type Ia (dot-dashed). To get a better idea of the evolution of the *fractional* contribution from recycled gas to the cosmic star formation history, we show the evolution of the cosmic average SFR_{rec}/SFR, as well as the fractional contribution per channel, in Fig. 2.3 (red).

At $z > 2$ there is little difference between the SFR density due to 'non-recycled' gas and the total SFR density. At these high redshifts, most of the fuel for star formation is due to unprocessed gas[4], since there has simply not been much time

---

[4]Note that this does not imply that most of the SFR, and hence stellar mass, is in the form of Pop III (i.e. metal-free) stars, because the stellar evolution products are mixed with the unprocessed material (in the simulations on the scale of a gas particle).

for stellar populations to evolve and to distribute a significant amount of gas that can be recycled. From the 'recycled' curve, we see that the SFR density fuelled by recycled stellar mass-loss rises rapidly at high redshift, peaks at $z \approx 1.3$, and then declines steadily towards $z = 0$. This trend is similar to the evolution of the total SFR density, although with a delay of ~ 1.5 Gyr (the total SFR density peaks at $z \approx 2$). Furthermore, the slope of the 'recycled' curve is steeper at high redshift and shallower at low redshift compared to that of the total SFR density, indicating that gas recycling becomes increasingly important for fuelling star formation. This is consistent with the rapid rise of the total SFR_{rec}/SFR with decreasing redshift in Fig. 2.3. Our fiducial EAGLE model indicates that 35% of the present-day cosmic SFR density is fuelled by recycled stellar mass-loss.

The right-hand panel of Fig. 2.2 shows the build-up of the cosmic stellar mass density, the total as well as the contributions from recycled and unprocessed gas. The evolution of the cosmic average $M_{*,rec}/M_*$ is shown in Fig. 2.3 (blue). The stellar mass density is related to the SFR density, as one can calculate the former by integrating the latter over time (while taking into account stellar mass-loss). Hence, similar to the SFR density, the stellar mass density is initially ($z \gtrsim 2$) dominated by star formation from unprocessed gas, while the contribution from recycling becomes increasingly important towards $z = 0$. EAGLE indicates that, at the present day, 19% of the cosmic stellar mass density has been formed from recycled stellar mass-loss.

Comparing the different sources of stellar mass-loss, we see that massive stars initially account for the majority of the SFR and stellar mass density from recycled gas. These stars have short lifetimes and are therefore the first to contribute to the mass-loss from a stellar population (see Fig. 2.1). Towards lower redshift the mass lost by AGB stars becomes increasingly important and even becomes the dominant contributor to the SFR density from recycled gas for $z \lesssim 0.4$ (while remaining sub-dominant in the case of the stellar mass density). As expected from Fig. 2.1, recycled SN Type Ia ejecta do not contribute significantly to the cosmic SFR density at any redshift.

2.3.2   Relation with metallicity at $z = 0$

Having studied the evolution of the cosmic average SFR_{rec}/SFR and $M_{*,rec}/M_*$, we will now take a closer look at the $z = 0$ values for individual galaxies in the *Ref-L100N1504* simulation. In the next section, we will give predictions for the fuelling of star formation by recycled stellar ejecta in present-day central and satellite galaxies as a function of their halo and stellar mass. To be able to relate these predictions to observational diagnostics, we first explore the relation between recycling-fuelled star formation and present-day metallicity. We will show that the fact that metals are synthesized in stars and are distributed over the ISM as the evolving stellar populations lose mass, makes them an excellent observational proxy for the contribution of stellar ejecta to the SFR and stellar mass.

To study the SFR_{rec}/SFR, we only consider subhaloes with a non-zero[5] SFR, while to study the $M_{*,rec}/M_*$, we only consider subhaloes with a non-zero stellar

---

[5] 'Non-zero' means containing at least one star-forming gas particle, which corresponds to a specific SFR (= SFR/M_*) of $> 10^{-12}$ yr^{-1} at $M_* \sim 10^9$ M$_\odot$ and $> 10^{-14}$ yr^{-1} at $M_* \sim 10^{11}$ M$_\odot$.
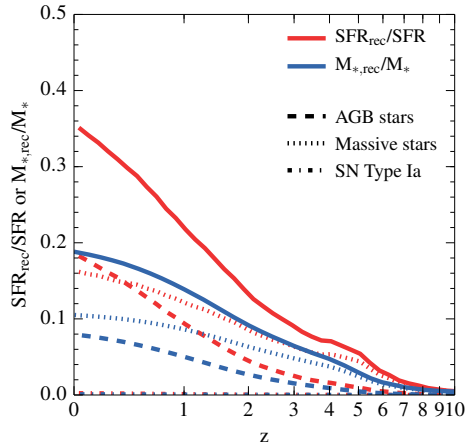
Figure 2.3: The evolution of the fractional contribution of recycled stellar mass-loss to the cosmic SFR density (red) and cosmic stellar mass density (blue), where we show the total (solid) as well as the contributions from AGB stars (dashed), massive stars (dotted) and SN Type Ia (dot-dashed). With decreasing redshift, an increasing fraction of the cosmic SFR and stellar mass density is fuelled by recycled gas, which we find to be 35% and 19%, respectively, at $z = 0$.
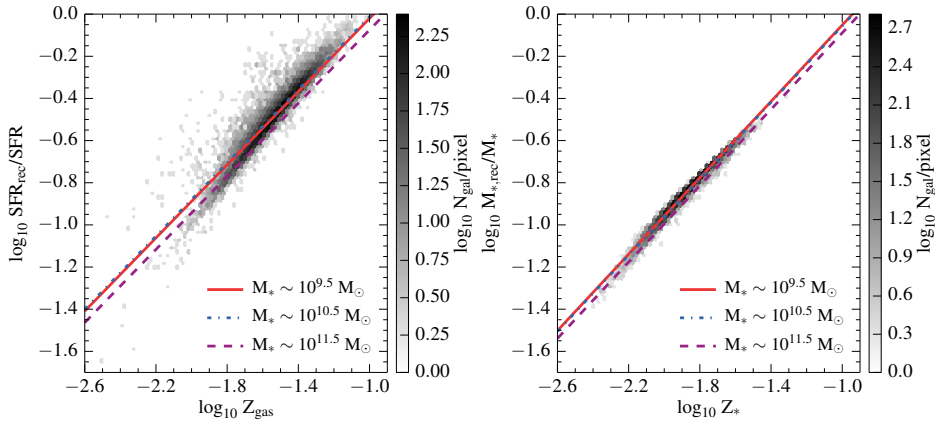
Figure 2.4: The fractional contribution of recycled stellar mass-loss to the SFR (left) and stellar mass (right) of central galaxies at $z = 0$ as a function of their average ISM and stellar metallicity, respectively. The grey-scale indicates the number of galaxies in each cell, where we only include galaxies with stellar masses corresponding to at least 100 gas particles. In the left-hand panel, we only consider subhaloes with a non-zero SFR. We find tight power-law relations between the recycled gas contributions and the respective metallicity measures. These relations exhibit a slight mass dependence as a result of the increasing contribution from massive stars relative to intermediate-mass stars to the SFR and stellar mass for $M_* \gtrsim 10^{10.5}\,M_\odot$. The best-fitting relations (equations 2.10 and 2.11), plotted for galaxies with $M_* \sim 10^{9.5}\,M_\odot$ (red, solid line), $M_* \sim 10^{10.5}\,M_\odot$ (blue, dot-dashed line) and $M_* \sim 10^{11.5}\,M_\odot$ (purple, dashed line), enable one to estimate the importance of gas recycling in present-day galaxies from their observed metallicity and α-enhancement.

mass. For our fiducial simulation this yields samples of 44 248 and 325 561 sub-haloes, respectively. In this section, however, we additionally require the subhaloes to have a galaxy stellar mass corresponding to at least 100 gas particles, which yields samples of 14 028 and 16 681 subhaloes, respectively.

Fig. 2.4 shows the fraction of the SFR (left-hand panel) and stellar mass (right-hand panel) fuelled by recycling as a function of, respectively, the mass-weighted absolute metallicity Z_{gas} of ISM gas (i.e. star-forming gas) and the mass-weighted absolute metallicity Z_* of stars, both for present-day central galaxies[6]. We find strong correlations between these quantities, with more metal-rich galaxies having a larger fraction of their SFR and stellar mass contributed by recycling. The figure reveals tight power-law relations between SFR_{rec}/SFR and Z_{gas}, characterized by a Pearson correlation coefficient of 0.95, and between $M_{*,rec}/M_*$ and Z_*, with a correlation coefficient of 0.99. For the former, we find a 1σ scatter of $\sim 0.1-0.2$ dex for $Z_{gas} < 10^{-1.9}$ and $\lesssim 0.05$ dex for $Z_{gas} > 10^{-1.9}$, while for the latter we find an even smaller 1σ scatter of $\sim 0.01-0.03$ dex. Furthermore, as we show in Appendix 2.B.2, both relations are converged with respect to the numerical resolution.

The tight relation between the contribution of recycled gas to star formation and metallicity is not surprising considering that heavy elements were produced in stars and that their abundance must therefore correlate with the importance of stellar ejecta as star formation fuel. The contribution of recycling to the stellar mass is equal to the ratio of the mean stellar metallicity ($\langle Z_* \rangle$) and the mean metallicity of the ejecta ($\langle Z_{ej} \rangle$) that were incorporated into the stars,

$$\frac{M_{*,rec}}{M_*} = \frac{\langle Z_* \rangle}{\langle Z_{ej} \rangle}. \tag{2.7}$$

The same holds for the contribution of stellar mass-loss to the SFR,

$$\frac{SFR_{rec}}{SFR} = \frac{\langle Z_{gas} \rangle}{\langle Z_{ej} \rangle}. \tag{2.8}$$

The metallicity of the ejecta depends on the age and metallicity of the SSP, as well as on the IMF. From Fig. 2.1, we can see that for our (Chabrier) IMF, $\langle Z_{ej} \rangle \approx 0.033/0.45 \approx 0.073$ for a 10 Gyr old SSP with solar metallicity. Hence, $\log_{10} M_{*,rec}/M_* \approx \log_{10} Z_* + 1.1$, where the slope and normalization are close to the best-fitting values that we determine below. Note that using ages of 100 Myr and 10 Myr instead of 10 Gyr gives normalizations of 0.91 and 0.77, respectively. Using an age of 10 Gyr but a stellar metallicity of 0.01 $Z_\odot$ instead of $Z_\odot$ yields a normalization of 1.2.

There is, however, an additional factor at play that may distort the one-to-one correlation between the contribution of recycled gas to the SFR (and therefore to the

---

[6]Although we do not explicitly show it, the results for central galaxies presented in this section are consistent with the results for satellite galaxies.
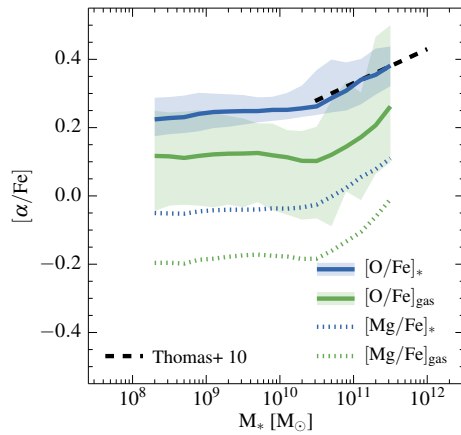
Figure 2.5: The α-element-to-iron abundance ratio of central galaxies at $z = 0$ as a function of stellar mass. We show [α/Fe], represented by [O/Fe] (solid) and [Mg/Fe] (dotted), of ISM gas (green) and stars (blue) as predicted by EAGLE, and compare with observations of the stellar [α/Fe] from Thomas et al. (2010) (converted to a solar abundance ratio of $X_\odot^O/X_\odot^{Fe} = 4.44$). The curves show the median value in each logarithmic mass bin of size 0.2 dex, if it contains at least 10 haloes and the stellar mass corresponds to at least 100 gas particles. The shaded regions mark the 10th to 90th percentiles, shown only for [O/Fe]. For $M_* \lesssim 10^{10.5}$ $M_\odot$, [O/Fe] ([Mg/Fe]) is approximately constant at ~ 0.1 (-0.2) for gas and at 0.25 (-0.05) for stars. For $M_* \gtrsim 10^{10.5}$ $M_\odot$, [O/Fe] and [Mg/Fe] increase with stellar mass, in such a way that the slope matches the observations, reflecting the enhancement in the contribution to the SFR and stellar mass from massive stars relative to that from intermediate-mass stars.

stellar mass) and metallicity, namely the relative significance of the different mass-loss channels. This depends on the time-scale on which stars are formed, but is also affected by processes like stellar and AGN feedback. Given that the ejecta from massive stars have ~ 4 – 6 times higher metallicity than those from intermediate-mass stars (dependent on metallicity; see Fig. 2.1), a higher contribution of the mass-loss from massive stars to the SFR (for fixed SFR_{rec}/SFR) would yield a higher ISM metallicity, and would hence change the relation between SFR_{rec}/SFR and Z_{gas}. As we will show in Section 2.3.3, the contribution to the SFR of the mass-loss from massive stars relative to that from AGB stars varies as a function of stellar mass, and in particular increases at the high-mass end. This introduces a mild mass dependence in the SFR_{rec}/SFR- Z_{gas} and $M_{*,rec}/M_*$- Z_* relations[7]. In order to relate this variation of the relative contribution from different mass-loss channels to an observational diagnostic, we consider the average α-enhancement, $[\alpha/Fe]$, represented by $[O/Fe]$ (as oxygen dominates the α-elements in terms of mass fraction), of ISM gas and stars. The fact that α-elements are predominantly synthesized in massive stars, whereas of iron ~ 50% is contributed by intermediate-mass stars in the form of SN Type Ia explosions and winds from AGB stars (e.g. Wiersma et al., 2009b), makes $[\alpha/Fe]$ a good tracer for the relative importance of massive stars.

Adopting the usual definition of the abundance ratio,

$$\left[\frac{O}{Fe} \right] = \log_{10} \left(\frac{X^O}{X^{Fe}} \right) - \log_{10} \left(\frac{X^O_\odot}{X^{Fe}_\odot} \right), \tag{2.9}$$

where X^x is the mass fraction of element x and $X^O_\odot / X^{Fe}_\odot = 4.44$ is the solar abundance ratio (Asplund et al., 2009), we show $[O/Fe]$ as a function of stellar mass in Fig. 2.5. The curves show the median in logarithmic mass bins of size 0.2 dex that contain at least 10 haloes and correspond to a stellar mass of at least 100 gas particles. The shaded regions mark the 10th to 90th percentile ranges. In both the gas-phase (green, solid) and the stellar phase (blue, solid), $[O/Fe]$ is approximately constant at ~ 0.1 and ~ 0.25, respectively, for $M_* \lesssim 10^{10.5}$ $M_\odot$, but increases with stellar mass for $M_* \gtrsim 10^{10.5}$ $M_\odot$. Comparing this to observations of the stellar $[\alpha/Fe]$ for a sample of 3360 early-type galaxies from Thomas et al. (2010, best-fitting relation, after correcting for the difference in the set of solar abundances used; black dashed line), we find excellent agreement in terms of the slope and the normalization. While this is encouraging, suggesting that we capture the right mass dependence in the SFR_{rec}/SFR- Z_{gas} and $M_{*,rec}/M_*$- Z_* relations and that the cooling rates (which are dominated by oxygen at $T \sim 2 \times 10^5$ K and by iron at $T \sim 10^6$ K; see Wiersma et al., 2009a) employed by the simulation are realistic, the predicted abundance ratio is uncertain by a factor of > 2 due to uncertainties in the nucleosynthetic yields and SN Type Ia rate (Wiersma et al., 2009b). It is therefore somewhat surprising that the agreement in the normalization is this good. If we consider $[Mg/Fe]$, which is another indicator of $[\alpha/Fe]$ often used in the literature, of ISM gas (blue, dotted)

---

[7]Another factor is that the metal yields depend on metallicity (Fig. 2.1). This can change the SFR_{rec}/SFR- Z_{gas} and $M_{*,rec}/M_*$- Z_* relations even if the contributions from the different channels remain fixed. However, even a factor of 100 variation in the metallicity changes the metallicity of the stellar ejecta by only a few percent, which is significantly smaller than the effect of the change in the relative channel contributions in massive galaxies.

and stars (green, dotted), we find an offset of ~ 0.3 dex with respect to the observed $[\alpha/\text{Fe}]$. Note that the size of this offset is dependent on the adopted set of solar abundances. The slope, on the other hand, still matches the observed one, implying that the offset can be attributed to a constant uncertainty factor in the (massive star) yields.

Motivated by the tight power-law relations shown in Fig. 2.4, we fit the relation between the recycled gas contribution to the SFR and ISM metallicity with the following function, including a term describing the variation in the relative channel contributions:

$$\log_{10}\frac{SFR_{\text{rec}}}{SFR} = 0.87\log_{10}Z_{\text{gas}} - 0.40\left[\frac{\text{O}}{\text{Fe}}\right]_{\text{gas}} + 0.90, \qquad (2.10)$$

where the values of the three free parameters have been obtained using least square fitting. Note that the metallicity Z is the average mass fraction of metals and is thus independent of the adopted solar value. Similarly, we determine the best-fitting relation between the recycled gas contribution to the stellar mass and stellar metallicity:

$$\log_{10}\frac{M_{*,\text{rec}}}{M_*} = 0.91\log_{10}Z_* - 0.28\left[\frac{\text{O}}{\text{Fe}}\right]_* + 0.92. \qquad (2.11)$$

We show these relations in Fig. 2.4 for galaxies with $M_* \sim 10^{9.5}$ $M_\odot$ (red, solid line), $M_* \sim 10^{10.5}$ $M_\odot$ (blue, dot-dashed line) and $M_* \sim 10^{11.5}$ $M_\odot$ (purple, dashed line), where we use the median values of $[\alpha/\text{Fe}]_{\text{gas}}$ and $[\alpha/\text{Fe}]_*$ in stellar mass bins of 0.2 dex centred on the respective masses. As expected from Fig. 2.5, the relations at $M_* \sim 10^{9.5}$ $M_\odot$ and $M_* \sim 10^{10.5}$ $M_\odot$ are consistent, as a result of the median $[\alpha/\text{Fe}]$ (of gas and stars) being constant for $M_* \lesssim 10^{10.5}$ $M_\odot$. On the other hand, galaxies with $M_* \sim 10^{11.5}$ $M_\odot$ have SFR_{rec}/SFR and $M_{*,\text{rec}}/M_*$ that are ~ 0.06 and ~ 0.04 dex *lower* at fixed metallicity due to an enhancement in the contribution from massive stars relative to that from intermediate-mass stars (reflected by their enhanced $[\alpha/\text{Fe}]$ abundance ratio). These offsets are somewhat larger than the 1σ scatter in the relation for all galaxy masses (which is set by the scatter at $M_* < 10^{10}$ $M_\odot$), indicating that the variation of the channel contributions at $M_* > 10^{10.5}$ $M_\odot$ significantly impacts upon the relation between metallicity and recycling-fuelled star formation in high-mass galaxies. It leads to a reduction of SFR_{rec}/SFR and $M_{*,\text{rec}}/M_*$ at fixed metallicity that increases with stellar mass, and will therefore make any turnover or flattening at the high-mass end of the relation between recycled gas contributions and stellar mass (as seen in the mass-metallicity relation; see Tremonti et al., 2004; Gallazzi et al., 2005; Kewley & Ellison, 2008; Andrews & Martini, 2013; Zahid et al., 2014a) more pronounced. We demonstrate the useful link that equations (2.10) and (2.11) provide between the importance of gas recycling and observational diagnostics in Section 2.3.3.

We note that the parameters of equations (2.10) and (2.11) are insensitive to the specific implementation of subgrid processes like star formation, stellar feedback and AGN feedback[8], as for EAGLE changing their implementation affects the

---

[8]The adopted IMF is an exception, as it determines the mass and metallicity of gas returned by stellar populations, as well as the relative contribution from massive stars with respect to intermediate-mass stars.

recycled gas contributions and metallicities in a similar way. Note that this may not be true if the metallicity of galactic winds differs significantly from the metallicity of the ISM, as might for example happen if metals are preferentially ejected (e.g. Mac Low & Ferrara, 1999; Creasey et al., 2015), or if instead galactic winds are metal-depressed (e.g. Zahid et al., 2014b).

2.3.3   Dependence on halo and galaxy mass at $z = 0$

In this section, we investigate how the fractional contribution of recycled gas to the present-day SFR and stellar mass of galaxies depends on their halo and stellar mass. Note that, because of the tight relation with metallicity that we established in Section 2.3.2, many conclusions that we draw here carry over to the mass-metallicity relation. We study both central (Section 2.3.3) and satellite (Section 2.3.3) galaxies and, in addition to the total contribution of gas recycling, assess the relative significance of the different mass-loss channels (Section 2.3.3). We also briefly explore how fuelling by gas recycling depends on the distance from the galactic centre (Section 2.3.3). While we mainly present results from our fiducial *Ref-L100N1504* simulation, we also show a brief comparison with the results from *Recal-L025N0752* for central galaxies.

Gas recycling in central galaxies

Fig. 2.6 shows the contribution of recycled stellar mass-loss to the present-day SFR and stellar mass of central galaxies as a function of their mass in the *Ref-L100N1504* (red) and *Recal-L025N0752* (purple) simulations. We plot $SFR_{\rm rec}/SFR$ in the top row and $M_{*,\rm rec}/M_*$ in the bottom row as a function of subhalo mass (left-hand column) and stellar mass (right-hand column). Focusing first on the fiducial *Ref-L100N1504* simulation, the general trend in all four panels is that, at masses $M_{\rm sub} \lesssim 10^{12.2}\ {\rm M_\odot}$ or $M_* \lesssim 10^{10.5}\ {\rm M_\odot}$, the fraction of the SFR and stellar mass contributed by recycling increases with mass. This is the regime where the greater depth of the gravitational potential well, as well as the higher pressure and density of the ISM and CGM, towards higher masses, make it harder for feedback (dominated by star formation) to eject gas from the galaxy. As we will show explicitly with a model comparison in Section 2.4, a reduced efficiency of stellar feedback at driving galactic outflows enhances the contribution from recycled gas to the SFR and stellar mass. This can be understood by considering that these winds (if stellar feedback is efficient) are launched from the dense star-forming regions with relatively high abundances of gas from stellar mass-loss. Hence, more efficient winds will preferentially reduce $SFR_{\rm rec}$ with respect to the total SFR (thereby reducing $SFR_{\rm rec}/SFR$), whereas in the case of less efficient winds this effect will be less (thereby enhancing $SFR_{\rm rec}/SFR$).

At the high-mass end, $SFR_{\rm rec}/SFR$ and $M_{*,\rm rec}/M_*$ turn over at $M_* \sim 10^{10.5}\ {\rm M_\odot}$ ($M_{\rm sub} \sim 10^{12.2}\ {\rm M_\odot}$), and then decrease and remain constant, respectively, at higher masses. In this mass regime, the trend is regulated by the efficiency of the feedback from AGN, which becomes stronger in more massive systems. Even though this type of feedback is not associated with any replenishment of the ISM gas reservoir (as
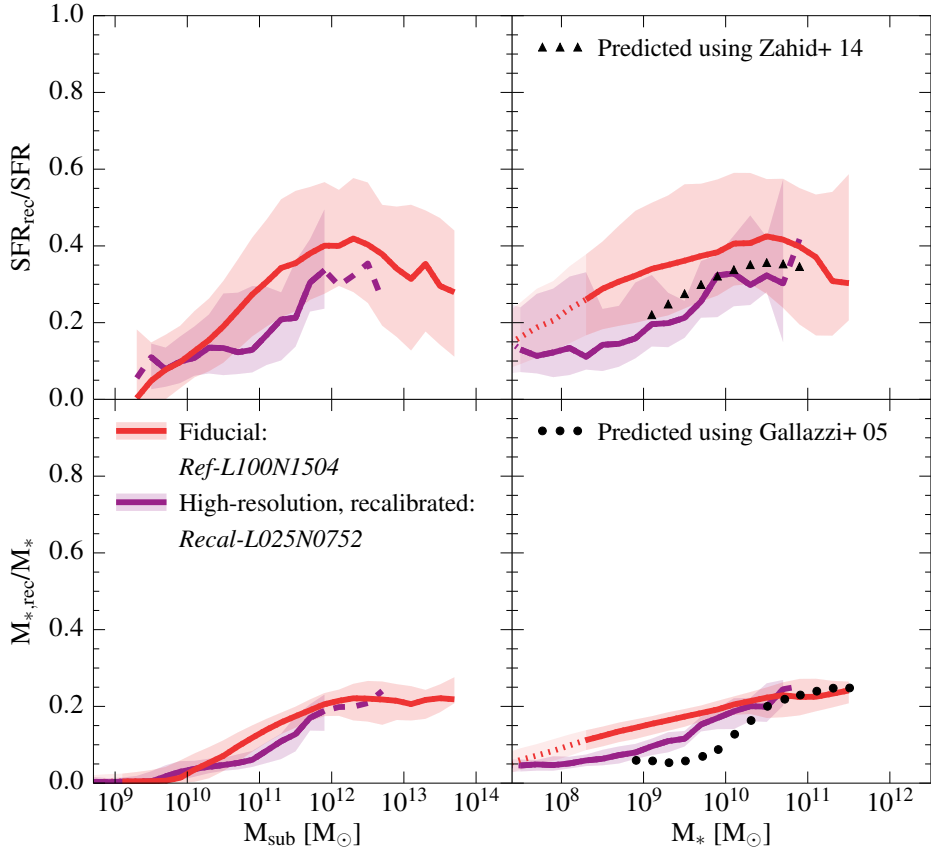
Figure 2.6: The fractional contribution of gas recycled from stellar mass-loss to the SFR (top) and stellar mass (bottom) of central galaxies at $z = 0$ as a function of their subhalo mass (left) and stellar mass (right). We show the results for the fiducial EAGLE model (*Ref-L100N1504*; red) and the high-resolution, re-calibrated model (*Recal-L025N0752*; purple). We only consider subhaloes with a non-zero SFR (top panels) or a non-zero stellar mass (bottom panels). The curves show the median value in each logarithmic mass bin of size 0.2 dex, if it contains at least 10 galaxies. The shaded regions mark the 10th to 90th percentile ranges. The solid curves become dotted when the subhalo (stellar) mass corresponds to fewer than 100 dark matter (baryonic) particles and become dashed (for *Recal-L025N0752* only) when there are less than 10 haloes per bin. The contribution of recycled gas to the SFR and stellar mass first increases with mass, turns over at $M_* \sim 10^{10.5}$ M$_\odot$ ($M_{sub} \sim 10^{12.2}$ M$_\odot$), and then decreases or remains constant at higher mass. This trend is regulated by the efficiency of the feedback from star formation (AGN) at low (high) masses: galactic winds eject gas from the ISM, where stellar mass-loss accumulates, and therefore preferentially reduce the SFR and stellar mass contributed by recycling. The black points represent our best estimate of the recycled gas contributions to the SFR and stellar mass (for a central galaxy with a Milky Way-like mass: 35% and 20%, respectively), calculated by applying equations (2.10) and (2.11) to the observed gas-phase metallicities from Zahid et al. (2014a) and the observed stellar metallicities from Gallazzi et al. (2005). For $M_* \gtrsim 10^{10}$ M$_\odot$, these estimates agree to better than a factor of ~ 1.6 (0.2 dex) with the median predictions computed directly from EAGLE.

opposed to feedback from star formation, which directly provides the gas for recycling), it does have a significant impact on the rate at which galaxies consume the enriched ISM gas. If AGN are efficient at launching galactic outflows, they preferentially remove or disperse the dense ISM gas from the central regions, in which the abundance of stellar ejecta is high, thereby reducing SFR_{rec}/SFR and $M_{*,rec}/M_*$.

We note that while AGN feedback regulates the turnover at $M_* \sim 10^{10.5}$ $M_\odot$, the use of the 30 pkpc 3D aperture also plays a role in shaping the behaviour of SFR_{rec}/SFR and $M_{*,rec}/M_*$ at the high-mass end. As we show in Appendix 2.C, SFR_{rec}/SFR and $M_{*,rec}/M_*$ at $M_* \gtrsim 10^{10.5}$ $M_\odot$ ($M_{sub} \gtrsim 10^{12.2}$ $M_\odot$) are somewhat enhanced, and their slopes become somewhat shallower, if an aperture is applied. This is consistent with the fraction of the SFR and stellar mass fuelled by recycled gas being larger in the inner parts of galaxies (see Fig. 2.10). Without an aperture, $M_{*,rec}/M_*$ decreases with halo and galaxy mass (similar to SFR_{rec}/SFR), instead of remaining roughly constant if an aperture is applied.

At the mass scale of the turnover, the fractional contribution of recycled gas to the SFR is at a maximum. A galaxy of this mass, $M_* \sim 10^{10.5}$ $M_\odot$, is too massive to have effective star formation-driven outflows but still too small for AGN feedback to be effective. Not surprisingly, this mass scale coincides with the peak in the galaxy formation efficiency (see fig. 8 of Schaye et al., 2015), which is consistent with the efficiency of feedback being the main driver of SFR_{rec}/SFR and $M_{*,rec}/M_*$. The fiducial EAGLE model indicates that for a Milky Way-like galaxy, which is at the peak of the galaxy formation efficiency, 40% of its present-day SFR and 20% of its present-day stellar mass is due to the recycling of stellar mass-loss.

Because of the tight correlation between recycling-fuelled star formation and metallicity, our findings have direct implications for the origin of the mass-metallicity relations for ISM gas and stars. They imply that the increase in metallicity with stellar mass at $M_* \lesssim 10^{10.5}$ $M_\odot$ is due to the decreasing efficiency of stellar feedback at driving galactic outflows, while the shape at higher mass is governed by the efficiency of AGN feedback (see also Zahid et al., 2014b; Peeples et al., 2014; Creasey et al., 2015, for discussion on the relation between feedback and metallicity). Conversely, the difference between the *Ref-L100N1504* and *Recal-L025N0752* simulations in Fig. 2.6, as well as their (expected) agreement with observations, should mimic the results for the mass-metallicity relation (see fig. 13 of Schaye et al., 2015). Indeed, while *Ref-L100N1504* and *Recal-L025N0752* yield similar trends, they do differ quantitatively by a factor of ~ 2 (0.3 dex) in SFR_{rec}/SFR and $M_{*,rec}/M_*$ at $M_* \sim 10^9$ $M_\odot$ ($M_{sub} \sim 10^{11}$ $M_\odot$). This difference decreases towards higher masses, where for $M_* \gtrsim 10^{9.8}$ $M_\odot$ ($M_{sub} \gtrsim 10^{11.6}$ $M_\odot$), *Ref-L100N1504* and *Recal-L025N0752* are converged in terms of $M_{*,rec}/M_*$ and broadly consistent in terms of SFR_{rec}/SFR (considering the substantial amount of scatter and relatively poor sampling of the high-mass regime by the *Recal-L025N0752* model). Schaye et al. (2015) showed that for $M_* \gtrsim 10^{9.8}$ $M_\odot$, the metallicities of galaxies in *Ref-L100N1504* and *Recal-L025N0752* agree with the observations equally well. They agree with the observed gas-phase metallicities from Zahid et al. (2014a) to better than 0.1 dex and with Tremonti et al. (2004) to better than 0.2 dex, and with the observed stellar metallicities from Gallazzi et al. (2005) to within the observational uncertainties (which are > 0.5 dex at $M_* < 10^{10}$ $M_\odot$ and smaller at higher masses). For

$M_* \lesssim 10^{9.8}$ M$_\odot$, on the other hand, the metallicities of galaxies in *Recal-L025N0752* are in better agreement with the observations, from which we conclude that the values of SFR_{rec}/SFR and $M_{*,rec}/M_*$ predicted by *Recal-L025N0752* are more reliable than those predicted by the fiducial model. Note, however, that the large systematic uncertainties associated with the calibration of the diagnostics prevent any strong conclusions. In order to limit the number of model curves plotted in each figure, from here on we only plot the results from *Ref-L100N1504* and ask the reader to keep in mind the slight overprediction of SFR_{rec}/SFR and $M_{*,rec}/M_*$ at $M_* \lesssim 10^{9.8}$ M$_\odot$.

Finally, in contrast to the predictions computed directly from EAGLE, which at low masses depend on the adopted numerical resolution, the relations between gas recycling and metallicity given in equations (2.10) and (2.11) provide a way of estimating SFR_{rec}/SFR and $M_{*,rec}/M_*$, that is independent of the resolution. Moreover, these relations are insensitive to the subgrid models for feedback. We apply the relations to the observed mass-metallicity relations from Zahid et al. (2014a) and Gallazzi et al. (2005), using the median [O/Fe] from EAGLE in each stellar mass bin, to estimate SFR_{rec}/SFR (triangular points, upper-right panel of Fig. 2.6) and $M_{*,rec}/M_*$ (circular points, lower-right panel of Fig. 2.6) as a function of stellar mass. These estimates agree qualitatively with SFR_{rec}/SFR and $M_{*,rec}/M_*$ computed directly from the fiducial EAGLE model, showing a steep increase with mass for $M_* \lesssim 10^{10.5}$ M$_\odot$, followed by turnover and even a slight downturn in SFR_{rec}/SFR at higher masses[9]. Quantitatively, the black points are in good agreement with the fiducial EAGLE model for $M_* \gtrsim 10^{10}$ M$_\odot$ and with *Recal-L025N0752* also at lower masses, as expected from the comparison of the mass-metallicity relation with the observations presented in Schaye et al. (2015). If the discrepancy between the predicted and observed mass-metallicity relation exceeds the systematic error due to calibration uncertainties in the observations, then the black points represent our best estimates of the recycled gas contributions to the SFR and stellar mass. For a Milky Way-like galaxy ($M_* \sim 10^{10.5}$ M$_\odot$), we find these contributions to be 35% and 20%, respectively.

Gas recycling in satellite galaxies

Having studied the recycling-fuelled star formation in present-day central galaxies, we now compare these with the results for present-day satellite galaxies. Fig. 2.7 shows the SFR and stellar mass contributed by recycling for both central (red; as in Fig. 2.6) and satellite (blue) galaxies, as predicted by the fiducial *Ref-L100N1504* simulation. In general, these are broadly similar for centrals and satellites. However, we identify two important differences. First, in the left panels, where we show the two ratios as a function of subhalo mass, the relations for satellite galaxies are shifted towards lower masses relative to those for central galaxies. Satellites lose a fraction of their dark matter subhalo mass (but less stellar mass) upon infall on to

---

[9]Note that, even though the mass-metallicity relation observed by Zahid et al. (2014a) does not exhibit a decrease in the metallicity at the high-mass end, the recycled gas contribution to the SFR can still show a slight downturn, due to the change in the relative contributions from the different mass-loss channels (as discussed in Section 2.3.2).
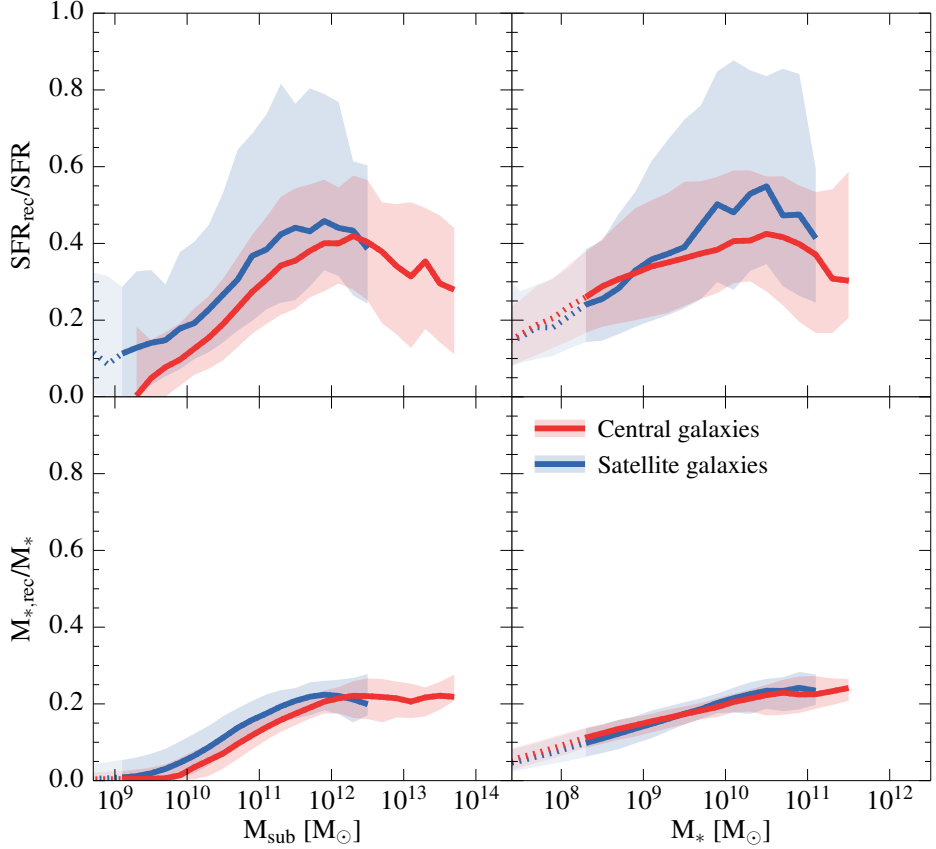
Figure 2.7: As Fig. 2.6, but showing the results for central (red) and satellite (blue) galaxies from the fiducial EAGLE model. The recycled gas contributions to the SFR and stellar mass in satellites are broadly consistent with the ones in similarly massive centrals, since the efficiency of stellar and AGN feedback is the controlling factor in fuelling star formation with recycled gas. However, in the inefficient feedback regime ($M_* \sim 10^{10.5}$ $M_\odot$), satellites with low gas fractions can reach recycling-fuelled SFR fractions as high as $\sim 90\%$, with a median that exceeds the one in similarly massive centrals (see also Fig. 2.8).

the group dark matter halo as a result of tidal stripping. Hence, this shift illustrates the fact that satellite galaxies live in smaller (sub)haloes than central galaxies of similar stellar mass. Secondly, in the top-right panel, at a mass scale of $M_* \sim 10^{10.5}$ $M_\odot$, satellites show significantly higher SFR_{rec}/SFR (with a median of ~ 0.5 and a 90th percentile value of ~ 0.85) than centrals, whereas at lower and higher masses this difference is smaller. Hence, in the regime where both stellar feedback and AGN feedback are relatively inefficient, gas recycling plays a more important role in fuelling ongoing star formation in satellite galaxies than in central galaxies. For $M_{*,rec}/M_*$, on the other hand, there is no difference between centrals and satellites, because satellites formed the majority of their stars while they were still centrals.

To get a better understanding of the difference between centrals and satellites, we consider the relation between SFR_{rec}/SFR and specific SFR ($= SFR/M_*$, sSFR). Fig. 2.8 shows this relation for centrals (upper panels) and satellites (lower panels) with masses $10^{9.5}$ $M_\odot < M_* < 10^{10.5}$ $M_\odot$ (left) and $10^{10.5}$ $M_\odot < M_* < 10^{11.5}$ $M_\odot$ (right), where the histograms at the top compare the distributions of sSFRs. In order to limit the dynamical range plotted, galaxies with $SFR/M_* < 10^{-12}$ yr^{-1} are shown as upper limits. The colour coding indicates the mass of the parent dark matter halo, M_{200}, in which these galaxies reside. For centrals, M_{200} is generally closely related to the mass of the subhalo and the stellar mass, whereas for satellites the mass of the host halo they have fallen on to is only weakly related to their own mass. For satellites, M_{200} instead serves as a proxy for the strength of any environmental effects like ram-pressure stripping (Gunn & Gott, 1972) or strangulation (Larson et al., 1980).

Focusing first on the centrals in the lower stellar mass bin, we see a clear anticorrelation between the fraction of the SFR that is fuelled by recycling and the sSFR. This can be explained by the fact that sSFR is closely related to the gas fraction ($= M_{gas}/(M_{gas} + M_*)$ with M_{gas} the ISM mass): higher gas fractions generally correspond to higher sSFRs. Also, since the ISM is comprised of both processed and unprocessed gas, whereas stellar mass only provides enriched gas for recycling, an enhanced gas fraction typically implies that a greater fraction of the star formation in the ISM is fuelled by unprocessed, 'non-recycled' gas (i.e. SFR_{rec}/SFR is low). On the other hand, galaxies with a low sSFR and a correspondingly low gas fraction will have a higher fraction of their SFR contributed by recycling. Considering the centrals in the higher mass bin, we see that while part of this relation is still in place, a significant fraction lies away from the main relation towards the lower left. This is the result of efficient AGN feedback, which suppresses both the sSFR ('quenching') and the SFR_{rec}/SFR of galaxies, as AGN feedback is more important at higher halo masses. This explanation is consistent with the enhanced halo masses of the galaxies in this regime ($M_{200} \sim 10^{13}$ $M_\odot$ for centrals with $SFR/M_* \sim 10^{-11.5}$ yr^{-1} and $SFR_{rec}/SFR \sim 0.2$, compared to $M_{200} \sim 10^{12}$ $M_\odot$ for centrals with $SFR/M_* \sim 10^{-10.5}$ yr^{-1} and $SFR_{rec}/SFR \sim 0.5$). At even higher central galaxy mass scales than shown in Fig. 2.8, the anticorrelation between sSFR and SFR_{rec}/SFR disappears entirely. Instead, the relation transforms into an AGN feedback-controlled *correlation* (although weak due to small number statistics, with a Pearson correlation coefficient of 0.43 for $M_* > 10^{11.0}$ $M_\odot$), such that the galaxies with the lowest sSFRs have the lowest recycling-fuelled SFRs.

Having investigated the mechanism driving the sSFR - SFR_{rec}/SFR trends in the two mass regimes for centrals, we now consider satellites. In the lower mass bin the anticorrelation between sSFR and SFR_{rec}/SFR is similar to that for centrals, although the histogram at the top shows that the sSFR distribution for satellites has larger scatter towards low sSFRs. This corresponds to a population of satellite galaxies at $SFR/M_* \sim 10^{-11}$ yr^{-1} with fractional contributions of recycled gas to their SFR as high as 90 – 95%. This high-SFR_{rec}/SFR regime is more frequently populated by satellites than similarly massive centrals, reflecting the substantially greater scatter in the satellite curves towards high values of SFR_{rec}/SFR at $M_* \sim 10^{10.5}$ seen in Fig. 2.7. As indicated by the colour coding in Fig. 2.8, this population of satellites is hosted by relatively massive group dark matter haloes ($M_{200} \sim 10^{14}$ M$_\odot$), implying that their low sSFRs and gas fractions are the result of the cessation of fresh gas infall (either because cooling is inefficient or because the satellite's hot gas reservoir was stripped), and/or a (partial) removal of cold gas from the disc (see e.g. Bahé & McCarthy, 2015; Mistani et al., 2016). Both scenarios lead to a depletion of the ISM gas reservoir and a greater dependence on stellar mass-loss for replenishing it.

Finally, we focus on the satellite galaxies in the higher mass bin, shown in the bottom-right of Fig. 2.8. Whereas most similarly massive central galaxies that have moved away from the sSFR - SFR_{rec}/SFR anticorrelation, have moved towards low sSFR and low SFR_{rec}/SFR under the influence of AGN feedback, there is still a significant population of satellite galaxies occupying the high-SFR_{rec}/SFR region. Inspecting the masses of the BHs residing in these satellites (not shown) we see that they are significantly lower than the masses of BHs in centrals of similar stellar mass. We infer that this is again due to the depletion of the satellite ISM gas, thereby preventing efficient BH growth. This explains why the AGN feedback in these satellites is unable to suppress the recycled gas contribution to the SFR.

We conclude that the SFR and stellar mass contributed by recycling are broadly consistent between central and satellite galaxies over a wide range of galaxy masses, because gas recycling is governed primarily by the efficiency of stellar and AGN feedback. However, in satellites with a stellar mass similar to that of the Milky Way, the mass scale at which feedback is least efficient at suppressing star formation, the recycled gas contribution to the SFR often exceeds the one in similarly massive centrals (and can even reach $\gtrsim$ 90%), as the depletion of their ISM gas reservoir makes them more reliant on stellar mass-loss for fuelling ongoing star formation.

Our findings are consistent with the observational inference that, at a given stellar mass, satellites are more metal-rich than centrals (Pasquali et al., 2012; Peng & Maiolino, 2014). We explain the origin of their different mass-metallicity relation as a consequence of satellites being subject to environmental processes like ram-pressure stripping and strangulation, which prevent the dilution of the ISM reservoir by metal-poor gas.

Contributions from AGB stars, SN Type Ia and massive stars

To assess the relative significance of the different stellar mass-loss channels for fuelling star formation in present-day centrals and satellites, we show in Fig. 2.9 the
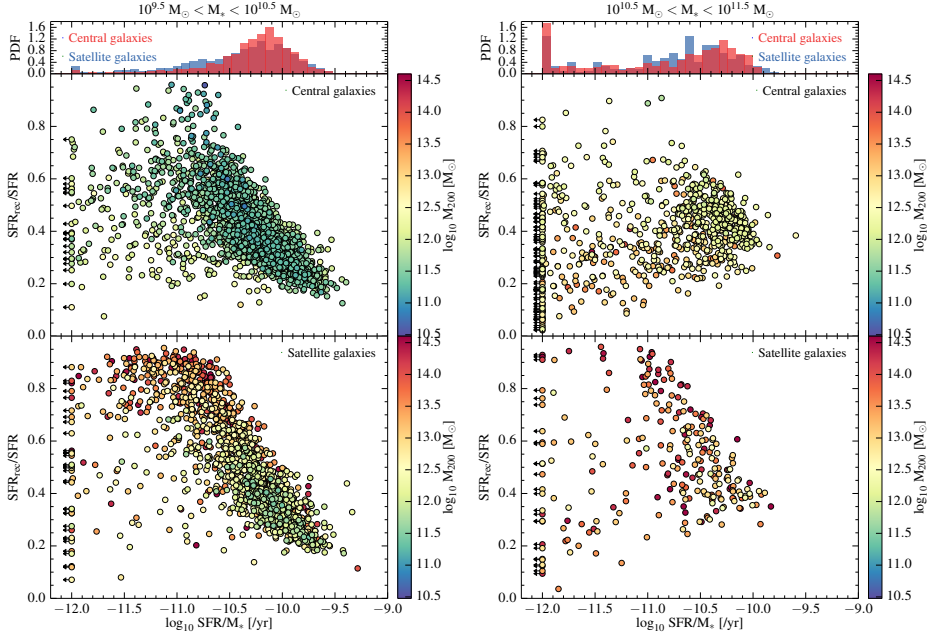
Figure 2.8: The SFR fuelled by recycling as a function of sSFR (= SFR/M_*), colour-coded by host halo mass (M_{200}), for central galaxies (upper panels) and satellite galaxies (lower panels) with stellar masses $10^{9.5}$ $M_\odot$ < M_* < $10^{10.5}$ $M_\odot$ (left) and $10^{10.5}$ $M_\odot$ < M_* < $10^{11.5}$ $M_\odot$ (right). The histograms at the top show the distributions of the sSFR for centrals and satellites in these two mass bins. Galaxies with SFR/M_* < 10^{-12} yr^{-1} are shown as upper limits. For the centrals, the relation between the recycling-fuelled SFR and the sSFR changes from an anticorrelation at lower mass, which is a result of the tight relation with ISM gas fraction, to a (weak) correlation at higher mass, which is driven by AGN feedback. The satellites, on the other hand, show a similar behaviour, but retain in both mass ranges a large population of low-sSFR galaxies that rely heavily on stellar mass-loss for fuelling ongoing star formation (contributing ≳ 90%).
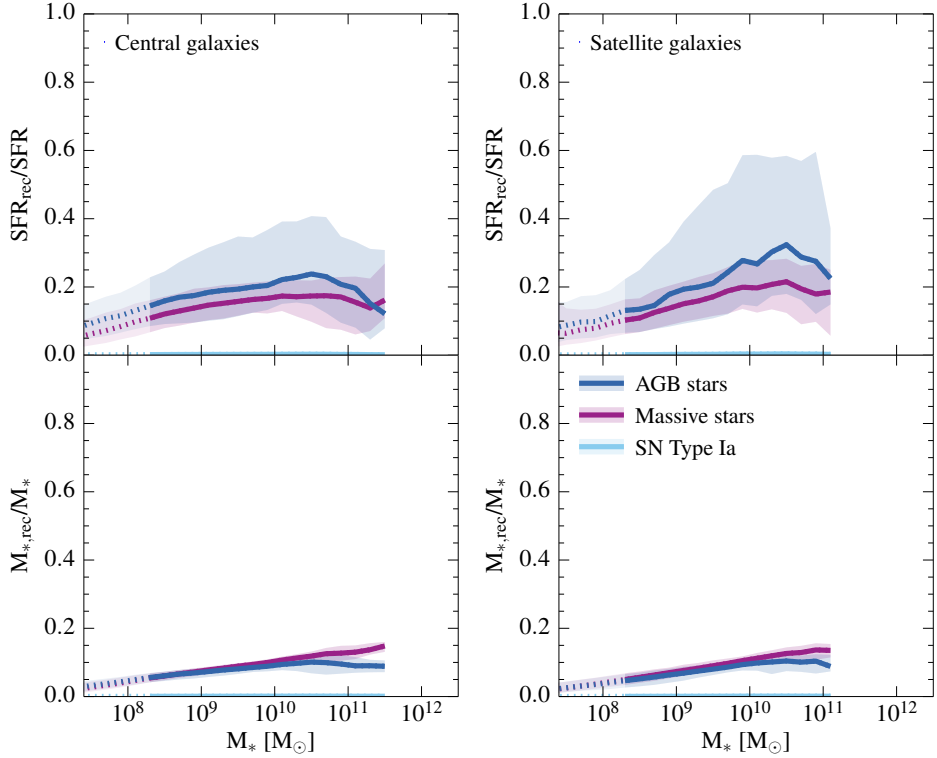
Figure 2.9: The contribution of gas from AGB stars (blue), massive stars (purple) and SN Type Ia (cyan) to the SFR (top) and stellar mass (bottom) of galaxies at $z = 0$ as a function of their stellar mass. The results for centrals and satellites are shown in the left- and right-hand panels, respectively. The curves and shaded regions indicate the medians and 10th to 90th percentile ranges, as in Fig. 2.7. In general, the gas from AGB stars and massive stars contributes about equally to the SFR and stellar mass in both centrals and satellites. However, there is a slight enhancement in the contribution from AGB stars to the SFR at all but the highest mass scales, due to the preferential removal of massive star ejecta by star formation-driven winds and by lock up in stellar remnants. AGB ejecta are also responsible for the high *SFR*rec/*SFR* values of some satellites, since these environmentally quenched objects have low sSFRs and cannot accrete gas. At the high-mass end, the relative contribution from AGB ejecta declines, because AGN feedback (which is unimportant at low mass) can drive them out even in the absence of star formation.

contribution of recycled gas to the SFR (top panels) and stellar mass (bottom panels) split into the contributions from AGB stars (blue), massive stars (purple) and SN Type Ia (cyan). These are plotted as a function of galaxy stellar mass for centrals (left panels) and satellites (right panels) at $z = 0$.

From the top panels, we see that AGB stars are of greater importance for fuelling present-day star formation than massive stars in all but the most massive central galaxies. Up to 24% (32%) of the SFR in centrals (satellites) is fuelled by gas recycled from AGB stars, while $\lesssim 17\%$ ($\lesssim 20\%$) is fuelled by gas from massive stars. Integrated over cosmic history (as quantified by $M_{*,\mathrm{rec}}/M_*$ in the lower panels), their contributions are approximately equal at all but the highest mass scales. This may appear difficult to reconcile with the timed mass release from intermediate-mass and massive stars for a single SSP presented in Fig. 2.1, where we showed that massive stars are the dominant source of (integrated) mass-loss for SSP ages $\lesssim 1$ Gyr and that massive stars and AGB stars contribute about equally at higher ages. Fig. 2.9 implies that stellar ejecta do not simply accumulate in the ISM, but that they are removed, either by star formation or by outflows, in a way that affects the ejecta from AGB stars and massive stars differently[10].

The ejecta from massive stars are released almost instantaneously compared to those from AGB stars (see Fig. 2.1). This means that, before AGB stars start to contribute significantly to the recycled gas, secondary generations of stars will already have formed from the massive star ejecta, causing an increasing fraction of these ejecta to become locked up in stellar remnants. While they then still contribute to the stellar mass of the galaxy, they no longer fuel ongoing star formation. Furthermore, a considerable amount of gas from massive stars will already have been ejected in galactic winds, before the AGB stars shed most of their mass. As a result, the contribution from massive stars to the present-day SFR is suppressed compared to that from AGB stars.

In general, if stars are older, the surrounding gas will contain a higher fraction of ejecta from intermediate-mass stars than from massive stars. This means that, at fixed stellar mass, galaxies with a low SFR (which includes passive galaxies) are expected to contain enhanced fractions of AGB ejecta, as only newly formed stars produce massive star ejecta, while evolved, intermediate-mass stars still shed mass in AGB winds. Not surprisingly, we see that the scatter to high values of SFR_{rec}/SFR for satellites with masses 10^{10} M$_\odot < M_* < 10^{11}$ M$_\odot$ (upper-right panel of Fig. 2.7) is mainly due to satellites with large fractions of the AGB ejecta being recycled, consistent with their low sSFRs (Fig. 2.8)[11].

Finally, in massive galaxies ($M_* \gtrsim 10^{10.5}$ M$_\odot$), there is a decline of the

---

[10]As our findings in Sections 2.3.3 and 2.3.3 already imply, the relation between the mass-loss from individual SSPs and the contribution of this mass-loss to the SFR and stellar mass on galactic scales is not straightforward, since the rate of gas accretion and the efficiencies of stellar and AGN feedback depend on the mass of the galaxy.

[11]Despite the shallow, but significant, decrease in the sSFRs with mass of galaxies with $M_* \lesssim 10^{10.5}$ M$_\odot$ (shown in fig. 11 of Schaye et al., 2015), we do not see an increase in the SFR_{rec}/SFR from AGB stars *relative* to SFR_{rec}/SFR from massive stars in this mass range. Note that we are now considering the *ratio* of the blue and purple curves in the upper and lower left panels (focusing on central galaxies). Instead, the relative contribution from massive stars, both to the SFR (upper panels) and stellar mass (lower panels), remains approximately constant. This is due to a competing effect, namely the decrease in star formation feedback efficiency, which mitigates the preferential expulsion of massive star ejecta.

$SFR_{\rm rec}/SFR$ and $M_{*,\rm rec}/M_*$ contributed by AGB stars, while the contributions from massive stars decrease only mildly (or flatten). This is consistent with the increase in the [O/Fe] abundance ratio, as shown in Fig. 2.5 of Section 2.3.2, where we discussed that this change in the relative significance of the different mass-loss channels introduces a mass dependence in the relation between recycling-fuelled star formation and metallicity. We attribute this effect to 'downsizing', a scenario in which the bulk of the stars in more massive galaxies has formed earlier and over a shorter period of time than in lower-mass counterparts (e.g. Cowie et al., 1996; Neistein et al., 2006; Cattaneo et al., 2008; Fontanot et al., 2009).

The rapid and efficient star formation in the progenitors of present-day massive galaxies is however suppressed at later times, when these progenitors have grown massive enough for AGN feedback to become efficient and the gas cooling rates to drop. Moreover, while winds driven by feedback from star formation will not be available to drive out AGB ejecta in quenched galaxies, AGN feedback can. Hence, this scenario is consistent with the reduction in the contribution from AGB stars, relative to that from massive stars, to both the SFR (upper panels) and the stellar mass (lower panels) at the highest mass scales shown in Fig. 2.9.

We infer that galaxies generally obtain most of their metals from massive star ejecta, as these ejecta have $4-6$ times higher metallicity than those from AGB stars, while the fraction of the (total) ISM mass and stellar mass contributed by massive star ejecta is similar to that contributed by AGB ejecta. This holds for metals in the gas-phase, but even more so for metals in the stellar phase. In both cases, the metal content contributed by massive star ejecta increases at the high-mass end ($M_* \gtrsim 10^{10.5}$ $M_\odot$) of the mass-metallicity relation. This is reflected by the trend of [O/Fe] with stellar mass as presented in Fig. 2.5, and is consistent with the abundance ratio trends observed for early-type galaxies (e.g. Schiavon, 2007; Thomas et al., 2010; Johansson et al., 2012; Conroy et al., 2014). Our results imply that this α-enhancement of massive galaxies is a consequence of AGN feedback.

Radial dependence of gas recycling

Having explored the importance of gas recycling on galaxy-wide scales, we now briefly investigate how the significance of recycling for fuelling star formation depends on the distance from the galactic centre. Note that the robustness of the results that we present in this section depends on the ability of the simulation to reproduce observed metallicity gradients. In addition, the results are subject to numerical uncertainties, like the mixing of metals, which may be underestimated by SPH simulations (see Wiersma et al., 2009b). This will be investigated in a future paper. In Fig. 2.10, we plot, similar to the left-hand column of Fig. 2.9, the contribution of gas from AGB stars (blue), massive stars (purple) and SN Type Ia (cyan) to the SFR (top) and stellar mass (bottom) of centrals at $z = 0$, now separated into gas and stars inside (solid lines) and outside (dashed lines) the stellar half-mass radius. This radius, denoted by R_{50}, is the 3D radius that encloses 50% of the stellar mass bound to the subhalo (within the 30 pkpc 3D aperture). It is typically ~ 4 pkpc for a $M_* \sim 10^{10}$ $M_\odot$ galaxy. Note that we split both the numerator and the denominator of $SFR_{\rm rec}/SFR$ and $M_{*,\rm rec}/M_*$ into $R < R_{50}$ and $R > R_{50}$. We also plot the total
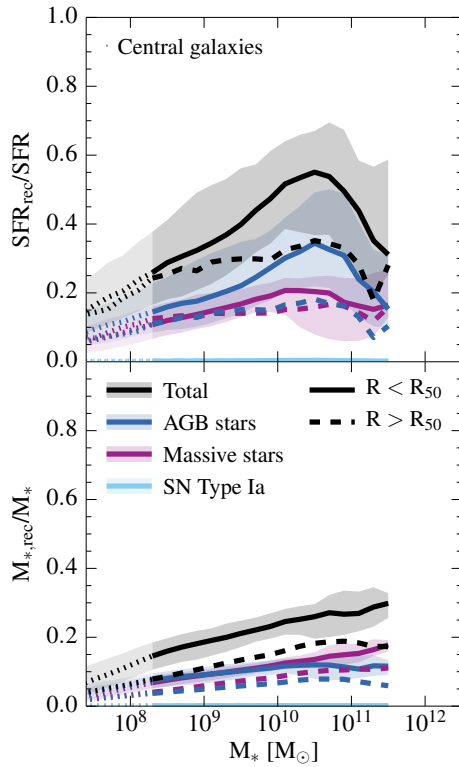
Figure 2.10: As the left-hand column of Fig. 2.9, but split into gas and stars inside the stellar half-mass radius R_{50} (solid) and outside R_{50} (dashed). The 10th to 90th percentile ranges are only shown for inside R_{50}. Gas recycling is more important for fuelling star formation (at the present day and in the past) in the inner parts of galaxies than in the outskirts. Consistent with inside-out growth, the gas in the central regions is comprised of an enhanced fraction of AGB ejecta, which is the main driver of the greater contribution of gas recycling to the star formation within R_{50}.

recycled gas contribution (black), which is the sum over the three stellar mass-loss channels, to the SFR and stellar mass in these two radial regimes.

Focusing first on the total (black lines), both panels consistently show that gas recycling is more important for fuelling star formation (at the present day and in the past) in the central parts of galaxies than in the outskirts. This is consistent with the observational inference that galaxies grow in an inside-out fashion (e.g. Muñoz-Mateos et al., 2007; Patel et al., 2013), with the oldest stars residing in the centre and the replenishment of the gas reservoir by late infall being primarily significant in the outskirts of the disc (owing to its relatively high angular momentum). From the black curves in the upper panel we see that, at the peak value, 55 – 60% of the SFR inside R_{50} is due to stellar mass-loss, compared to only 35 – 40% outside R_{50}. As a result, also a higher fraction of the stellar mass inside R_{50} comes from recycling, ~ 30% at the mass scale where recycling is most significant, compared to ~ 20% in the outskirts.

To investigate what drives this radial dependence, we turn to the relative significance of the different sources of mass-loss. While outside R_{50} AGB stars (blue, dashed) and massive stars (purple, dashed) contribute about equally to the SFR for all masses, inside R_{50} the contribution from AGB stars (blue, solid) is significantly larger than the contribution from massive stars (purple, solid). As discussed in the previous section, the gas around older stellar populations contains higher fractions of AGB ejecta. Hence, the difference between the inner and outer parts reflects the radial age gradient of the stars, due to the inside-out growth of the galaxy.

The drop in the AGB contribution at the high-mass end that we saw in Fig. 2.9, is present in both the inner and outer parts, but it is much stronger near the galactic centre. This is consistent with it being due to a lack of intermediate-age stars and the ability of AGN to drive out the AGB ejecta even in the absence of star formation.

The radial variation of SFR_{rec}/SFR and $M_{*,\mathrm{rec}}/M_*$ is consistent with the negative metallicity gradients observed in local disc galaxies (e.g. Zaritsky et al., 1994; Moustakas et al., 2010; Sánchez et al., 2014). Our results imply that, although the majority of the metals in galaxies (both in the ISM and stars) comes from massive star ejecta, the relative contribution from AGB ejecta is on average larger near the galactic centre than in the outskirts. This holds in particular for the ISM metal content of Milky Way-like ($M_* \sim 10^{10.5}$ M$_\odot$) galaxies.

2.4   Exploring model variations with OWLS

In this section, we assess the sensitivity of our results from the EAGLE simulation presented in Section 2.3 to the physical processes included in the subgrid model. We do this by comparing a set of OWLS simulations (Schaye et al., 2010) in which the subgrid model is systematically varied. In particular, we explore variations of the feedback from star formation and AGN (Section 2.4.1), in combination with metal-line cooling, by explicitly turning on or off a particular process. The variation of SFR_{rec}/SFR and $M_{*,\mathrm{rec}}/M_*$ with galaxy mass in Figs. 2.6, 2.7, 2.9 and 2.10 is already suggestive of the important role played by these feedback processes and we will now show this explicitly. We also vary the adopted IMF (Section 2.4.2), as this

Recycling of stellar ejecta

Table 2.1: Set of OWLS simulations that vary in terms of the feedback implementation (upper section) or the adopted IMF (lower section). From left to right, the columns show the model name, whether or not there is energy feedback associated with star formation (SF feedback), metal-line cooling and AGN feedback, the adopted IMF, the fraction of kinetic energy available from SN Type II that is used to drive galactic winds (f_{th}), the initial wind velocity (v_w) and the wind mass loading parameter (η).

Name	SF feedback	Metal-line cooling	AGN feedback	IMF	f_{th}	v_w [km/s]	η
Feedback variations							
REF	✓	✓	–	Chabrier	0.40	600	2.0
NOZCOOL	✓	–	–	Chabrier	0.40	600	2.0
NOSN	–	✓	–	Chabrier	0.40	600	2.0
NOSN_NOZCOOL	–	–	–	Chabrier	0.40	600	2.0
AGN	✓	✓	✓	Chabrier	0.40	600	2.0
IMF variations							
IMFSALP	✓	✓	–	Salpeter	0.66	600	2.0
DBLIMFCONTSFML14	✓	✓	–	Top-heavy[a]	0.40	600	14.6
DBLIMFCONTSFV1618	✓	✓	–	Top-heavy[a]	0.40	1618	2.0

[a]At high pressures ($P/k > 2.0 \times 10^6$ cm^{-3} K) the IMF switches from Chabrier (2003) to a top-heavy power-law $dN/dM \propto M^{-1}$.

determines the fraction of the stellar mass that is released by a stellar population[12]. The sets of variations are summarized in Table 2.1 and are described in more detail below.

We start this section with a brief overview of the OWLS simulation set-up and the implemented subgrid physics, focusing in particular on the differences with respect to EAGLE (for a detailed description of the differences, we refer the reader to Schaye et al., 2015). The OWLS simulations were run with a modified version of the SPH code GADGET3, but in contrast to EAGLE it uses the entropy formulation of SPH implemented by Springel & Hernquist (2002). The adopted cosmological parameters, $[\Omega_{\rm m}, \Omega_{\rm b}, \Omega_{\Lambda}, \sigma_8, n_{\rm s}, h]$ = $[0.238, 0.0418, 0.762, 0.74, 0.951, 0.73]$, are consistent with Wilkinson Microwave Anisotropy Probe (WMAP) 3-yr (Spergel et al., 2007) and WMAP 7-yr data (Komatsu et al., 2011). The simulations used here were run in periodic volumes of size $L = 100\ h^{-1}$ cMpc.[13], containing $N = 512^3$ dark matter particles with initial mass $m_{\rm dm} = 4.1 \times 10^8\ h^{-1}\ {\rm M}_\odot$ and an equal number of baryonic particles with initial mass $m_{\rm b} = 8.7 \times 10^7\ h^{-1}\ {\rm M}_\odot$. The gravitational softening length is $7.81\ h^{-1}$ ckpc, limited to a maximum of $2.00\ h^{-1}$ pkpc.

The implementations of radiative cooling and heating, and stellar evolution, are nearly the same as in EAGLE. Hence, the timed mass release by an SSP, as presented in Section 2.2.2, is nearly identical in OWLS. On the other hand, differences in the OWLS subgrid physics include the use of a fixed density threshold in the implementation of star formation and the kinetic implementation of star formation-driven winds. A fixed fraction $f_{\rm th}$ of the available feedback energy is injected locally, where it directly (by 'kicking' gas particles surrounding newly formed star particles) generates galactic winds with initial velocity $v_{\rm w}$ and mass loading η (following Dalla Vecchia & Schaye, 2008). The prescriptions for BH growth and AGN feedback (Booth & Schaye, 2009), which are only included in the OWLS model *AGN*, employ a Bondi-Hoyle accretion rate with a density-dependent correction term, and a slightly lower thermal heating temperature than in EAGLE.

2.4.1 Effect of feedback processes and metal-line cooling

We consider the following set of feedback variations, combined with variations in the metal-line cooling, as the latter may also impact upon the efficiency of the feedback.

- *REF* is the OWLS fiducial model, which serves as the reference in the model comparison. It includes radiative cooling and heating, star formation, stellar evolution and kinetic energy feedback (with $f_{\rm th} = 0.40$, $v_{\rm w} = 600$ km s^{-1} and $\eta = 2$) from star formation. Note that it does *not* include prescriptions for BH growth and AGN feedback. All model variations listed below are varied with respect to this model.

---

[12]We use the OWLS simulations to perform the model comparison, as this suite provides both the extreme feedback variations and IMF variations we need. Note that while the stellar and AGN feedback models in OWLS are slightly different from those in EAGLE, and that OWLS does not reproduce the observed $z \simeq 0$ GSMF, we can still use the OWLS suite to study the *relative* changes in $SFR_{\rm rec}/SFR$ and $M_{*,\rm rec}/M_*$ (at least qualitatively).

[13]Note that for OWLS, the box size and particle masses are given in units with h^{-1}.
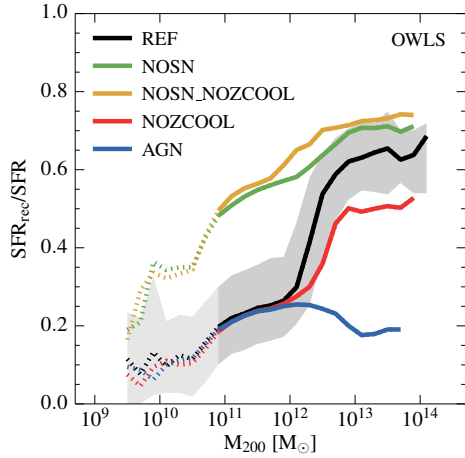
Figure 2.11: Comparison of a set of OWLS models to explore the effects of star formation feedback, AGN feedback and metal-line cooling on the contribution of recycled gas to the SFR at $z = 0$. The curves show the median (in logarithmic mass bins of size 0.2 dex containing at least 10 haloes) contribution of recycled gas to the SFR as a function of halo mass. The grey shaded region shows the 10th to 90th percentile region for the OWLS fiducial model (black curve). The solid curves become dotted when the halo mass corresponds to fewer than 100 dark matter particles. We find that the efficiency of the feedback associated with star formation (in low-mass galaxies) and the feedback of AGN (in high-mass galaxies) determines how much gas from stellar mass-loss contributes to the SFR. A higher feedback efficiency results in a lower contribution from recycled gas.

- In *NOZCOOL*, the cooling rates are calculated using primordial element abundances, i.e. $X = 0.76$ and $Y = 0.24$.

- *NOSN* turns off all energy feedback mechanisms associated with star formation. However, the mass-loss and metal production by massive stars, SN Type Ia and AGB stars are still present.

- *NOSN_NOZCOOL* is a combination of the previous two models. It does not include galactic winds and the cooling rates are based on primordial element abundances.

- *AGN* includes models for the growth of BHs and feedback from AGN.

Fig. 2.11 shows the effects of star formation feedback, AGN feedback and metal-line cooling on SFR_{rec}/SFR as a function of halo mass, M_{200}[14]. Note that the mass scale corresponding to 100 dark matter particles, below which the curves are shown as dotted lines, is a factor of ~ 58 greater than in the EAGLE fiducial simulation.

---

[14]Note that we do not treat central and satellite galaxies separately, but instead consider the total amount of star formation taking place within the group halo as a whole (without applying an aperture when calculating SFR_{rec}/SFR). Also, while we only present the results for SFR_{rec}/SFR as a function of halo mass, they are consistent with the results for $M_{*,rec}/M_*$, as well as for both ratios as functions of stellar mass.

First comparing *NOSN* (green curve) to *REF* (black curve), we see that the feedback associated with star formation dramatically reduces the contribution of recycled gas to the SFR at all mass scales, in particular for $M_{200} \lesssim 10^{12}$ M$_\odot$, where the regulation of star formation is largely governed by feedback from star formation. Here, the contribution drops from ~ 55% (without star formation feedback, *NOSN*) to ~ 25% (with star formation feedback, *REF*). The large reduction can be explained if we consider the environments from which these star formation-driven winds are launched. The outflows originate in the dense ISM, which is the environment into which stellar mass-loss is deposited. These stellar ejecta, which could be recycled into new generations of star formation, are prevented from forming stars if the winds eject the gas from the ISM in such a way that it does not return and become sufficiently dense again on short time-scales. If, on the other hand, star formation feedback is inefficient, then this gas remains in the ISM and fuels star formation. The *REF* model shows an increasing SFR_{rec}/SFR with mass, which becomes increasingly similar to the *NOSN* model. This is consistent with SN feedback becoming less efficient as the depth of the potential well and the density and pressure in the ISM increase. Hence, the decreasing efficiency of the feedback leads to gas recycling being increasingly important for fuelling star formation in more massive systems.

A notable feature in the curve of the *REF* model is the sharp upturn of SFR_{rec}/SFR at a halo mass of $M_{200} \sim 10^{12}$ M$_\odot$. Clearly, the feedback suddenly becomes very inefficient at this mass scale. As explained by Dalla Vecchia & Schaye (2012), this is due to strong artificial radiative losses in the ISM as the gas (which has a high pressure and density in these high-mass systems) gets shock-heated by the star formation-driven winds. Kinetic energy is thermalized to temperatures at which the cooling time is short relative to the sound crossing time, and is quickly radiated away. As a consequence, the winds stall in the ISM before they can escape the galaxy, which drives up the value of SFR_{rec}/SFR. For a fixed initial velocity of the kinetically implemented winds, this effect causes a sharp transition at the mass scale for which artificial losses become significant. This results in unrealistic stellar mass fractions in haloes of $M_{200} > 10^{12}$ M$_\odot$ (Haas et al., 2013) and a failure of the model to reproduce the observed GSMF (Crain et al., 2009). Comparing *REF* to *NOZCOOL* (red), we see that the upturn becomes less pronounced if the cooling rates are reduced. Lower cooling rates, as a result of neglecting metal-line cooling (*NOZCOOL*), reduce the artificial thermal losses in the ISM and therefore enable the feedback to remain more efficient to higher mass scales. This results in lower values of SFR_{rec}/SFR in the most massive systems.

In addition to its impact upon the feedback efficiency, a change in the cooling rates also affects the accretion rate on to the galaxy, therefore impacting upon SFR_{rec}/SFR in a more direct fashion. However, from comparing *NOSN* (with metal-line cooling; green) and *NOSN_NOZCOOL* (without metal-line cooling; yellow) we see that, in the absence of energy feedback associated with star formation, the effect of changing the cooling rates on SFR_{rec}/SFR is small, especially considering the expected amount of scatter in the two relations (from the grey shaded region). Hence, we conclude that a change in the cooling rates, as a result of turning metal-line cooling on or off, mainly affects the contribution of recycled gas to the SFR by changing the (partly numerical) efficiency of the star formation feedback implemen-

tation.

Finally, to investigate the effect of AGN feedback on SFR_{rec}/SFR as a function of halo mass, we compare the *AGN* model (blue curve), which includes AGN feedback, to the *REF* model. Since BHs live in the dense, central regions of galaxies, where a large fraction of the stellar ejecta are deposited, we again expect a low recycling-fuelled SFR if the AGN feedback is strong enough to eject gas from the ISM. The *AGN* model curve indeed shows that at masses $M_{200} \gtrsim 10^{12}$ M$_\odot$, where feedback from AGN becomes important, the values of SFR_{rec}/SFR decrease towards higher masses. At a halo mass of $M_{200} \sim 10^{13}$ M$_\odot$, recycled gas contributes only $\sim 20\%$ to the SFR. This is in stark contrast to the *REF* model, for which the contribution reaches $\sim 65\%$, indicating the strong impact of AGN feedback on the SFR_{rec}/SFR in the regime where the feedback from star formation is inefficient and AGN are the main drivers of galactic winds. This highlights the importance of including AGN feedback in the subgrid model. Qualitatively, we conclude that for massive galaxies the increasing efficiency of AGN feedback towards higher masses leads to gas recycling being less important for fuelling present-day star formation.

2.4.2   Effect of changing the stellar initial mass function

We consider the following variations with respect to the fiducial Chabrier (2003) IMF.

- *IMFSALP* adopts a Salpeter (1955) IMF, spanning the same stellar mass range as the Chabrier IMF used by the fiducial model. The corresponding change in the amplitude of the observed Kennicutt (1998) relation is taken into account. While v_w and η in the implementation of star formation-driven winds are kept the same, as is the total wind energy per unit stellar mass (which is proportional to $v_w \eta^2$), f_{th} is increased to 0.66.

- *DBLIMFCONTSFML14* assumes an IMF that becomes top-heavy in high-pressure environments. For $P/k > 2.0 \times 10^6$ cm^{-3} K, the IMF switches from a Chabrier IMF to a power-law $dN/dM \propto M^{-1}$. In these environments, there is 7.3 times more stellar feedback energy available per unit stellar mass to drive galactic winds. In this model, the additional energy is used to increase the wind mass loading by a factor of 7.3.

- As the previous model, *DBLIMFCONTSFV1618* switches to a top-heavy power-law IMF for stars forming in high-pressure regions. However, the additional stellar feedback energy is now used to increase the initial velocity of the winds: v_w is a factor of $\sqrt{7.3}$ higher than in the reference model.

Fig. 2.12 shows the effect of varying the choice of IMF. A comparison of *IMF-SALP* (red curve) and *REF* (black curve) shows that adopting a more bottom-heavy IMF like Salpeter reduces the values of SFR_{rec}/SFR over the whole mass range. This was expected, because both the total mass and the metal mass released by stellar populations are lower than for a Chabrier IMF (compare Figs. 2.1 and 2.13). In low-mass galaxies (in haloes with masses $M_{200} \lesssim 10^{12}$ M$_\odot$) the contribution of recycled gas to the SFR drops from $\sim 25\%$ to $\sim 15\%$, while in high-mass galaxies it
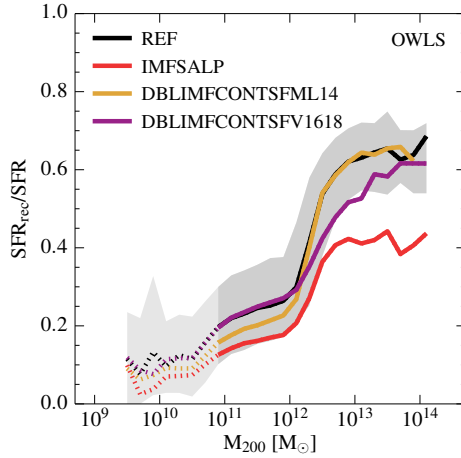
Figure 2.12: As Fig. 2.11, but showing a set of OWLS models with different IMFs. We find that adopting a more bottom-heavy (top-heavy) IMF reduces (enhances) the contribution from recycled gas to the SFR, but only if the feedback energy used to initiate star formation-driven galactic winds is kept fixed. If the extra stellar feedback energy from adopting a top-heavy IMF is used to either increase the mass loading or the wind velocity, then the recycled gas contributions decrease, showing that other IMF-related effects are more than compensated for by the increased efficiency of the star formation feedback.

drops from ~ 65% to ~ 40%. In the high-mass systems, we expect that the reduction is partly due to a reduction of the cooling rates, which causes a slight increase of the efficiency of star formation feedback. This is the result of the reduced metal mass released by stellar populations, similar to disabling metal-line cooling in the *NOZCOOL* model (see Section 2.4.1). However, note that since the total wind energy per unit stellar mass is kept fixed when switching from *REF* to the *IMFSALP* model, the feedback efficiency is affected only by a change in the cooling rates.

On the other hand, the switch to a top-heavy IMF as implemented in *DBLIMFCONTSFML14* and *DBLIMFCONTSFV1618*, leads to competing effects. A top-heavy IMF yields more stellar mass-loss, but also yields more stellar feedback energy to drive galactic winds, which is partly dissipated due the increased metal mass-loss. Comparing *REF* with *DBLIMFCONTSFML14* (increased η) and *DBLIMFCONTSFV1618* (increased v_w) enables us to determine which effect dominates. We have investigated (but do not show here) the effects of increasing the mass loading or the initial wind velocity without changing the IMF. We find that if the winds efficiently escape the galaxy (in low-mass systems, $M_{200} \lesssim 10^{12}\ \mathrm{M}_\odot$) the mass loading mainly determines the gas mass that is ejected, whereas the initial velocity is of little importance. On the other hand, in high-mass systems ($M_{200} \gtrsim 10^{12}\ \mathrm{M}_\odot$), where the artificial radiative losses are high and star formation-driven winds are not efficient in escaping the galaxy, we find that increasing the mass loading has little effect, as these losses remain too significant. Boosting instead the initial wind velocity, alleviates these losses and increases the efficiency of the wind, because the wind now thermalizes at a higher temperature (Haas et al., 2013).

This is consistent with the IMF variations, *DBLIMFCONTSFML14* (yellow curve) and *DBLIMFCONTSFV1618* (purple curve), shown in Fig. 2.12. For *DBLIMFCONTSFML14* the values of SFR_{rec}/SFR are reduced at low masses and consistent with *REF* at high masses, whereas for *DBLIMFCONTSFML14* SFR_{rec}/SFR is consistent at low masses and reduced at high masses. Hence, we infer that the feedback efficiency is the dominant factor in determining SFR_{rec}/SFR as a function of halo mass. Despite the fact that, naively, we might have expected an *increase* of SFR_{rec}/SFR upon adopting a top-heavy IMF in high-pressure regions, as a result of the larger fraction of the stellar material available for recycling, the *decrease* of SFR_{rec}/SFR in the *DBLIMFCONTSFML14* and *DBLIMFCONTSFV1618* models compared to the *REF* model shows that this effect is more than compensated for by the increased efficiency of the stellar feedback.

From the OWLS model comparisons presented in this section we conclude that the efficiency of the feedback from star formation and AGN is key for regulating the fuelling of star formation with recycled gas. The choice of the IMF sets the total mass of gas that is potentially available for recycling, but the feedback efficiency determines how much gas recycled from stellar mass-loss actually contributes to the SFR (and hence the stellar mass) of galaxies. This makes the contribution from recycled gas to the SFR and stellar mass sensitive to the mass of the galaxy.

2.5   Summary and discussion

We have investigated the significance of stellar ejecta as fuel for star formation using the *Ref-L100N1504* cosmological simulation from the EAGLE project. We studied the contribution of gas from evolved stellar populations to the SFR and stellar mass, as a cosmic average as a function of redshift and within individual galaxies as a function of metallicity and galaxy stellar mass at $z = 0$. We treated the galaxies identified as 'centrals' separately from those identified as 'satellites'. Since the mass released by AGB stars, SN Type Ia and massive stars was explicitly followed in the simulation, we were able to assess the relative significance of these different mass-loss channels for fuelling star formation. We also explored the radial dependence of gas recycling, by comparing the significance of recycling-fuelled star formation in the inner and outer parts of galaxies. Our results can be summarized as follows.

1. The contribution of recycled gas to the present-day SFR and stellar mass of galaxies is strongly, positively correlated with, respectively, the metallicity of the ISM and stars. Therefore, many of our conclusions on the role of stellar ejecta in fuelling star formation as a function of galaxy mass and type carry over to the mass-metallicity relation. The relations between the contribution of stellar mass-loss and metallicity do exhibit a slight dependence on galaxy stellar mass, as a result of the increasing contribution of mass-loss from massive stars relative to that from intermediate-mass stars to the SFR and stellar mass for $M_* \gtrsim 10^{10.5}$ M$_\odot$ (Fig. 2.9, Section 2.3.3). We provide the best-fitting relations (equations 2.10 and 2.11), including a term with the [O/Fe] abundance ratio, which enable one to estimate the importance of gas recy-

cling in present-day galaxies from the observed metallicity and α-enhancement (Fig. 2.4, Section 2.3.2).

2. We apply the relations between the SFR contributed by recycling and ISM metallicity and between the stellar mass contributed by recycling and stellar metallicity from EAGLE to the observed mass-metallicity relations to estimate the recycled gas contributions as a function of galaxy stellar mass. Since we find these relations to be insensitive to the subgrid models for feedback, applying them to the observed mass-metallicity relations yields more accurate estimates for the contribution of recycling than the direct predictions of EAGLE, provided that the (systematic) uncertainty in the calibration of the observed mass-metallicity relation is smaller than the discrepancy between the mass-metallicity relation predicted by EAGLE and the observed relation. For central galaxies with a stellar mass similar to that of the Milky Way ($M_* \sim 10^{10.5}$ $M_\odot$), which corresponds to the mass scale of the peak in the galaxy formation efficiency, 35% of the present-day SFR and 20% of the present-day stellar mass is due to recycled stellar mass-loss (Fig. 2.6, Section 2.3.3).

3. Recycling of stellar mass-loss becomes increasingly important for fuelling star formation towards lower redshift. At the present day, the fiducial EAGLE model (i.e. as computed directly from the simulation) indicates that approximately 35% of the cosmic SFR density and 19% of the cosmic stellar mass density is contributed by recycling (Figs. 2.2 and 2.3, Section 2.3.1).

4. The fraction of the present-day SFR and stellar mass of central galaxies contributed by recycling shows a characteristic trend with the mass of the galaxy and its subhalo: for $M_* \lesssim 10^{10.5}$ $M_\odot$ ($M_{sub} \lesssim 10^{12.2}$ $M_\odot$) the contribution increases with mass, while for $M_* \gtrsim 10^{10.5}$ $M_\odot$ the contribution turns over and decreases with mass (in case of the SFR) or remains approximately constant (in case of the stellar mass). We infer that this trend is regulated by the efficiency of the feedback associated with star formation (at low-mass scales) and AGN (at high-mass scales). If feedback is efficient in driving galactic winds and thereby ejecting gas from the ISM, which is the environment into which stellar mass-loss is deposited, then this will preferentially reduce the SFR and stellar mass contributed by recycled gas (Figs. 2.6 and 2.7, Section 2.3.3).

5. The importance of gas recycling for fuelling ongoing star formation in satellite galaxies is broadly consistent with that for central galaxies over a wide range of masses, as recycling is mainly governed by the efficiency of feedback. However, the fiducial EAGLE model indicates that in satellites with a Milky Way-like mass the fraction of the SFR contributed by recycled gas significantly exceeds the one in similarly massive centrals, and even reaches $\gtrsim 90\%$ for satellites with the lowest gas fractions (Fig. 2.7, Section 2.3.3). We infer that this results from a depletion of the ISM gas reservoir of the satellite, either due to the cessation of fresh infall or the removal of gas from the disc, which makes them more reliant on stellar mass-loss for fuelling ongoing star formation (Fig. 2.8, Section 2.3.3).

6. As a cosmic average, the gas from AGB stars accounts for an increasing fraction of the recycled stellar mass-loss towards lower redshift. At $z \gtrsim 0.4$, however, massive stars still provide the majority of the gas that fuels the cosmic SFR density through recycling. As a result, massive stars dominate the recycling-fuelled stellar mass density at all redshifts. The contribution from SN Type Ia is always small (Figs. 2.2 and 2.3, Section 2.3.1).

7. Within individual galaxies, AGB stars and massive stars contribute approximately equally to the present-day SFR and stellar mass of centrals and satellites. The contribution from AGB stars to the SFR is slightly enhanced with respect to the massive star contribution at all but the highest mass scales, which results from the preferential ejection of massive star ejecta by star formation-driven winds and their early lock up in stellar remnants. At the highest mass scales ($M_* \gtrsim 10^{10.5}$ M$_\odot$), on the other hand, we find a relative enhancement in the contributions from massive stars, which we attribute to a downsizing effect, with more massive galaxies forming their stars earlier and more rapidly. Their stellar mass therefore preferentially consists of massive star ejecta, which are recycled on short time-scales (Fig. 2.9, Section 2.3.3).

8. Exploring the radial dependence of gas recycling within central and satellite galaxies, we find that recycling is more important for fuelling star formation (at the present day and in the past) in the central parts of galaxies (within R_{50}) than in the outskirts (outside R_{50}), which is consistent with the observationally inferred inside-out growth of galaxies. We find that the difference between these two radial regimes is predominantly driven by the difference in the fractional contribution from AGB stars to the SFR (stellar mass), which is significantly higher than (roughly equal to) the one from massive stars inside R_{50} and roughly equal (lower) outside R_{50}. This radial trend directly reflects the negative stellar age gradient with increasing distance from the galactic centre (Fig. 2.10, Section 2.3.3).

Finally, we assessed the sensitivity of our results from the EAGLE simulation to the physical processes in the subgrid model using a suite of simulations from the OWLS project. The suite is comprised of a set of extreme variations of the feedback model, in which star formation feedback, AGN feedback and metal-line cooling are switched on or off entirely (Fig. 2.11, Section 2.4), as well as a set of variations of the adopted IMF (Fig. 2.12, Section 2.4). A systematic comparison of the results shows that while the total fraction of the stellar mass that is available for recycling is determined by the adopted IMF, the fraction of the stellar mass-loss that is actually used to fuel star formation is controlled by the efficiency of the feedback associated with star formation and the feedback from AGN, each affecting the galaxy mass regime where the respective feedback process regulates the star formation.

Consistent with previous studies (e.g. Kennicutt et al., 1994; Leitner & Kravtsov, 2011; Voit & Donahue, 2011), our results emphasize the importance of modelling the recycling of stellar ejecta in simulations of galaxy formation, and the necessity of accounting for such gas in assessments of the 'fuel budget' of present-day galaxies. The fractional contribution of recycled ejecta to the SFR and stellar mass is not

dominant, but it is also not negligible, and it extends the gas consumption time-scale significantly beyond that implied by the ratio of the instantaneous gas mass and SFR of galaxies.

The relatively small contribution of recycling to the SFR and stellar mass of massive galaxies in our simulations is contrary to the naive expectation that the establishment of a hot CGM quenches gas infall and renders the galaxy reliant on recycling for continued fuelling. Instead, the simulations indicate that the ongoing star formation in massive galaxies is sustained mostly by unprocessed gas. An interesting route for future studies will be to explore whether this gas originates in cooling flows, or is stripped from infalling satellite galaxies.

Acknowledgements

2.A   Mass released by an SSP with a Salpeter IMF

Fig. 2.13 shows the total (left) and metal (right) mass released by an SSP with a Salpeter (1955) IMF (solid lines) and by an SSP with a Chabrier (2003) IMF (dotted lines) in the range $0.1-100\,M_\odot$ as a function of age for solar metallicity. The colours in both panels have the same meaning as in Fig. 2.1. The (metal) mass-loss is lower for a Salpeter IMF than for a Chabrier IMF by a factor of ~ 1.5 over the whole range of SSP ages plotted. The relative contributions from massive stars and AGB stars are somewhat lower and higher, respectively. The metal mass-loss from SN Type Ia is higher for a Salpeter IMF, accounting for $\sim 8\%$ of the total metal mass released. In general, adopting a Salpeter IMF instead of a Chabrier IMF increases the relative contributions from intermediate-mass stars to the (metal) mass-loss, as expected for a more bottom-heavy IMF.
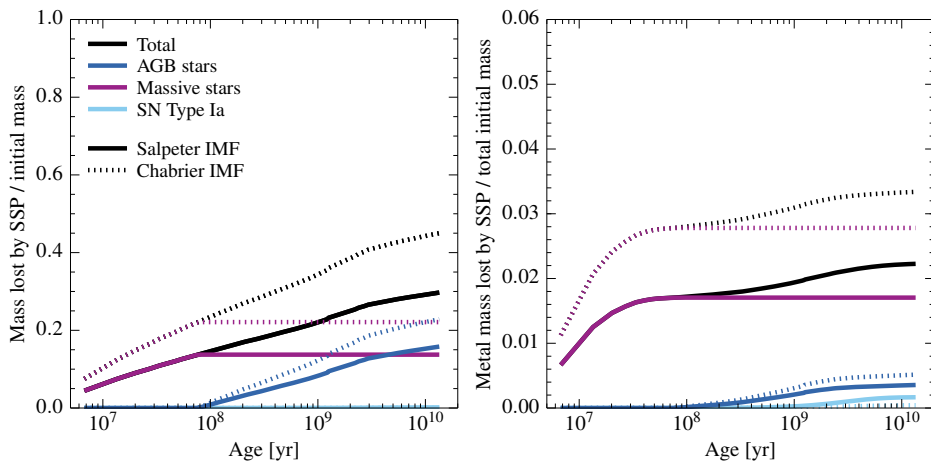
Figure 2.13: The cumulative fraction of the initial mass (total: left-hand panel; in the form of metals: right-hand panel) that is released by an SSP as a function of its age, adopting a Salpeter (1955) IMF (solid lines) or a Chabrier (2003) IMF (dotted lines). The curves show the contributions from AGB stars (blue), massive stars (purple) and SN Type Ia (cyan), as well as the total (metal) mass ejected by the SSP (black) for solar stellar metallicity. The total (metal) mass-loss is lower for a Salpeter IMF than for a Chabrier IMF by a factor of ~ 1.5. Adopting a Salpeter IMF increases the relative contributions from AGB stars and SN Type Ia, which have intermediate-mass progenitor stars.

2.B   Numerical convergence

2.B.1   Relation between recycled gas contributions and stellar mass

We test for numerical convergence with respect to resolution of the SFR_{rec}/SFR- M_* and $M_{*,rec}/M_*$- M_* relations using a set of three EAGLE simulations that were run in volumes of size $L = 25$ cMpc. We consider both 'weak' and 'strong' convergence (following the nomenclature introduced by Schaye et al., 2015) by comparing simulations with recalibrated and non-recalibrated subgrid physics, respectively. We use

- one simulation with $N = 376^3$ and with the same subgrid model parameters as our fiducial $L = 100$ cMpc, $N = 1504^3$ simulation that was used throughout this work. This simulation (denoted *Ref-L025N376*) has the same resolution as the fiducial simulation.

- One simulation with $N = 752^3$ and the same subgrid model parameters as the fiducial simulation, but with eight times higher mass resolution (*Ref-L025N752*).

- One simulation with $N = 752^3$ and with a *recalibrated* set of subgrid model parameters for star formation feedback, AGN feedback and the accretion on to BHs, in order to improve the match with the observed $z \simeq 0$ GSMF at this
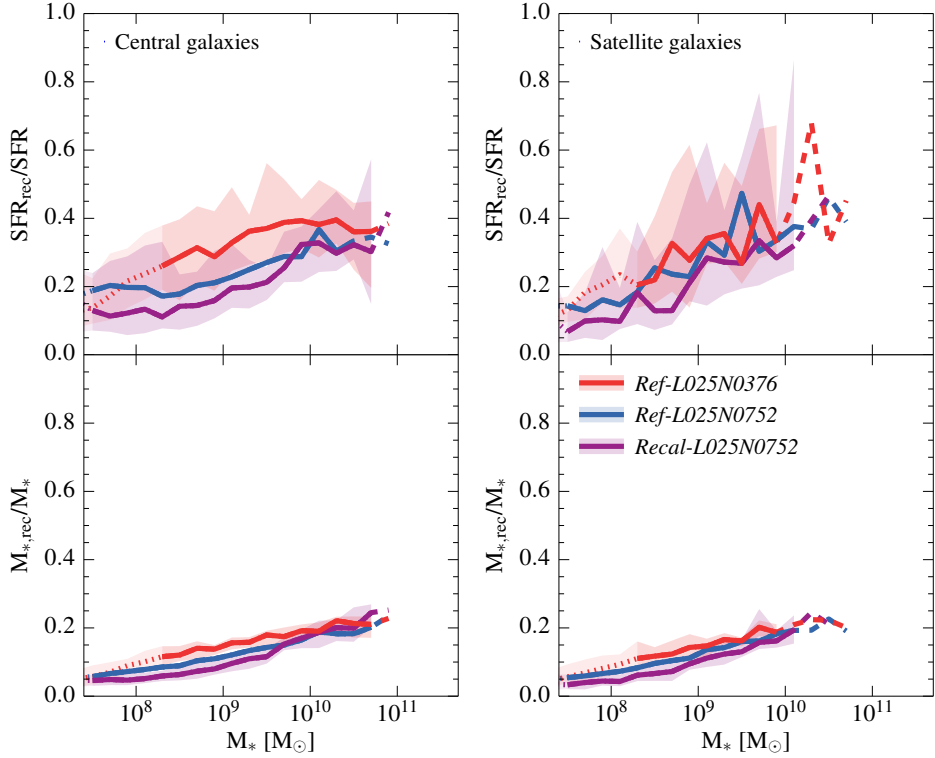
Figure 2.14: Test for numerical convergence of the *SFR*$_{rec}$/*SFR*- M_* (top) and $M_{*,rec}/M_*$- M_* (bottom) relations (presented in Figs. 2.6 and 2.7) for central (left) and satellite (right) galaxies at $z = 0$, comparing an EAGLE simulation with the fiducial resolution (*Ref-L025N376*; red) to two EAGLE simulations with eight times higher mass resolution, with (*Recal-L025N0752*; purple) and without (*Ref-L025N0752*; blue) recalibrated subgrid feedback parameters. All three simulations were run in volumes of size $L = 25$ cMpc. The curves and shaded regions have the same meaning as in Fig. 2.6, but for clarity we only show the 10th to 90th percentile range for the *Ref-L025N376* and *Recal-L025N752* simulations. For galaxies with $M_* \gtrsim 10^{9.8}$ M$_\odot$, *SFR*$_{rec}$/*SFR* and $M_{*,rec}/M_*$ as a function of stellar mass are reasonably well converged. For galaxies with $M_* \lesssim 10^{9.8}$ M$_\odot$, the fiducial EAGLE simulation likely overpredicts the SFR and stellar mass contributed by recycling, by at most a factor of ~ 2 (~ 0.3 dex) at $M_* \sim 10^9$ M$_\odot$.

eight times higher mass resolution (*Recal-L025N752*). In short, the recalibration corresponds to a change in the density dependence of the stellar feedback efficiency parameter f_{th}, such that the feedback efficiency is increased in higher density gas while keeping the average f_{th} roughly equal to 1. This is done in order to compensate for the increase in cooling losses, which arise as a result of the locally higher gas densities that are resolved in the higher resolution model.

A comparison of these three EAGLE simulations is shown in Fig. 2.14, where we plot SFR_{rec}/SFR (top) and $M_{*,rec}/M_*$ (bottom) as a function of stellar mass. We show these relations for both central galaxies (left) and satellite galaxies (right). Since our conclusions about resolution convergence are broadly consistent between centrals and satellites (although with somewhat poorer sampling for the latter), we will focus the discussion below on central galaxies.

Comparing the fiducial resolution simulation (*Ref-L025N0376*; red) to the two higher-resolution simulations, with (*Recal-L025N0752*; purple) and without (*Ref-L025N0752*; blue) recalibrated subgrid feedback parameters, we infer that for central galaxies with $M_* \lesssim 10^{9.8}$ $M_\odot$, SFR_{rec}/SFR and $M_{*,rec}/M_*$ as a function of stellar mass are not numerically converged at the fiducial resolution. The 'strong' convergence is somewhat better than the 'weak' convergence. At $M_* \sim 10^9$ $M_\odot$, SFR_{rec}/SFR and $M_{*,rec}/M_*$ in *Ref-L025N0376* are almost a factor of 2 (0.3 dex on a logarithmic scale) higher than in *Recal-L025N0752*. This is not surprising considering the level of agreement between *Ref-L100N1504* and *Recal-L025N0752* for the mass-metallicity relations, where the latter is in better agreement with the observations (see fig. 13 of Schaye et al., 2015).

At masses $M_* \gtrsim 10^{9.8}$ $M_\odot$, the relation between $M_{*,rec}/M_*$ and stellar mass is fully converged (both 'weakly' and 'strongly'), while SFR_{rec}/SFR as a function of stellar mass shows substantial overlap between *Ref-L025N0376*, *Ref-L025N0752* and *Recal-L025N0752*. Due to the small box size, however, SFR_{rec}/SFR is not well sampled around $M_* \sim 10^{10.5}$ $M_\odot$, the mass scale at which SFR_{rec}/SFR reaches a maximum in our fiducial $L = 100$ cMpc model (see Fig. 2.6).

2.B.2   Relation between recycled gas contributions and metallicity

Fig. 2.15 shows the numerical convergence test of the SFR_{rec}/SFR- Z_{gas} (left) and $M_{*,rec}/M_*$- Z_* (bottom) relations for central galaxies, comparing the fiducial EAGLE model (*Ref-L100N1504*; red) and the high-resolution, recalibrated model (*Recal-L025N0752*; purple). While *Recal-L025N0752* spans a metallicity range that is shifted towards somewhat lower values with respect to *Ref-L100N1504*, due to its smaller box size and eight times higher mass resolution (we select stellar masses corresponding to at least 100 gas particles at each resolution), the SFR_{rec}/SFR- Z_{gas} and $M_{*,rec}/M_*$- Z_* relations are converged with resolution over the whole metallicity range probed here. Where *Recal-L025N0752* and *Ref-L100N1504* overlap, their medians agree to better than 0.05 dex in SFR_{rec}/SFR and to better than 0.04 dex in $M_{*,rec}/M_*$.

One might wonder whether the secondary dependence on α-enhancement (hence, implicitly on stellar mass; see Fig. 2.5) affects the convergence of these rela-
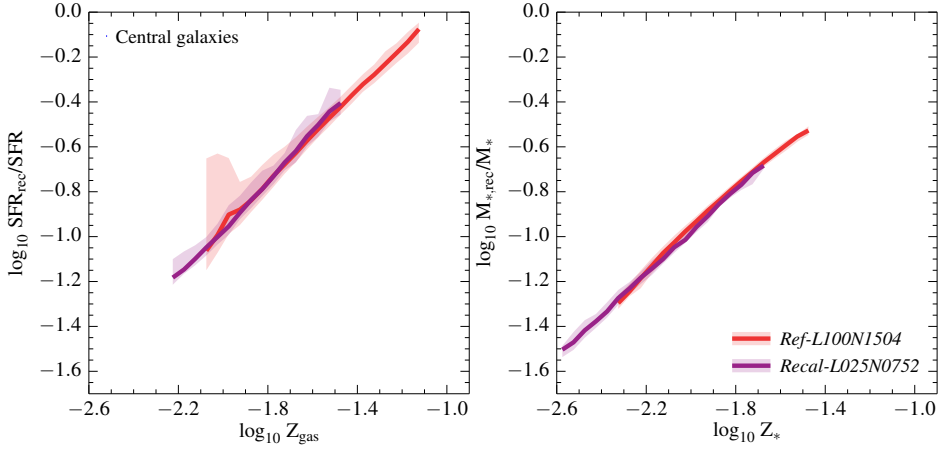
Figure 2.15: Test for numerical convergence of the SFR_{rec}/SFR- Z_{gas} (left) and $M_{*,rec}/M_*$- Z_* (right) relations (presented in Fig. 2.4) for central galaxies at $z = 0$, comparing the fiducial EAGLE model (*Ref-L100N1504*; red) and the high-resolution, recalibrated model (*Recal-L025N0752*; purple). We only consider galaxies with stellar masses corresponding to at least 100 gas particles, at the respective resolution. In the left-hand panel, we only consider subhaloes with a non-zero SFR. The curves show the median value in each logarithmic metallicity bin of size 0.05 dex, if it contains at least 10 galaxies. The shaded regions mark the 10th to 90th percentile ranges. The SFR_{rec}/SFR- Z_{gas} and $M_{*,rec}/M_*$- Z_* relations are converged at the fiducial resolution over the whole metallicity range.

tions. However, the dependence on stellar mass only becomes significant for $M_* \gtrsim 10^{10.5}$ M$_\odot$, which is the regime where *Ref-L100N1504* and *Recal-L025N0752* are converged (in terms of $M_{*,rec}/M_*$ and Z_*) or at least broadly consistent (in terms of SFR_{rec}/SFR and Z_{gas}). As a consistency check, we repeat the calculation of SFR_{rec}/SFR and $M_{*,rec}/M_*$ by applying the relations between recycling and metallicity to the observed mass-metallicity relations (as done in Section 2.3.3) at higher resolution using *Recal-L025N0752*. We find agreement with the results from *Ref-L100N1504* to better than a factor of ~ 1.07 (0.03 dex) over the whole stellar mass range.

2.C   Effect of using a 3D aperture

Fig. 2.16 shows the effect of using a 30 pkpc 3D aperture on the contribution of recycled gas to the SFR (top) and stellar mass (bottom) in central galaxies at $z = 0$ as a function of their subhalo mass (left) and stellar mass (right). We compare results from the EAGLE fiducial model, *Ref-L100N1504*, with (red) an without (purple) the aperture. Recall that the aperture only applies to galaxy properties, hence the subhalo mass is not affected.

While the majority of the star formation takes places within the central 30 pkpc, causing the effect of the aperture on the total SFR to be small, there is still an enhancement in SFR_{rec}/SFR (upper panels) inside the aperture compared to its value
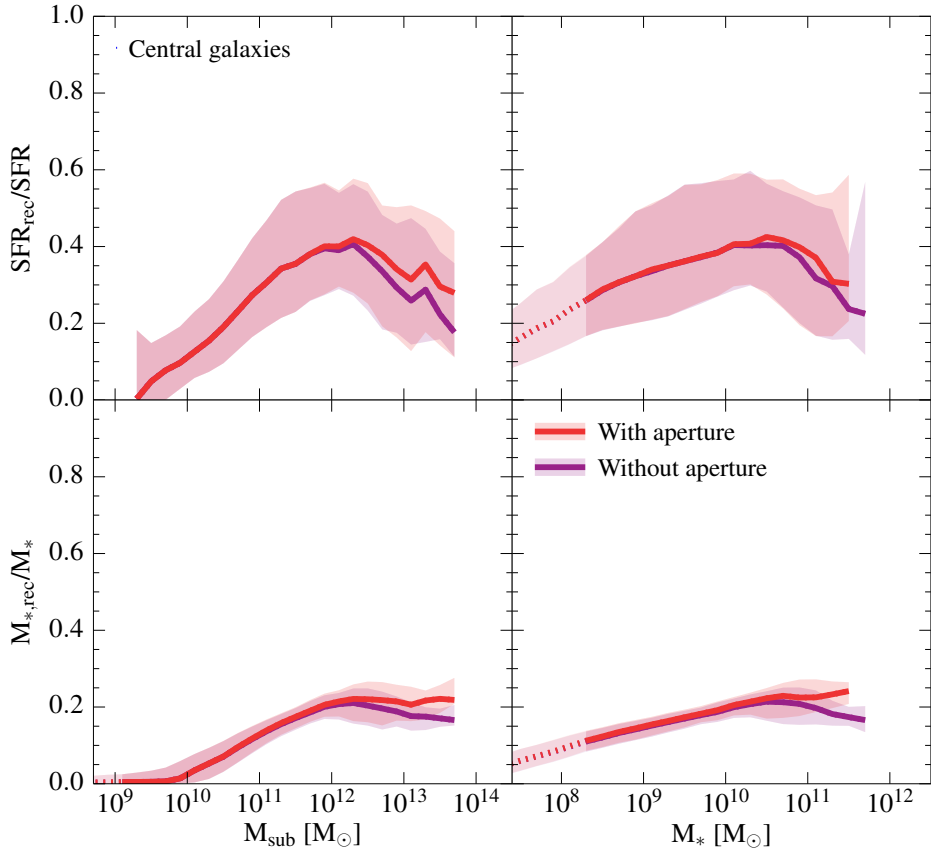
Figure 2.16: The effect of using a 30 pkpc 3D aperture, comparing results from the EAGLE fiducial model, *Ref-L100N1504*, with (red) and without (purple) applying the aperture in calculating galaxy properties. The curves show the fraction of the SFR (top) and stellar mass (bottom) contributed by recycling for central galaxies at $z = 0$ as a function of their subhalo mass (left) and stellar mass (right). The curves and shaded regions have the same meaning as in Fig. 2.6. The effect of using an aperture is a change in the slope of the two recycled gas fractions at $M_* \gtrsim 10^{11}$ $M_\odot$ ($M_{sub} \gtrsim 10^{12.5}$ $M_\odot$), which becomes somewhat shallower. For the fraction of the stellar mass contributed by recycling this results in a roughly flat trend instead of a decrease with subhalo and stellar mass, hence mitigating the effect of increasing AGN feedback efficiency.

over the whole galaxy. This enhancement is consistent with recycling-fuelled star formation being more important in the central parts of galaxies (see Fig. 2.10). The effect is significant for $M_* \gtrsim 10^{11}$ $M_\odot$ ($M_{sub} \gtrsim 10^{12.5}$ $M_\odot$) and increases with mass up to a difference of a factor of ~ 1.5 (~ 0.18 dex) in the left-hand panel, whereas in the right-hand panel the effect is smaller (up to a factor of ~ 1.2, or ~ 0.08 dex) due to the simultaneous decrease in the stellar mass if an aperture is applied.

Similarly, in the lower panels, $M_{*,rec}/M_*$ is enhanced if an aperture is applied. In this case, the effect of using an aperture is that the decrease of $M_{*,rec}/M_*$ with mass for $M_* \gtrsim 10^{10.5}$ $M_\odot$ ($M_{sub} \gtrsim 10^{12.2}$ $M_\odot$) becomes a flattening at a roughly constant value (~ 22% instead of 17% at $M_* \sim 10^{11.5}$ $M_\odot$).

3

The origin of the α-enhancement of massive galaxies

We study the origin of the stellar α-element-to-iron abundance ratio, $[\alpha/\mathrm{Fe}]_*$, of present-day central galaxies, using cosmological, hydrodynamical simulations from the Evolution and Assembly of GaLaxies and their Environments (EAGLE) project. For galaxies with stellar masses of $M_* > 10^{10.5}$ M$_\odot$, $[\alpha/\mathrm{Fe}]_*$ increases with increasing galaxy stellar mass and age. These trends are in good agreement with observations of early-type galaxies, and are consistent with a 'downsizing' galaxy formation scenario: more massive galaxies have formed the bulk of their stars earlier and more rapidly, hence from an interstellar medium that was mostly α-enriched by massive stars. In the absence of feedback from active galactic nuclei (AGN), however, $[\alpha/\mathrm{Fe}]_*$ in $M_* > 10^{10.5}$ M$_\odot$ galaxies is roughly constant with stellar mass and decreases with mean stellar age, extending the trends found for lower mass galaxies in both simulations with and without AGN. We conclude that AGN feedback can account for the α-enhancement of massive galaxies, as it suppresses their star formation, quenching more massive galaxies at earlier times, thereby preventing the iron from longer lived intermediate-mass stars (supernova Type Ia) from being incorporated into younger stars.

Marijke C. Segers, Joop Schaye, Richard G. Bower,
Robert A. Crain, Matthieu Schaller and Tom Theuns

3.1 Introduction

The elemental abundances of galaxies hold valuable information about their formation and evolution. Galaxies build up their stellar content from gas accreted from the intergalactic medium (IGM; e.g. Kereš et al., 2005; van de Voort et al., 2011b) and by recycling the stellar mass released by evolved stellar populations (e.g. Kennicutt et al., 1994; Leitner & Kravtsov, 2011; Segers et al., 2016). While the former is predominantly metal-poor, stellar ejecta are intrinsically metal-rich. Stellar populations enrich the interstellar medium (ISM) by means of supernova (SN) explosions and winds from massive and asymptotic giant branch (AGB) stars, where the ejecta from each channel are characterized by a distinctive abundance pattern and are released into the ISM on different time-scales. However, IGM accretion dilutes the enriched ISM, and galactic outflows can remove enriched gas from the ISM, thereby altering its chemical content. Since stars retain the abundances of the ISM in which they were formed, the stellar abundances of galaxies represent a fossil record of their formation history.

In particular, core collapse SNe release mostly α-elements, i.e. elements that are built from the progressive addition of He (α) particles – including O, Ne, Mg, and Si (e.g. Woosley & Weaver, 1995). In contrast, SN Type Ia ejecta, which are released with a temporal delay relative to core collapse SN ejecta, consist almost entirely of Fe (e.g. Thielemann et al., 2003). As a consequence, the O/Fe mass ratio in the ejecta of a simple stellar population generally decreases with time (see fig. 3 of Wiersma et al. 2009b: from 10 Myr to 10 Gyr, this ratio decreases by about 0.3 dex). The α-element-to-iron abundance ratio (also referred to as α-enhancement, when it is compared to the solar abundance ratio) has therefore been used extensively to study the formation history of local, mainly early-type, galaxies (e.g. Trager et al., 2000; Thomas et al., 2010; Johansson et al., 2012; Conroy et al., 2014). A common finding of these studies is that the α-enhancement increases with increasing galaxy stellar mass or velocity dispersion, which is generally interpreted as evidence for galactic 'downsizing'. In this galaxy formation scenario, massive galaxies form the bulk of their stars earlier and over a shorter period of time than low-mass galaxies (e.g. Cowie et al., 1996; Neistein et al., 2006), which is reflected by their chemical content: due to their short formation time-scales, their stars are primarily enriched in α-elements, released by massive stars on short time-scales. The crucial element in the downsizing scenario is a mechanism that efficiently quenches star formation in massive galaxies, and in such a way that more massive galaxies are quenched at earlier times. An obvious candidate is the energy feedback from active galactic nuclei (AGN; e.g. Di Matteo et al., 2005).

In this Letter, we use simulations from the Evolution and Assembly of GaLaxies and their Environments (EAGLE) project (Schaye et al., 2015; Crain et al., 2015) to study the relation of stellar α-enhancement with galaxy stellar mass and age of central galaxies at $z = 0$, and investigate the role played by AGN feedback in reproducing the trends observed for massive, early-type galaxies. The fiducial EAGLE 'reference' model reproduces key observational galaxy properties such as the evolution of the galaxy stellar mass function (Furlong et al., 2015), the sizes of active and passive galaxies and their evolution (Furlong et al., 2017), and the distribution

of galaxies in the colour-magnitude diagram (Trayford et al., 2015). The present-day mass-metallicity relation is reproduced over the mass range of interest here ($M_* \gtrsim 10^{10}$ M$_\odot$; Schaye et al., 2015) [and higher resolution EAGLE simulations of smaller volumes extend this agreement to lower masses; Schaye et al. 2015]. In addition to the reference model, we use a model variation in which AGN feedback has been turned off to isolate its effect on galaxy α-enhancement. In Section 3.2, we describe the simulation set-up and implemented subgrid physics. In Section 3.3, we present galaxy α-enhancement as a function of stellar mass and age, and show that AGN feedback is responsible for the trends that are also observed for massive, early-type galaxies. We give our conclusions in Section 3.4.

3.2 Simulations

The EAGLE simulations were run with a modified version of the smoothed particle hydrodynamics (SPH) code GADGET3 (last described by Springel, 2005). Changes include the use of a pressure-entropy formulation of SPH (Hopkins 2013; see also Schaller et al. 2015a) and the time-step limiter of Durier & Dalla Vecchia (2012). The simulations adopt a Λ cold dark matter cosmology with parameters taken from Planck Collaboration et al. (2014): $[\Omega_{\mathrm{m}}, \Omega_{\mathrm{b}}, \Omega_\Lambda, \sigma_8, n_{\mathrm{s}}, h] = [0.307, 0.04825, 0.693, 0.8288, 0.9611, 0.6777]$.

To investigate the effect of AGN feedback on galaxy α-enhancement, we compare the results from two simulations: the EAGLE reference model (denoted by *Ref* in Schaye et al., 2015) and a model for which the AGN feedback subgrid implementation has been turned off, while keeping all the other subgrid parameters the same (*NoAGN*). These were run in periodic volumes of size $L = 50$ comoving Mpc, containing $N = 752^3$ dark matter particles with mass $m_{\mathrm{dm}} = 9.7 \times 10^6$ M$_\odot$ and an equal number of baryonic particles with initial mass $m_{\mathrm{b}} = 1.8 \times 10^6$ M$_\odot$. The gravitational softening length is set to 2.66 comoving kpc and limited to a maximum of 0.7 proper kpc at low redshift. In addition, since we are primarily concerned with high-mass ($M_* > 10^{10}$ M$_\odot$) galaxies, we also use the $L = 100$ Mpc, $N = 1504^3$ (hence identical mass resolution and softening length) simulation of the reference model to improve the sampling of the massive galaxy population.

The simulations include a number of subgrid models for physical processes that originate on unresolved scales. These include star formation, which is modelled with a metallicity-dependent threshold (Schaye, 2004) and a pressure-dependent star formation law that reproduces the Kennicutt-Schmidt relation (Schaye & Dalla Vecchia, 2008). Star particles represent stellar populations of a single age, with their mass (distributed according to the Chabrier 2003 initial mass function; IMF) and metallicity inherited from their progenitor gas particles. The simulations follow the abundances of 11 elements (including O and Fe) as they are gradually released into the ISM according to the prescriptions of Wiersma et al. (2009b). These abundances are used to calculate the rates of radiative cooling and heating (Wiersma et al., 2009a). For each star particle, the rate of SN Type Ia per unit stellar mass is $\nu e^{-t/\tau}$, where t is the stellar age, and the parameters $\tau = 2$ Gyr and $\nu = 2 \times 10^{-3}$ M$_\odot^{-1}$ were chosen to reproduce the evolution of the observed SN Type Ia rate density (Schaye

et al., 2015).

The reference model includes a prescription for the growth of black holes (BHs), which increase their mass via mergers and gas accretion, where the accretion rate depends on the angular momentum of the gas (Rosas-Guevara et al., 2015; Schaye et al., 2015). Energy feedback from star formation and AGN (the latter is omitted in the *NoAGN* model) is implemented by stochastically heating gas particles surrounding newly formed star particles and BH particles, respectively (Dalla Vecchia & Schaye, 2012), so that galactic winds develop naturally without turning off the radiative cooling or hydrodynamics. The subgrid parameters governing the efficiencies of stellar and AGN feedback have been calibrated to reproduce the observed present-day galaxy stellar mass function and the relation between stellar mass and BH mass, with the additional constraint that the sizes of galaxies must be reasonable (Crain et al., 2015; Schaye et al., 2015).

Haloes are identified using the Friends-of-Friends and SUBFIND algorithms (Dolag et al., 2009). In this work, we are only concerned with 'central' galaxies, which are the galaxies residing at the minimum of the halo potentials. Following Schaye et al. (2015), we use a spherical aperture of radius 30 kpc to calculate galaxy properties.

We adopt the usual definition of the stellar abundance ratio,

$$\left[\frac{\mathrm{O}}{\mathrm{Fe}}\right]_* = \log_{10}\left(\frac{X^{\mathrm{O}}}{X^{\mathrm{Fe}}}\right) - \log_{10}\left(\frac{X_\odot^{\mathrm{O}}}{X_\odot^{\mathrm{Fe}}}\right), \tag{3.1}$$

where in our case $X^x = \Sigma_i m_i^{\mathrm{O}}/\Sigma_i m_i$ is the galaxy stellar mass fraction in element x, with m_i^{O} and m_i being the oxygen and total particle masses, respectively. $X_\odot^{\mathrm{O}}/X_\odot^{\mathrm{Fe}} = 4.44$ is the solar abundance ratio (Asplund et al., 2009). Throughout this work, we will use $[\mathrm{O}/\mathrm{Fe}]_*$ as a proxy for $[\alpha/\mathrm{Fe}]_*$ in EAGLE, as oxygen dominates the mass fraction of α-elements.

3.3   Results

To investigate the effect of AGN feedback on the stellar α-enhancement of galaxies, we first show the impact on the trend with stellar mass. Then, since α-enhancement is often used as a proxy for galaxy age (see e.g. Renzini 2006 for a review), we explore the impact of AGN feedback on the relation between $[\alpha/\mathrm{Fe}]_*$ and age.

3.3.1   Relation with stellar mass

Fig. 3.1 shows the stellar α-enhancement, $[\alpha/\mathrm{Fe}]_*$ (represented by $[\mathrm{O}/\mathrm{Fe}]_*$), as a function of galaxy stellar mass, comparing EAGLE simulations with and without AGN feedback. As we showed previously (Segers et al., 2016), in the EAGLE reference simulation $[\alpha/\mathrm{Fe}]_*$ is ~ 0.25 for $M_* \lesssim 10^{10.5}$ $M_\odot$ and increases with stellar mass for $M_* \gtrsim 10^{10.5}$ $M_\odot$, in excellent agreement with the observed $[\alpha/\mathrm{Fe}]_*$-M_* relation for early-type galaxies reported by Thomas et al. (2010). This trend is also in qualitative agreement with the observations from de La Rosa et al. (2011) and Conroy et al. (2014). For the latter, we only include their measurements at $M_* > 10^{10}$
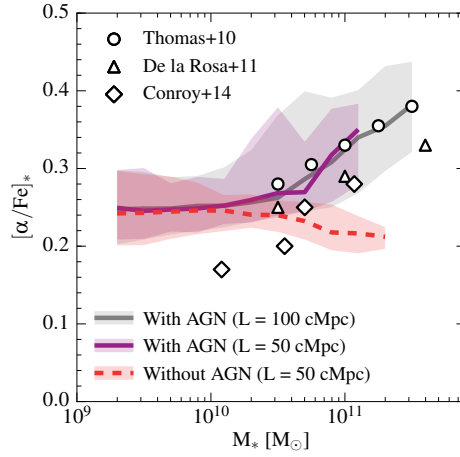
Figure 3.1: The effect of AGN feedback on the α-element-to-iron abundance ratio as a function of galaxy stellar mass for present-day central galaxies. The curves show the median $[\alpha/\mathrm{Fe}]_*$ (represented by $[\mathrm{O}/\mathrm{Fe}]_*$) in logarithmic mass bins of size 0.2 dex, as predicted by the simulations with and without AGN feedback. The shaded regions mark the 10th to 90th percentile range. We only show bins containing at least 10 galaxies and corresponding to a stellar mass of at least 1000 particles. In the fiducial model, $[\alpha/\mathrm{Fe}]_*$ increases with mass for $M_* \gtrsim 10^{10.5}$ $\mathrm{M}_\odot$, in excellent agreement with the observations from Thomas et al. (2010), and in qualitative agreement with those of de La Rosa et al. (2011) and Conroy et al. (2014, all converted to a solar abundance ratio of $\mathrm{X}_\odot^\mathrm{O}/\mathrm{X}_\odot^\mathrm{Fe} = 4.44$). In the model without AGN feedback, however, $[\alpha/\mathrm{Fe}]_*$ is roughly constant over the whole mass range.

$M_\odot$, where EAGLE galaxies are predominantly early type (Schaye et al., 2015; Trayford et al., 2015). The relation between $[\alpha/Fe]_*$ and stellar velocity dispersion, σ_*, matches the observations equally well. We show the relation with stellar mass here, since the simulation includes late-type galaxies for which rotation may influence the velocity dispersion. In addition, we explore the effect of calculating $[\alpha/Fe]_*$ as a luminosity-weighted average, using the r-band luminosities of EAGLE star particles as computed by Trayford et al. (2015), and in the absence of dust, instead of a ratio of mass fractions [equation (3.1)]. We find that the difference is marginal, typically within ±0.05 dex, and that it leaves the high-mass end slope unchanged.

We note that the normalization of the simulated relation is uncertain by a factor of ~ 2 due to uncertainties in the nucleosynthetic yields and SN Type Ia rate (Wiersma et al., 2009b), while the normalization of the observed relations varies as a result of uncertainties in the stellar population modelling. The systematic uncertainty in the observed $[\alpha/Fe]_*$ is typically estimated to be ~ $0.05 - 0.1$ dex (Thomas et al., 2010; de La Rosa et al., 2011; Johansson et al., 2012; Conroy et al., 2014).

The reference model ran in the smaller volume ($L = 50$ Mpc) yields results consistent with the $L = 100$ Mpc simulation. Comparing this model to the one without AGN feedback, we find that in the absence of AGN feedback, $[\alpha/Fe]_*$ does not increase with stellar mass. The relation in fact exhibits a mildly negative gradient. From this, we infer that feedback from AGN, becoming effective at $M_* \sim 10^{10.5}$ $M_\odot$, is responsible for the α-enhancement of present-day massive galaxies. It suppresses star formation in the progenitor galaxies, when these progenitors and their central BHs have grown massive enough for AGN feedback to be efficient, which happens earlier for more massive galaxies. Hence, since most stars formed before AGN feedback became active, these galaxies have earlier and shorter formation times, which naturally lead to enhanced enrichment of the stellar phase by ejecta from short-lived massive stars. In the absence of this quenching mechanism, late star formation is not suppressed efficiently enough to prevent the incorporation of iron from longer lived intermediate-mass stars (mainly SN Type Ia) into secondary generations of stars. Considering the time-scale on which the Fe from SN Type Ia is released, we infer that AGN must significantly suppress star formation within $\lesssim 1$ Gyr.

Reproducing the observed relation between $[\alpha/Fe]_*$ and stellar mass (or, equivalently, stellar velocity dispersion) for early-type galaxies has been a problem for many models of galaxy formation (e.g. Nagashima et al., 2005; Pipino et al., 2009), although recently a few semi-analytic models have been more successful (Arrigoni et al., 2010; Yates et al., 2013). While it has been argued that a variable IMF is necessary to reproduce the observed trend (Calura & Menci, 2009; Gargiulo et al., 2015), our results and those of Yates et al. (2013) show that this can also be achieved with a universal Chabrier IMF. Our model comparison shows that the inclusion of AGN feedback is sufficient to generate a sufficiently steep $[\alpha/Fe]_*$-M_* relation. The effect of AGN feedback on this relation has been demonstrated before, by Calura & Menci (2011) using a semi-analytic model that broadly reproduces the observed $[\alpha/Fe]_*$-σ relation, if both AGN feedback and interaction triggered starbursts are included. Furthermore, using low-resolution hydrodynamical simulations, Taylor & Kobayashi (2015) find an effect on two example galaxies that is in qualitative agreement with our results. However, in contrast to this work, the effect on the over-

all (massive) galaxy population is small, and their implementation of AGN feedback does not reproduce the observed trend.

3.3.2 Relation with stellar age

If AGN feedback is the mechanism that quenches star formation in galaxies, turning off AGN feedback should affect the ages of galaxies. Before comparing models with and without AGN feedback, we first show in the top panel of Fig. 3.2 the relation between $[\alpha/\text{Fe}]_*$ and age for the $L = 100$ Mpc reference simulation. Here, 'age' refers to the average stellar age, weighted by the initial mass of the stellar population (star particle), i.e. the mass at the time it was formed. Galaxies with $M_* \geq 10^{10}$ M$_\odot$ are shown as filled circles, where the colour indicates their stellar mass. Galaxies with 1.8×10^9 M$_\odot$ $< M_* < 10^{10}$ M$_\odot$ are shown as grey contours depicting the 68th and 95th percentiles of the distribution.

The two mass regimes show opposite trends. For $M_* < 10^{10}$ M$_\odot$, galaxies of increasing mean stellar age have lower $[\alpha/\text{Fe}]_*$. These galaxies are still forming stars from gas that becomes increasingly Fe-enriched by SN Type Ia as time progresses. Therefore, the oldest galaxies, which have had the longest time to enrich their ISM and stars with Fe, have the lowest $[\alpha/\text{Fe}]_*$. Note that the negative trend between $[\alpha/\text{Fe}]_*$ and mean stellar age for low-mass galaxies, as well as the positive trend for high-mass galaxies, is consistent with a positive correlation between age and $[\alpha/\text{Fe}]_*$ for *individual* stars within a galaxy. This is shown in Fig. 3.3 for galaxies with $M_*/\text{M}_\odot \sim 10^9, 10^{10}, 10^{11}$ from the $L = 100$ Mpc reference simulation. Star particles that were formed earlier, have higher $[\alpha/\text{Fe}]_*$, since the ISM at their formation time was less enriched by SN Type Ia than at later times. The trends in Fig. 3.3, which are similar for all three galaxy mass bins, agree qualitatively with observations of stellar populations in the Milky Way (e.g. Haywood et al., 2013; Ramírez et al., 2013). It is the distribution of the star particle ages, which are shown as histograms at the bottom of Fig. 3.3, which causes the median *galactic* $[\alpha/\text{Fe}]_*$ of $M_* \sim 10^{11}$ M$_\odot$ galaxies to be enhanced with respect to those of the less massive galaxies.

Galaxies with $M_* \geq 10^{10}$ M$_\odot$ (coloured circles in Fig. 3.2) show a transition from $[\alpha/\text{Fe}]_*$ *decreasing* with age ($M_* \lesssim 10^{10.5}$ M$_\odot$) to $[\alpha/\text{Fe}]_*$ *increasing* with age ($M_* \gtrsim 10^{10.5}$ M$_\odot$). The latter trend is consistent with the downsizing scenario for early-type galaxies, in which older galaxies have formed the bulk of their stars from a less Fe-enriched ISM, before their star formation was quenched (as illustrated by the $M_* \sim 10^{11}$ M$_\odot$ galaxies in Fig. 3.3). The colour coding in Fig. 3.2 indicates that more massive galaxies typically have higher ages and higher $[\alpha/\text{Fe}]_*$ ratios, consistent with Fig. 3.1.

For early-type galaxies, there are a number of observational studies on ages and abundance ratios to compare with. The black symbols in Fig. 3.2 show the observed $[\alpha/\text{Fe}]_*$ (or $[\text{O}/\text{Fe}]_*$) as a function of luminosity-weighted stellar age from Thomas et al. (2010) and Conroy et al. (2014), and $[\alpha/\text{Fe}]_*$ as a function of mass-weighted stellar age from de La Rosa et al. (2011). These correspond to the same mass bins as in Fig. 3.1. We also show the observed relation between $[\text{O}/\text{Fe}]_*$ and luminosity-weighted age from Johansson et al. (2012), by evaluating their best-fitting relations at six stellar velocity dispersions between $10^{1.9}$ and $10^{2.4}$ km s^{-1} (spaced by 0.1 dex).
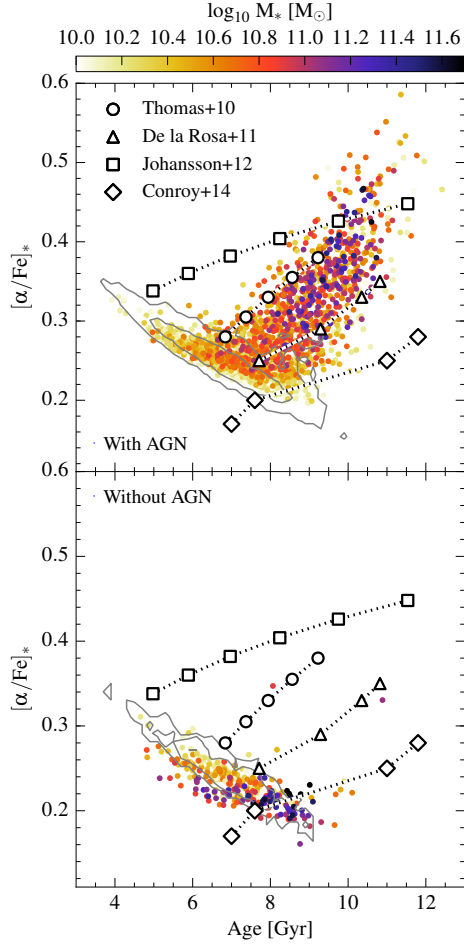
Figure 3.2: The effect of AGN feedback on the relation between $[\alpha/\text{Fe}]_*$ and mass-weighted mean stellar age. The top and bottom panels show the results from the simulations with ($L = 100$ Mpc) and without ($L = 50$ Mpc) AGN feedback, respectively. Galaxies with $M_* \geq 10^{10}$ $M_\odot$ are shown as filled circles, coloured by their stellar mass, while the distribution for 1.8×10^9 $M_\odot < M_* < 10^{10}$ $M_\odot$ galaxies is shown as grey contours enclosing the 68th and 95th percentiles. There are fewer objects in the bottom panel due to the smaller simulation volume. In both models, galaxies with $M_* \lesssim 10^{10.5}$ $M_\odot$ have lower $[\alpha/\text{Fe}]_*$ with increasing age, since they are increasingly enriching their ISM and stars with Fe as they continue to form stars. In contrast, because star formation in galaxies with $M_* \gtrsim 10^{10.5}$ $M_\odot$ is quenched, they are less Fe-enriched when they are older, in qualitative agreement with observations of early-type galaxies (Thomas et al., 2010; de La Rosa et al., 2011; Johansson et al., 2012; Conroy et al., 2014, all converted to a solar abundance ratio of $X_\odot^O/X_\odot^{Fe} = 4.44$). In the absence of AGN feedback, however, the $M_* \gtrsim 10^{10.5}$ $M_\odot$ galaxies follow the trend of the lower mass galaxies, decreasing their $[\alpha/\text{Fe}]_*$ with time as they continue to form stars.
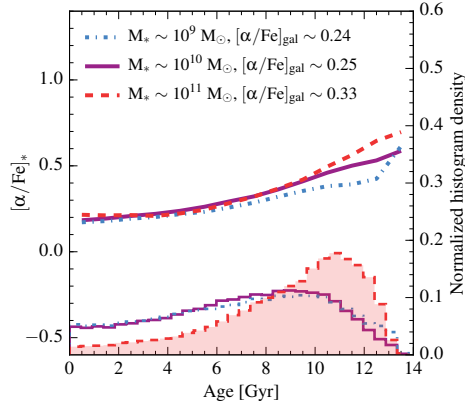
Figure 3.3: The relation between $[\alpha/\text{Fe}]_*$ and age for individual star particles in galaxies with stellar masses of $M_*/M_\odot \sim 10^9, 10^{10}, 10^{11}$, selected from the $L = 100$ Mpc reference simulation. The 0.1 dex galaxy mass bins contain 748, 300, 92 galaxies, respectively. The upper curves show, for all the star particles in the galaxies of the respective mass bin, the median $[\alpha/\text{Fe}]_*$ in each $\Delta\text{age} = 1$ Gyr bin with at least 10 particles, while the (normalized) histograms at the bottom show the distributions of star particle ages, weighted by their current mass. While the relation between $[\alpha/\text{Fe}]_*$ and age of individual star particles is similar for all three galaxy mass bins, the different age distributions lead to different values of the galactic $[\alpha/\text{Fe}]_*$.

Note that the systematic offsets between the different observed relations is large. In addition to uncertainties in the stellar population modelling (systematic uncertainties in the stellar age are typically estimated to be $\sim 0.1 - 0.2$ dex), this may be due to the size of the aperture used, and the fact that luminosity-weighted ages are typically lower than mass-weighted ages, as young stars generally dominate the population luminosity (e.g. Trager & Somerville, 2009). Comparing the observed relations to the relation predicted by EAGLE, we see that they all agree qualitatively on the positive correlation between $[\alpha/\text{Fe}]_*$ and age, as shown by the $M_* \gtrsim 10^{10.5}$ $M_\odot$ EAGLE galaxies (which are predominantly early-type galaxies). Weighting the average stellar ages in EAGLE by the r-band luminosity of the star particles (instead of their mass) yields ages that are lower by $\sim 1 - 2$ Gyr. However, this does not have a significant impact on the slopes of the two galaxy populations.

To illustrate the effect of AGN feedback on the ages of galaxies, we show in the bottom panel of Fig. 3.2 the relation between $[\alpha/\text{Fe}]_*$ and age for the $L = 50$ Mpc simulation without AGN feedback. While the two models agree for $M_* \lesssim 10^{10.5}$ $M_\odot$, the increase in $[\alpha/\text{Fe}]_*$ with age for $M_* \gtrsim 10^{10.5}$ $M_\odot$ galaxies in the reference model is absent in the model without AGN feedback. Instead, the high-mass galaxies also show an inverted $[\alpha/\text{Fe}]_*$- age relation, with a slope and normalization similar to that of the low-mass population.

3.4   Conclusions

We have investigated the effect of AGN feedback on the stellar α-enhancement of present-day central galaxies, using cosmological simulations from the EAGLE project. We compared results from the EAGLE fiducial model, which includes energy feedback from AGN, to results from a model without AGN feedback. We found that in the presence of AGN feedback, the $[\alpha/\text{Fe}]_*$ of $M_* \gtrsim 10^{10.5}$ $M_\odot$ galaxies increases with both increasing galaxy stellar mass and age. These trends are in good agreement with observations of early-type galaxies, and are consistent with galactic downsizing: the earlier and more rapid formation time-scales of massive galaxies result in higher $[\alpha/\text{Fe}]_*$, as the bulk of their stars was formed from a mostly α-enriched ISM, before their star formation was quenched significantly. In the model without AGN feedback, however, $[\alpha/\text{Fe}]_*$ of galaxies is insensitive to stellar mass and decreases with increasing mean stellar age, following the relation found for $M_* \lesssim 10^{10.5}$ $M_\odot$ galaxies, also by the model that includes AGN feedback. In the absence of a quenching mechanism, galaxies continue to form stars from an increasingly Fe-enriched ISM, decreasing their $[\alpha/\text{Fe}]_*$ as they age. Consistent with earlier suggestions by Calura & Menci (2011) and Taylor & Kobayashi (2015), we conclude – for the first time using cosmological, hydrodynamical simulations that successfully reproduce the relations observed for early-type galaxies – that star formation quenching by AGN feedback can account for the α-enhancement of massive galaxies.

Acknowledgements

4

Metals in the circumgalactic medium are out of ionization equilibrium due to fluctuating active galactic nuclei

We study the effect of a fluctuating active galactic nucleus (AGN) on the abundance of circumgalactic Ovɪ in galaxies selected from the Evolution and Assembly of GaLaxies and their Environments simulations. We follow the time-variable Ovɪ abundance in post-processing around four galaxies – two at $z = 0.1$ with stellar masses of $M_* \sim 10^{10}\,\mathrm{M}_\odot$ and $M_* \sim 10^{11}\,\mathrm{M}_\odot$, and two at $z = 3$ with similar stellar masses – out to impact parameters of twice their virial radii, implementing a fluctuating central source of ionizing radiation. Due to delayed recombination, the AGN leave significant 'AGN proximity zone fossils' around all four galaxies, where Ovɪ and other metal ions are out of ionization equilibrium for several megayears after the AGN fade. The column density of Ovɪ is typically enhanced by $\approx 0.3 - 1.0$ dex at impact parameters within $0.3R_{\mathrm{vir}}$, and by $\approx 0.06 - 0.2$ dex at $2R_{\mathrm{vir}}$, thereby also enhancing the covering fraction of Ovɪ above a given column density threshold. The fossil effect tends to increase with increasing AGN luminosity, and towards shorter AGN lifetimes and larger AGN duty cycle fractions. In the limit of short AGN lifetimes, the effect converges to that of a continuous AGN with a luminosity of $(f_{\mathrm{duty}}/100\%)$ times the AGN luminosity. We also find significant fossil effects for other metal ions, where low-ionization state ions are decreased (Siɪv, Cɪv at $z = 3$) and high-ionization state ions are increased (Cɪv at $z = 0.1$, Nevɪɪɪ, Mgx). Using observationally motivated AGN parameters, we predict AGN proximity zone fossils to be ubiquitous around $M_* \sim 10^{10-11}\,\mathrm{M}_\odot$ galaxies, and to affect observations of metals in the circumgalactic medium at both low and high redshifts.

Marijke C. Segers, Benjamin D. Oppenheimer,
Joop Schaye and Alexander J. Richings

4.1   Introduction

Active galactic nuclei (AGN) play an important role in the formation and evolution of galaxies. Powered by the accretion of gas on to the central black hole (BH; e.g. Salpeter, 1964; Lynden-Bell, 1969), AGN are the most luminous objects in the Universe, releasing vast amounts of energy into the interstellar medium of their host galaxies and beyond. The various scaling relations between the properties of AGN and those of their host galaxies (see e.g. Kormendy & Ho 2013 for a review), as well as the apparent tendency of AGN to reside in star-forming galaxies (e.g. Lutz et al., 2008; Santini et al., 2012), suggest a close correlation between AGN activity and the star formation (SF) activity of the host. This is also supported by the remarkably similar evolution of the cosmic SF rate density and the cosmic BH accretion rate density (e.g. Boyle & Terlevich, 1998; Silverman et al., 2008; Mullaney et al., 2012b), which are both found to peak at $z \approx 2$. A correlation between AGN and SF activity is consistent with the prediction that both phenomena are fuelled by a common supply of cold gas (e.g. Hopkins & Quataert, 2010), as well as with observational evidence that AGN affect the SF in the host by acting as a local triggering mechanism (e.g. Begelman & Cioffi, 1989; Elbaz et al., 2009), and by regulating SF galaxy-wide (e.g. Di Matteo et al., 2005) as they drive galactic outflows (i.e. ejective feedback) and heat the gas in the halo (i.e. preventative feedback).

Furthermore, as powerful sources of radiation, AGN not only provide radiative feedback in the form of pressure and photoheating, they also affect the ionization state of the gas in and around the host galaxies. In particular, the abundance of neutral hydrogen (HI), as measured from the Lyα absorption along the light-of-sight towards a quasar[1], is observed to be suppressed in proximity to the quasar (e.g. Carswell et al., 1982; Scott et al., 2000; Dall'Aglio et al., 2008), consistent with the expected local enhancement of the HI ionizing radiation field relative to the extragalactic background. This effect is referred to as the line-of-sight proximity effect.

Using pairs of quasars, it is possible to probe the ion abundances in the circumgalactic medium (CGM) of a foreground quasar host in the transverse direction, by analysing the absorption in the spectrum of the background quasar. As studies of this transverse proximity effect generally find no reduction (and in some cases even an enhancement; see e.g. Prochaska et al., 2013) of the HI optical depth close to the foreground quasar (e.g. Schirber et al., 2004; Kirkman & Tytler, 2008), but do find effects of enhanced photoionization on the abundances of metal ions (e.g. CIV and OVI; see Gonçalves et al., 2008), it is clear that transverse proximity effects are not straightforward to interpret. Quasar radiation being anisotropic (e.g. Liske & Williger, 2001; Prochaska et al., 2013) or the fact that quasars tend to live in overdense regions of the Universe (e.g. Rollinde et al., 2005; Guimarães et al., 2007) might play a role. Nevertheless, these studies indicate that the response of HI to a local enhancement of the ionizing radiation field is vastly different from that of metal ions. While hydrogen has only two ionization states, such that the HI fraction decreases with an increasing ionization field strength, heavy elements like

---
[1]Throughout this work, we will use the words 'AGN' and 'quasar' interchangeably.

oxygen have multiple ionization levels, where the ion fractions peak at particular temperatures and densities that depend on the local photoionization rate.

The differences between H<small>I</small> and metal ions become even more evident when considering their behaviour in a fluctuating ionizing radiation field (Oppenheimer & Schaye, 2013a). After the local radiation source has faded, the time-scale on which ion species return to ionization equilibrium depends on the recombination time-scale, as well as on the ion fraction of the recombined species in equilibrium: the latter can be close to one for metal ions, while being typically $\lesssim 10^{-4}$ for H<small>I</small> in the CGM. This leads to significantly longer 'effective' recombination time-scales for metals than for hydrogen, which are even further extended due to the multiple ionization levels that metals need to recombine through. Oppenheimer & Schaye (2013a) showed that, in contrast to H<small>I</small>, metal ions at typical CGM densities can remain out of ionization equilibrium up to a few tens of megayears, as a result of delayed recombination after the enhanced AGN radiation field turns off. They define these out-of-equilibrium regions as AGN proximity zone fossils.

Both observations and theory indicate that the radiation output from AGN is not continuous, but rather happens in intermittent bursts. This is potentially due to instabilities in the accretion disc that fuels the BH or the clumpiness of the accreting material. Simulations following nuclear gas accretion down to sub-kpc scales (e.g. Hopkins & Quataert, 2010; Novak et al., 2011; Gabor & Bournaud, 2013) generally predict that the mass growth of the central BH predominantly happens through short, repeated accretion events, which naturally give rise to episodic bursts of AGN activity. Direct observational evidence for AGN variability comes from ionization echoes in the form of [O<small>III</small>] emitting clouds (including the prototypical quasar ionization echo 'Hanny's Voorwerp', published in Lintott et al. 2009; many have been found thereafter, see e.g. Keel et al. 2012; Schirmer et al. 2013), and from delayed Lyα emission from nearby Lymanα blobs (Schirmer et al., 2016). In both of these, recent AGN activity is required to account for the degree of ionization of the emitting gas. In the Milky Way, the observed γ-ray emitting *Fermi* bubbles provide evidence of nuclear activity in the Galactic Centre roughly ~ 1 Myr ago (e.g. Su et al., 2010; Zubovas et al., 2011). Furthermore, AGN variability has been invoked to explain the absence of a correlation between AGN luminosity and host SF rate as reported by a number of observational studies, despite the expected close relation between SF and AGN activity (see e.g. Alexander & Hickox 2012 and Hickox et al. 2014, although McAlpine et al. 2017 argue that AGN variability is only part of the explanation). Hence, the facts that AGN are likely transient phenomena and that all galaxies are thought to harbour a BH in their centre, suggest that all galaxies are potential AGN hosts, although they are not necessarily active at the time of observation.

Rough estimates of the fraction of time that the AGN in a given galaxy is 'on', also referred to as the AGN duty cycle fraction f_{duty}, follow from comparing the number densities of AGN and their host haloes, where the observed AGN clustering strength is used to infer the typical host halo mass (see e.g. Haiman & Hui, 2001; Martini & Weinberg, 2001; Shen et al., 2007, who consider $z \simeq 2-4$), and from comparing the time integral of the quasar luminosity function to the estimated present-day BH number density (e.g. Yu & Tremaine, 2002; Haiman et al., 2004; Marconi

et al., 2004). These observational constraints typically yield $f_{duty} \sim 0.1 - 10\%$, although a related approach by Shankar et al. (2010) at $z = 3 - 6$ derives duty cycle fractions as high as $f_{duty} \sim 10 - 90\%$. Studies measuring the AGN occurrence in galaxies from their optical emission lines (e.g. Kauffmann et al., 2003; Miller et al., 2003; Choi et al., 2009) or X-ray emission (e.g. Bongiorno et al., 2012; Mullaney et al., 2012a) generally find that the fraction of galaxies with active AGN depends on stellar mass and redshift, as well as on the selection diagnostics used, but typical fractions range from $\sim 1\%$ to 20% in the galaxy mass range that we consider here.

The time per 'cycle' that the AGN is on, which we will refer to as the AGN lifetime, t_{AGN}, can also be constrained observationally, using quasar proximity effects on the surrounding gas probed in absorption (e.g. Schirber et al., 2004; Gonçalves et al., 2008; Kirkman & Tytler, 2008; Syphers & Shull, 2014). Typical estimates are $t_{AGN} \sim 1 - 30$ Myr. However, these constraints are indirect and limited by the fact that t_{AGN} is potentially longer than the time that the AGN has been on for now, while it is also possible that the AGN has turned off and on again since it irradiated the absorbing gas. Furthermore, based on a statistical argument, using the fraction of the X-ray detected AGN that is optically elusive and the light-travel time across the host galaxy, Schawinski et al. (2015) derived an estimate of the AGN lifetime of $t_{AGN} \sim 10^5$ yr.

In this work, we investigate how the fluctuating photoionizing radiation field from a central AGN affects the metal ion abundances in the CGM of the host galaxy. We mainly focus on Ovɪ, which is a widely studied ion in observations of quasar absorption-line systems, in particular at low redshift (e.g. Prochaska et al., 2011; Tumlinson et al., 2011), but also at high redshift (e.g. Carswell et al., 2002; Lopez et al., 2007; Turner et al., 2015). Observations with the Cosmic Origins Spectrograph (COS), taken as part of the COS-Halos survey, found high abundances of Ovɪ in the CGM of $z \sim 0.2$ star-forming galaxies, extending out to at least 150 kpc, which is ≈ 0.5 times the virial radius for the typical galaxy mass that was probed (Tumlinson et al., 2011). However, cosmological hydrodynamical simulations has so far not succeeded in reproducing these high Ovɪ columns (e.g. Hummels et al., 2013; Ford et al., 2016; Oppenheimer et al., 2016; Suresh et al., 2017): they generally underpredict the observed column densities by a factor of $\approx 2 - 10$ (see e.g. McQuinn & Werk 2017 for further discussion). Here, we show that fluctuating AGN strongly enhance the Ovɪ in the CGM of galaxies with stellar masses of $M_* \sim 10^{10-11} M_\odot$, both at $z = 0.1$ and at $z = 3$, and that this enhancement remains for several megayears after the central AGN fade. Hence, this provides a potential way of reconciling the predicted Ovɪ column densities with the observed ones. This is explored in more detail by Oppenheimer et al. (2017).

Continuing the work by Oppenheimer & Schaye (2013a), who considered a single gas pocket exposed to fluctuating AGN radiation, we here consider the CGM of galaxies selected from the Evolution and Assembly of GaLaxies and their Environments (EAGLE) simulations (Schaye et al., 2015; Crain et al., 2015), where we include enhanced photoionization from a local AGN in post-processing. We follow the time-evolving abundance of circumgalactic Ovɪ using a reaction network (Oppenheimer & Schaye, 2013b) that captures the non-equilibrium behaviour of 133 ions. To quantify to what extent AGN proximity zone fossils affect the interpreta-

tion of CGM column density measurements from quasar absorption-line systems, we present predictions of the average enhancement of the Ovɪ column density and covering fraction in a fluctuating AGN radiation field. Furthermore, we calculate the probability of observing a significant AGN fossil effect[2] (i.e. a CGM Ovɪ column density that is out of equilibrium by at least 0.1 dex), while the central AGN in the galaxy is inactive. This gives an indication of the fraction of quasar absorption-line systems that are likely affected by AGN fossil effects. We explore the dependence on impact parameter, galaxy stellar mass and redshift, as well as the dependence on the adopted parameters used to model the fluctuating AGN: we vary the AGN luminosity (by varying the Eddington ratio, L/L_{Edd}, where L_{Edd} is the Eddington luminosity), lifetime and duty cycle fraction.

This paper is organized as follows. In Section 4.2, we describe the simulation output used, the AGN model that we implement in post-processing and our method for calculating the time-variable column densities of CGM ions. We also introduce the three quantities we use to quantify the significance of the AGN fossil effect. In Section 4.3, we present our results for Ovɪ and show how they depend on the properties of the galaxy and the adopted AGN model parameters. We briefly present results for other metal ions in Section 4.4 and we summarize our findings in Section 4.5.

4.2 Methods

We begin by giving a brief overview of the EAGLE simulation code and the non-equilibrium ionization module, followed by a description of the fluctuating AGN model used to photoionize the CGM of the selected galaxies. We then describe how we calculate column densities from the ion abundances predicted by the simulation, and how we quantify the significance of the AGN fossil effects.

4.2.1 EAGLE simulations

The EAGLE simulations were run with a heavily modified version of the smoothed particle hydrodynamics (SPH) code GADGET3 (last described by Springel, 2005). A collection of updates, referred to as ANARCHY (Appendix A of Schaye et al. 2015; see also Schaller et al. 2015a), has been implemented into the code, including the use of a pressure-entropy formulation of SPH (Hopkins, 2013). The adopted cosmological parameters are taken from Planck Collaboration et al. (2014): $[\Omega_{\mathrm{m}}, \Omega_{\mathrm{b}}, \Omega_{\Lambda}, \sigma_8, n_{\mathrm{s}}, h] = [0.307, 0.04825, 0.693, 0.8288, 0.9611, 0.6777]$.

The implemented subgrid physics is described in detail in Schaye et al. (2015). In brief, SF is modelled as the stochastic conversion of gas particles into star particles, following the pressure-dependent prescription of Schaye & Dalla Vecchia (2008) in combination with a metallicity-dependent density threshold (given by Schaye, 2004). Because the simulations do not model a cold phase, a global temperature floor, corresponding to the equation of state $P \propto \rho^{4/3}$ and normalized to 8000 K

---

[2]We note that the 'fossil effect' that we refer to in this work, includes the effects from both the finite light-travel time (i.e. ionization echoes) and from delayed recombination after the enhanced incident radiation ceases.

at a density of $n_H = 0.1$ cm^{-3}, is imposed on the gas in the interstellar medium. When computing the ionization balance (Section 4.2.2), we set the temperature of star-forming gas to $T = 10^4$ K, as its temperature given in the simulation merely reflects an effective pressure due to the imposed temperature floor.

Star particles enrich their surroundings through the release of mass and metals in stellar winds and supernova explosions (Type Ia and Type II) according to the prescriptions of Wiersma et al. (2009b). The adopted stellar initial mass function is taken from Chabrier (2003). During the course of the simulation, the abundances of 11 elements (i.e. H, He, C, N, O, Ne, Mg, Si, Fe, Ca and Si) are followed, which are used to calculate the equilibrium rates of radiative cooling and heating in the presence of cosmic microwave background and Haardt & Madau (2001, HM01) UV and X-ray background radiation (Wiersma et al., 2009a). The time-dependent abundances of 133 ion species are calculated in post-processing, as we describe in Section 4.2.2, and are not used for the cooling and heating rates.

Energy feedback from SF and AGN is implemented by stochastically heating gas particles surrounding newly formed star particles and BH particles, respectively (Dalla Vecchia & Schaye, 2012). The BHs, with which haloes are seeded as in Springel (2005), grow through mergers and gas accretion, where the accretion rate takes into account the angular momentum of the gas (Rosas-Guevara et al., 2015; Schaye et al., 2015). The subgrid parameters in the models for stellar and AGN feedback have been calibrated to reproduce the observed present-day galaxy stellar mass function, the sizes of galaxies, and the relation between stellar mass and BH mass.

In this work, we focus on four galaxies selected from the EAGLE reference simulation. This simulation (referred to as *Ref-L100N1504* in Schaye et al., 2015) was run in a periodic, cubic volume of $L = 100$ comoving Mpc on a side. It contains $N = 1504^3$ dark matter particles and an equal number of baryonic particles with (initial) masses of $m_{dm} = 9.7 \times 10^6$ M$_\odot$ and $m_b = 1.8 \times 10^6$ M$_\odot$, respectively, and with a gravitational softening length of 2.66 comoving kpc, limited to a maximum physical scale of 0.7 proper kpc.

Haloes and galaxies are identified from the simulation using the Friends-of-Friends and SUBFIND algorithms (Dolag et al., 2009). Galaxies are subdivided into 'centrals' and 'satellites', where the former are the galaxies residing at the minimum of the halo potential. The mass of the halo, referred to as the virial mass M_{vir}, is defined as the mass enclosed within a spherical region centred on the minimum potential, within which the mean density equals 200 times the critical density of the Universe. The corresponding virial radius and temperature are denoted by R_{vir} and T_{vir}, respectively.

4.2.2   Non-equilibrium ionization module

To model the time-variable abundances of ion species in the CGM of our simulated galaxies, we use the reaction network introduced by Oppenheimer & Schaye (2013b). It follows the 133 ionization states of the 11 elements that are used to compute the (equilibrium) cooling rates in the simulation, as well as the number density of electrons. The reactions included in the network are those corresponding

to radiative and di-electric recombination, collisional ionization, photoionization, Auger ionization and charge transfer. Given the set of reaction rates, the module calculates the ionization balance as a function of time, without making the assumption that the gas is in ionization equilibrium. While it is possible to integrate the module into the simulation and to calculate ion abundances and ion-by-ion cooling rates on the fly (Richings & Schaye, 2016; Oppenheimer et al., 2016), we here work strictly in post-processing. This means that we do not include dynamical evolution or evolution of the temperature when we solve for the ionization state of the gas. We note that, in contrast to the cooling rates, which are calculated from 'kernel-smoothed' element abundances (i.e. the ratio of the mass density of an element to the total mass density per particle; Wiersma et al., 2009b), we use particle-based element and ion abundances (i.e. the fraction of the mass in an element or ion) in the reaction network.

The non-equilibrium ionization module enables us to explore the effect on the CGM of a time-variable source of ionizing radiation, in our case of an AGN positioned in the centre of the galaxy. A source with specific intensity f_ν photoionizes ions of atomic species x from state i to $i + 1$ at a rate

$$\Gamma_{x_i,\mathrm{AGN}} = \int_{\nu_{0,x_i}}^\infty \frac{f_\nu}{h\nu} \sigma_{x_i}(\nu)\, \mathrm{d}\nu, \qquad (4.1)$$

where ν is the frequency, ν_{0,x_i} is the ionization frequency, h is the Planck constant and $\sigma_{x_i}(\nu)$ is the photoionization cross-section. The evolution of the number density n_{x_i} of ions in state x_i is then given by

$$\frac{\mathrm{d}n_{x_i}}{\mathrm{d}t} = n_{x_{i+1}}\alpha_{x_{i+1}}n_\mathrm{e} + n_{x_{i-1}}\left(\beta_{x_{i-1}}n_\mathrm{e} + \Gamma_{x_{i-1},\mathrm{EGB}}\right.$$
$$\left. +\Gamma_{x_{i-1},\mathrm{AGN}}\right) - n_{x_i}\left(\left(\alpha_{x_i} + \beta_{x_i}\right)n_\mathrm{e} + \Gamma_{x_i,\mathrm{EGB}} + \Gamma_{x_i,\mathrm{AGN}}\right), \quad (4.2)$$

where charge transfer and Auger ionization have been omitted from the equation for simplicity. Here, n_e is the free electron number density, which depends mostly on the abundance and ionization state of hydrogen. α_{x_i} and β_{x_i} are the rates of recombination (including both radiative and di-electric) and collisional ionization, respectively, which depend on the local temperature. The photoionization rate from the extragalactic background, $\Gamma_{x_i,\mathrm{EGB}}$, is calculated from equation (4.1) using the redshift-dependent HM01 spectral shape, consistent with the background radiation included in the simulation.

4.2.3 Ion column densities

We compute column densities (N) of ions in the CGM by projecting a cylindrical region with a radius of $2R_\mathrm{vir}$ and a line-of-sight length of 2 Mpc, centred on the centre of the galaxy, on to a 2D grid of 1000×1000 pixels[3]. For each grid pixel, we calculate the ion column densities from the particle ion abundances using two-dimensional, mass-conserving SPH interpolation. Throughout this work, we will

---

[3]We have checked that the number of grid pixels is sufficiently high so that the CGM column densities are converged.

mainly focus on O$\textsc{vi}$. We therefore define the quantities we use to quantify the significance of the AGN fossil effect specifically for O$\textsc{vi}$. However, these quantities are defined for other ions in a similar way.

We consider the column density of circumgalactic O$\textsc{vi}$ up to impact parameters (i.e. projected galactocentric distances) of $2R_{\mathrm{vir}}$. To construct column density profiles, which we denote by $N_{\mathrm{Ovi}}(R)$, we take the median column density of all the grid pixels within an impact parameter range centred on R. We take the median, rather than the mean or the total number of ions divided by the area of the bin, since this mimics the cross-section-weighted observations of column densities in quasar absorption-line studies more closely.

4.2.4   Galaxy sample

To explore how the strength of AGN proximity zone fossils depends on galaxy mass and redshift, we consider two (central) galaxies with stellar masses of $M_* \sim 10^{10}\,\mathrm{M_\odot}$ and $M_* \sim 10^{11}\,\mathrm{M_\odot}$ at $z = 3$ and two galaxies with similar stellar masses at $z = 0.1$[4]. These galaxies have been selected to be 'representative' galaxies, with stellar-to-halo mass ratios that are close to the mean and median value at the respective stellar mass and redshift. Fig. 4.1 shows maps of their hydrogen number density (left column), temperature (middle column) and metallicity (right column). These maps have been made by projecting a cylindrical region with a radius of $2R_{\mathrm{vir}}$ and a length of 2 Mpc, centred on the galaxy, on to a 2D grid (similarly to how we compute ion column densities; see Section 4.2.3) and calculating the mass-weighted quantity in each grid cell using SPH interpolation. The stellar masses, halo masses, virial radii and virial temperatures of the galaxies are listed on the left. The most evident difference between $z = 0.1$ and $z = 3$ is the higher density of the CGM at high redshift, with the galaxies being more embedded in filamentary structures.

Without any AGN proximity effects, the column density profiles of the different oxygen ions in the CGM of the four galaxies are as given in Fig. 4.2. In general, the ionization state of the gas increases with increasing impact parameter: the column densities of the lower state ions (O$\textsc{i}$ - O$\textsc{v}$) decrease significantly, while the profiles of the higher state ions are flatter. This is related to the fact that the density (and hence, the recombination rate) is lower at larger galactocentric radii, while the gas still receives the same background radiation. At a fixed R/R_{vir}, the ionization state is higher for more massive galaxies, owing to their higher CGM temperatures (see Fig. 4.1).

Evident for all four galaxies is that the column density of O$\textsc{vi}$ is relatively low compared to the column densities of the other oxygen ions. The dominant oxygen state is generally O$\textsc{vii}$ - O$\textsc{viii}$ for the galaxies at low redshift, and O$\textsc{viii}$ - O$\textsc{ix}$ at high redshift. As was e.g. pointed out by Oppenheimer et al. (2016), O$\textsc{vi}$ is only the tip of the iceberg of the CGM oxygen content. Since the ion fraction of O$\textsc{vi}$ in collisional ionization equilibrium peaks at $T_{\mathrm{peak}} \sim 10^{5.5}$ K, where gas cooling is fast, significant quantities of collisionally ionized O$\textsc{vi}$ only exist if the virial

---

[4]These correspond to the galaxies with G$\textsc{alaxy}$ID = 19523883, 18645002, 10184330, 15484683 in the publicly available EAGLE catalogue at `http://www.eaglesim.org/database.php` (McAlpine et al., 2016).
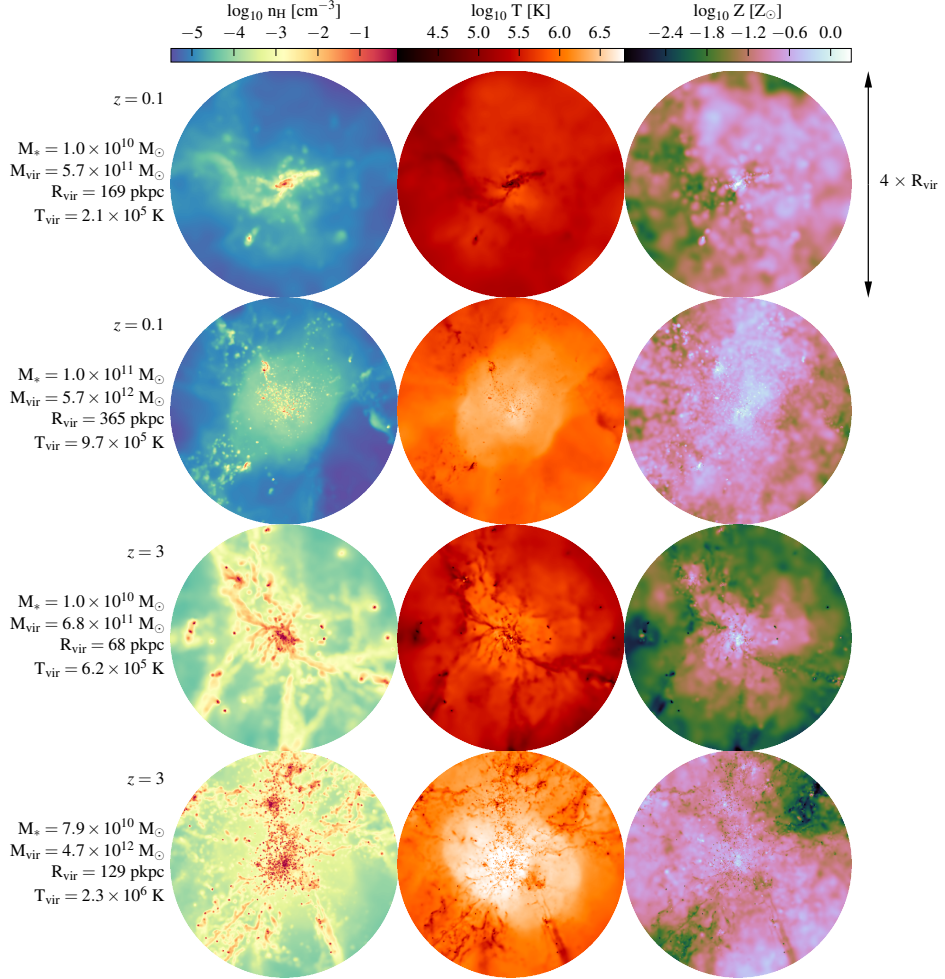
Figure 4.1: Maps of the hydrogen number density (left), temperature (middle) and metallicity (right; normalized to the solar metal mass fraction $Z_\odot = 0.0129$) for the CGM of the four galaxies considered in this work. These are all central galaxies and have been selected from the EAGLE *Ref-L100N1504* simulation. Their stellar mass ($M_* \sim 10^{10}\,M_\odot$ and $M_* \sim 10^{11}\,M_\odot$), redshift ($z = 0.1$ and $z = 3$) and virial properties are listed on the left. The colour-coding indicates the mass-weighted quantity projected on to a 2D grid with radius $2R_{vir}$ using SPH interpolation, within a slice of 2 Mpc thickness centred on the galaxy.
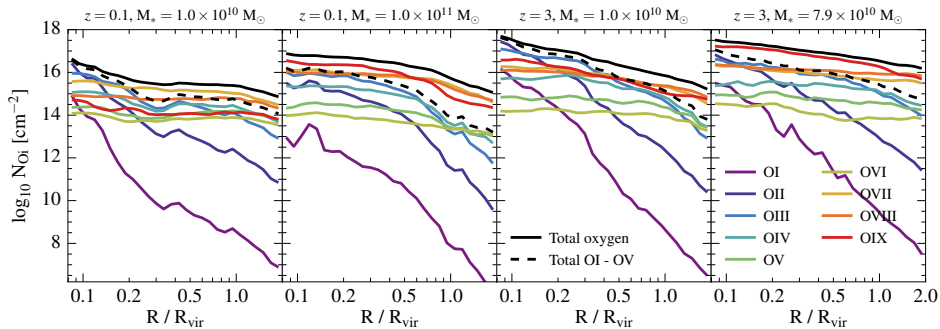
Figure 4.2: Equilibrium column density profiles of oxygen ions for, from left to right, the $M_* \sim 10^{10}\,M_\odot$ and $M_* \sim 10^{11}\,M_\odot$ galaxies at $z = 0.1$, and the $M_* \sim 10^{10}\,M_\odot$ and $M_* \sim 10^{11}\,M_\odot$ galaxies at $z = 3$. The coloured curves show the individual ion column densities as a function of impact parameter, given by the median column density in logarithmic impact parameter intervals between $R/R_{\rm vir} = 0.08$ and $R/R_{\rm vir} = 2.0$. The black, solid (dashed) curves show the total column density of oxygen (of ion states OI to OV). Most of the oxygen resides in the high ion states (mostly in OVII - OVIII for the galaxies at $z = 0.1$, and in OVIII - OIX at $z = 3$). The OVI state is always subdominant.

temperature of the halo is close to $T_{\rm peak}$. Otherwise, gas predominantly exists at $T < 10^5$ K or at $T > 10^6$ K, where the ion fraction is lower, which is why $N_{\rm OVI}$ in the CGM of $M_{\rm vir} \gtrsim 10^{12}\,M_\odot$ galaxies decreases with increasing halo mass (see fig. 4 of Oppenheimer et al., 2016). The photoionized phase of OVI arises at $T < 10^5$ K and at lower densities than the collisionally ionized phase. Therefore, the CGM of low-mass galaxies, with $T_{\rm vir} \ll T_{\rm peak}$, exhibits a significant fraction of gas in a temperature and density regime where the ion fraction of OVI is also high. However, if the galaxy stellar mass is low, the metallicity and total mass in oxygen are also low, which results in a low $N_{\rm OVI}$ despite the high ion fraction.

The galaxies with $M_* \sim 10^{10}\,M_\odot$ considered in this work have virial temperatures that are close to $T_{\rm peak}$ (somewhat lower for the one at $z = 0.1$ and somewhat higher for the one at $z = 3$), while the galaxies with $M_* \sim 10^{11}\,M_\odot$ have $3 - 7$ times higher virial temperatures than $T_{\rm peak}$. This means that especially at small radial distances from the high-mass galaxies, the OVI is mostly collisionally ionized. At larger distances, in particular for the low-mass galaxies, an increasing fraction of the OVI is photoionized (see Section 4.3).

4.2.5   AGN model

Having selected our four galaxies, we include a variable photoionizing radiation field in post-processing as follows. We assume that the radiation source is located at the minimum of the potential of the galaxy (including its subhalo), that irradiates the gas isotropically with a certain luminosity, spectral shape and periodicity. The ionizing radiation propagates through the galaxy and CGM with the speed
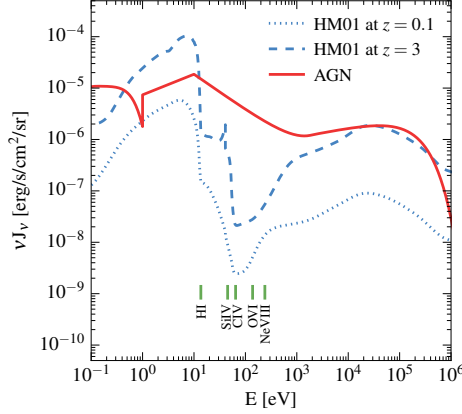
Figure 4.3: The model spectrum for the homogenous UV background at $z = 0.1$ (blue, dotted line) and $z = 3$ (blue, dashed line), adopted from Haardt & Madau (2001), and the model spectrum for the AGN (red, solid line), adopted from Sazonov et al. (2004; i.e. the 'unobscured' quasar model spectrum). Note that $f_\nu = 4\pi J_\nu$. The normalization of the AGN spectrum corresponds to an AGN with $L/L_{\mathrm{Edd}} = 1$, where $M_{\mathrm{BH}} = 10^7\,\mathrm{M}_\odot$, at a distance of 100 pkpc. This is equivalent to a bolometric luminosity of $L = 1.3 \times 10^{45}$ erg/s and a strength of $J_\nu = 10^{-20.3}$ erg/s/cm^2/Hz/sr at $E = 1$ Ryd. The ionization energies of a few commonly observed metal ions are indicated at the bottom.

Table 4.1: Parameter values for the AGN model explored in this work: the AGN luminosity as a fraction of the Eddington luminosity (L/L_{Edd}), the AGN lifetime per cycle (t_{AGN}) and the fraction of time that the AGN is on (f_{duty}).

Parameter	Values
L/L_{Edd}	$0.01, 0.1, 1.0$
t_{AGN}	$10^5, 10^6, 10^7$ yr
f_{duty}	$1, 2, 5, 10, 20, 50\%$

of light[5], where the spatial position, density and temperature of the gas have been fixed to those output by the simulation at the respective redshift. Note that this means that we do not include the effect of photoheating by the local AGN. However, Oppenheimer & Schaye (2013a) show that the change in the temperature due to photoheating is generally small (e.g. $\Delta \log_{10} T \lesssim 0.1$ dex at 100 kpc from an AGN that is comparable to a local Seyfert). In Appendix 4.A, we explicitly show for our set-up that the effect of photoheating on the Ovɪ abundance of the CGM is expected to be small compared to the effect of photoionization.

We assume that the gas in and around the galaxy is optically thin, as we only consider high-ionization state ions, which occur in low-density CGM gas where self-shielding against ionizing radiation is unimportant. It is, however, possible that optically thick structures are present near the centre of the galaxy, in the form of a dusty torus surrounding the BH or dense gas in clumps or in the galactic disc, that would make the radiation field from the AGN anisotropic. Oppenheimer et al. (2017) explore the AGN fossil effect in an anisotropic radiation field, using a bi-cone model with 120° opening angles, mimicking an obscuring nuclear torus either aligned with the galactic rotation axis or at a random orientation: they find that, even though only half of the CGM volume is irradiated at each AGN episode, the fossil effect is more than half as strong as in the isotropic case. This is because, on the one hand, a 2π steradian solid angle still affects the majority of the sightlines through the CGM, and, on the other hand, because the AGN eventually ionizes more than half of the CGM volume as the cone direction varies with time, as a result of the significant recombination time-scales of the metal ions. Any other obscuring structures, in the galactic disc or in isolated clumps, likely cover a much smaller solid angle, so we expect their effect on the strength of the fossil effect to be small. Moreover, anisotropic AGN radiation would require larger duty cycle fractions for the same observed quasar luminosity function, which reduces (and perhaps compensates entirely for) any effects of anisotropic radiation, as larger duty cycle fractions tend to increase the strength of the fossil effect (see Section 4.3.3).

Switching the AGN on or off happens instantaneously (i.e. the AGN is either off or at a fixed luminosity). As soon as the ionization front reaches a gas parcel, the AGN flux is added to the uniform HM01 background flux. Fig. 4.3 shows a comparison between the HM01 spectrum (at $z = 0.1$ and $z = 3$) and the AGN spectral shape, which we adopt from Sazonov et al. (2004). In this work, we explore variations of the AGN Eddington ratio L/L_{Edd}, lifetime t_{AGN} and duty cycle fraction f_{duty}, where we base our choices of these parameters on observational constraints compiled from the literature. The parameter values we explore are listed in Table 4.1.

We consider Eddington ratios of 0.01, 0.1 and 1.0, which we convert into a (bolometric) luminosity using the standard expression for the Eddington luminosity,

$$L_{\mathrm{Edd}} = \frac{4\pi G m_{\mathrm{p}} c}{\sigma_{\mathrm{T}}} M_{\mathrm{BH}}. \qquad (4.3)$$

Here, G is the gravitational constant, m_{p} is the proton mass, c is the speed of light and σ_{T} is the Thomson scattering cross-section. We fix the mass of the BH, M_{BH},

---

[5]Note that while we account for the finite light-travel time of the AGN radiation through the CGM, we do not consider the differential light-travel times from different parts of the CGM to the observer.

to $M_{BH} = 10^{-3} M_*$ at both $z = 0.1$ and $z = 3$[6], which is approximately the local relation observed over a wide range of galaxy masses (e.g. Merritt & Ferrarese, 2001; Marconi & Hunt, 2003; Häring & Rix, 2004). There are, however, indications that the normalization increases with increasing redshift (see e.g. Salviander & Shields 2013 or fig. 38 of Kormendy & Ho 2013; but see Sun et al. 2015), but it remains uncertain to what extent. Note that our exploration of different Eddington ratios can be interpreted as varying the $M_{BH}(M_*)$ relation (or both the L/L_{Edd} and the $M_{BH}(M_*)$ relation). At high redshift ($0.5 \lesssim z < 4 - 5$), AGN are often found to exhibit near-Eddington luminosities, with narrow (width $\lesssim 0.3$ dex) L/L_{Edd} distributions, typically peaking in between 0.1 and 1.0 (e.g. Kollmeier et al., 2006; Netzer et al., 2007; Shen et al., 2008). At low redshift ($z \lesssim 0.3$), however, observations of L/L_{Edd} find distributions that are wider and that span values significantly lower than 1 (typically $\lesssim 0.1$; see e.g. Heckman et al., 2004; Greene & Ho, 2007; Kauffmann & Heckman, 2009). Hence, we adopt default values of $L/L_{Edd} = 0.1$ at $z = 0.1$ and $L/L_{Edd} = 1$ at $z = 3$, when we compare galaxies at different redshifts. We investigate the impact of adopting a higher or a lower L/L_{Edd} for the $M_* \sim 10^{11}$ $M_\odot$ galaxy at $z = 0.1$ and the $M_* \sim 10^{10}$ $M_\odot$ galaxy at $z = 3$ in Section 4.3.3.

Since the EAGLE simulations lack the resolution to make reliable predictions on the periodicity of nuclear gas accretion, we rely on observations for constraints on the AGN lifetime and duty cycle fraction. Statistical arguments and observations of individual absorption systems and Lyα emitters near bright quasars constrain the typical AGN lifetime to $t_{AGN} = 10^5 - 10^7$ yr (see Section 4.1 for references). Estimates of the AGN duty cycle fraction, which are generally derived from the fraction of a sample of galaxies hosting active AGN, also span a large range of values: they range from less than 1% to as high as 90% (see Section 4.1). Hence, we explore duty cycles of $f_{duty} = 1, 2, 5, 10, 20, 50\%$. We refer to t_{AGN} as the 'AGN-on' time and to the time in between two subsequent AGN-on phases as the 'AGN-off' time (t_{off}). We refer to the sum of one AGN-on phase and one AGN-off phase as one full AGN cycle:

$$t_{cycle} = t_{AGN} + t_{off} = t_{AGN} \frac{100\%}{f_{duty}}. \tag{4.4}$$

4.2.6 Quantifying the AGN fossil effect

The imprint on the column densities of CGM ions of past AGN activity after the AGN has faded, is what characterizes an AGN proximity zone fossil. We quantify the fossil effect for OVI by measuring the (logarithmic) difference between the current OVI column density and its initial value in ionization equilibrium, $N_{OVI}^{t=0}$. For example, to explore the spatial variation of the fossil effect at a given time-step, we calculate

$$\Delta \log_{10} N_{OVI} \equiv \log_{10} \left(N_{OVI}/cm^{-2} \right) - \log_{10} \left(N_{OVI}^{t=0}/cm^{-2} \right) \tag{4.5}$$

at every pixel of the projection grid.

---

[6]We adopt $M_{BH} = 10^{-3} M_*$ to calculate L_{Edd}, rather than the BH mass from the simulation, in order to have an AGN luminosity that is representative for the whole galaxy population at the given redshift and stellar mass. In this way, L_{Edd} is insensitive to the deviation of the simulated M_{BH} from the median $M_{BH}(M_*)$ relation for the four galaxies considered in this work.

To quantify the significance of the AGN fossil effect in a statistical way and to enable a comparison between different AGN set-ups, we consider

- 7 logarithmic impact parameter bins of width 0.2 dex between $0.08R_{\mathrm{vir}}$ and $2R_{\mathrm{vir}}$, in which we take the median column density of all grid pixels (as described in Section 4.2.3) to obtain $\log_{10} N_{\mathrm{OVI}}(R)$;

- the time average of $\log_{10} N_{\mathrm{OVI}}(R)$ during the AGN-off time, i.e. in between two AGN-on phases. For combinations of AGN model parameters for which the fossil effect accumulates over multiple cycles (i.e. short t_{AGN} and large f_{duty}; see Section 4.3.3), we calculate the average of $\log_{10} N_{\mathrm{OVI}}(R)$ over t_{off} after the fluctuating $\log_{10} N_{\mathrm{OVI}}(R)$ has reached an asymptotic value, reflecting a net balance between the number of ionizations and recombinations per cycle.

For each galaxy and AGN set-up, this yields a single quantity as a function of impact parameter,

$$\langle \log_{10} N_{\mathrm{OVI}} \rangle_{\mathrm{t}}(R) \equiv \frac{1}{t_{\mathrm{cycle}} - t_{\mathrm{AGN}}} \int_{t_{\mathrm{AGN}}}^{t_{\mathrm{cycle}}} \log_{10} N_{\mathrm{OVI}}(R) \, \mathrm{d}t, \qquad (4.6)$$

that can be compared to the corresponding value in equilibrium.

Another commonly measured quantity in studies of CGM ion abundances, is the ion covering fraction. We define the OVI covering fraction, $f_{\mathrm{cov}}^{\mathrm{OVI}}(R)$, as the fraction of the pixels within the impact parameter range around R that have $N_{\mathrm{OVI}} > 10^{14.0} \, \mathrm{cm}^{-2}$. Similarly to the average column density, we calculate its average over the AGN-off time:

$$\left\langle f_{\mathrm{cov}}^{\mathrm{OVI}} \right\rangle_{\mathrm{t}}(R) \equiv \frac{1}{t_{\mathrm{cycle}} - t_{\mathrm{AGN}}} \int_{t_{\mathrm{AGN}}}^{t_{\mathrm{cycle}}} f_{\mathrm{cov}}^{\mathrm{OVI}}(R) \, \mathrm{d}t. \qquad (4.7)$$

While $\langle \log_{10} N_{\mathrm{OVI}} \rangle_{\mathrm{t}}(R)$ and $\left\langle f_{\mathrm{cov}}^{\mathrm{OVI}} \right\rangle_{\mathrm{t}}(R)$ characterize the *strength* of the fossil effect averaged over time, we define one additional quantity to indicate the *probability* of observing a significant AGN fossil effect while the AGN is off. We calculate the fraction of the time in between two AGN-on phases for which $\log_{10} N_{\mathrm{OVI}}(R)$ is offset from equilibrium by at least 0.1 dex. This again is a function of impact parameter, and allows a comparison between different galaxies and AGN set-ups.

4.3   Results for OVI

Prior to exploring the dependence of AGN fossil effects on the impact parameter (Section 4.3.1), the stellar mass and redshift of the galaxy (Section 4.3.2) and the strength, lifetime and duty cycle of the AGN (Section 4.3.3), we will show how the column density of circumgalactic OVI changes as a function of time for one particular set of AGN model parameters. We focus here on the $M_* = 1.0 \times 10^{10} \, \mathrm{M}_\odot$ galaxy at $z = 3$.

The maps at the top of Fig. 4.4 show the OVI column density (upper row) at $t = 0, 1, 2, 4, 8$ Myr, for an AGN with an Eddington ratio of $L/L_{\mathrm{Edd}} = 1.0$ that is
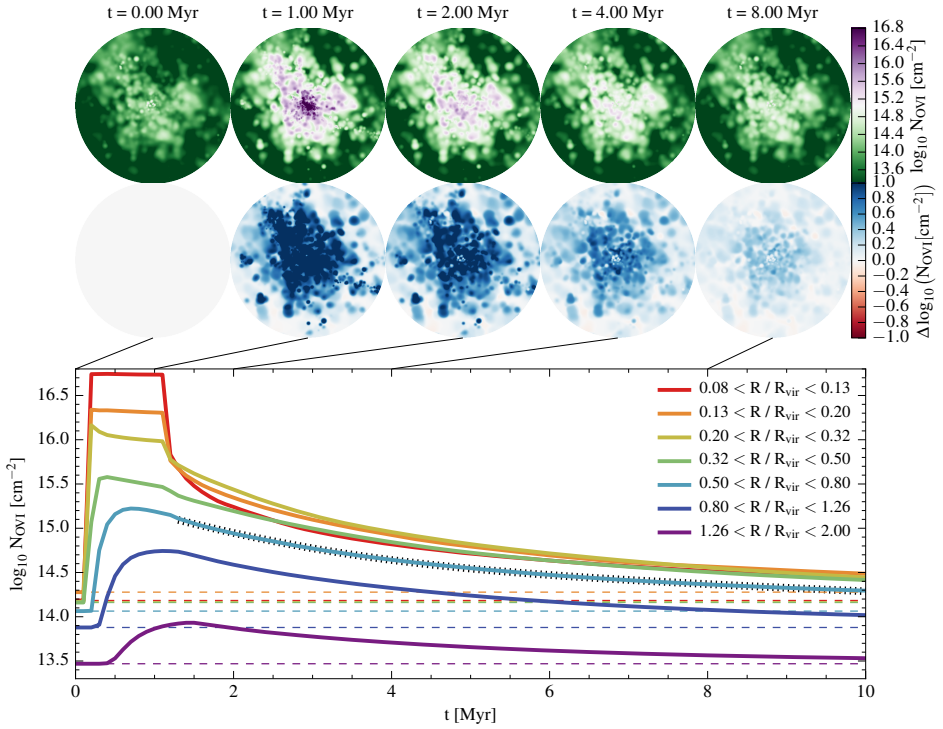
Figure 4.4: The evolution of the Ovɪ column density around the $M_* = 1.0 \times 10^{10}$ M$_\odot$ galaxy at $z = 3$, for an $L/L_{\rm Edd} = 1.0$ AGN that is on for 1 Myr and off for 9 Myr (i.e. $t_{\rm AGN} = 10^6$ yr and $f_{\rm duty} = 10\%$). The maps show the Ovɪ column density (upper row) and difference in $\log_{10} N_{\rm Ovɪ}$ with respect to $t = 0$ Myr (equation 4.5; lower row) at $t = 0, 1, 2, 4, 8$ Myr. The bottom panel shows the evolution of the median $N_{\rm Ovɪ}$ (solid lines), as well as the equilibrium value at $t = 0$ Myr (dashed lines), in 7 logarithmic impact parameter intervals between $0.08R_{\rm vir}$ and $2R_{\rm vir}$. The fit to $N_{\rm Ovɪ}(R)$ at $0.5 < R/R_{\rm vir} < 0.8$ (black, dotted line) shows that the evolution of $N_{\rm Ovɪ}(R)$ after the AGN turns off is well approximated by a sum of two exponential functions (equation 4.9).

on for 1 Myr and off for 9 Myr (i.e. $t_{AGN} = 10^6$ yr and $f_{duty} = 10\%$). The maps in the lower row show the difference in $\log_{10} N_{OVI}$, $\Delta \log_{10} N_{OVI}$ (equation 4.5), with respect to the equilibrium value at $t = 0$ Myr. As in Fig. 4.1, all maps show the circumgalactic gas up to impact parameters of $2R_{vir}$. From $t = 0$ Myr to $t = 1$ Myr, the enhanced radiation field from the AGN ionizes a significant fraction of the lower state oxygen ions to OVI, leading to a large increase in the column density. After $t = 1$ Myr, when the AGN switches off and the radiation field returns instantaneously to the uniform HM01 background, this OVI enhancement starts decreasing again. However, due to the significant recombination times of oxygen ions, and the series of ions that the oxygen needs to recombine through, the gas is left in an overionized state for several megayears. This remnant of past AGN activity in which ionization equilibrium has not been achieved yet, is what characterizes an AGN proximity zone fossil. The fossil effect is illustrated more quantitatively in the bottom panel of the figure, which shows the evolution of the median OVI column density in 7 impact parameter bins (solid lines). Naturally, the AGN-induced boost in N_{OVI} with respect to the equilibrium value (dashed lines) is stronger at smaller galactocentric distances[7]: at $R \sim R_{vir}$ the boost is about 0.8 dex, while for $R \lesssim 0.5R_{vir}$ it is $\gtrsim 1.4$ dex. Except in the outer two bins, N_{OVI} even slightly decreases again during the AGN-on time, as OVI is ionized to higher states.

After the AGN turns off, the time-scale on which N_{OVI} returns to equilibrium depends mostly on the recombination time of OVI to OV, t_{rec}^{OVI}, and the recombination time of OVII to OVI, t_{rec}^{OVII}. The latter is important as it is associated with the recombination of higher state oxygen ions to OVI, t_{rec}^{OVII} being the bottleneck in this recombination sequence. For $t > t_{AGN}$ (+ the radius-dependent time delay), when the gas is left in an overionized state, the evolution of the surplus of OVI number density can be approximated as a combination of two recombination processes:

$$\frac{dn_{OVI}}{dt} = n_{OVII}\alpha_{OVII}n_e - n_{OVI}\alpha_{OVI}n_e. \tag{4.8}$$

For fixed values of α_{OVI}, α_{OVII} and n_e the solution to this differential equation is a sum of two exponential functions,

$$n_{OVI}(t) = C_1 e^{-\alpha_{OVI}n_e t} + C_2 e^{-\alpha_{OVII}n_e t}, \tag{4.9}$$

where C_1 and C_2 are normalization constants. The exponential decay rates are related to the recombination time-scales as $t_{rec}^{OVI} = 1/(\alpha_{OVI}n_e)$ and $t_{rec}^{OVII} = 1/(\alpha_{OVII}n_e)$, which describe the evolution of n_{OVI} on short and long time-scales, respectively. We find that, even though equation (4.9) describes the evolution of the OVI number density, the evolution of $N_{OVI}(R)$ after AGN turn-off can also be approximated by a sum of two exponentials. We show the fit (performed in logarithmic space) for $N_{OVI}(R)$ and $0.5 < R/R_{vir} < 0.8$ (black, dotted line) in Fig. 4.4 to illustrate this. The best-fitting t_{rec}^{OVI} and t_{rec}^{OVII} then give us an indication of the effective re-equilibration time-scales of OVI: we find $t_{rec}^{OVI} = 1.4$ Myr and $t_{rec}^{OVII} = 12.1$ Myr at $0.5 < R/R_{vir} < 0.8$, which are similar to the expected recombination time-scales in

---

[7]Note that the short time delay in the increase and decrease of N_{OVI} is due to the light-travel time of the ionization front.
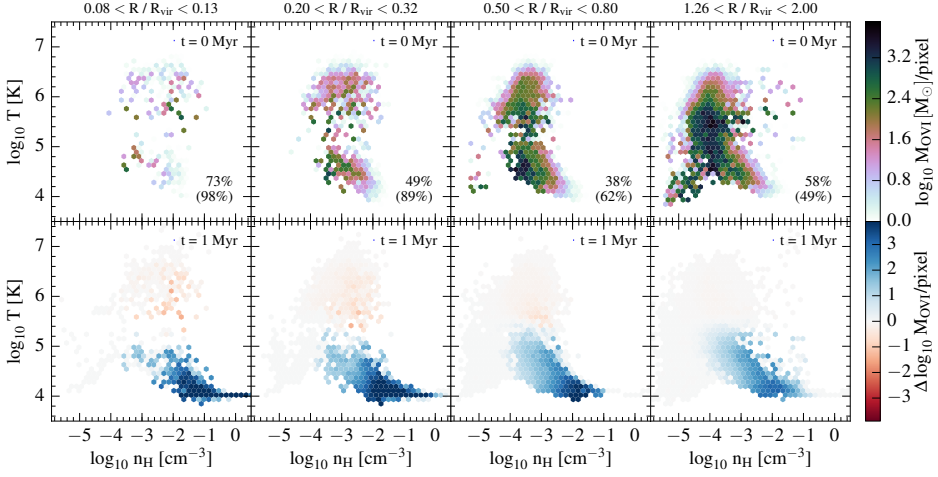
Figure 4.5: The distribution of OVI mass, M_{OVI}, in $T - n_{\mathrm{H}}$ space for different impact parameter intervals for the $M_* \sim 10^{10}\,\mathrm{M}_\odot$ galaxy at $z = 3$. The upper row shows the equilibrium distribution at $t = 0$ Myr, while the lower row shows the difference in $\log_{10} M_{\mathrm{OVI}}$ per pixel between $t = 1$ Myr (after the AGN has been on for 1 Myr) and $t = 0$ Myr. In each of the upper panels, the top (bottom) percentage indicates the OVI mass fraction at $T > 10^5$ K per impact parameter (3D radial distance) bin with boundaries given at the top. The AGN predominantly affects the photoionized gas at $T \lesssim 10^5$ K: the enhancement of OVI in this temperature regime is what drives the evolution of N_{OVI}.

$n_{\mathrm{H}} \sim 10^{-3.5}$ cm^{-3} and $T \sim 10^{4.5}$ K gas. However, in reality $t_{\mathrm{rec}}^{\mathrm{OVI}}$ and $t_{\mathrm{rec}}^{\mathrm{OVII}}$ are not constants: they depend on the local temperature and density (and on the ionization state of hydrogen through n_{e}). Since the gas in a certain impact parameter range spans a range of densities and temperatures, the best-fit $t_{\mathrm{rec}}^{\mathrm{OVI}}$ and $t_{\mathrm{rec}}^{\mathrm{OVII}}$ can only be seen as an approximation to the recombination time-scales.

For the $M_* = 1.0 \times 10^{10}\,\mathrm{M}_\odot$ galaxy at $z = 3$, as well as for the two galaxies at $z = 0.1$, the evolution of $N_{\mathrm{OVI}}(R)$ after AGN turn-off is well-described by a sum of two declining exponentials. However, for the $M_* = 7.9 \times 10^{10}\,\mathrm{M}_\odot$ galaxy at $z = 3$ (not shown here) a local density and temperature variation at $0.3 < R/R_{\mathrm{vir}} < 1.3$ causes the decrease of $N_{\mathrm{OVI}}(R)$ with time to be non-monotonic for the first 3 Myr after AGN turn-off. After that, $N_{\mathrm{OVI}}(R)$ decreases monotonically again, with a shape similar to equation (4.9).

In order to investigate at what temperatures and densities the OVI at different impact parameters arises, and what gas is predominantly affected by the AGN, we plot in Fig. 4.5 the equilibrium OVI mass distribution (upper row) in $T - n_{\mathrm{H}}$ space for 4 R/R_{vir} intervals, as well as the difference between the distributions at $t = 1$ Myr and $t = 0$ Myr (lower row). Clearly, at all impact parameters, OVI occurs in both collisionally ionized ($T \gtrsim 10^5$ K) and photoionized ($T \lesssim 10^5$ K) gas. Contrary to what one might expect, the mass fraction of gas at $T > 10^5$ K (the top percentage indicated in each panel) does not decrease with increasing impact parameter. The reason is that especially the small impact parameter bins include significant quan-

tities of photoionized O VI residing at large 3D radial distances because the O VI profile is relatively flat (see Fig. 4.2). The fraction of $T > 10^5$ K gas per 3D radial distance bin (indicated by the bottom percentage) does, however, decrease with increasing impact parameter, showing that an increasing fraction of the O VI resides in the photoionized phase[8]. This is in qualitative agreement with other theoretical studies of circumgalactic O VI (e.g. Ford et al., 2013; Shen et al., 2013), which generally find O VI to be mostly collisionally ionized at small galactocentric distances and mostly photoionized at large distances. Furthermore, Fig. 4.5 is also in line with the observations, which show that O VI can occur in both collisionally ionized and photoionized gas (e.g. Carswell et al., 2002; Prochaska et al., 2011; Savage et al., 2014; Turner et al., 2015).

However, the gas that is most affected by the AGN is the photoionized gas. Apart from a slight decrease of O VI in the $T \gtrsim 10^{5.3}$ K gas at $R/R_{vir} < 0.5$, the main effect is an increase of the O VI mass at $T \lesssim 10^5$ K. This change in the O VI abundance at $T \lesssim 10^5$ K is what predominantly drives the evolution of N_{OVI} shown in Fig. 4.4. Which densities and temperatures dominate O VI absorption depends on the gas distribution in $T - n_H$ space and the O VI ion fraction as a function of T and n_H (see e.g. Oppenheimer et al., 2016). Due to the additional radiation from the AGN, the O VI fraction as a function of density in photoionized gas shifts to somewhat higher densities, leading to an increase of the O VI mass at $n_H = 10^{-4} - 10^{-1}$ cm^{-3}. Note that this density range in which O VI is enhanced is roughly the same at all impact parameters, even though the typical density of CGM gas decreases with increasing impact parameter (as, for example, seen in the upper panels). The corresponding re-equilibration time-scale of N_{OVI} after AGN turn-off is therefore also expected to be roughly independent of impact parameter. This is consistent with Fig. 4.4, where at all $R/R_{vir} > 0.2$ $N_{OVI}(R)$ reaches 37% of its peak value (i.e. approximately the e-folding time-scale) $\approx 4 - 5$ Myr after the AGN turns off (correcting for the light-travel time delay). At $0.08 < R/R_{vir} < 0.2$, this time-scale is slightly shorter, $\approx 2 - 3$ Myr, mainly due to a deficit of low-density gas.

4.3.1   Dependence on impact parameter

In this and the next section we investigate the strength of the AGN fossil effect, quantified by the deviation in the average O VI column density and covering fraction from the respective equilibrium values, in the CGM of the four galaxies shown in Fig. 4.1. For all galaxies, we adopt the same AGN lifetime and duty cycle fraction as in the previous section: $\{t_{AGN} = 10^6 \text{ yr}, f_{duty} = 10\%\}$. For the Eddington ratio, we take $L/L_{Edd} = 1.0$ at $z = 3$ and $L/L_{Edd} = 0.1$ at $z = 0.1$.

Fig. 4.6 shows $\langle \log_{10} N_{OVI} \rangle_t (R)$ (solid lines; left-hand panels), as defined in equation (4.6), and $\langle f_{cov}^{OVI} \rangle_t (R)$ (solid lines; right-hand panels), as defined in equation (4.7), as a function of normalized impact parameter for the $M_* \sim 10^{10}$ M$_\odot$ (blue) and $M_* \sim 10^{11}$ M$_\odot$ (red) galaxies at $z = 0.1$ (upper panel) and $z = 3$ (lower panel). The column density and covering fraction profiles in equilibrium are indicated by dashed lines. For all four galaxies, the deviation in $\langle \log_{10} N_{OVI} \rangle_t (R)$ and

---

[8]Although we do not show it here, we find qualitatively similar trends for the other three galaxies.

$\left\langle f_{\mathrm{cov}}^{\mathrm{OVI}} \right\rangle_{\mathrm{t}} (R)$ from equilibrium decreases with increasing impact parameter. This is mainly because the flux of ionizing photons from the AGN decreases as R^{-2}, but also because the column densities of the OI - OV oxygen ions decrease with increasing impact parameter (see Fig. 4.2). This causes a larger initial offset in $N_{\mathrm{OVI}}(R)$ – and related to this, a larger initial offset in $f_{\mathrm{cov}}^{\mathrm{OVI}}(R)$ – at small R/R_{vir}, while the re-equilibration time-scale on which $N_{\mathrm{OVI}}(R)$ and $f_{\mathrm{cov}}^{\mathrm{OVI}}(R)$ decrease after AGN turn-off is roughly the same at all R/R_{vir}. In general, the fact that there is a significant offset in $\left\langle \log_{10} N_{\mathrm{OVI}} \right\rangle_{\mathrm{t}} (R)$ and $\left\langle f_{\mathrm{cov}}^{\mathrm{OVI}} \right\rangle_{\mathrm{t}} (R)$ over the whole R/R_{vir} range for all four galaxies, indicates that the recombination time-scales in the CGM are sufficiently long to establish AGN proximity zone fossils out to at least twice the virial radius from $M_* \sim 10^{10}\,\mathrm{M_\odot}$ and $M_* \sim 10^{11}\,\mathrm{M_\odot}$ galaxies at both $z = 0.1$ and $z = 3$.

4.3.2 Dependence on galaxy mass and redshift

As we already discussed in Section 4.2.4, the column density of OVI and the relative abundances of the different oxygen ions (i.e. the overall ionization state of the gas) are sensitive to a number of factors that are related to the mass of the galaxy – like the halo virial temperature and the galaxy metallicity. Also, more massive galaxies host more massive BHs (e.g. Merritt & Ferrarese, 2001), suggesting that the AGN are also more luminous during their active phase. Hence, we expect the effect of a fluctuating AGN on the CGM to be dependent on the mass of the galaxy. Furthermore, since AGN are generally observed to be more luminous at higher redshift (e.g. Kollmeier et al., 2006), and the density of the Universe increases with increasing redshift, the effect is not necessarily quantitatively similar for galaxies of a similar stellar mass at different redshifts.

To investigate the dependence of the AGN fossil effect on galaxy stellar mass, we start by comparing the $M_* \sim 10^{10}\,\mathrm{M_\odot}$ and $M_* \sim 10^{11}\,\mathrm{M_\odot}$ galaxies at $z = 3$ (lower panels of Fig. 4.6). For a fluctuating AGN in the $M_* \sim 10^{11}\,\mathrm{M_\odot}$ galaxy, $\left\langle \log_{10} N_{\mathrm{OVI}} \right\rangle_{\mathrm{t}} (R)$ and $\left\langle f_{\mathrm{cov}}^{\mathrm{OVI}} \right\rangle_{\mathrm{t}} (R)$ are generally $\approx 0.2 - 0.4$ dex and $\approx 0.04 - 0.2$, respectively, higher than in the equilibrium case, and the offsets change only mildly with impact parameter. For the $M_* \sim 10^{10}\,\mathrm{M_\odot}$ galaxy, however, the significance of the fossil effect changes more rapidly, causing the effect to be somewhat smaller than for the $M_* \sim 10^{11}\,\mathrm{M_\odot}$ galaxy at large impact parameters ($R/R_{\mathrm{vir}} \gtrsim 1.3$), but significantly larger at small impact parameters ($R/R_{\mathrm{vir}} \lesssim 0.8$). For $R/R_{\mathrm{vir}} < 0.5$, the offsets in $\left\langle \log_{10} N_{\mathrm{OVI}} \right\rangle_{\mathrm{t}} (R)$ and $\left\langle f_{\mathrm{cov}}^{\mathrm{OVI}} \right\rangle_{\mathrm{t}} (R)$ with respect to equilibrium increase to $\gtrsim 0.5$ dex and $\gtrsim 0.2$, respectively.

Similar to the dependence on impact parameter, the dependence of the fossil effect on galaxy stellar mass can be explained by considering the difference in the ionizing flux, the re-equilibration time-scale and the abundance of low-state ions. For an AGN with a fixed Eddington ratio, the flux at a fixed R/R_{vir} scales with the stellar mass as $\propto M_*^{1/3}$, since $L_{\mathrm{Edd}} \propto M_{\mathrm{BH}} \propto M_*$ and $R_{\mathrm{vir}} \propto M_{\mathrm{vir}}^{1/3} \propto M_*^{1/3}$ approximately. The gas around the $M_* \sim 10^{11}\,\mathrm{M_\odot}$ galaxy therefore receives a ≈ 2 times higher AGN flux than the gas at the same R/R_{vir} receives from the AGN in the $M_* \sim 10^{10}\,\mathrm{M_\odot}$ galaxy. The re-equilibration time-scale of OVI is similar for both galaxies, since the OVI (enhancement) occurs at similar densities at a fixed fraction
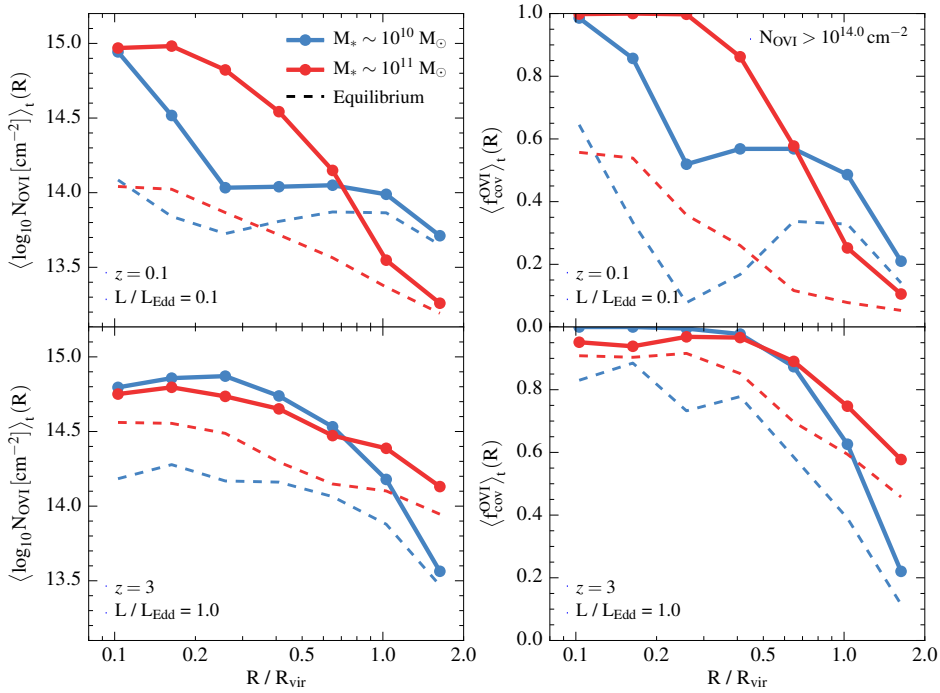
Figure 4.6: The strength of the AGN fossil effect as a function of impact parameter, normalized by the virial radius, for the $M_* \sim 10^{10}\,M_\odot$ (blue) and $M_* \sim 10^{11}\,M_\odot$ (red) galaxies at $z = 0.1$ (upper panels) and $z = 3$ (lower panels). The adopted AGN parameters are $t_{AGN} = 10^6$ yr and $f_{duty} = 10\%$, with $L/L_{Edd} = 0.1$ at $z = 0.1$ and $L/L_{Edd} = 1.0$ at $z = 3$. The solid curves show the average OVI column density, $\langle \log_{10} N_{OVI} \rangle_t (R)$ (equation 4.6; left-hand panels), and average covering fraction of $N_{OVI} > 10^{14.0}\,cm^{-2}$ gas, $\langle f_{cov}^{OVI} \rangle_t (R)$ (equation 4.7; right-hand panels), in 7 logarithmic impact parameter bins of size 0.2 dex. The dashed curves show the corresponding profiles in equilibrium. At $z = 3$, the fossil effect at $R/R_{vir} \lesssim 0.8$ around the $M_* \sim 10^{10}\,M_\odot$ galaxy is significantly larger than around the $M_* \sim 10^{11}\,M_\odot$ galaxy, despite the ≈ 2 times lower AGN flux that the gas at a fixed R/R_{vir} receives. This is due to the larger abundance of OI - OV oxygen ions that can be ionized to OVI. At $z = 0.1$, the fossil effect is largest around the $M_* \sim 10^{11}\,M_\odot$ galaxy over the whole impact parameter range. Even though the gas at a fixed R/R_{vir} at $z = 0.1$ receives $60 - 80$ times lower AGN flux than the gas around a similarly massive galaxy at $z = 3$, the fossil effect at $z = 0.1$ is often larger, owing to the ~ 10 times longer OVI re-equilibration time-scale.

of the virial radius. Hence, the fact that we find a larger fossil effect at $R/R_{\rm vir} \lesssim 0.8$ around the $M_* \sim 10^{10}\,{\rm M_\odot}$ galaxy must be due to a larger abundance of low-state oxygen ions (see Fig. 4.2). This causes a larger initial boost in $\log_{10} N_{\rm OVI}(R)$ than for the $M_* \sim 10^{11}\,{\rm M_\odot}$ galaxy, despite the fact that the flux from the AGN is lower. At large impact parameters ($R/R_{\rm vir} \gtrsim 1.3$), however, the fossil effect is larger for the $M_* \sim 10^{11}\,{\rm M_\odot}$ galaxy, which can be attributed to a combination of higher AGN flux and the larger abundance of low-state ions in this $R/R_{\rm vir}$ regime.

The opposite trend with stellar mass is seen at $z = 0.1$ (upper panels): the fossil effect around the $M_* \sim 10^{11}\,{\rm M_\odot}$ galaxy is much larger than around the $M_* \sim 10^{10}\,{\rm M_\odot}$ galaxy (except for the innermost $R/R_{\rm vir}$ bin), and increases strongly with decreasing impact parameter. The difference is particularly evident at $0.2 \lesssim R/R_{\rm vir} \lesssim 0.8$, where the offsets of $\langle \log_{10} N_{\rm OVI} \rangle_{\rm t}(R)$ and $\langle f_{\rm cov}^{\rm OVI} \rangle_{\rm t}(R)$ from equilibrium are $\approx 0.6 - 1.0$ dex and $\approx 0.5 - 0.6$, respectively, in the high-mass case and $\approx 0.2 - 0.3$ dex and $\approx 0.2 - 0.4$, respectively, in the low-mass case.

When comparing galaxies with a similar stellar mass at different redshifts, the re-equilibration time-scale does play an important role. Since the virial radii of the two galaxies at $z = 0.1$ are $2.5 - 2.8$ times larger than those of the similarly massive galaxies at $z = 3$, and the AGN implemented at $z = 0.1$ have a 10 times lower Eddington ratio, gas at a fixed $R/R_{\rm vir}$ receives a $60 - 80$ times lower AGN flux at $z = 0.1$ than at $z = 3$. In combination with the lower abundance of low-state oxygen ions, it may seem surprising that we see a fossil effect at $z = 0.1$ at all. The reason is the significantly longer recombination time-scales in the CGM: by comparing figures similar to Fig. 4.5 for all four galaxies, we find that the AGN-induced OVI enhancement (in a fixed $R/R_{\rm vir}$ interval) occurs at ~ 10 times lower densities for the galaxies at $z = 0.1$ than for those at $z = 3$. Hence, the expected re-equilibration time-scale of OVI is ~ 10 times longer at $z = 0.1$ than at $z = 3$. For the $z = 0.1$ galaxy with $M_* \sim 10^{10}\,{\rm M_\odot}$, the offsets of $\langle \log_{10} N_{\rm OVI} \rangle_{\rm t}(R)$ and $\langle f_{\rm cov}^{\rm OVI} \rangle_{\rm t}(R)$ from equilibrium at $R/R_{\rm vir} \gtrsim 0.2$ are still smaller than for its high-redshift equivalent. However, the offsets are large enough to substantially enhance OVI in low-redshift CGM observations, as is explored by Oppenheimer et al. (2017). For the $z = 0.1$ galaxy with $M_* \sim 10^{11}\,{\rm M_\odot}$, the fossil effect at impact parameters of $R/R_{\rm vir} \lesssim 0.8$ does become much larger than at high redshift, owing to the significantly prolonged recombination phase after AGN turn-off.

To quantify the probability of observing a significant AGN fossil effect, we calculate the fraction of the time in between two AGN-on phases for which $\log_{10} N_{\rm OVI}$ is offset from the equilibrium value by > 0.1 dex. This can be interpreted as the probability that an observation of circumgalactic OVI is significantly affected by AGN fossil effects, even though the galaxy would not be identified as an active AGN host. For the $M_* \sim 10^{11}\,{\rm M_\odot}$ galaxy at $z = 3$, this probability varies between ≈ 0.5 and ≈ 1.0 over the whole impact parameter range, while for the $M_* \sim 10^{10}\,{\rm M_\odot}$ galaxy at $z = 3$, it is ≈ 1.0 for $R/R_{\rm vir} < 1.3$ and drops steeply at higher $R/R_{\rm vir}$ (although still being ≈ 0.4 for $1.3 < R/R_{\rm vir} < 2.0$). Hence, the OVI around the $M_* \sim 10^{10}\,{\rm M_\odot}$ galaxy out to $R/R_{\rm vir} = 1.3$ is constantly kept out of equilibrium, even though the AGN duty cycle fraction is only 10%. At $z = 0.1$, the probability of observing a significant fossil effect changes even more abruptly with impact parameter: while it is ≈ 1.0 for $R/R_{\rm vir} < 1.3$, the probability is zero at larger $R/R_{\rm vir}$, independent
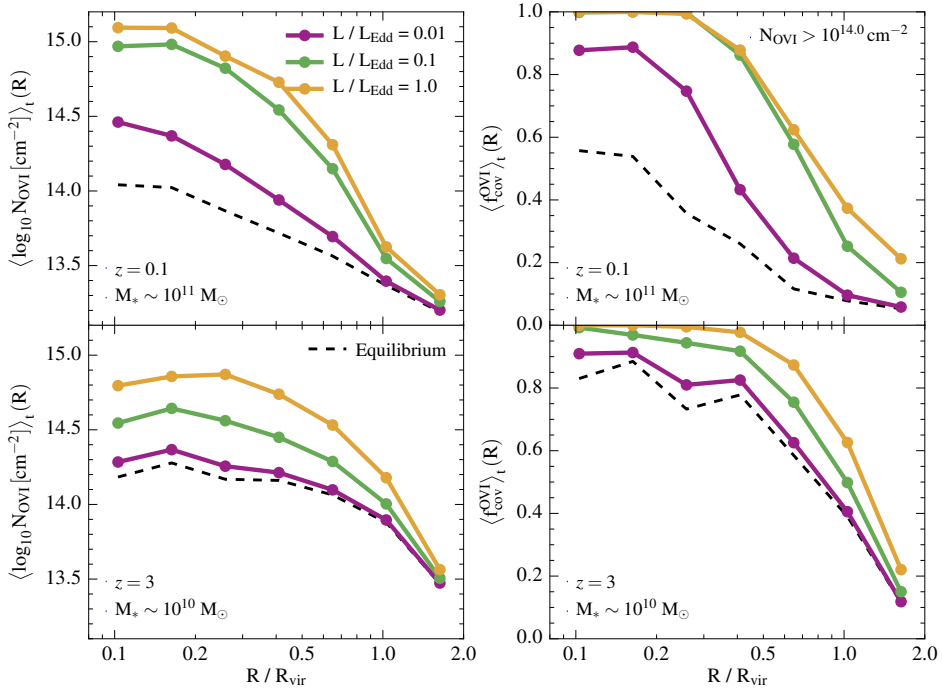
Figure 4.7: The impact of the AGN Eddington ratio on the fossil effect for the $M_* \sim 10^{11} \, \mathrm{M_\odot}$ galaxy at $z = 0.1$ (upper panels) and the $M_* \sim 10^{10} \, \mathrm{M_\odot}$ galaxy at $z = 3$ (lower panels). The plotted quantities, including the equilibrium profiles for the respective galaxies (black, dashed lines), are the same as in Fig. 4.6, but now we compare different Eddington ratios: $L/L_{\mathrm{Edd}} = 0.01$ (purple), $L/L_{\mathrm{Edd}} = 0.1$ (green) and $L/L_{\mathrm{Edd}} = 1.0$ (yellow). We still adopt $t_{\mathrm{AGN}} = 10^6$ yr and $f_{\mathrm{duty}} = 10\%$. For a sufficiently high AGN luminosity, as in the case of the $M_* \sim 10^{11} \, \mathrm{M_\odot}$ galaxy at $z = 0.1$, the increase in $\langle \log_{10} N_{\mathrm{OVI}} \rangle_t (R)$ and $\langle f_{\mathrm{cov}}^{\mathrm{OVI}} \rangle_t (R)$ with respect to equilibrium depends on the adopted luminosity in a non-linear way. This is related to the increase in the photoionization rate from OVI to higher states as well as from OV to OVI.

of galaxy mass. Hence, we expect that both at $z = 0.1$ and at $z = 3$ galaxies with $M_* = 10^{10-11} \, \mathrm{M_\odot}$ are significantly affected by AGN fossil effects: AGN with the luminosity, lifetime and duty cycle fraction adopted here, keep circumgalactic OVI continuously out of equilibrium up to impact parameters that extend beyond the virial radius ($R/R_{\mathrm{vir}} < 1.3$).

4.3.3 Dependence on AGN properties

AGN luminosity

Observationally, AGN are found to exhibit a wide variety of Eddington ratios, which are generally smaller and span a larger range of values at low redshift than at high redshift (e.g. Kollmeier et al., 2006; Kauffmann & Heckman, 2009). We therefore explore the dependence of the AGN fossil effect on the Eddington ratio,

mainly focusing on $z = 0.1$. We adopt the same t_{AGN} and f_{duty} as in the previous sections.

The upper panels of Fig. 4.7 compare our fiducial $L/L_{\mathrm{Edd}} = 0.1$ (green) to a 10 times lower (purple) and a 10 times higher (yellow) Eddington ratio for the $M_* \sim 10^{11}\,\mathrm{M_\odot}$ galaxy at $z = 0.1$. The ratio $L/L_{\mathrm{Edd}} = 0.1$ corresponds to a (bolometric) luminosity of $L = 1.3 \times 10^{45}$ erg/s, or $L_{0.5-2\ \mathrm{keV}} = 2.6 \times 10^{43}$ erg/s in the soft X-ray band (0.5 – 2 keV) and $L_{2-10\ \mathrm{keV}} = 3.5 \times 10^{43}$ erg/s in the hard X-ray band (2 – 10 keV), which we calculate by integrating the AGN spectrum over the appropriate energy interval. These $L_{0.5-2\ \mathrm{keV}}$ and $L_{2-10\ \mathrm{keV}}$ correspond to AGN strengths that are commonly observed at $z \approx 0.1$, where these luminosities are close to the knee of the X-ray AGN luminosity function (e.g. Ueda et al., 2003; Hasinger et al., 2005; Aird et al., 2010)[9]. The value $L/L_{\mathrm{Edd}} = 1.0$ then represents a more extreme case, while $L/L_{\mathrm{Edd}} = 0.01$ corresponds to a more moderate AGN.

Over the whole impact parameter range, the offsets of $\langle \log_{10} N_{\mathrm{Ovi}} \rangle_{\mathrm{t}} (R)$ and $\langle f_{\mathrm{cov}}^{\mathrm{Ovi}} \rangle_{\mathrm{t}} (R)$ for $L/L_{\mathrm{Edd}} = 0.01$ are significantly smaller than those for $L/L_{\mathrm{Edd}} = 0.1$. Within $R/R_{\mathrm{vir}} = 0.8$, the offsets are $\approx 0.1 - 0.4$ dex and $\approx 0.1 - 0.4$, respectively, for $L/L_{\mathrm{Edd}} = 0.01$, compared to $\approx 0.6 - 1.0$ dex and $\approx 0.4 - 0.6$ for $L/L_{\mathrm{Edd}} = 0.1$. The 10 times lower Eddington ratio also causes the fossil effect to be observable out to smaller impact parameters: Ovi is observed to be continuously out of equilibrium (i.e. a probability of 1.0) out to $0.8R/R_{\mathrm{vir}}$ instead of $1.3R/R_{\mathrm{vir}}$. While the $L/L_{\mathrm{Edd}} = 0.01$ AGN therefore affects a ≈ 4 times smaller volume in the CGM of individual galaxies, they are ≈ 10 times more common than the $L/L_{\mathrm{Edd}} = 0.1$ AGN according to the luminosity function from Aird et al. (2010, comparing the occurrence of $L_{2-10\ \mathrm{keV}} = 3.5 \times 10^{42}$ erg/s to $L_{2-10\ \mathrm{keV}} = 3.5 \times 10^{43}$ erg/s). Hence, the total volume in the Universe that these low-luminosity AGN are expected to affect is larger.

In the high Eddington ratio ($L/L_{\mathrm{Edd}} = 1.0$) case, the offsets of $\langle \log_{10} N_{\mathrm{Ovi}} \rangle_{\mathrm{t}} (R)$ and $\langle f_{\mathrm{cov}}^{\mathrm{Ovi}} \rangle_{\mathrm{t}} (R)$ from equilibrium are larger than in the $L/L_{\mathrm{Edd}} = 0.1$ case. However, the difference is not as significant as between $L/L_{\mathrm{Edd}} = 0.1$ and $L/L_{\mathrm{Edd}} = 0.01$. This is related to the fact that adopting a 10 times higher AGN luminosity does not only increase the photoionization rate from Ov to Ovi, but also increases the rate from Ovi to Ovii and to higher oxygen states. Hence, the increase in $\langle \log_{10} N_{\mathrm{Ovi}} \rangle_{\mathrm{t}} (R)$ and $f_{\mathrm{cov}}^{\mathrm{Ovi}}$ is not linearly dependent on the AGN luminosity. These quantities can even show a deficit with respect to equilibrium for extremely high AGN luminosities, when most of the oxygen ions are ionized from Oi - Ovi to higher states. We see a similar effect if we consider metal ion species with a lower ionization energy than Ovi (see Section 4.4).

Despite the limited increase in the fossil effect from $L/L_{\mathrm{Edd}} = 0.1$ to $L/L_{\mathrm{Edd}} = 1.0$, the high Eddington ratio AGN establishes a continuously observable fossil effect out to the largest impact parameters that we consider here. While this affects a ≈ 4 times larger volume around individual galaxies than in the $L/L_{\mathrm{Edd}} = 0.1$ case, AGN with $L_{2-10\ \mathrm{keV}} = 3.5 \times 10^{44}$ erg/s are $\approx 20 - 30$ times less common than AGN with $L_{2-10\ \mathrm{keV}} = 3.5 \times 10^{43}$ erg/s (Aird et al., 2010), thereby affecting a smaller total volume in the Universe.

---

[9]The knee shifts to approximately an order of magnitude higher luminosity from $z = 0$ to $z = 3$, justifying our choice of adopting a 10 times higher fiducial Eddington ratio at $z = 3$ than at $z = 0.1$.
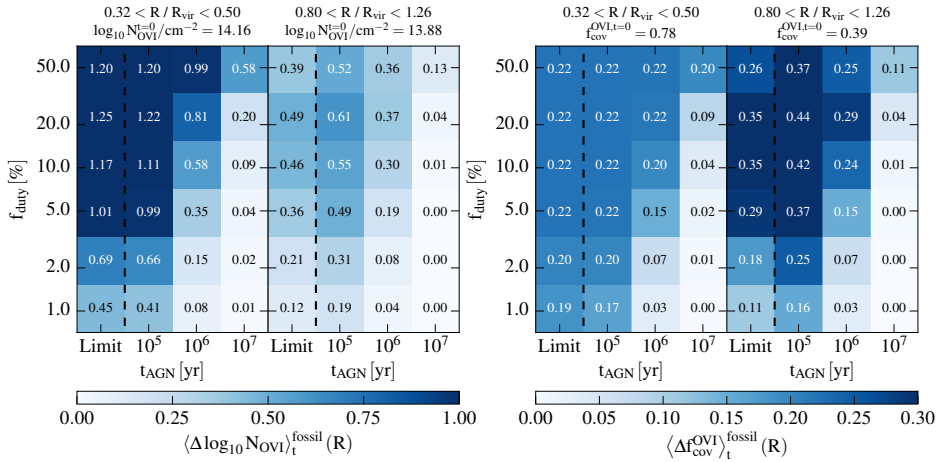
Figure 4.8: The impact of varying the AGN lifetime and duty cycle fraction on the strength of the AGN fossil effect for the $M_* \sim 10^{10}\,\mathrm{M}_\odot$ galaxy at $z = 3$ (with an AGN with $L/L_{\mathrm{Edd}} = 1.0$). The left-hand and right-hand panels show the average out-of-equilibrium offsets of the O VI column density and covering fraction (equation 4.10), respectively. We focus on two impact parameter intervals. For each t_{AGN} and f_{duty}, the offsets are shown as both a colour-coding and a number, while the corresponding equilibrium values are indicated at the top. The fossil effect tends to be stronger for shorter AGN lifetimes and larger duty cycle fractions, as the time in between subsequent AGN-on phases is shorter. In the limit of very short AGN lifetimes, the effect of a fluctuating AGN on the O VI column density and covering fraction converges to the effect of a continuously radiating AGN with a luminosity equal to ($f_{\mathrm{duty}}/100\%$) times the original luminosity (leftmost column in each panel: 'Limit').

The lower panels of Fig. 4.7 show the dependence of the high-redshift fossil effect on the AGN Eddington ratio, where we focus on the $M_* \sim 10^{10}\,\mathrm{M}_\odot$ galaxy at $z = 3$. Increasing the Eddington ratio from $L/L_{\mathrm{Edd}} = 0.01$ to $L/L_{\mathrm{Edd}} = 0.1$ has a similar effect on $\langle \log_{10} N_{\mathrm{O VI}} \rangle_{\mathrm{t}} (R)$ and $\langle f_{\mathrm{cov}}^{\mathrm{O VI}} \rangle_{\mathrm{t}} (R)$ as increasing the ratio from $L/L_{\mathrm{Edd}} = 0.1$ to $L/L_{\mathrm{Edd}} = 1.0$. The increasing photon flux primarily enhances the ionization from low oxygen states to O VI: there is no 'saturation' of the O VI enhancement like at $z = 0.1$. Furthermore, the faint-end slope of the X-ray luminosity function at $z = 3$ is flatter than at low redshift, making AGN with a 10 times lower L/L_{Edd} only $\approx 2.5-4$ more common (Aird et al., 2010; comparing the occurrence of the corresponding $L_{2-10\,\mathrm{keV}}$ values, which are all well below the knee of the luminosity function at $z = 3$). Hence, in contrast with low redshift, the more luminous AGN are expected to affect a larger volume in the Universe than the low-luminosity AGN, as the AGN with $L/L_{\mathrm{Edd}} = 1.0$ ($L/L_{\mathrm{Edd}} = 0.1$) affects a ≈ 200 (≈ 40) times lager volume around individual galaxies than the AGN with $L/L_{\mathrm{Edd}} = 0.01$.

AGN lifetime and duty cycle

The wide range of observational estimates of t_{AGN} and f_{duty} presented in the literature shows that either AGN exhibit a large variety of lifetimes and duty cycle fractions, or that these parameter values are highly uncertain (as they are mostly

based on indirect constraints). We therefore explore the impact of t_{AGN} and f_{duty} on the AGN fossil effect. We focus on the $M_* \sim 10^{10}\,\mathrm{M}_\odot$ galaxy at $z = 3$, but for high stellar mass or low redshift the conclusions are qualitatively similar.

In Fig. 4.8, we show

$$\left\langle \Delta \log_{10} N_{\mathrm{O VI}} \right\rangle_t^{\mathrm{fossil}} (R) \equiv \left\langle \log_{10} N_{\mathrm{O VI}} \right\rangle_t (R) - \log_{10} N_{\mathrm{O VI}}^{t=0}(R) \qquad (4.10)$$

in the left two panels and $\left\langle \Delta f_{\mathrm{cov}}^{\mathrm{O VI}} \right\rangle_t^{\mathrm{fossil}} (R)$, defined in a similar way, in the right two panels, for different choices of t_{AGN} and f_{duty} (the extra column called 'Limit' will be discussed below). We focus here on two impact parameter intervals. Both quantities show that the AGN fossil effect tends to become stronger towards smaller AGN lifetimes and larger duty cycle fractions. This is related to the fact that the AGN-off time (i.e. the time in between two subsequent AGN-on phases) decreases with decreasing t_{AGN} and increasing f_{duty}. For example, while $t_{\mathrm{off}} = 90$ Myr for $t_{\mathrm{AGN}} = 10^7$ yr and $f_{\mathrm{duty}} = 10\%$, $t_{\mathrm{off}} = 0.9$ Myr for $t_{\mathrm{AGN}} = 10^5$ yr and $f_{\mathrm{duty}} = 10\%$. This is a significant difference considering the typical re-equilibration time-scale of O VI (i.e. the $N_{\mathrm{O VI}}(R)$ enhancement returns to 37% of its peak value in $\approx 2-5$ Myr). The small t_{off} leads to average enhancements in the column density and covering fraction up to $\left\langle \Delta \log_{10} N_{\mathrm{O VI}} \right\rangle_t^{\mathrm{fossil}} (R) = 1.22$ dex and $\left\langle \Delta f_{\mathrm{cov}}^{\mathrm{O VI}} \right\rangle_t^{\mathrm{fossil}} (R) = 0.22$ (i.e. reaching $f_{\mathrm{cov}}^{\mathrm{O VI}} = 1.0$) for $0.3 < R/R_{\mathrm{vir}} < 0.5$, and up to $\left\langle \Delta \log_{10} N_{\mathrm{O VI}} \right\rangle_t^{\mathrm{fossil}} (R) = 0.61$ dex and $\left\langle \Delta f_{\mathrm{cov}}^{\mathrm{O VI}} \right\rangle_t^{\mathrm{fossil}} (R) = 0.44$ for $0.8 < R/R_{\mathrm{vir}} < 1.3$.

In general, an AGN proximity zone fossil is created most efficiently if the AGN lifetime is comparable to or longer than the ionization time-scale from O V to O VI (e.g. $\sim 10^5$ yr at $R/R_{\mathrm{vir}} \approx 0.8$), so as to ionize significant quantities of oxygen to O VI, and if the AGN-off time is similar or shorter than the re-equilibration time-scale of O VI. For $t_{\mathrm{AGN}} = 10^5$ yr this is roughly the case for $f_{\mathrm{duty}} = 2\%$ (where $t_{\mathrm{off}} = 4.9$ Myr), for $t_{\mathrm{AGN}} = 10^6$ yr at $f_{\mathrm{duty}} = 20\%$ (where $t_{\mathrm{off}} = 4.0$ Myr) and for $t_{\mathrm{AGN}} = 10^7$ yr at $f_{\mathrm{duty}} \gtrsim 50\%$ (where $t_{\mathrm{off}} \lesssim 10$ Myr). This approximately corresponds to the regime in Fig. 4.8 where we find a significant AGN fossil effect.

The probability of observing a significant fossil effect while the AGN is inactive, which is shown as a function of t_{AGN} and f_{duty} in Fig. 4.9, is close to or equal to 1.0 if $t_{\mathrm{off}} \lesssim 10$ Myr (to the left of the grey, dotted line). This means that throughout the whole AGN-off time, $N_{\mathrm{O VI}}$ is offset from equilibrium by at least 0.1 dex, indicating that the O VI is constantly kept in an overionized state. This limit of $t_{\mathrm{off}} \approx 10$ Myr is roughly independent of impact parameter. The fact that $N_{\mathrm{O VI}}$ is continuously kept out of equilibrium also causes the enhancement of $N_{\mathrm{O VI}}$ to build up over many cycles. This is illustrated for an AGN with $t_{\mathrm{AGN}} = 10^5$ yr and $f_{\mathrm{duty}} = 10\%$ (red, solid lines) in Fig. 4.10, for the same galaxy and AGN set-up as in Figs. 4.8 and 4.9, and for $0.3 < R/R_{\mathrm{vir}} < 0.5$. The net evolutionary trend is an increase of $N_{\mathrm{O VI}}$ over a time-scale of a few megayears. Eventually, the increase flattens off and O VI reaches a new equilibrium, where the combined photoionization from the HM01 background and the AGN (in addition to collisional ionization) balances the recombinations per cycle. Similar asymptotic behaviour is shown by the O VI covering fraction. As we mentioned in Section 4.2.6, we calculate $\left\langle \log_{10} N_{\mathrm{O VI}} \right\rangle_t (R)$ and $\left\langle f_{\mathrm{cov}}^{\mathrm{O VI}} \right\rangle_t (R)$ only after such a new ionization balance has been reached (for this combination of t_{AGN} and
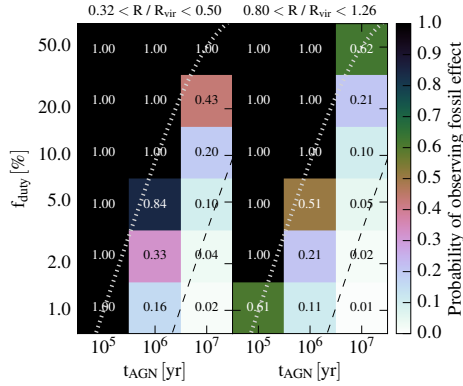
Figure 4.9: The impact of varying the AGN lifetime and duty cycle fraction on the probability of observing a significant AGN fossil effect (i.e. $\log_{10} N_{OVI}$ offset from equilibrium by > 0.1 dex during the AGN-off time) for the $M_* \sim 10^{10}\,M_\odot$ galaxy at $z = 3$ with a $L/L_{Edd} = 1.0$ AGN. If the time in between subsequent AGN-on phases is $t_{off} \lesssim 10$ Myr (to the left of the grey, dotted lines), the OVI is continuously kept in an out-of-equilibrium state, and the OVI enhancement accumulates over multiple cycles. For $t_{off} \gtrsim 300$ Myr (to the right of the black, dashed line), the time in between subsequent AGN-on phases is too long to see a significant fossil effect for a significant fraction of the time.

f_{duty} and other combinations in Figs. 4.8 and 4.9 to which this applies).

If we now consider AGN with $t_{AGN} = 10^4$ yr (yellow, solid line) and $t_{AGN} = 10^3$ yr (green, solid line), while keeping the duty cycle fraction the same at $f_{duty} = 10\%$, we find that in both cases the net evolution is the same as for $t_{AGN} = 10^5$ yr. It just takes more cycles, with smaller individual fluctuations, when t_{AGN} is shorter[10]. This suggests that, as could have been expected, in the limit of $t_{AGN} \to 0$, the behaviour of N_{OVI} converges to the result obtained for an AGN radiating continuously at 10% of the original flux. Indeed, a continuously radiating AGN with $L/L_{Edd} = 0.1$ (black, dashed line) traces the net N_{OVI} evolution of the fluctuating AGN with $L/L_{Edd} = 1.0$ and $f_{duty} = 10\%$[11].

The fact that the evolution of N_{OVI} converges in the limit of small t_{AGN}, also means that we can calculate the offsets of $\langle \Delta \log_{10} N_{OVI} \rangle_t^{fossil} (R)$ (and $\langle \Delta f_{cov}^{OVI} \rangle_t^{fossil} (R)$) from equilibrium in the limit of small t_{AGN}. We calculate these asymptotic offsets for $f_{duty} = 1, 2, 5, 10, 20, 50\%$ by considering continuously radiating AGN with $L/L_{Edd} = 0.01, 0.02, 0.05, 0.1, 0.2, 0.5$, respectively, and show these values as separate columns in Fig. 4.8 (called 'Limit'). The asymptotic offsets generally increase with increasing f_{duty}, although they are slightly lower for $f_{duty} = 50\%$ than for $f_{duty} = 20\%$. This is due to the non-linear relation between OVI enhancement and AGN luminosity (see also Section 4.3.3): the OVI abundance in

---

[10]Note that in this way, despite the fact that the AGN lifetime is shorter than the ionization time-scale of OV to OVI, the fluctuating AGN still give rise to a significant fossil effect.

[11]Note that after the initial (net) increase in N_{OVI} for $0 < t < 2$ Myr, N_{OVI} first decreases slightly – corresponding to the ionization of OVI to higher states – before a new equilibrium is established. This is seen in the trends of both the continuous and fluctuating AGN (although it is less visible for the latter).
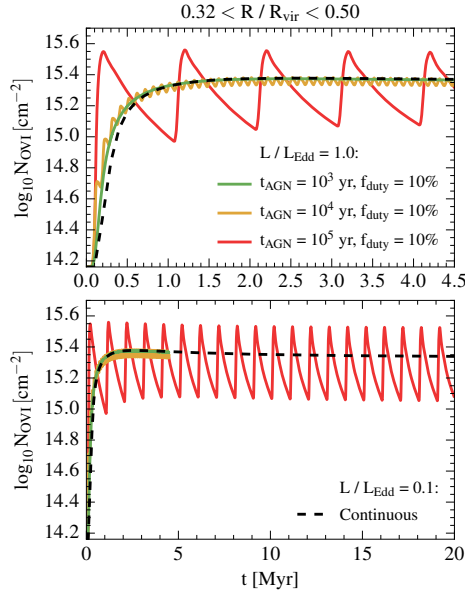
Figure 4.10: The OVI column density at $0.3 < R/R_{vir} < 0.5$ from the $M_* \sim 10^{10}\,M_\odot$ galaxy at $z = 3$ as a function of time, for different values of the AGN lifetime: $t_{AGN} = 10^3$ yr (green, solid line), $t_{AGN} = 10^4$ yr (yellow, solid line) and $t_{AGN} = 10^5$ yr (red, solid line). The AGN has $L/L_{Edd} = 1.0$ and is fluctuating with a constant duty cycle fraction of $f_{duty} = 10\%$. The upper panel zooms in on the $0 < t < 4.5$ Myr range of the lower panel. Since the time in between AGN-on phases for these combinations of t_{AGN} and f_{duty} is sufficiently short, the OVI enhancement accumulates over multiple cycles, until a new equilibrium (cycle average) has been reached. In the limit of small t_{AGN}, the net evolutionary trend converges to a trend corresponding to an AGN continuously radiating at $L/L_{Edd} = f_{duty}/100\% = 0.1$ (black, dashed line).

the newly established ionization balance between photoionization from the HM01 background and the AGN, collisional ionization and recombination, will *increase* with increasing AGN luminosity if the AGN photoionizing flux is relatively low, as an increasing fraction of the oxygen is ionized from O I - O v to O VI. However, if the AGN flux is sufficiently high, the O VI abundance will *decrease* with increasing AGN luminosity, as an increasing fraction of the oxygen ends up in higher states than O VI.

Returning to Fig. 4.9, while for $t_{\rm off} \lesssim 10$ Myr (to the left of the grey, dotted line) the O VI is continuously kept in an overionized state, for $t_{\rm off} \gtrsim 300$ Myr (to the right of the black, dashed line) there is hardly any AGN fossil effect at all. In this regime of long $t_{\rm AGN}$ and small $f_{\rm duty}$, the time in between two subsequent AGN-on phases is too long for an AGN-induced change in the O VI to be observable for a significant fraction of the time.

Finally, in our post-processing calculation we neglect the effect of AGN photoheating, as we assume that the temperature of the gas is fixed. However, we expect this to have little impact on the CGM O VI abundance, at least when the AGN is only on for a small fraction of the time. In Appendix 4.A, we show that even in the limit where the time in between subsequent AGN-on phases is infinitely small – adopting a continuously radiating AGN with $L/L_{\rm Edd} = 0.1$ in the $M_* \sim 10^{10}$ M$_\odot$ galaxy at $z = 3$ –, the effect of AGN photoheating on the O VI abundance is negligibly small compared to the effect of AGN photoionization. We find that the latter is generally about an order of magnitude larger.

4.4   Results for other metal ions

While this work focuses on O VI, the abundances of other commonly observed ions – like Si IV and C IV– are also affected by fluctuating AGN. However, the strength of the fossil effect, and whether it induces an increase or decrease of the ion column density, depends on the ionization energies of the associated ions (Oppenheimer & Schaye, 2013a). Since the ionization energies of C III and Si III are significantly lower than that of O v, for the same AGN luminosity the flux of ionizing photons is higher. Hence, the AGN yields a higher ionization rate from the low carbon and silicon states to C IV and Si IV, respectively, but also from C IV and Si IV to higher states. This leads to $\langle \log_{10} N_{\rm C IV} \rangle_{\rm t} (R)$ and $\langle f_{\rm cov}^{\rm C IV} \rangle_{\rm t} (R)$ (adopting a column density threshold of $N_{\rm C IV} > 10^{13.5}$ cm^{-2}) at $z = 3$ that are, in contrast with O VI, *lower* than in equilibrium. However, at $z = 0.1$, where the ionizing flux at a fixed $R/R_{\rm vir}$ is lower, $\langle \log_{10} N_{\rm C IV} \rangle_{\rm t} (R)$ and $\langle f_{\rm cov}^{\rm C IV} \rangle_{\rm t} (R)$ are enhanced with respect to equilibrium. This is illustrated in Fig. 4.11, which shows a comparison between $\langle \log_{10} N_{\rm C IV} \rangle_{\rm t} (R)$, $\langle f_{\rm cov}^{\rm C IV} \rangle_{\rm t} (R)$ and the respective profiles in equilibrium for the four galaxies, adopting the same AGN parameters as in Fig. 4.6. We note that the C IV enhancement for the $M_* \sim 10^{11}$ M$_\odot$ galaxy at $z = 0.1$ is relatively small, in contrast to the large fossil effect seen for O VI. This is due to the higher flux of C IV-ionizing photons, which ionizes significant quantities of carbon to states higher than C IV, thereby roughly cancelling out the positive offset. Furthermore, while for our fiducial choice of $t_{\rm AGN} = 10^6$ yr and $f_{\rm duty} = 10\%$ the decrease in $\langle \log_{10} N_{\rm C IV} \rangle_{\rm t} (R)$ around the $M_* \sim 10^{10}$ M$_\odot$ galaxy
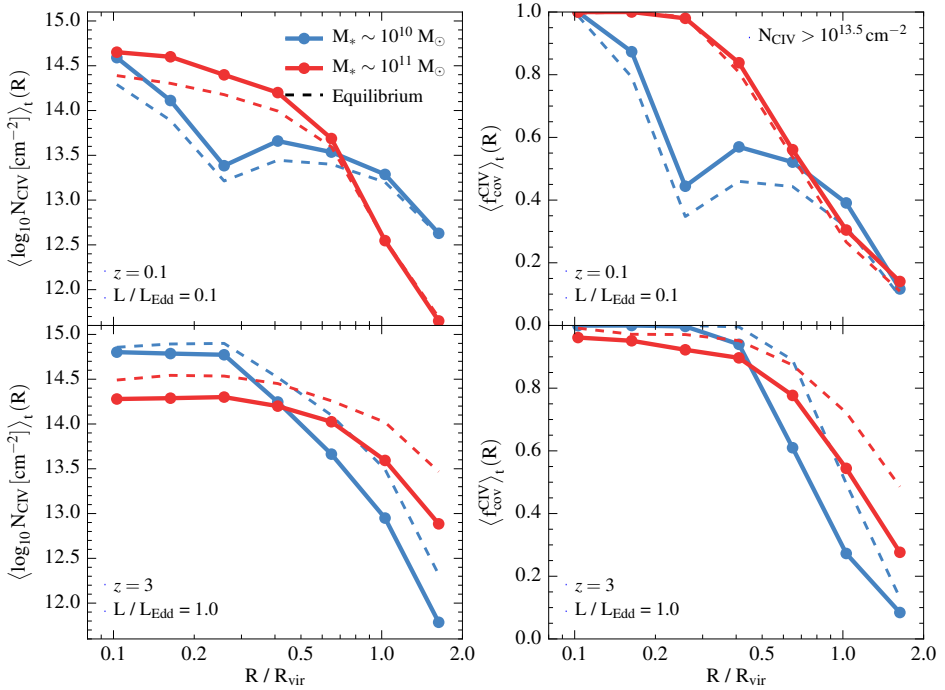
Figure 4.11: As Fig. 4.6, but showing the fossil effect for Cɪᴠ. For the covering fraction, we adopt a column density threshold of $N_{CIV} > 10^{13.5}$ cm^{-2}. While Cɪᴠ is enhanced with respect to equilibrium at $z = 0.1$, $\left\langle \log_{10} N_{CIV} \right\rangle_t (R)$ and $\left\langle f_{cov}^{CIV} \right\rangle_t (R)$ are lower than in equilibrium at $z = 3$. This is in contrast to Oᴠɪ, which is enhanced at both $z = 0.1$ and $z = 3$, and is due to the difference in ionization energy.

at $z = 3$ is $\approx 0.1 - 0.5$ dex, for $t_{AGN} = 10^5$ yr and $f_{duty} = 50\%$ the decrease becomes as large as $\gtrsim 1.0$ dex.

For Si IV (not shown), which has a 1.4 times lower ionization energy than C IV, the AGN causes a deficit of $\langle \log_{10} N_{Si IV} \rangle_t (R)$ and $\langle f_{cov}^{Si IV} \rangle_t (R)$ with respect to equilibrium for all four galaxies, irrespective of the redshift. While the decrease in $\langle \log_{10} N_{Si IV} \rangle_t (R)$ around the $M_* \sim 10^{10}$ M$_\odot$ galaxy at $z = 3$ is $\approx 0.2 - 1.0$ dex for the fiducial $t_{AGN} = 10^6$ yr and $f_{duty} = 10\%$, the decrease is as large as $\approx 2.0 - 3.0$ dex for $t_{AGN} = 10^5$ yr and $f_{duty} = 50\%$.

For ions with ionization energies higher than O VI– like Ne VIII and Mg X– the AGN fossil effect causes an enhancement of their column density and covering fraction, but the enhancement is less strong than for O VI. This is due to the significantly lower flux of radiation above the ionization energy, which is required to enhance the ion column densities during the AGN-on phase. As a result, only for combinations of t_{AGN} and f_{duty} for which $t_{off} \lesssim 1$ Myr ($t_{off} \lesssim 0.1$ Myr) we find $\langle \log_{10} N_{Ne VIII} \rangle_t (R)$ ($\langle \log_{10} N_{Mg X} \rangle_t (R)$) to be offset from equilibrium by more than 0.1 dex.

4.5   Conclusions

We have studied the impact of photoionization by fluctuating AGN on the O VI abundance in the CGM of the host galaxies. We selected four galaxies from the *Ref-L100N1504* simulation from the EAGLE project: two galaxies with stellar masses of $M_* \sim 10^{10}$ M$_\odot$ and $M_* \sim 10^{11}$ M$_\odot$ at $z = 0.1$, and two galaxies with similar stellar masses at $z = 3$. We implemented the sources of ionizing radiation in the centres of these galaxies in post-processing, and followed the time-variable abundances of 133 ion species out to impact parameters of $2R_{vir}$. Due to the significant recombination time-scales of the oxygen ions, and the multiple levels that the ions need to recombine through, the central AGN leaves the CGM gas in an overionized state after it fades: this is what defines an AGN proximity zone fossil. This affects the CGM O VI abundance, as one would for example measure in observations of quasar absorption-line systems, even though the galaxy would not be classified as an active AGN host at the moment of observation.

To quantify the significance of this fossil effect, we presented predictions of the average O VI column density and covering fraction enhancement in between subsequent AGN-on phases, as well as the fraction of the time in between the two phases that the O VI column density is out of equilibrium by at least 0.1 dex. The latter quantity reflects the probability of observing a significant AGN fossil effect around a non-active AGN host. We investigated how these quantities depend on impact parameter, galaxy redshift, galaxy stellar mass, and on the AGN luminosity, lifetime and duty cycle fraction, where we explored a range of AGN parameters as constrained by observations. Our results can be summarized as follows.

1. For our fiducial choice of AGN luminosity ($L/L_{Edd} = 0.1$ at $z = 0.1$ and $L/L_{Edd} = 1.0$ at $z = 3$), lifetime ($t_{AGN} = 10^6$ yr) and duty cycle fraction ($f_{duty} = 10\%$), we find that all four galaxies are significantly affected by AGN fossil effects out to impact parameters of $R/R_{vir} = 2$. After the central AGN fades, the

oxygen in the CGM is left in an overionized state for several megayears. For $R/R_{\text{vir}} < 1.3$, the next AGN-on phase starts before the gas can return to ionization equilibrium, keeping the OVI abundance continuously enhanced. We find offsets in the time-averaged OVI column density and covering fraction with respect to equilibrium that range from $\approx 0.3 - 1.0$ dex and $\approx 0.05 - 0.6$, respectively, at $R/R_{\text{vir}} \lesssim 0.3$ to $\approx 0.06 - 0.2$ dex and $\approx 0.05 - 0.1$ at $R/R_{\text{vir}} \approx 2$ (Fig. 4.6).

2. The AGN predominantly affects the photoionized gas at $T < 10^5$ K, while the change in the OVI abundance in collisionally ionized gas ($T > 10^5$ K) is negligible. In the photoionized regime, the AGN increases the OVI mass at $n_{\text{H}} = 10^{-4} - 10^{-1}$ cm^{-3} at $z = 3$ ($n_{\text{H}} = 10^{-5} - 10^{-2}$ cm^{-3} at $z = 0.1$). The affected density range is roughly constant as a function of impact parameter, even though the typical density of CGM decreases with increasing impact parameter. The re-equilibration time-scale of OVI, after the AGN turns off, is therefore also roughly independent of impact parameter (Fig. 4.5).

3. The dependence of the strength of the fossil effect on impact parameter, galaxy stellar mass and redshift follows from the difference in the ionizing photon flux, the abundance of OI - OV oxygen ions and the OVI re-equilibration time-scale. The fossil effect is largest at small impact parameters for all four galaxies. At $z = 0.1$ and fixed R/R_{vir}, the fossil effect is stronger around the $M_* \sim 10^{11}$ M$_\odot$ galaxy than around the $M_* \sim 10^{10}$ M$_\odot$ galaxy, as a result of the ≈ 2 times higher photon flux, the higher abundance of low-state oxygen ions and a similar re-equilibration time-scale. At $z = 3$, the fossil effect is stronger around the lower mass galaxy (except for $R/R_{\text{vir}} \gtrsim 1.3$), which is solely due to the higher abundance of low-state oxygen ions. While the gas at a fixed R/R_{vir} at $z = 0.1$ receives a $60 - 80$ times lower photon flux than the gas around a galaxy with the same stellar mass at $z = 3$, the ~ 10 times longer re-equilibration time-scale at $z = 0.1$ causes the OVI column density and covering fraction to be strongly offset from equilibrium on average, yielding a particularly strong fossil effect for the $M_* \sim 10^{11}$ M$_\odot$ galaxy (Fig. 4.6).

4. The strength of the fossil effect tends to increase if the AGN lifetime is longer or if the duty cycle fraction larger, since the time in between subsequent AGN-on phases decreases. For the $M_* \sim 10^{10}$ M$_\odot$ galaxy at $z = 3$, OVI is kept out of equilibrium continuously if $t_{\text{off}} \lesssim 10$ Myr. For these combinations of t_{AGN} and f_{duty}, the OVI enhancement accumulates over multiple cycles, until the gas eventually reaches a new (net) ionization equilibrium, where the combined photoionization from the HM01 background and the AGN (in addition to collisional ionization) balances the recombinations per cycle (Figs. 4.8 - 4.10).

5. The strength of the fossil effect increases with increasing AGN luminosity. However, if the AGN luminosity becomes sufficiently high, the OVI enhancement no longer scales linearly with AGN luminosity: for the $M_* \sim 10^{11}$ M$_\odot$ galaxy at $z = 0.1$, we find that the OVI enhancement increases if we increase the Eddington ratio from $L/L_{\text{Edd}} = 0.1$ to $L/L_{\text{Edd}} = 1.0$, but not as significantly as if we increase the Eddington ratio from $L/L_{\text{Edd}} = 0.01$ to $L/L_{\text{Edd}} = 0.1$

(Fig. 4.7). This is due to the fact that the ionization state is sensitive to the ionization rates at all ions levels, hence to the rate from Ovi to Ovii as well as the rate from Ov to Ovi.

6. For low-ionization energy ions like Siiv and Civ, the AGN fossil effect causes a decrease in the CGM column density and covering fraction at $z = 3$, and an increase (Civ) or a decrease (Siiv) at $z = 0.1$ (Fig. 4.11). However, for the high-ionization energy ions Neviii and Mgx, we find only a significant fossil effect (enhancement) if $t_{off} \lesssim 1$ Myr and $t_{off} \lesssim 0.1$ Myr, respectively, which is due to the low flux of ionizing photons.

7. In the limit of short AGN lifetimes, the effect of a fluctuating AGN on the Ovi column density and covering fraction converges to the effect of a continuously radiating AGN with a luminosity equal to ($f_{duty}/100\%$) times the original luminosity (Fig. 4.10).

Our results suggest that AGN proximity zone fossils are ubiquitous around $M_* \sim 10^{10-11}\,M_\odot$ galaxies, and that these are expected to affect observations of metals in the CGM at both low and high redshifts. Since the AGN predominantly affect the low-temperature ($T < 10^5$ K), photoionized gas, fossil effects are expected to particularly alter the column densities of narrow absorption lines. Broad absorption lines, which mostly arise from high-temperature, collisionally ionized gas, will generally be insensitive to AGN fossil effects. However, since the total column density of an absorption system depends on the strength of both the photoionized and collisionally ionized components, the AGN affect measurements of the total column density, even if in ionization equilibrium most of the absorption is expected to be due to collisionally ionized gas. Furthermore, neglecting the impact of AGN fossil effects on the different metal ions may lead to significant errors in the inferred gas properties like density, metallicity and cloud size, when the observed absorption system is assumed to be in ionization equilibrium with the extragalactic background.

We have shown that for our fiducial and observationally motivated choice of AGN parameters, the probability that a measurement of the CGM Ovi abundance is affected by AGN fossil effects, while the galaxy would not be identified as an active AGN host, is $\approx 100\%$ out to impact parameters of at least one virial radius. The typical offsets in the Ovi column densities are comparable to the factor of $\approx 2 - 10$ discrepancy between the high Ovi columns found in observations and those predicted by simulations. This suggests that including the effect of fluctuating AGN in models of the CGM may be key to reproducing the observed abundances of metal ions. A detailed comparison, using a set of high-resolution EAGLE zoom simulations, with the Ovi observed around the $z \sim 0.2$ star-forming galaxies from the COS-Halos sample is presented by Oppenheimer et al. (2017).

Acknowledgements

4.A   Impact of AGN photoheating

We compare the impact of photoheating by the radiation from the AGN on the CGM Ovi abundance to the effect of photoionization. The reaction network includes the option to explore photoheating effects from a time-variable source by allowing the gas temperatures to vary. In principle, we can explore these effects by comparing two network calculations, for the same set of AGN model parameters, with and without thermal evolution. However, one important complication is that the particle temperatures in EAGLE are not necessarily in thermal equilibrium to begin with. (Note that we work on simulation snapshot output(s) in post-processing.) They reflect the instantaneous state of the CGM, including shock-heated gas that is at a much higher temperature than expected based on its density. Once the temperature in the network calculation is allowed to vary, this gas will cool down, which will affect the abundance of Ovi, irrespective of whether an AGN is present.

Hence, in order to isolate the effect of AGN photoheating (focusing on the $M_* = 1.0 \times 10^{10}\,\mathrm{M_\odot}$ galaxy at $z = 3$), we run a separate calculation, where we start from an artificial state with the $T < 10^5$ K gas in thermal (and ionization) equilibrium. For this gas, we run the reaction network including AGN radiation twice: once with the gas temperature kept fixed (hence, including only photoionization) and once where the temperature is allowed to vary (including both photoionization and photoheating). We consider a continuously radiating AGN with $L/L_{\mathrm{Edd}} = 0.1$ – corresponding to a fluctuating AGN with $L/L_{\mathrm{Edd}} = 1.0$ and $f_{\mathrm{duty}} = 10\%$ in the limit of small t_{AGN} (see Section 4.3.3) – and let the gas evolve until it reaches a new ionization and thermal equilibrium. For the gas at $T > 10^5$ K, which is approximately the regime where gas must have been shock heated in the simulation, we fix its temperature to the one taken from the EAGLE snapshot, and only consider photoionization when AGN radiation is included. The red, dashed line in Fig. 4.12 shows the Ovi column density profile for the initial state of this calculation ('Thermal equilibrium'). Since Ovi-bearing photoionized gas is generally very close to being in thermal equilibrium already, the column density profile is only slightly different from the one calculated directly from the EAGLE snapshot (assuming only ionization equilibrium; black, dashed line).

AGN photoionization increases N_{Ovi} by $\approx 0.2 - 2.2$ dex (red, solid line). In-
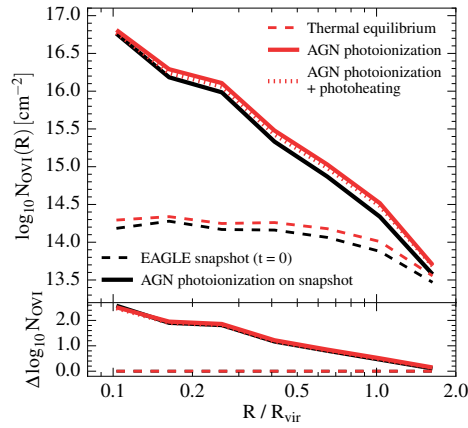
Figure 4.12: The impact of AGN photoheating on the OVI column density profile of the M_* = $1.0 \times 10^{10}\,\mathrm{M}_\odot$ galaxy at $z = 3$, adopting a continuously radiating AGN with $L/L_{\mathrm{Edd}} = 0.1$. The red lines correspond to an artificial state with the $T < 10^5$ K gas in thermal and ionization equilibrium without AGN radiation (dashed) and in a new thermal and ionization equilibrium in the presence of the AGN radiation, where the gas temperature was kept fixed (solid) or allowed to vary (dotted). The temperature of the $T > 10^5$ K gas was kept fixed to the one in the EAGLE snapshot in both cases. For comparison, the black lines show the profile as calculated directly from the EAGLE snapshot assuming ionization equilibrium (dashed), and the profile corresponding to the new ionization equilibrium due to AGN photoionization using the snapshot temperatures (solid). The bottom panel indicates the difference in $\log_{10} N_{\mathrm{OVI}}$ with respect to the dashed lines of the respective colour. The increase in N_{OVI} with respect to thermal equilibrium (red, dashed line) due to AGN photoheating and photoionization (red, dotted line) is only $\lesssim 0.05$ dex lower than the increase due to AGN photoionization (red, solid line), indicating that AGN photoheating does not have a significant impact on N_{OVI}.

cluding the effect of AGN photoheating slightly increases the temperature of the $T < 10^5$ K gas, by ≈ 0.23 dex on average (weighted by the total oxygen mass) at $0.08 < R/R_{\mathrm{vir}} < 2$. However, the resulting change in N_{OVI} is only modest: the increase with respect to thermal equilibrium due to AGN photoheating and photoionization (red, dotted line) is only $\lesssim 0.05$ dex lower than the increase due to just AGN photoionization. Hence, we conclude that AGN photoheating does not significantly affect the OVI abundance in CGM gas, as the effect of AGN photoionization is generally larger by about an order of magnitude.

5
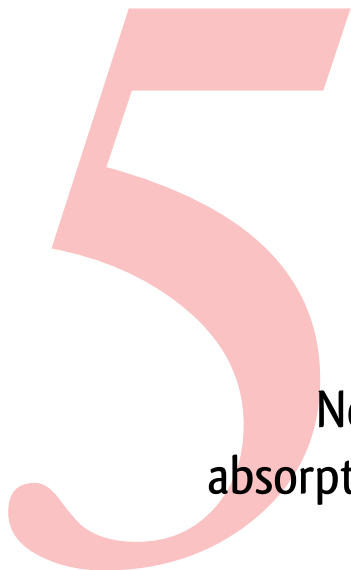
Neutral hydrogen and metal-line absorption around $z < 1$ star-forming galaxies detected with MUSE

We study the abundance of neutral hydrogen and the metal ions Ovi and Ciii in the circumgalactic medium (CGM) of 208 galaxies at $z < 1$, that are detected with the Multi Unit Spectroscopic Explorer in the fields centred on 16 bright quasars with archival Cosmic Origins Spectrograph spectra. The, predominantly low-mass (median stellar mass of $M_\star = 10^{8.9}\,\mathrm{M}_\odot$ and median star formation rate of $SFR = 0.21\,\mathrm{M}_\odot\,\mathrm{yr}^{-1}$), galaxies are selected blindly – without prior knowledge of the absorption data – by their continuum emission, and we measure their redshifts from their emission (or absorption) lines. Using the pixel optical depth technique, we find that the strength of the median Hi and metal-line absorption decreases with increasing line-of-sight (LOS) velocity (v_{LOS}) and projected distance (both in physical units, d_{trans}, and as a fraction of the halo virial radius, $d_{\mathrm{trans}}/R_{\mathrm{vir}}$) from the galaxies. Along the LOS direction, the absorption signals start to deviate from the approximately flat trend at small v_{LOS} at $v_{\mathrm{drop}} \approx 50$ km/s for Hi and at $v_{\mathrm{drop}} \approx 80$ km/s for the metal ions. For Hi and Ovi, we find a significant (> 95% confidence) absorption enhancement, with respect to the detection limit, out to $v_{\mathrm{LOS}} \approx 260$ km/s (≈ 3.2 pMpc in the case of pure Hubble flow) and $v_{\mathrm{LOS}} \approx 115$ km/s (≈ 1.3 pMpc), respectively, in the LOS direction, and out to $d_{\mathrm{trans}} \approx 300$ pkpc (which is the maximum distance we can probe) in the transverse direction. In normalized units, the transverse extent of the Hi and Ovi signals is equal to at least four times the halo virial radius. For Ciii, the signal extends to $v_{\mathrm{los}} \approx 115$ km/s (≈ 1.3 pMpc; > 68% confidence) and $d_{\mathrm{trans}} \approx 120$ pkpc (> 95% confidence). We do not find evidence for significant evolution of the Hi optical depth over the range $0.30 < z < 0.48$, and of the Ovi optical depth over the range $0.38 < z < 0.74$, where an unbiased assessment of the redshift dependence is possible. At fixed v_{LOS} and d_{trans}, the Ovi absorption strength within $v_{\mathrm{LOS}} = 100$ km/s increases with increasing galaxy stellar mass and star formation rate (SFR), and weakly decreases with increasing specific SFR. It also increases with increasing stellar mass at fixed $d_{\mathrm{trans}}/R_{\mathrm{vir}}$. However, the dependence of the signal (both its strength and extent along the LOS direction) on stellar mass is only evident when comparing the $M_\star < 10^{8.5}\,\mathrm{M}_\odot$ and $M_\star > 10^{8.5}\,\mathrm{M}_\odot$ stellar mass regimes, while the signal exhibits no mass dependence for $M_\star > 10^{8.5}\,\mathrm{M}_\odot$. This likely

reflects the decreasing ability of galactic winds to drive out metals into the CGM in higher mass galaxies.

Marijke C. Segers, Joop Schaye et al.
In preparation

5.1   Introduction

Galaxies enrich their circumgalactic medium (CGM) with a range of metal species like carbon, oxygen and silicon. While metals are synthesised in stars, residing in the dense parts of the galaxies, they can travel out to large distances, enriching the diffuse gas around galaxies and in the intergalactic medium (IGM), as they are expelled by galaxy-scale outflows. These outflows are believed to be driven by feedback processes resulting from star formation or due to active galactic nuclei (AGN). The ubiquity of galactic winds in star-forming galaxies at $0.5 \lesssim z \lesssim 3$, as implied by observations (e.g. Pettini et al., 2001; Steidel et al., 2010; Weiner et al., 2009; Rubin et al., 2014), supports this picture. Furthermore, various theoretical studies employing hydrodynamical simulations of galaxy formation have emphasised the importance of galactic winds for enriching the CGM and IGM to the observed levels (e.g. Aguirre et al., 2001b,a; Oppenheimer & Davé, 2006; Cen & Chisari, 2011; Wiersma et al., 2011).

Observing the CGM by probing different metal ionization states provides information about the composition, density, temperature and kinematics of the gas around galaxies, and therefore about the galaxies themselves: it gives insight into their star formation history and the processes through which they interact with their surroundings. However, as the gas in the CGM and IGM is generally too diffuse to be detected in emission, a common approach is to observe it in absorption against the light from a bright quasi-stellar object (QSO). This technique has been used to study a wide range of ion transitions at both low and high redshift, in particular MgII (e.g. Petitjean & Bergeron, 1990; Bowen et al., 1995; Chen et al., 2010; Nielsen et al., 2013), CIV (e.g. Chen et al., 2001; Schaye et al., 2003; Cooksey et al., 2013; Bordoloi et al., 2014; Liang & Chen, 2014) and OVI (e.g. Carswell et al., 2002; Danforth & Shull, 2005; Aguirre et al., 2008; Wakker & Savage, 2009; Prochaska et al., 2011; Turner et al., 2014), as well as neutral hydrogen (HI; e.g. Wakker & Savage, 2009; Rakic et al., 2012; Rudie et al., 2012; Tumlinson et al., 2013).

A crucial step in the interpretation of CGM observations within the framework of galaxy formation, is to connect the absorption features from the QSO spectra to the galaxies that are associated with the absorbing gas. For a sample of absorption systems (i.e. the absorber-centred approach; see e.g. Stocke et al., 2006; Burchett et al., 2016), this is generally done by selecting the galaxy that is 'closest' to each absorber, considering both its projected distance to the QSO sightline and its velocity offset along the line-of-sight (LOS). The galaxy association is, however, not unambiguous, as multiple galaxies might be similarly close and it is not obvious whether the absolute distance or the distance relative to the galaxy size should be considered. Furthermore, the association is complicated by the possibility that the true galaxy giving rise to the absorption is too faint to be detected with the instrument that is used. For example, Rahmati & Schaye (2014) found that this could explain the low success rate of observational searches for galaxy counterparts of optically thick HI absorbers. The alternative approach of connecting galaxies and absorbers is to select the absorber that is closest to each galaxy (i.e. the galaxy-centred approach; see e.g. Bowen et al., 1995; Rakic et al., 2012; Tumlinson et al.,

2013; Turner et al., 2014). While the absorption is not necessarily most closely associated with the respective galaxy, this approach does enable one to study the CGM of detected galaxies in a systematic way, e.g. by measuring the absorption strength (or constraining it by placing upper or lower limits) around each galaxy individually, or by measuring the mean or median absorption strength for a sample of galaxies. In the latter case, which is the method we employ in this work, the result is independent of the particular identification of galaxy-absorber pairs, as the absorption is measured in a statistical sense for a sample of many galaxies.

Various studies of metal absorbers and their relation to galaxies have found that they generally reside at relatively small distances to galaxies (i.e. close enough to be considered part of their CGM), as opposed to weak HI absorbers appearing as Lyα forest absorbers, which are believed to trace the filamentary large-scale structure of the Universe (e.g. Cen et al., 1994; Davé et al., 1999; Schaye, 2001). Stocke et al. (2006) found that for each of the $z < 0.15$ OVI absorbers in their sample, a galaxy resides within a 3D distance (corrected for increased distances along the LOS) of 800 proper kpc (pkpc), with the maximum distance reducing to 400 pkpc in regions that are complete down to galaxy luminosities of $L = 0.1L^*$. They also derived a median distance of 625 pkpc from the OVI absorber to the nearest $L > L^*$ galaxy, and a distance of 335 pkpc to the nearest $L > 0.1L^*$ galaxy. Based on these results, they argued that OVI-bearing gas is predominantly associated with individual galaxies rather than with galaxy voids. The studies by Wakker & Savage (2009) and Prochaska et al. (2011) found similar distances from OVI absorbers to the nearest $0.1L^*$ and L^* galaxies.

Galaxy-centred surveys typically find the metal-enriched CGM of low-redshift ($z < 1$) galaxies to extend to a few hundred kpc, or distances comparable to the virial radius ($R_{\rm vir}$) of the galaxies. Also at high redshift ($z \approx 2.4$), Turner et al. (2014) found that the absorption of metal ions like SiIV, CIV and OVI is enhanced relative to randomly located regions out to projected distances of at least 180 pkpc. Liang & Chen (2014) observed a number of low- to intermediate-ionization species – including CII, SiIII and CIV– to have a covering fraction of $\gtrsim 50\%$ out to $0.6R_{\rm vir}$ (corresponding to ≈ 100 pkpc for their sample), and to have a steeply declining incidence rate beyond that. For CIV, similar results have been obtained by Chen et al. (2001) and Bordoloi et al. (2014, probing $\lesssim 0.1L^*$ galaxies), while the typical extent of MgII-bearing gas seems to be lower (e.g. Bowen et al., 1995; Chen et al., 2010). In contrast, OVI is found to be somewhat more extended than the low ionization species, as it is observed with near-unity covering fractions out to distances of ≈ 200 pkpc, or $\approx 1 - 2R_{\rm vir}$, around (sub-)L^* galaxies (e.g. Prochaska et al., 2011; Tumlinson et al., 2011; Johnson et al., 2015, where the second study, the COS-Halos survey, only probes distances up to 150 pkpc). Johnson et al. (2015) even detected some OVI out to a distance of $3R_{\rm vir}$. Furthermore, while it is known that low-ionization species trace cold ($T \sim 10^4$ K), photoionized gas, the origin of the gas traced by OVI is still a topic of debate: observations seem to suggest that OVI can arise in both photoionized and collisionally ionized gas (see e.g. Carswell et al., 2002; Thom & Chen, 2008; Savage et al., 2014; Stocke et al., 2014).

In this work, we study the abundance of HI, OVI and CIII, where we mainly focus on OVI, in the CGM of $z < 1$ galaxies detected using the Multi Unit Spectro-

scopic Explorer (MUSE; Bacon et al., 2010) on the Very Large Telescope (VLT). We detect these galaxies by their Hα ($z_{\mathrm{em}} \lesssim 0.4$), Oıı ($z_{\mathrm{em}} \gtrsim 0.25$), Oııı ($z_{\mathrm{em}} \lesssim 0.85$) or Hβ ($z_{\mathrm{em}} \lesssim 0.9$) emission in the fields centred on 16 sightlines towards bright QSOs ($z_{\mathrm{QSO}} = 0.4 - 1.5$) that have been observed with the Cosmic Origins Spectrograph (COS; Green et al., 2012) on board the Hubble Space Telescope (HST). This enables us to probe the galaxy CGM in absorption out to projected distances of ≈ 300 pkpc. This study is part of the MUSE Quasar-field Blind Emitter Survey (MUSE-QuBES), which aims to study the CGM of star-forming galaxies in absorption by conducting a search for line-emitting galaxies in the fields near QSO sightlines for which high-quality spectra are available. The survey is blind in the sense that the QSOs were not selected based on the presence of any particular absorbers or nearby galaxies. Complementary to the sample of 16 low-redshift QSO fields, MUSE-QuBES also targets 8 high-redshift QSO fields (with QSOs at $z_{\mathrm{QSO}} = 3.6 - 4.0$), to study the CGM of Lyα-emitting galaxies at $3 < z < 4$ (Muzahid et al., in prep.).

The fact that MUSE is an Integral Field Spectrograph (IFS) enables us to compile a sample of a few hundred galaxies around QSO sightlines very efficiently: while non-IFS studies need to carry out spectroscopic follow-up observations to accurately determine the redshifts of the galaxies after detecting them through imaging, we can detect the galaxies and measure their redshifts both at the same time. While the galaxies do not necessarily have to be continuum sources to be able to detect them with MUSE and determine their redshifts, we do focus our current study on continuum-detected galaxies only. In the future, we will extend the sample by also including purely line-emitting galaxies.

Our deep MUSE observations – ranging from two to ten hours of exposure time per field – of a relatively small survey volume yield a sample of predominantly low-mass (i.e. with stellar masses of $M_* < 10^{10}\,\mathrm{M_\odot}$) galaxies. As measured in the Cousins R band, the median luminosity of the sample is $\approx 0.09 L^*$. Sub-L^* galaxies are interesting targets for studies of CGM metals, as the majority of the Oıı absorbers is likely to be associated with galaxies with luminosities significantly below L^* (e.g. Stocke et al., 2006; Wakker & Savage, 2009; Prochaska et al., 2011) (even though the Oıı abundance around individual galaxies likely peaks for $L \approx L^*$ galaxies; Oppenheimer et al., 2016). By comparing the observed rate of incidence of Oıı absorbers with the occurrence of low-redshift galaxies, Tumlinson & Fang (2005) inferred that $L \gtrsim L^*$ galaxies alone cannot account for the observed population of Oıı absorbers, unless their surroundings are enriched out to unrealistically large distances. The theoretical study by Wiersma et al. (2010) also emphasised the role of low-mass galaxies in the enrichment of the IGM, predicting that more than half of the IGM metal mass at $z = 0$ is contributed by $M_* < 10^9\,\mathrm{M_\odot}$ galaxies, while Booth et al. (2012) inferred from observations of Cıv that the low-density IGM at $z = 3$ was primarily enriched by galaxies residing in $M_{\mathrm{vir}} < 10^{10}\,\mathrm{M_\odot}$ haloes.

In this work, we study the CGM abundance of Hı, Oıı and Cııı by measuring the median pixel optical depth in the QSO spectra as a function of LOS velocity and projected distance to the galaxies. We study the extent of the absorption signal in both the LOS and projected directions, and we investigate how the absorption strength of Hı and Oıı evolves over the redshift range probed. We also explore the dependence of the Oıı absorption strength on galaxy stellar mass and star for-

mation rate (SFR). A study of the $O{\scriptstyle VI}$ covering fraction around MUSE galaxies as a function of $O{\scriptstyle VI}$ column density, and how it depends on the different galaxy properties, will be presented in Straka et al. (in prep.).

This work is organized as follows. In Section 5.2, we give an overview of the sample of QSO targets and the MUSE observations. We also explain how we identify galaxies and measure their redshifts and other properties. In Section 5.3, we describe the characteristics of the COS spectra, the optical depth recovery performed on the spectra and the construction of the median optical depth profiles. We present our results in Section 5.4: we show the $H{\scriptstyle I}$, $O{\scriptstyle VI}$ and $C{\scriptstyle III}$ absorption strength as a function of LOS velocity and transverse distance (Section 5.4.1), and its dependence on galaxy redshift ($H{\scriptstyle I}$ and $O{\scriptstyle VI}$; Section 5.4.2), stellar mass ($O{\scriptstyle VI}$; Section 5.4.3) and SFR ($O{\scriptstyle VI}$; Section 5.4.4). We summarise our conclusions in Section 5.5. Throughout this work, we adopt a Λ cold dark matter cosmology with parameters $\Omega_m = 0.3$, $\Omega_\Lambda = 0.7$, and $H_0 = 70$ km s^{-1} Mpc^{-1}.

5.2   Galaxy sample

We carry out a blind spectroscopic redshift survey in the fields centred on 16 QSOs using the MUSE instrument, which is mounted on the VLT. In this section, we first describe our criteria for selecting the QSO targets. Then, we describe the MUSE observations, carried out as part of the MUSE Guaranteed Time Observations, and the method we use to detect galaxies and determine their redshifts. We also explain how we obtain an estimate of the galaxy stellar mass and SFR.

5.2.1   QSO sample selection

All QSO targets have high-quality absorption spectra from HST/COS, with coverage in both the G130M and G160M gratings. The QSOs are sufficiently luminous, with a V-band magnitude of $m_V \leq 18$, to have a relatively high signal-to-noise ratio (S/N) over the majority of the COS wavelength range. Their redshifts are chosen to be both high enough ($z_{QSO} > 0.4$) so that the full range for which $H\alpha$ emission is observable with MUSE can be studied in absorption (i.e. $z < z_{QSO}$), and low enough ($z_{QSO} < 1.5$) to limit the amount of blended absorption in the spectra. The maximum redshift of 1.5 corresponds to the maximum redshift at which $O{\scriptstyle II}$ emission can be detected with MUSE. Furthermore, to be able to observe the targets from Paranal Observatory, we only select QSOs with a declination below +30°. The properties of our final sample of 16 QSOs are summarized in Table 5.1.

5.2.2   MUSE observations

The MUSE observations of the 16 QSO fields were conducted between September 2014 and September 2016 (ESO programmes 094.A-0131, 095.A-0200, 096.A-0222 and 097.A-0089). The total amount of exposure time is 60.75 h, where all fields have been observed for at least 2 h and 4 fields have been observed for 8 – 10 h. An overview of the exposure time per field is given in Table 5.2. Each observation block of 1 h was split into 4×900 s exposures, which were rotated by 90° and offset

Table 5.1: Sample of QSO targets. From left to right, the columns show the QSO name, right ascension (J2000), declination (J2000), redshift, V-band magnitude, exposure time (t_{exp}) with the COS/G130M grating, S/N per resolution element at λ = 1250 Å, exposure time with the COS/G160M grating, S/N per resolution element at λ = 1650 Å and the HST programme ID of the COS observations.

QSO name	RA	Dec.	z_{QSO}	m_V	G130M		G160M		PID
					t_{exp} [h]	S/N	t_{exp} [h]	S/N	
HE 0435-5304	04 36 50.8	-52 58 49	0.425	16.4	2.3	14.5	2.5	5.8	11520
HE 0153-4520	01 55 13.2	-45 06 12	0.451	15.2	1.5	28.6	1.6	17.2	11541
RXS J02282-4057	02 28 15.2	-40 57 16	0.494	14.3	1.9	41.4	2.2	21.6	11541
PKS 0405-12	04 07 48.5	-12 11 36	0.574	14.9	6.7	87.1	3.1	34.7	11508, 11541
HE 0238-1904	02 40 32.6	-18 51 51	0.631	15.0	4.0	32.6	2.1	20.6	11541, 12505
3C 57	02 01 57.1	-11 32 34	0.669	16.4	3.0	29.1	2.4	13.9	12038
PKS 0552-640	05 52 24.6	-64 02 11	0.680	15.0	2.6	30.8	2.3	20.1	11692
PB 6291	01 10 16.3	-02 18 51	0.956	17.6	5.9	13.3	5.9	7.9	11585
Q 0107-0235	01 10 13.2	-02 19 53	0.958	17.8	7.8	14.8	12.3	11.0	11585
HE 0439-5254	04 40 11.9	-52 48 18	1.053	16.1	2.3	19.9	2.5	8.8	11520
HE 1003+0149	10 05 35.2	+01 34 44	1.078	16.9	3.1	11.0	6.2	9.6	12264
TEX 0206-048	02 09 30.8	-04 38 27	1.128	17.2	3.9	16.6[a]	7.8	13.9	12264
Q 1354+048	13 57 26.2	+04 35 41	1.234	17.2	3.9	16.9	7.8	6.9	12264
Q 1435-0134	14 37 48.2	-01 47 11	1.310	15.8	6.2	35.3	9.5	23.8	11741
PG 1522+101	15 24 24.5	+09 58 30	1.324	16.2	4.6	25.0	6.4	18.1	11741
PKS 0232-04	02 35 07.2	-04 02 05	1.438	16.5	4.4	19.4	6.3	13.1	11741

[a]This is the S/N at λ = 1350 Å. Due to a Lyman-limit system at z = 0.390, there is no flux at λ < 1280 Å.

Table 5.2: Overview of the MUSE observations. From left to right, the columns show the QSO name, exposure time, effective seeing measured at $\lambda = 7000$ Å and number of galaxies per QSO field included in our galaxy catalogue.

QSO name	t_{exp} [h]	Seeing [″]	Number of galaxies
HE 0435-5304	2	0.97	0
HE 0153-4520	2	0.78	5
RXS J02282-4057	8	0.56	8
PKS 0405-12	9.75	0.72	6
HE 0238-1904	10	0.76	5
3C 57	2	0.70	14
PKS 0552-640	2	0.77	11
PB 6291	2	1.20	11
Q 0107-0235	2	1.07	18
HE 0439-5254	2	0.70	23
HE 1003+0149	2	0.90	14
TEX 0206-048	8	0.70	29
Q 1354+048	2	0.56	17
Q 1435-0134	3	0.54	20
PG 1522+101	2	0.59	19
PKS 0232-04	2	0.83	8

by a small $\approx 1-5''$ shift from each other. The effective seeing per field, corresponding to the full width at half maximum (FWHM) of a 2D Gaussian profile fitted to a point source at $\lambda = 7000$ Å in the reduced and combined data cube, varies between $0.54''$ and $1.20''$, but is typically $0.7-0.8''$ (see Table 5.2).

With the MUSE field-of-view (FoV) of $1' \times 1'$ centred on the QSO, we are able to observe a region of 480×480 pkpc around the QSO at $z \approx 1$ (110×110 pkpc at $z \approx 0.1$). The field is spatially sampled by a grid of $0.2'' \times 0.2''$ pixels. All observations were carried out using the standard wavelength range of $4750-9300$ Å, sampled by 1.25 Å spectral pixels. The spectral resolution ranges from $R \approx 1800$ at $\lambda = 5000$ Å to $R \approx 3500$ at $\lambda = 9000$ Å, corresponding to a FWHM of 167 km/s to 86 km/s.

Data reduction

The data reduction is performed using the standard MUSE data reduction pipeline (v1.2; Weilbacher et al., 2012, in prep.), adopting the default set of parameters. First, a number of basic reduction steps – like bias subtraction, flat-fielding, illumination correction and wavelength calibration – is carried out for each individual science exposure, where the calibration frames are used that were taken closest in time to the respective science frames. We then perform an initial sky subtraction, using the appropriate line spread function (LSF) calibration frames, and construct a 2D white-light image for each exposure by collapsing the corresponding data cube along the wavelength direction. Note that this initial sky subtraction is only done to facilitate the detection of continuum sources in the exposure white-light images, which are used to determine the dithering offset between the exposures: the actual

sky subtraction on the data used for our science is performed using CUBESHARP (as described below). Based on the spatial positions of the point sources (preferably two or more stars, otherwise the QSO and a star) detected in the white-light images, we calculate the offset of each exposure with respect to a reference frame, which we choose to be the first exposure of the field. These offsets are then used to realign the calibrated, non-sky subtracted science frames to the same coordinate system, so that they can be combined after the final data reduction steps without shifting them.

We perform a few additional reduction procedures using the CUBEXTRACTOR package (Cantalupo et al., in prep.). These are described by Borisova et al. (2016), and we will only briefly outline the main steps. For each exposure, the CUBEFIX routine applies a flat-fielding correction to the individual slices ('spatial segments') of the Integral Field Unit (IFU) and to the individual IFU channels ('wavelength segments'). It utilises the sky continuum and sky lines as spatially uniform sources to normalize each of the slices per channel to the same median flux value, and it then normalizes each of the channels to the same median flux value. Masks are created to cover any gaps in between the IFU slices and slice edges that have significant flat-fielding residuals. Next, the CUBESHARP routine is used to perform a sky subtraction, which is uses the shape of the sky LSF obtained from the data itself and is flux-conserving by design. The data cubes from the individual exposures are then combined (by taking a 3σ-clipped mean for each spatial pixel) and converted into one white-light image. After the bright continuum objects in the field have been identified using the CUBEX routine, the procedures with CUBEFIX and CUBESHARP as outlined above are repeated, this time with the bright objects masked out. This improves the flat-fielding of the IFU slices and channels. After the second round of sky subtraction, the exposure files are combined into the final data cube for the QSO field.

The wavelengths in the MUSE data cubes are given in air. However, all redshifts given in this work correspond to vaccum redshifts, as we apply the appropriate corrections while building the galaxy catalogue.

5.2.3 Galaxy identification

We compile a sample of galaxies in the 16 QSO fields by detecting them in the MUSE data through their continuum emission, and measuring their redshifts from their emission-line (or absorption-line) features. For each QSO field, we construct a white-light image from the final MUSE data cube. We run the SOURCE EXTRACTOR (SEXTRACTOR; Bertin & Arnouts, 1996) package on each image, using a detection threshold of 1σ per pixel (DETECT_TRESH = 1) and requiring a minimum number of neighbouring pixels above the threshold of 3 (DETECT_MINAREA = 3). This yields a sample of 2299 continuum-detected objects.

We then use a modified version of the application MARZ (Hinton et al., 2016) to identify galaxies and determine their redshifts based on their spectral features. For every object, we extract a 1D spectrum from the MUSE data cube using a segmentation map from SEXTRACTOR, where we sum the flux, weighted by the variance, from all pixels associated to the object that are 0.5σ above the background in the white-light image. This spectrum is loaded into the interactive MARZ interface to

Table 5.3: Adopted rest-frame wavelengths of absorption-line species studied in the COS spectra (upper part) and emission-line features used to measure galaxy redshifts from the MUSE data (lower part). In case of a line doublet, the wavelengths of both components are given.

Name	Rest-frame wavelength [Å]
Absorption	
CIII	977.02
OVI	1031.93, 1037.62
HI Lyα	1215.67
Emission	
OII	3727.09, 3729.88
Hβ	4862.69
OIII	4960.30, 5008.24
Hα	6564.61

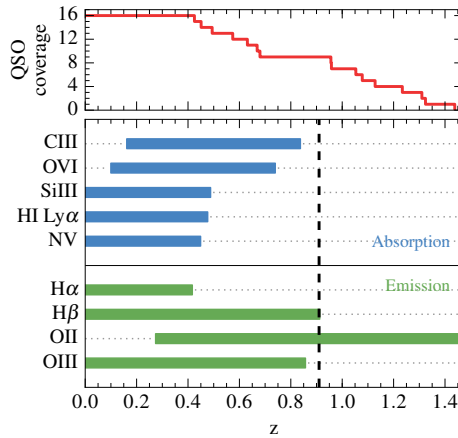**Figure 5.1:** Redshift ranges where absorption-line (blue) and emission-line (green) species can be observed, based on the wavelength coverage of COS and MUSE, respectively. The top panel shows the number of QSO sightlines covering each redshift interval (i.e. the number of QSOs with $z_{QSO} > z$ at each z). We select galaxies below a redshift of $z = 0.91$ (vertical dashed line), where their CGM can be studied in absorption.

classify the object as a galaxy or a star (or an instrumental artifact), based on an automated matching algorithm. In brief, the observed spectrum is compared to a number of template spectra and, in the case of a galaxy, aligned to measure the redshift. Instead of the standard set of templates, we use a set of 23 stellar spectra, ranging from O stars to white dwarfs, and a set of 20 representative galaxy spectra, which were taken from MUSE observations of the Hubble Ultra Deep Field (Bacon et al., in press; Paalvast et al., in prep.). These galaxy templates cover a range of galaxy types (late-type, early-type, transitional), a range of emitter types (as it depends on the redshift which lines are visible in the optical), and allow a weak or strong continuum relative to the emission lines. MARZ selects the best-fitting template by performing a cross-correlation, but the user is allowed to select a different template based on visual inspection. The objects classified as galaxies are then automatically assigned a redshift, which we manually assign a quality flag (QOP) indicating its reliability.

The most prominent emission lines that are used for the redshift determination are Hα, Hβ, O$_{II}$, and O$_{III}$. Their adopted rest-frame wavelengths[1] are summarized in the bottom part of Table 5.3 and their observable redshift range, given the wavelength coverage of MUSE, is shown in the bottom panel of Fig. 5.1. In addition, some galaxies (about 20% of the final sample) show interstellar absorption lines, of which the calcium II H and K lines (at 3968.47 Å and 3933.66 Å, respectively) are the most prominent ones. When available, these are also used for the redshift determination.

Out of the 2299 objects detected in the white-light images, we can estimate the redshift of 868 galaxies. In this work, we only use the galaxies with the highest quality flag, $QOP = 3$, for which the redshift estimate is based on multiple spectral features – either two or more emission lines or multiple absorption lines (at least the Ca$_{II}$ H and K lines). This corresponds to $\approx 44\%$ of the 868 galaxies. The flags $QOP = 1$ and $QOP = 2$ refer to galaxies with redshift estimates based on only one spectral feature, where its identification is based on the line shape or the absence of other lines, or to galaxies with a noisy spectrum or weak spectral features, that make the redshift estimate less robust. We will refer to the galaxy redshift as z_{em}, since for the majority of the galaxies the redshift is derived from their emission lines.

As the redshifts resulting from the galaxy template match by MARZ can be uncertain by $\sim 10^2$ km/s, we use a modified version of the code PLATEFIT (Tremonti et al., 2004; Brinchmann et al., 2004) to further refine the redshifts. This routine constrains the local continuum and fits (positive and negative) Gaussian profiles to a large set of emission and absorption lines. Doublet features like O$_{II}$ are fit with a double Gaussian profile. In this version of PLATEFIT, the redshifts of both the Balmer lines and the forbidden lines are tied together, allowing common shifts up to ±300 km/s with respect to the original value from MARZ. The routine therefore enables us to refine the redshift estimates, but also to measure the flux in various emission lines, which we will use to obtain an estimate of the SFR (see Section 5.2.4). We note that we apply two corrections to the error estimates on the line fluxes re-

---

[1]Note that these wavelengths are given in vacuum. Even though the original MUSE data cube contains wavelengths in air, MARZ corrects for this by converting the wavelengths to vacuum before determining the redshift.

turned by PLATEFIT. As will be described by Bacon et al. (in press), to take into account the correlation between adjacent pixels, the noise estimate per pixel (and therefore the error on the line flux) needs to be multiplied by a factor of $1/0.60$, so that it reflects the true pixel-to-pixel standard deviation. Furthermore, to correct for the fact that PLATEFIT does not automatically include all sources of error – such as the uncertainty in the continuum subtraction – in its estimate of the error on the line flux, we multiply the errors by a factor of 2.2 for OII and the Balmer lines and by a factor of 1.3 for forbidden lines (following Brinchmann et al., 2008). Hence, we adopt line flux errors that are 3.7 times larger than the original values from PLATEFIT in the case of OII and the Balmer lines, and errors that are 2.2 times larger in the case of OIII. These errors are used to assess the significance (S/N) of the emission lines.

Having refined our redshift estimates, we apply the following selection cuts to the galaxy sample. As we aim to study the CGM of the galaxies in absorption, we only select galaxies at $z_{em} < 0.91$, which corresponds to the redshift range in which the HI Lyα, OVI or CIII absorption lines are observable with COS (as indicated in blue in Fig. 5.1). The upper bound of 0.91 on the redshift includes a velocity range up to $\approx$ 10,000 km/s redwards of the maximum CIII redshift covered by COS, corresponding to the velocity range in which we plot the absorption signal (see Section 5.4). This yields a sample of 233 galaxies. Furthermore, for the 7 QSO fields with $z_{QSO} < 0.91$, we only select galaxies that are at redshifts at least 3000 km/s[2] bluewards of the redshift of the QSO, in order to avoid QSO proximity effects. Our final galaxy catalogue includes 208 galaxies, with a median redshift of $z_{em} = 0.52$. For each QSO field, the number of galaxies included in the catalogue is listed in the fourth column of Table 5.2. Note that for one QSO field, HE 0435-5304, we do not detect any galaxies below the QSO redshift (neither with $QOP = 3$, nor with $QOP = 1$ or $QOP = 2$). Hence, we will not consider this field in our absorption analysis.

Fig. 5.2 shows the projected proper distance from the galaxy to the QSO sightline, referred to as the galaxy impact parameter, as a function of the galaxy redshift. The impact parameters range from 11 to 304 pkpc (with a median of 141 pkpc), limited at the low end by the extent of the QSO point spread function (PSF; which we aim to improve in future work) and at the high end by the size of the MUSE FoV. In units of the halo virial radius, which we define as the radius at which the mean enclosed density is 200 times the critical density of the Universe (see Section 5.2.4 for its derivation), the impact parameters range from $0.062R_{vir}$ to $5.2R_{vir}$ and have a median of $1.6R_{vir}$. Fig. 5.3 shows the distribution of 'normalized' impact parameters, and how they vary as a function of the galaxy redshift.

To assess the type of emission exhibited by the galaxies in our sample, we show in Fig. 5.4 the galaxy redshift distribution split by emitter type. The red histograms include all galaxies for which the indicated emission line has S/N > 3. Hence, some galaxies occur in multiple panels. For 69 out of the 208 galaxies, Hα is detected with S/N > 3. This number is relatively low, as Hα is only observable with MUSE

---

[2]We note that the adopted velocity limit of 3000 km/s is, in this case, equivalent to a limit of 6000 km/s, as the 7 QSO fields with $z_{QSO} < 0.91$ do not contain galaxies with redshifts between 6000 km/s and 3000 km/s below the QSO redshift.
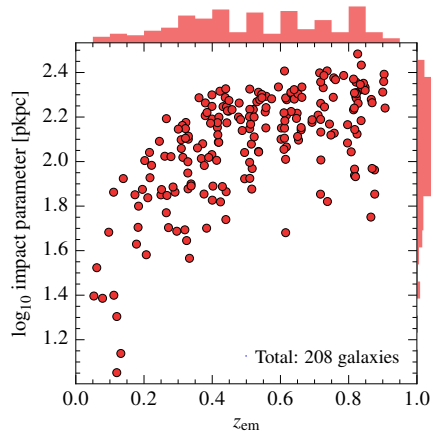
Figure 5.2: Galaxy impact parameter as a function of galaxy redshift for our final sample of 208 galaxies detected with MUSE. The histograms at the top and on the right show the individual distributions of redshift and impact parameter, respectively.

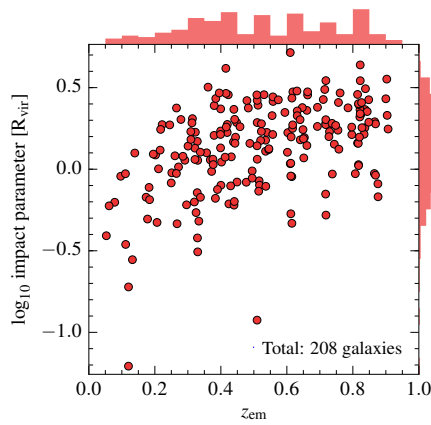**Figure 5.3:** Galaxy impact parameter, in units of the halo virial radius, as a function of galaxy redshift for the total sample of 208 galaxies. The histograms at the top and on the right show the individual distributions of redshift and normalized impact parameter, respectively.
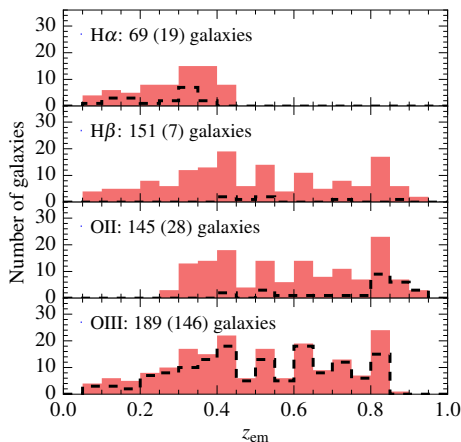
Figure 5.4: The galaxy redshift distribution split by emitter type. The red (black) histogram in each panel includes galaxies for which the respective emission line has S/N > 3 (has S/N > 3 *and* a higher S/N than the other lines), where the total number of galaxies included is indicated by the first (second) number in the legend. Hence, while for the red histograms a single galaxy can occur in multiple panels, for the black histograms each galaxy occurs only once. All but 8 galaxies exhibit at least one of the Hα, Hβ, O$_{II}$ or O$_{III}$ lines with S/N > 3, where for the majority of the galaxies O$_{III}$ has the highest S/N.

at z_{em} < 0.42: if we focus solely on that redshift range, then we find that ≈ 91% of the galaxies has significant (i.e. S/N > 3) Hα emission. The Hβ and O$_{II}$ lines, which are observable over most of the redshift range (O$_{II}$ at z_{em} > 0.27), are significantly detected for approximately 70% of the galaxies, while O$_{III}$ is significantly detected for ≈ 91% of the galaxies. For the majority of the galaxies, O$_{III}$ is also the line that exhibits the highest S/N (compared to the other three lines), as illustrated by the black, dashed histograms. Only at the low- and high-redshift ends of the distribution, a significant fraction of the galaxies exhibits the highest S/N in the Hα and O$_{II}$ emission lines, respectively. Overall, we find that only 8 galaxies in our sample do not show any emission with S/N > 3 in either Hα, Hβ, O$_{II}$ or O$_{III}$. One of these, however, shows O$_{III}$ emission with S/N = 2.5, where both O$_{III}$ components with rest-frame wavelengths 5008 Å and 4960 Å are visible in the spectrum, and Hβ and O$_{II}$ emission with S/N ≈ 0.7. We therefore consider its identification to be robust. For the other 7 galaxies, their identification and redshift measurement is solely based on interstellar absorption lines, where in all cases the spectrum exhibits strong absorption in at least the Ca$_{II}$ H and K lines.

   In future work, we will expand the catalogue with a sample of purely line-emitting galaxies. This requires the detection of emission-lines sources in 3D, as these sources do not have counterparts in the white-light image. There are a number of tools available, like CubEx (Cantalupo et al., in prep.) and LSDCat (Herenz & Wisotzki, 2017), that are specifically designed for MUSE data. The CubEx detection algorithm is based on finding and connecting 3D pixels above a certain S/N threshold. In this case, great emphasis is placed on the identification afterwards in
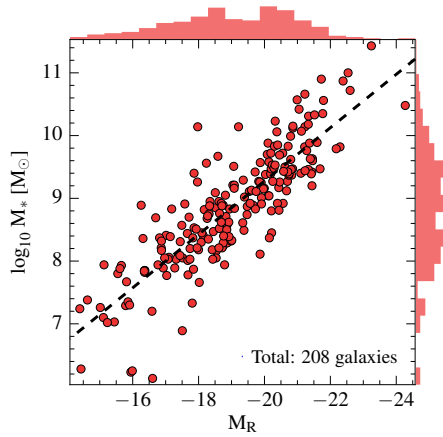
Figure 5.5: Galaxy stellar mass as a function of Cousins *R* broadband magnitude. The histograms at the top and on the right show the individual distributions of *R*-band magnitude and stellar mass, respectively. The galaxies exhibit a positive correlation between the stellar mass and the brightness in the *R*-band: the best-fitting relation (equation 5.1) is shown by the black, dashed line.

constructing a sample of objects that are physically real. The LSDCat package instead takes a matched filtering approach, where the data cube is first convolved with the expected 3D signal of a compact emission line before 3D pixels above a certain S/N threshold are detected and grouped into objects.

5.2.4 Derivation of galaxy properties

Stellar mass and *R*-band magnitude

To estimate the stellar masses of the galaxies, we use the FAST code (v1.0; Kriek et al., 2009), which fits stellar population synthesis (SPS) templates to a set of photometric flux values. Since for the majority of the QSO fields, there is not sufficient ancillary photometric data available[3], we calculate for every galaxy the flux in a number of pseudo filters from the MUSE data. We use a set of 11 adjacent boxcar filters, with a width of 400 Å each and spanning the wavelength range from 4800 Å to 9200 Å. We calculate the filter flux by convolving the 1D galaxy spectrum – the same one as used for the redshift determination with MARZ – with a boxcar function centred at $\lambda = 5000, 5400, \ldots$ Å. As the models only fit the continuum, we mask bright emission lines by excluding a velocity range of ±200 km/s around emission lines detected with S/N > 1 (and ±500 km/s around lines with S/N > 3) and interpolating the continuum, after smoothing it by a low-order spline function, across the gaps. Since the CUBESHARP algorithm used for the sky subtraction is designed to conserve the continuum flux, the boxcar filter fluxes are not affected by any sky

---

[3]Some of the QSO fields do have HST imaging, but in a limited number of filters.
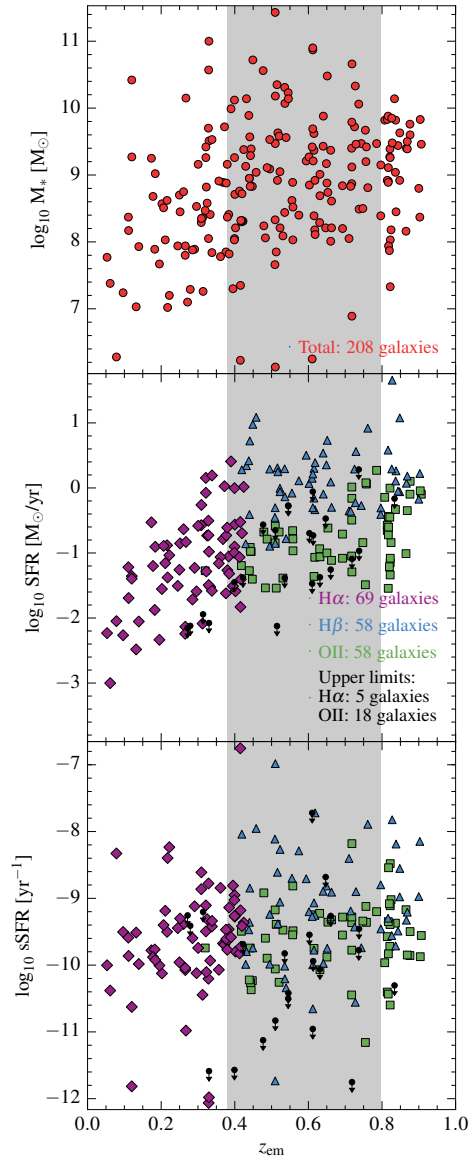
Figure 5.6: Galaxy stellar mass (top panel), SFR (middle panel) and specific SFR (= *SFR/M⋆*; bottom panel) as a function of emission redshift. While the top panel shows the full sample, the middle and bottom panels only show galaxies for which we could obtain an estimate of the SFR, derived from the Hα (purple diamonds), Hβ (blue triangles) or OII (green squares) emission-line flux. The black symbols indicate upper limits. The grey shading indicates the redshift range in which we study the dependence of the OVI absorption strength on various galaxy properties, which we select in order to reduce the correlation between the absorption strength and properties other than the one under consideration (see Section 5.4.1 for details).

line residuals. FAST then uses χ^2 minimalization to determine the best-fitting spectrum from a grid of SPS template spectra. We use the SPS models from Bruzual & Charlot (2003), assuming a Chabrier (2003) stellar initial mass function (IMF) from 0.1 – 100 $M_\odot$, an exponentially declining star formation history with characteristic timescale τ and a Calzetti et al. (2000) dust law. The grid of model spectra is constructed for τ varying between $10^{8.5}$ yr and 10^{11} yr in steps of 0.5 dex, the age of the stellar population varying between 10^7 yr and 10^{10} yr in steps of 0.2 dex, the visual extinction varying between $A_V = 0$ mag and $A_V = 3$ mag in steps of 0.1 mag and adopting values for the metallicity of $Z = 0.004, 0.008, 0.02, 0.05$ (where Z refers to the mass fraction of metals).

The histogram on the right side of Fig. 5.5 shows the distribution of best-fitting stellar masses for the total sample of 208 galaxies, while the upper panel of Fig. 5.6 shows the stellar mass as a function of redshift. The sample has a median stellar mass of $M_* = 10^{8.9}$ $M_\odot$, with a standard deviation of 0.9 dex. Hence, the majority of the galaxies have a stellar mass $< 0.1 M^*$, where $M^* \approx 10^{10.7-11.0}$ $M_\odot$ is the characteristic turnover mass of the galaxy stellar mass function at $z < 1$ (see e.g. Baldry et al., 2012; Moustakas et al., 2013; Muzzin et al., 2013). The galaxies in the sample have much lower masses than the galaxy used in other quasar absorption-line studies such as the COS-Halos survey (Tumlinson et al., 2013; Werk et al., 2013). Even compared to the $z < 1$ CGM studies by Bordoloi et al. (2014, i.e. the COS-Dwarfs survey) and Liang & Chen (2014), which are specifically focused on low-mass galaxies, our sample contains a factor of $\approx 2 - 10$ more galaxies with $M_* < 10^9$ $M_\odot$. The typical mass of our galaxy sample is also significantly lower than the mass of the Lyman Break Galaxies studied in the Keck Baryonic Structure Survey (KBSS) at $z \sim 2 - 3$ (Rudie et al., 2012; Turner et al., 2014), which have $M_* \sim 10^{10}$ $M_\odot$.

The stellar mass of the galaxies is positively correlated with their brightness, as measured with the Cousins R broadband magnitude M_R (as shown in Fig. 5.5). We calculate M_R by constructing a pseudo-broadband image from the MUSE data cube using the Cousins R filter transmission curve, and running SEXTRACTOR with the same parameters as on the white-light image. The magnitude zeropoint is derived from the magnitudes of objects in the fields that have a known brightness. We apply a K-correction to each galaxy magnitude, assuming an Sab galaxy type. We find that the best-fitting relation between M_* and M_R is

$$\log_{10} \frac{M_*}{M_\odot} = -0.43 \log_{10} M_R + 0.77, \tag{5.1}$$

where the values of the two free parameters have been obtained using least square fitting. This relation is shown by the black, dashed line in Fig. 5.5.

For each galaxy, we estimate the halo mass and halo virial radius, defined as the mass and radius of a spherical region within which the mean density is equal to 200 times the critical density of the Universe, from its stellar mass and redshift, using the abundance matching relation from Moster et al. (2013). The sample has a median halo mass of $M_{vir} = 10^{11.1}$ $M_\odot$ (with a standard deviation of 0.6 dex) and a median virial radius of $R_{vir} = 86$ pkpc (with a standard deviation of 0.2 dex). We note that for satellite galaxies the Moster et al. (2013) relation is actually not applicable. For satellites, the halo mass derived from abundance matching is a poor estimate of the
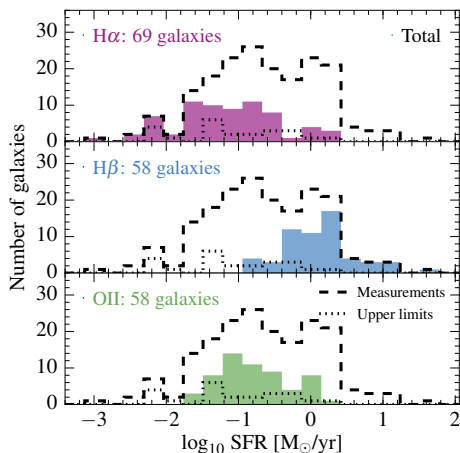
Figure 5.7: The distribution of SFRs for the 185 out of 208 galaxies with an estimate of their SFR, from either the Hα (purple; top panel), Hβ (blue; middle panel) or O$\textsc{ii}$ (green; bottom panel) emission-line flux. The total distribution (dashed) and distribution of upper limits (dotted) are shown in black (all panels). Galaxies with Hα-based SFR estimates mainly populate the low end of the distribution, as they are restricted to low redshifts ($z_{em} < 0.42$), while galaxies with Hβ-based SFRs (by construction) mainly populate the high end.

current current halo mass, but will be closer the maximum past halo mass (typically reached at the time of infall on to a larger halo), as the mass, especially in the outer regions, is reduced due to tidal stripping. Hence, for $\approx$ 50% of the galaxies, which have a neighbouring galaxy within the MUSE FoV that resides within a LOS velocity difference of $|\Delta v| = 300$ km/s, we are likely to underestimate the halo mass.

Star formation rate

We use the emission-line fluxes of the Balmer lines and O$\textsc{ii}$ to derive an estimate of the SFR of the galaxies. For galaxies at $z_{em} \lesssim 0.4$, we can estimate the SFR from the luminosity of the Hα line ($L_{H\alpha}$), using the relation from Kennicutt (1998),

$$\frac{SFR}{M_\odot \, yr^{-1}} = 4.8 \times 10^{-42} \frac{L_{H\alpha}}{erg \, s^{-1}}. \tag{5.2}$$

We have decreased the amplitude of the relation by a factor of 1.65 with respect to the original value used by Kennicutt (1998), to account for the fact that we adopt a Chabrier IMF rather than a Salpeter (1955) IMF. We require the Hα emission line to be detected with at least S/N = 3. Otherwise, we use SFR estimators based on Hβ or O$\textsc{ii}$ (see below).

We correct the Hα emission-line flux for dust extinction by using the flux ratio of the Hα and Hβ Balmer lines. By comparing Hα/Hβ to its intrinsic value of 2.85, which corresponds to Case B recombination at a temperature of $T \sim 10^4$ K and electron densities of $n_e \sim 10^2 - 10^4$ cm^{-3} (Osterbrock & Ferland, 2006), we derive
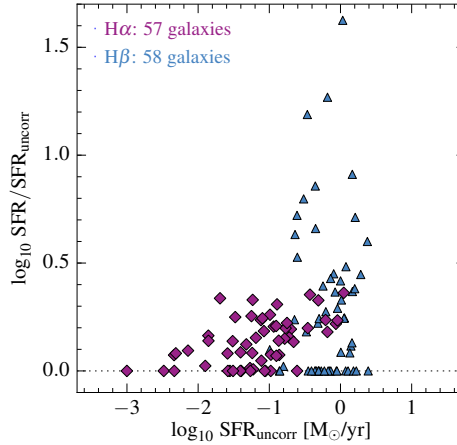
Figure 5.8: The size of the dust correction as a function of the uncorrected SFR for the 115 galaxies for which the Hα flux (purple) or the Hβ flux (blue) could be corrected for dust extinction (using the Hα/Hβ and Hβ/Hγ ratios, respectively). The largest dust corrections are generally associated with the galaxies with the highest uncorrected SFRs.

a correction for the Hα flux, assuming a Cardelli et al. (1989) reddening curve. As for Hα, we require the Hβ line to be detected with at least S/N = 3 for performing the dust correction. Otherwise, the SFR is calculated using the uncorrected Hα flux.

If Hα is not detected with S/N > 3, for example if it falls in a spectral region with significant sky line residuals or if the galaxy redshift is too high for Hα to be detected with MUSE, we use Hβ to calculate the SFR, under the condition that we can correct the line flux for dust extinction using the Hβ/Hγ ratio. This requires that both Hβ and Hγ are detected with S/N > 3. We then convert the corrected Hβ flux into an estimate of the SFR using equation (5.2), making use of the known intrinsic ratio between the Hα and Hβ flux.

Finally, if the SFR cannot be estimated from the Hα line or the dust-corrected Hβ line, we estimate it from the OII luminosity (L_{OII}) using the relation from Kewley et al. (2004),

$$\frac{SFR}{\mathrm{M_\odot \, yr^{-1}}} = 4.0 \times 10^{-42} \frac{L_{\mathrm{OII}}}{\mathrm{erg \, s^{-1}}},\qquad(5.3)$$

which has been adjusted from a Salpeter to a Chabrier IMF. We note that this relation does not take into account the metallicity variation between galaxies. As before, we require $S/N > 3$ for the total emission-line flux of the OII doublet.

For the galaxies with an OII-based SFR, we do not perform a dust correction. These galaxies lack S/N = 3 detections of Hβ and Hγ (otherwise we would have derived the SFR from Hβ), so that this would require using Hδ or higher-order Balmer lines (the use of Hβ and Hγ is not possible for this subset of galaxies). Not only is the emission component of Hδ expected to be a factor of ≈ 11 (≈ 4) weaker than that of Hα (Hβ), but the Balmer absorption originating from stellar

atmospheres is also strongest at the Hδ line. This causes Hδ to be rarely detected with a high significance. Furthermore, the intrinsic weakness of the line makes the fit to the absorption component performed by PLATEFIT highly uncertain.

For galaxies without S/N > 3 detections of Hα, Hβ (in combination with Hγ) or OII, which corresponds to $\approx$ 11% of the sample, we are not able to obtain a reliable estimate of the SFR. For these galaxies, we use the PLATEFIT error on the Hα (for z_{em} < 0.42) or OII (for z_{em} > 0.42) line flux to derive a 3σ upper limit on the SFR. For one galaxy (at z_{em} = 0.51, with the redshift estimated from the CaII H and K lines), the PLATEFIT fit in the emission-line regions failed and therefore did not return a reliable estimate of the OII line flux error. In this case, we derive a 3σ upper limit on the SFR by calculating the 3σ upper limit on the flux in the object spectrum in a 20 Å region around the OII wavelength (and converting using equation 5.3). We exclude the galaxies with SFR upper limits from the sample when we explore the CGM OVI absorption for different galaxy samples split according to their SFR. However, we confirm that if we do include them, either by considering the 3σ upper limits on the SFR as the actual values or by including them in the sample containing the lowest SFRs, our conclusions remain unchanged. For the rest of the absorption analysis presented in this work, we do include the whole sample of galaxies.

Fig. 5.7 shows the distribution of the SFRs (total: black, dashed; excluding upper limits), which for 69 galaxies has been obtained from the Hα flux (purple), for 58 from the Hβ flux (blue), and for 58 from the OII flux (green). The distribution of upper limits is shown by the black, dotted line. While the Hα sample mainly populates the lower end of the SFR distribution (median SFR = 0.069 $M_\odot$ yr^{-1}), due to their restriction to z < 0.42, the Hβ sample by construction mainly populates the upper end of the distribution (median SFR = 1.3 $M_\odot$ yr^{-1}). The median of the OII sample, SFR = 0.14 $M_\odot$ yr^{-1}, is close to the median of the total sample, SFR = 0.21 $M_\odot$ yr^{-1}. Together, these samples exhibit a common trend of SFR increasing with increasing redshift, as shown in the middle panel of Fig. 5.6. The specific SFR (sSFR; = SFR/M_*) is approximately constant as a function of redshift (bottom panel). The upper limits on the SFR and sSFR, as derived from the upper limit on the Hα or OII flux, are shown in black in this figure.

Fig. 5.8 shows the size of the dust correction as a function of the uncorrected SFR, for the 115 galaxies for which we could perform a dust correction using either the Hα/Hβ (purple) or the Hβ/Hγ (blue) ratio. The median dust correction is 0.14 dex, with a median of 0.14 dex for the Hα/Hβ-based corrections and 0.20 dex for the Hβ/Hγ-based corrections. The largest dust corrections are applied to the highest (uncorrected) SFRs, with corrections of up to 1.6 dex. For 35 galaxies we find a Balmer line ratio that is smaller than the intrinsic one, possibly as a result of uncertainties in the line fluxes. As this would correspond to a 'negative' dust correction, which would be unphysical, we assume the dust correction in these cases to be zero.

For a fraction of the galaxies in our sample, the emission spectrum is expected to be dominated by an AGN component. In that case, the Hα, Hβ or OII emission-line flux is a poor indicator of the SFR. Kauffmann et al. (2003) showed that typically a few per cent of the galaxies with M_* = 10^{10-11} $M_\odot$ shows signs of optical AGN activity, but that this percentage is likely to decrease towards lower stellar masses.

For the 26 galaxies for which we detect O$\textsc{iii}$ $\lambda5007$, Hβ, N$\textsc{ii}$ $\lambda6583$ and Hα with S/N > 3, we estimate their locations in the Baldwin, Phillips, & Terlevich (BPT; 1981) diagram based on the O$\textsc{iii}$ 5007/Hβ and N$\textsc{ii}$ 6583/Hα emission-line ratios. However, we find no galaxies that satisfy the AGN classification, either according to the criterion from Kewley et al. (2001) or the criterion from Kauffmann et al. (2003). The individual line flux ratios span ranges of O$\textsc{iii}$ 5007/Hβ = 0.4 – 6.2 and N$\textsc{ii}$ 6583/Hα = 0.02 – 0.35. As we could only derive the BPT classification for $\approx$ 13% of the galaxies, we do not rule out that some fraction of the rest of the sample harbours optical AGN.

Uncertainties on galaxy properties

We note that estimating the statistical and systematic uncertainties on the stellar masses, SFRs and dust corrections is still work in progress. Once we have derived the errors on the boxcar filter fluxes, we can obtain the statistical uncertainties on the stellar masses from FAST, which performs a Monte Carlo simulation by running the fitting procedure 500 times while varying the input flux values according to their errors. Comparing our derived stellar masses with already published values in the fields overlapping with other surveys, can give us an idea of the systematic errors on the stellar masses. Statistical uncertainties on the SFRs and dust corrections can be derived similarly to those on the stellar masses, by using Monte Carlo methods to propagate the errors on the emission-line fluxes. Comparing the SFRs using different tracers for the galaxies that either have both significant Hα and O$\textsc{ii}$ or both Hβ and O$\textsc{ii}$ emission lines, will give an indication of the systematic errors on the SFRs. In future work, we also aim to explore the effect of neglecting the dust corrections for galaxies for which we found these corrections to be 'negative'.

5.3 Absorption data analysis

We study the abundances of H$\textsc{i}$, C$\textsc{iii}$ and O$\textsc{vi}$ in the CGM of the galaxies found in our blind search with MUSE, by analysing the absorption signal in the QSO spectra. Instead of identifying and fitting absorption lines associated with individual galaxies, we take a statistical approach by measuring the median pixel optical depth for a sample of galaxies as a function of distance to those galaxies. This method was earlier applied to the CGM of $z \sim 2$ star-forming galaxies by Rakic et al. (2012) for H$\textsc{i}$ and by Turner et al. (2014) for H$\textsc{i}$ and metals. The method is independent of the specific identification of galaxy-absorber pairs and the details of modelling the absorption systems, and thus provides a simple and objective way of studying the ion abundance around the 'average' galaxy. In this section, we first describe the properties of the COS spectra and their analysis using the pixel optical depth method. Then, we explain how we construct galaxy-centred profiles of the median optical depth as a function of velocity along the LOS for a given sample of galaxies.

5.3.1 COS spectra

We obtain the 16 HST/COS spectra in reduced form from the HST Spectroscopic Legacy Archive[4]. This archive provides science-grade reduced spectra combining all COS data that is available for each target. The reduction pipeline uses the individual exposure files that were processed by CALCOS (v3.1.1), aligns them in velocity space and coadds the count rates per pixel. The velocity alignment is done by cross-correlating the positions of strong Galactic absorption lines (e.g. SiII, CII and AlII), thereby correcting for the small offsets in the wavelength solution between individual exposures. We take the separate coadded spectra of the medium-resolution ($R \approx$ 18,000, FWHM $\approx$ 16 km/s) G130M and G160M gratings and splice them together at the wavelength in the overlap region where the S/N per pixel becomes equal (typically around λ = 1425 Å). The final spectrum covers a wavelength range from $\approx$ 1150 Å to $\approx$ 1800 Å. The uncertainty in the COS wavelength calibration (even after aligning the individual exposures) is estimated to be $\approx 20 - 30$ km/s (e.g. Savage et al., 2011; Tumlinson et al., 2011; Wakker et al., 2015), due to both velocity shifts that vary with wavelength and the uncertainty in the zero-point velocity. For our analysis, we keep the original pixel scale: hence, the final spectrum has a dispersion of 0.010 Å per pixel in the G130M part and 0.012 Å per pixel in the G130M part. Due to differences in the total exposure time and the brightness of the QSO, the spectra show a large variation in S/N. Typically, S/N $\approx 15 - 35$ per resolution element at λ = 1250 Å in G130M and S/N $\approx 10 - 20$ per resolution element at λ = 1650 Å in G160M (see Table 5.1). We normalize each spectrum by the unabsorbed quasar continuum, which we estimate by fitting smooth low-order polynomials through a manually selected set of points in regions without absorption.

5.3.2 Pixel optical depth recovery

We measure the strength of HI and metal absorption in the COS spectra using the pixel optical depth method, applying the routine PODPY[5] developed by Turner et al. (2014), which is based on the method from Aguirre et al. (2002) and earlier works (Cowie & Songaila, 1998; Ellison et al., 2000; Schaye et al., 2000). Here, we only highlight the most important aspects of the method and refer the reader to Appendix A of Turner et al. (2014) for a more detailed description. Note that while the pixel optical depth method was originally developed to study absorption in Keck/HIRES and VLT/UVES spectra at $z \gtrsim 2$, we apply the method to COS spectra to study absorption at $z < 1$. Since the density of Lyman series lines (which are a source of contamination for other transitions) is much lower at low than at high redshifts, we do not restrict our analysis to the absorption overlapping with the QSO Lyα forest (or the Lyβ forest in the case of OvI) as in previous works. Furthermore, since COS spectra have significantly lower S/N than HIRES or UVES spectra, we run PODPY with the significance parameter set to $N_\sigma = 1$ (rather than $N_\sigma = 3$).

---

[4]http://archive.stsci.edu/hst/spectral_legacy
[5]This code is available at http://github.com/turnerm/podpy.

For each pixel, we obtain the optical depth τ from the continuum-normalized flux F as

$$\tau = -\ln(F), \tag{5.4}$$

where we set the optical depth to $\tau = 10^{-6}$ for $F > 1$. We will denote the optical depth of an ion species Z with rest-frame wavelength λ_0 (using the strongest transition in the case of a multiplet) at pixel wavelength $\lambda = \lambda_0(1 + z)$ by $\tau_Z(z)$. To infer an estimate of the 'true' optical depth from the observed spectrum, which is affected by noise, saturation and contamination, a number of corrections is applied. For H I, saturated absorption in the Lyα transition, where saturation is defined as $F(\lambda) < N_\sigma \sigma(\lambda)$, with $\sigma(\lambda)$ the continuum-normalized noise array, is corrected using the optical depth of the higher-order Lyman transitions (i.e. Lyβ and higher): we take the minimum optical depth, scaled to that of Lyα, of 16 higher-order pixels at the corresponding z, selecting only those pixels that are significantly offset from the continuum (by $> N_\sigma \sigma(\lambda)$) and that are not saturated themselves. If a correction is not possible, we set the Lyα optical depth to 10^4, so that the pixel does not affect the measured median. Furthermore, we use the higher-order transitions to identify any Lyα pixels (saturated or non-saturated) that are contaminated by metal absorption, by comparing the observed optical depth at each transition to the one expected based on Lyα. We discard the contaminated pixels from the analysis.

For metal ions, we correct for contamination by H I absorption by subtracting the optical depth contributions from 5 higher-order Lyman transitions[6], scaled from the recovered Lyα optical depth. For example, correcting C III absorption at $z_{\mathrm{C III}}$ for contamination from H I Lyβ involves using the recovered H I Lyα optical depth at

$$z_{\mathrm{H I}} = \frac{\lambda_0^{\mathrm{C III}}}{\lambda_0^{\mathrm{Ly}\beta}}(1 + z_{\mathrm{C III}}) - 1, \tag{5.5}$$

where $\lambda_0^{\mathrm{C III}} = 977.02$ Å and $\lambda_0^{\mathrm{Ly}\beta} = 1025.72$ Å. Note that due to the limited wavelength range covered by COS, we can only correct for H I contamination at $z_{\mathrm{H I}} < 0.48$, which for O VI and C III corresponds to redshifts of $z_{\mathrm{O VI}} < 0.47$ and $z_{\mathrm{C III}} < 0.55$, respectively. In the case of saturated metal pixels, we either do not apply an H I contamination correction, or we discard the pixels entirely, if the saturated absorption can be fully attributed to overlapping higher-order H I components.

Finally, for O VI, we make use of the information from the two doublet transitions to further refine the correction for contamination. After performing the H I subtraction for both doublet components, we take $\tau_{\mathrm{O VI}}$ to be the minimum optical depth of the two components, where the optical depth of the weaker component has been scaled to that of the stronger one. However, in the presence of noise taking the minimum at each pixel will cause the optical depths to be biased low. We therefore only use the scaled optical depth from the weaker component as the final recovered optical depth if it is significantly lower (i.e. taking into account the $N_\sigma \sigma(\lambda)$ noise level at the wavelengths of both transitions) than that of the stronger component.

---

[6]Before submitting this work for publication, we will explore the impact of using a lower or higher number of Lyman transitions for the contamination correction.

5.3.3   Construction of median optical depth profiles

Using the recovered pixel optical depth spectra, we measure the strength of the CGM absorption signal for a given sample of galaxies as follows. We construct profiles of the median pixel optical depth as a function of the absolute LOS velocity, v_{LOS}, from the galaxies. We make the profiles by binning the spectral pixels according to their velocity separation from each galaxy redshift z_{em}, and calculating the median $\log_{10} \tau_Z$ per v_{LOS} interval. For example, for $v_{\mathrm{LOS}} = [v_1, v_2]$, we select all pixels corresponding to ion redshifts $z_Z = \lambda/\lambda_0 - 1$ in the range

$$\frac{v_1}{c}(1 + z_{\mathrm{em}}) + z_{\mathrm{em}} < z_Z < \frac{v_2}{c}(1 + z_{\mathrm{em}}) + z_{\mathrm{em}}, \tag{5.6}$$

where c is the speed of light[7]. Note that we combine the selected pixels from all galaxies in the sample before taking the median. However, to avoid contamination from unrelated absorption and QSO proximity effects, we exclude the pixels from the following regions:

- Redshifts less than 3000 km/s below the QSO redshift, $z > z_{\mathrm{QSO}} - \frac{3000\,\mathrm{km/s}}{c}(1 + z_{\mathrm{QSO}})$;

- Wavelengths contaminated by HI Lyα emission and absorption damping wings from the Milky Way, 1212 Å $< \lambda <$ 1220 Å;

- Wavelengths contaminated by OI emission from the Milky Way, 1301 Å $< \lambda <$ 1307 Å;

- The region at $\lambda < 1280$ Å in the TEX 0206-048 spectrum and at $\lambda < 1220$ Å in the Q 1354+048 spectrum, where (most of) the flux is absorbed due to Lyman-limit systems at $z = 0.390$ and at $z = 0.329$, respectively.

While including all galaxies identified in the MUSE fields yields the LOS absorption profile for our total sample (Section 5.4.1), computing the absorption profiles for different subsamples of galaxies enables us to study the dependence of the absorption strength on various galaxy properties. In Sections 5.4.1 and 5.4.1, we divide the sample according to the galaxy impact parameter to study the HI, OVI and CIII absorption strength as a function of (normalized) transverse distance from the galaxies. We also explore the dependence of the HI and OVI absorption strength on galaxy redshift (Section 5.4.2), and the dependence of the OVI absorption strength on galaxy stellar mass and SFR (Sections 5.4.3 and 5.4.4).

5.4   Results

In this section, we present the results of our measurements of the HI, OVI and CIII abundances around the galaxies blindly selected with MUSE. The wavelength coverage of COS enables us to measure the absorption strength of HI Lyα out to redshifts

---

[7]We acknowledge the fact that for $v \sim 10{,}000$ km/s, the assumption of $v \ll c$ underlying the equation (5.6) is no longer valid and we should use the more general formula for relativistic velocities. We will address this issue for our future publication.

of 0.48, while the absorption of O$\textsc{vi}$ and C$\textsc{iii}$ is observable at $0.10 < z < 0.74$ and $0.16 < z < 0.84$, respectively. These redshift ranges are indicated by the blue bars in Fig. 5.1. In addition to O$\textsc{vi}$ and C$\textsc{iii}$, we also examined the absorption of the metal ion transitions Si$\textsc{ii}$ (1260.42 Å; $z < 0.43$), C$\textsc{ii}$ (1334.53 Å; $z < 0.35$), Si$\textsc{iii}$ ($z < 0.49$), Si$\textsc{iv}$ ($z < 0.29$), C$\textsc{iv}$ ($z < 0.16$) and N$\textsc{v}$ ($z < 0.45$), but except for N$\textsc{v}$, we found no significant absorption signal (see Appendix 5.A).

5.4.1 Full sample

Dependence on LOS velocity

Fig. 5.9 shows the absorption strength of H$\textsc{i}$, O$\textsc{vi}$ and C$\textsc{iii}$ for the full sample of galaxies (squares). In the left-hand panels, we plot the median $\log_{10} \tau_Z$ as a function of LOS velocity from the galaxies. The axis at the top indicates the corresponding absolute LOS Hubble distance in the case of pure Hubble flow,

$$d_{\mathrm{LOS}} = \frac{v_{\mathrm{LOS}}}{H(z)}, \tag{5.7}$$

where $H(z)$ is the Hubble parameter at redshift z. We assume $z = 0.5$, which is close to the median redshift of the sample. For both H$\textsc{i}$ and the metal ions, the strength of the absorption (red squares) decreases as the LOS velocity from the galaxies increases. We find that the absorption remains enhanced with respect to the absorption in random regions (red, dashed lines) out to $v_{\mathrm{LOS}} \sim 100$ km/s ($d_{\mathrm{LOS}} \sim 1$ pMpc).

The optical depth of random regions, which can be considered as the detection limit (τ_{lim}), is calculated as the median $\log_{10} \tau_Z$ of all pixels at $15{,}000 < v_{\mathrm{LOS}} < 25{,}000$ km/s from the galaxies contributing to the corresponding absorption profile, which are 106, 171 and 200[8] galaxies in total for H$\textsc{i}$, O$\textsc{vi}$ and C$\textsc{iii}$, respectively. In this way, τ_{lim} is estimated from regions that are sufficiently far away from the targeted galaxies, but still mimic the specific redshift distribution of the galaxy sample. This is necessary because the sampling of redshift space in our survey is non-uniform, as a result of the differences in the redshift path length below z_{QSO} and the exposure time of the MUSE observation between different QSO targets.

We estimate the uncertainties in the median optical depth values by dividing the total absorption distance, ΔX (Bahcall & Peebles, 1969), of the 15 QSO spectra into chunks and bootstrap resampling the chunks 1000 times. For ion Z, the absorption distance per QSO spectrum is given by

$$\Delta X_Z = \int_{z_{\mathrm{min}}}^{z_{\mathrm{max}}} \frac{(1+z)^2}{\sqrt{\Omega_{\mathrm{M}}(1+z)^3 + \Omega_{\Lambda}}} \, \mathrm{d}z, \tag{5.8}$$

with integration limits $z_{\mathrm{min}} = \max(z_{Z,\mathrm{min}}, 0)$ and $z_{\mathrm{max}} = \min(z_{Z,\mathrm{max}}, z_{\mathrm{QSO}})$, where $z_{Z,\mathrm{min}}$ and $z_{Z,\mathrm{max}}$ are the minimum and maximum ion redshifts covered by COS.

---

[8]Note that since we consider absorption up to $v_{\mathrm{LOS}} = 10{,}000$ km/s from the galaxy redshift, galaxies above or below the ion redshift range covered by COS can contribute to the absorption profile (as long as they are at least 3000 km/s below the redshift of the QSO).
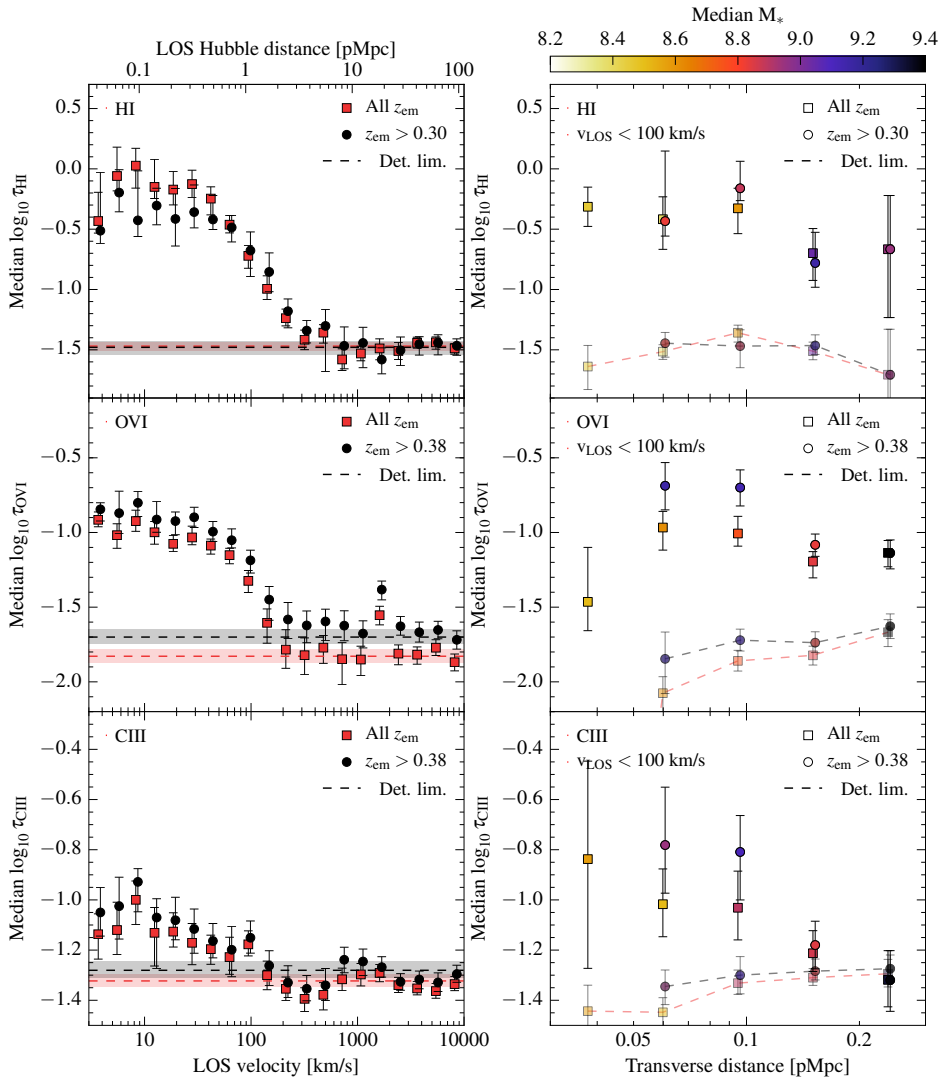
Figure 5.9: The median pixel optical depth of H I (top), O VI (middle) and C III (bottom) as a function of LOS velocity (left) and transverse distance (right). While the squares show the absorption signal for the full sample of galaxies, the circles (which, for clarity, have been offset horizontally by 0.02 dex and 0.006 dex in the left- and right-hand panels, respectively) show the signal for galaxies in a restricted redshift range. Along the LOS direction, the median $\log_{10} \tau_Z$ is calculated in 20 logarithmic bins between $v_{LOS} = 3$ km/s and $v_{LOS} = 10{,}000$ km/s, where the corresponding absolute LOS Hubble distance, assuming $z = 0.5$ and pure Hubble flow, is indicated at the top. The horizontal dashed lines show the detection limit, calculated as the median $\log_{10} \tau_Z$ at $15{,}000 < v_{LOS} < 25{,}000$ km/s from the galaxies contributing to the profile of the respective colour. Along the transverse direction, the median $\log_{10} \tau_Z$ is calculated, using only pixels at $v_{LOS} < 100$ km/s, in 5 logarithmic bins between $d_{trans} = 30$ pkpc and $d_{trans} = 300$ pkpc, where we only show bins containing at least three galaxies. The points are colour-coded by the median galaxy stellar mass in each bin. The detection limit is calculated separately for each transverse distance bin, and shown by the light-coloured symbols connected by dashed lines. In all panels, the error bars (and shaded regions) show the 1σ confidence interval on the median optical depth.

The total ion absorption distances covered by the 15 QSO spectra are $\Delta X_{\text{HI}} = 10.6$, $\Delta X_{\text{OVI}} = 14.9$ and $\Delta X_{\text{CIII}} = 15.8$. We divide these into $N_{\text{chunk}} = 353$, 497 and 528 chunks, respectively, in order to have a chunk size of $\Delta X \approx 0.03$, which is about 3 times larger than the velocity extent of the largest galaxy group[9] identified in our fields. This ensures that different chunks are independent. In each bootstrap realization, we select N_{chunk} chunks with replacement, take the galaxies with redshifts within the selected chunks, and calculate the median absorption optical depth per v_{LOS} interval. The error bars on the points and the shaded regions on the dashed lines in Fig. 5.9 indicate the 16th to 84th percentile ranges of the resulting distributions.

To assess the significance of the enhancement in the absorption with respect to the detection limit, we calculate the fraction, f_{high}, of bootstrap realizations for which $\tau^i_{\text{lim}} > \tau^i_{\text{Z}}$, where i denotes the ith bootstrap iteration. We refer to $1 - 2f_{\text{high}}$ as the confidence level of the absorption enhancement. For HI and OVI, we find a confidence level of $> 95\%$ (2σ)[10] out to $v_{\text{LOS}} = 260$ km/s and $v_{\text{LOS}} = 115$ km/s[11], respectively. These LOS velocities correspond to LOS Hubble distances of $d_{\text{LOS}} = 3.2$ pMpc and $d_{\text{LOS}} = 1.3$ pMpc at the median redshifts of the galaxies contributing to the absorption, $z^{\text{HI}}_{\text{med}} = 0.36$ and $z^{\text{OVI}}_{\text{med}} = 0.45$. For CIII, the dynamic range of optical depths is smaller, and we find a $> 68\%$ (1σ) confidence level out to $v_{\text{LOS}} = 115$ km/s ($d_{\text{LOS}} = 1.3$ pMpc at $z^{\text{CIII}}_{\text{med}} = 0.53$).

Studies of the optical depth around galaxies from the KBSS (HI: Rakic et al. 2012; HI and metal ions: Turner et al. 2014) have suggested that the extent of the absorption signal along the LOS direction depends on the peculiar velocities of the absorbing gas, related to infall, outflows or virial motions, rather than errors in the galaxy redshifts. Using mock spectra generated from the EAGLE simulations (Schaye et al., 2015; Crain et al., 2015), Turner et al. (2017) showed that this is indeed the case: while the presence of redshift errors somewhat reduces the optical depth profile at small LOS velocities, the velocity extent of the absorption enhancement is governed by peculiar velocities. Furthermore, Turner et al. (2017) explored the radial velocities of the gas traced by HI (and metal ions CIV and SiIV) and showed that this gas is mostly infalling, where the gas velocities are sensitive to the host halo mass (and insensitive to changes in the strength of the stellar feedback). This suggests that the velocity scale of the drop in the optical depth profile is related to the typical velocity of infalling gas, which is likely close to the circular velocity (v_{circ}) of the halo. For our sample, the median circular velocity is $v_{\text{circ}} = 81$ km/s. While this is a factor of $\approx 2 - 4$ smaller than the maximum LOS velocity extent of the detected enhancement in the HI and OVI absorption, we note that our sample contains a range of stellar masses (with a standard deviation of 0.9 dex about the

---

[9]We define a galaxy group as a set of galaxies that have, when ordered by redshift, a velocity difference of less than 300 km/s between subsequent galaxies. We do not impose a constraint on their transverse distance separation, as the size of the MUSE FoV is $\lesssim 500$ pkpc.

[10]To indicate the significance and extent of the absorption enhancement, we choose the 95% and 68% confidence levels as characteristic values. However, at LOS velocities (and transverse distances) smaller than the indicated maximum extent, the confidence levels for HI and OVI reach 100%.

[11]There is also a significant offset of τ_{OVI} from τ_{lim} at $v_{\text{LOS}} \approx 1600$ km/s. However, we attribute this to a combination of residual contamination from HI Lyβ and the weak OVI doublet component (despite the corrections performed during the optical depth recovery).

median), which are also associated to a range of host halo masses, even at a fixed stellar mass. Since a 10 times higher halo mass corresponds to a 2.2 times higher circular velocity, the contribution from the most massive halos in the sample likely extends the absorption signal to $v_{LOS} \gg 81$ km/s. We do note that $v \approx 80$ km/s seems to be similar to the velocity scale at which the optical depth profiles start to fall off from the roughly flat trend at small v_{LOS} towards the detection limit. For H I and O VI, we estimate the velocity scales of the drop to be $v_{drop} \approx 50$ km/s and $v_{drop} \approx 80$ km/s, respectively. For C III, it is difficult to see, but the profile shape seems to be consistent with that of O VI. Fitting, for example, a sigmoid function to the profiles would yield a more accurate estimate of the typical drop-off velocity, which we plan to do in the future.

In the case of the KBSS, the redshift errors were $\approx 2 - 10$ times smaller than the typical halo circular velocity of the survey. For our study, we also need to verify that the redshift errors are sufficiently small that they do not dominate the shape of the absorption signal in Fig. 5.9. Based on MUSE observations of the Hubble Ultra Deep Field (which are somewhat deeper than our observations: nine $1' \times 1'$ fields with $t_{exp} = 10$ h and one $1' \times 1'$ field with $t_{exp} = 30$ h), the error on spectroscopic redshifts from MUSE is estimated to be $\sigma_{error} \approx 40$ km/s (Inami et al., in press). We confirm that adding random velocity offsets, assuming a Gaussian distribution with a width of 40 km/s, to the galaxy redshifts (adopting the approach from Appendix A of Rakic et al. (2012)), does not have a significant effect on the H I and O VI optical depths.

Dependence on transverse distance

In the right-hand panels of Fig. 5.9, we show the median optical depth as a function of transverse distance (d_{trans}; i.e. projected distance on the sky) from the galaxies, where we only include pixels at $v_{LOS} < 100$ km/s, in order to maximize the strength of the signal. As in the left-hand panels, the squares show the results for the total sample. In contrast to the absorption profile along the LOS direction, different transverse distance intervals contain different galaxies (according to their impact parameter to the QSO sightline), which makes each point independent. The confidence interval on the median $\log_{10} \tau_Z$, as well as τ_{lim} and corresponding confidence interval (now indicated by light-coloured symbols), is therefore calculated separately for each d_{trans} bin.

In general, for $d_{trans} > 50$ pkpc, the median H I, O VI and C III optical depths decrease as the transverse distance from the galaxies increases. A slight drop in all three profiles is seen at $d_{trans} \approx 120$ pkpc. Assessing the confidence level of the absorption enhancement with respect to the detection limit, we find enhanced H I and O VI absorption at > 95% confidence out to the largest transverse distance probed, $d_{trans} = 300$ pkpc[12]. This is roughly three times the size of the estimated median virial radius of our sample, and comparable to the estimated virial radius of the

---

[12]For the innermost d_{trans} bin of the O VI profile (containing 3 galaxies, all at $0.15 < z_{em} < 0.35$), $\log_{10} \tau_{lim} = -6$, the artificial minimum employed by the pixel optical depth method. This is potentially due to the H I contamination correction (which is especially important at low redshift), which assigns pixels $\log_{10} \tau_Z = -6$ if the the absorption can be fully accounted for by H I.

most massive galaxies in the sample. For CIII, we find a > 95% confidence level out to d_{trans} = 120 pkpc, while the 120 < d_{trans} < 190 pkpc bin has a confidence level of 84%.

The size of the MUSE FoV complicates a comparison of the extent of the absorption signal along the LOS and transverse directions, as was done for the KBSS. Studying the 2D distribution of optical depths, Rakic et al. (2012) and Turner et al. (2014) reported a significant elongation of the HI and metal absorption along the LOS direction on scales of ~ 0.1 – 1 pMpc ($\approx$ 20 – 200 km/s), as result of gas peculiar velocities smearing the signal along the LOS but not in the transverse direction. While we cannot conclude definitively that the small-scale elongation along the LOS direction is also present in our data (except for CIII perhaps), we do conclude that the median HI and OVI optical depth as a function of transverse distance starts to decrease at a distance that is ~ 10 smaller than the scale at which the optical depths fall off along the LOS direction.

Dependence on normalized transverse distance

As our sample contains a wide range of stellar masses, it might be more appropriate to consider the optical depth as a function of $d_{\mathrm{trans}}/R_{\mathrm{vir}}$, the transverse distance normalized by the virial radius, instead of d_{trans}: this likely gives a better indication of how the absorption strength varies from the inner to the outer halo. Hence, in Fig. 5.10, we show the median HI, OVI and CIII optical depth profiles in the transverse direction (squares), as in the right-hand column of Fig. 5.9, but now by binning the galaxies according to their impact parameter in units of the halo virial radius. We only show bins that contain at least three galaxies, which excludes the innermost bin (0.2 < $d_{\mathrm{trans}}/R_{\mathrm{vir}}$ < 0.4) for OVI and CIII.

The median absorption strength (of both HI and the metal ions) generally decreases as a function of $d_{\mathrm{trans}}/R_{\mathrm{vir}}$, although the median OVI optical depth seems to decrease for $d_{\mathrm{trans}}/R_{\mathrm{vir}}$ < 0.7. For all three profiles, a tentative drop, comparable to the twice the size of the estimated error on the median optical depth, is seen at $d_{\mathrm{trans}}/R_{\mathrm{vir}} \approx 1.2$. We find that that for HI and OVI, the absorption is significantly enhanced (with > 95% confidence) with respect to τ_{lim} over the whole range plotted, hence out to at least $d_{\mathrm{trans}}/R_{\mathrm{vir}}$ = 4.0. For CIII, we only find a > 95% confidence level at 0.7 < $d_{\mathrm{trans}}/R_{\mathrm{vir}}$ = 1.2, as the bin at 0.4 < $d_{\mathrm{trans}}/R_{\mathrm{vir}}$ = 0.7 has a confidence level of 94%.

Imposing a minimum emitter redshift

So far, we have presented the results for the full sample of galaxies. As we showed in Sections 5.2.3 and 5.2.4, these galaxies span a wide range of redshifts, stellar masses and SFRs. When we explore the dependence of the strength of the absorption signal on these galaxy properties (in Sections 5.4.2, 5.4.3 and 5.4.4), ideally we would keep all other properties constant while varying the property of interest. However, due to correlations between galaxy characteristics, which have a physical origin or are the result of observational bias (or a combination of both), this condition is not automatically satisfied: Fig. 5.2 shows that our sample lacks high-impact parameter galaxies at low redshift (due to the limiting physical size of the
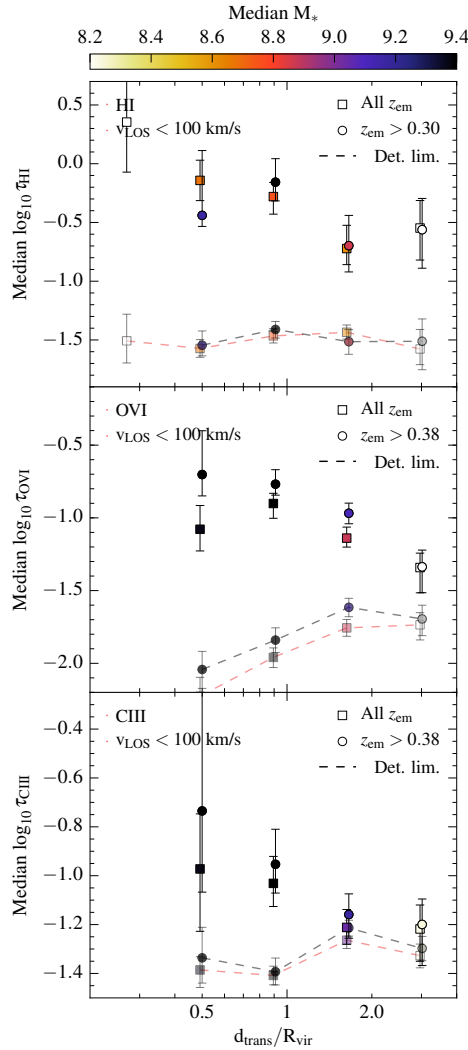
Figure 5.10: As in the right-hand column of Fig. 5.9, but showing the median pixel optical depths as a function of transverse distance normalized by the virial radius. We calculate the median $\log_{10} \tau_Z$ and τ_{lim} in 5 logarithmic bins between $d_{\mathrm{trans}}/R_{\mathrm{vir}} = 0.2$ and $d_{\mathrm{trans}}/R_{\mathrm{vir}} = 4.0$. For clarity, the points are offset horizontally from each other by 0.0075 dex. For both H I and the metal ions, the absorption strength generally decreases as a function of $d_{\mathrm{trans}}/R_{\mathrm{vir}}$ and shows a tentative drop at $d_{\mathrm{trans}}/R_{\mathrm{vir}} \approx 1.2$. For H I and O VI, the absorption is enhanced with respect to τ_{lim} at > 95% (2σ) confidence out to $d_{\mathrm{trans}}/R_{\mathrm{vir}} = 4.0$. For C III, we only find a > 95% confidence level at $0.7 < d_{\mathrm{trans}}/R_{\mathrm{vir}} = 1.2$.

MUSE FoV), and low-impact parameter galaxies at all but the lowest redshifts (due to the increasing physical size of the QSO PSF with increasing redshift). This causes galaxies at smaller impact parameters to have, on average, lower redshifts. Furthermore, stellar mass and SFR exhibit positive correlations with redshift (see Fig. 5.6), as well as with each other. When these correlations are not taken into account, a correlation between the absorption strength and the value of one property might be incorrectly interpreted as a causal relation, while the correlation is actually driven by a second property.

In the following sections, we therefore apply selection cuts to the galaxy redshifts, which largely remove the correlations of impact parameter, stellar mass and SFR with redshift, and thereby also the correlation of stellar mass and SFR with impact parameter. In Appendix 5.B, we additionally apply cuts on the stellar mass and SFR, in order to isolate the effects of varying these two properties independently. We always try to find a balance between the strictness of the cut and the number of selected galaxies, in order to maintain a reasonable sample size for each comparison. However, before we turn to an investigation of the impact of galaxy redshift, stellar mass and SFR on the absorption signal, we first revisit the relation between absorption strength and (normalized) impact parameter presented in Sections 5.4.1 and 5.4.1.

While for the full sample (squares in the right-hand panels of Fig. 5.9), the median optical depths of H$\textsc{i}$, O$\textsc{vi}$ and C$\textsc{iii}$ at $d_{\mathrm{trans}} > 50$ pkpc generally decrease with increasing transverse distance from the galaxies, this trend is not independent of redshift. The median redshift of the galaxies contributing to the signal in each impact parameter bin increases from $\approx 0.2 - 0.3$ at $d_{\mathrm{trans}} < 75$ pkpc to ≈ 0.6 at $d_{\mathrm{trans}} > 190$ pkpc in the case of O$\textsc{vi}$ and C$\textsc{iii}$, and to ≈ 0.4 in the case of H$\textsc{i}$. For O$\textsc{vi}$ and C$\textsc{iii}$, this is reflected by the (slight) increase in τ_{lim}, which is higher at higher redshifts. Even though we show in Section 5.4.2 that we do not find evidence for significant evolution of the absorption signal, the correlation between redshift and stellar mass causes also the median stellar mass of the galaxies to increase with impact parameter. As indicated by the colour coding, the median stellar mass increases from $M_* = 10^{8.4-8.5}\,\mathrm{M_\odot}$ at $d_{\mathrm{trans}} < 75$ pkpc to $M_* = 10^{9.4}\,\mathrm{M_\odot}$ at $d_{\mathrm{trans}} > 190$ pkpc (to $M_* = 10^{9.0}\,\mathrm{M_\odot}$ in the case of H$\textsc{i}$). Furthermore, the median SFR of the galaxies increases by a factor of $\approx 3 - 5$ from small to large impact parameters. The effect is particularly evident for O$\textsc{vi}$: the optical depth within $d_{\mathrm{trans}} \approx 50$ pkpc seems to be significantly lower than at $d_{\mathrm{trans}} \gtrsim 50$ pkpc, where we note that the difference in τ_{lim} has only a minor effect.

In order to minimize the effect of any stellar mass or SFR dependence on the signal, we impose a minimum redshift cut on the galaxy sample. Based on visual inspection, we find that a cut of $z_{\mathrm{em}} > 0.30$ for H$\textsc{i}$ and a cut of $z_{\mathrm{em}} > 0.38$ for O$\textsc{vi}$ and C$\textsc{iii}$ eliminates most of the correlation of impact parameter with redshift (see Fig. 5.2), and of stellar mass and SFR with redshift (see Fig. 5.6, where the shaded area marks the redshift range selected for O$\textsc{vi}$), while still maintaining a reasonable sample size[13]. As a result, when we apply these redshift cuts, the median stellar mass of the galaxies is also approximately constant across the impact parameter range.

---

[13] We adopt a lower redshift cut of $z_{\mathrm{em}} < 0.30$ for H$\textsc{i}$, as it is only observable at $z < 0.48$.

The resulting median $\log_{10} \tau_Z$ as a function of transverse distance is shown by the circles in the right-hand column of Fig. 5.9. Note that the innermost bin is not shown, as there are no galaxies at those impact parameters above the imposed redshift cut. We also show the median $\log_{10} \tau_Z$ as a function of LOS velocity (left-hand panels), where we include all galaxies in the selected subsamples (73 galaxies for H I, 116 for O VI and 150 for C III): the result for H I is similar to that of the full sample, while the O VI and C III optical depths are somewhat higher than for the full sample. This is caused by an increase of the O VI and C III optical depths within $d_{\text{trans}} \approx 120$ pkpc[14], which also results in a more steeply decreasing trend with increasing d_{trans}. The roughly constant τ_{lim} as a function of transverse distance is consistent with the fact that these different d_{trans} bins exhibit similar redshift distributions. Interestingly, the optical depth profile of H I (as well as τ_{lim}) for the $z_{\text{em}} > 0.30$ subsample is similar to that of the full sample, even though the median redshift, stellar mass and SFR increase with d_{trans} for the latter. This is perhaps due to the less stringent redshift cut imposed on H I than on the metals, or due to a lack of correlation between absorption strength and stellar mass.

Similarly to Fig. 5.9, the median redshift of the galaxies in each $d_{\text{trans}}/R_{\text{vir}}$ bin in Fig. 5.10 increases from $\approx 0.2 - 0.3$ at $d_{\text{trans}}/R_{\text{vir}} \approx 0.2$ to ≈ 0.6 at $d_{\text{trans}}/R_{\text{vir}} \approx 4.0$ (and to ≈ 0.4 in the case of H I). After imposing the minimum redshift cuts, the trend of increasing τ_{lim} with increasing $d_{\text{trans}}/R_{\text{vir}}$ becomes shallower (in the case of O VI) and the trends of decreasing O VI and C III optical depths become steeper. Unlike in Fig. 5.9, however, the redshift cut does not eliminate the correlation between stellar mass and $d_{\text{trans}}/R_{\text{vir}}$[15]. The finding that the optical depths decrease more steeply with $d_{\text{trans}}/R_{\text{vir}}$ than with d_{trans} may be caused by a slight *enhancement* of the variation in median stellar mass from low to high normalized impact parameters. For the full sample, the median stellar mass decreases from $M_* = 10^{9.4}\,\mathrm{M_\odot}$ at $d_{\text{trans}}/R_{\text{vir}} < 1.2$ to $M_* = 10^{8.2}\,\mathrm{M_\odot}$ at $d_{\text{trans}}/R_{\text{vir}} \approx 4.0$ (in the case of O VI and C III; for H I, the trend is non-monotonic). For the subsamples with the restricted redshift range (shown by the circles), the median stellar mass at small $d_{\text{trans}}/R_{\text{vir}}$ is even higher (by ≈ 0.2 dex), as excluding low-redshift galaxies removes galaxies with low stellar masses at low $d_{\text{trans}}/R_{\text{vir}}$. Hence, the fact that the optical depths in Fig. 5.10 decrease as a function of $d_{\text{trans}}/R_{\text{vir}}$, could be due to a combination of a decrease in stellar mass and an increase in d_{trans}.

5.4.2   Dependence on redshift

As the cumulative mass in metals produced by stars grows with time, one might expect that the metal ion abundance in the CGM of individual galaxies is an increasing function of decreasing redshift. However, the CGM abundance of metal ions does not only depend on the level of enrichment, which itself depends on factors like the current and past efficiency of galactic winds in driving out metals, but

---

[14]Note that the increase in the median $\log_{10} \tau_Z$ cannot be attributed solely to an increase in τ_{lim}. In fact, (linearly) normalizing the optical depths from the subsample and the total sample to a common τ_{lim}, has negligible effect on the optical depths at $v_{\text{LOS}} < 100$ km/s and at all d_{trans}.

[15]We acknowledge that for this reason, the application of the redshift cut has no advantage. For our future publication, we therefore plan to include the full galaxy sample when considering optical depth profiles as a function of $d_{\text{trans}}/R_{\text{vir}}$.
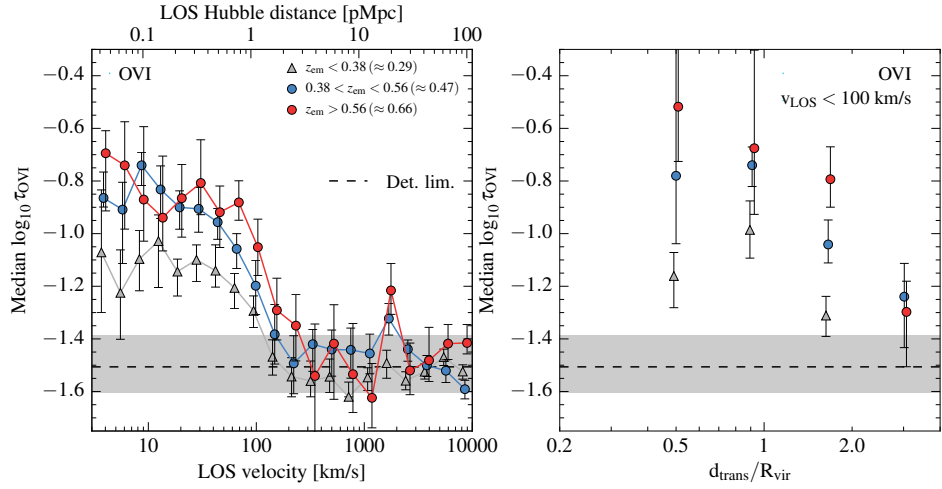
Figure 5.11: The dependence on galaxy redshift of the median Ovɪ optical depth as a function of LOS velocity (left) and normalized transverse distance (using only pixels at $v_{LOS} < 100$ km/s; right). The grey triangles, blue circles and red circles show the median $\log_{10} \tau_{OvI}$ (binned as in Figs. 5.9 and 5.10) for galaxies at $z_{em} < 0.38$, $0.38 < z_{em} < 0.56$ and $z_{em} > 0.56$, respectively, where the optical depths have been linearly shifted to the same τ_{lim} (horizontal dashed line). The median redshift of each sample is indicated in the legend. We only show d_{trans}/R_{vir} bins containing at least three galaxies. For clarity, the points are offset horizontally from each other by 0.02 dex and 0.075 dex in the left- and right-hand panels, respectively. The velocity axis shows the absolute LOS Hubble distance at $z = 0.5$. We find no evidence for significant evolution of the Ovɪ optical depth over the range $0.38 < z < 0.74$. For the galaxies below the $z_{em} = 0.38$ redshift cut (see Section 5.4.1), the lower optical depth at small LOS velocities and transverse distances might also be due to the lower stellar masses and SFRs compared to the galaxies at $z_{em} > 0.38$.

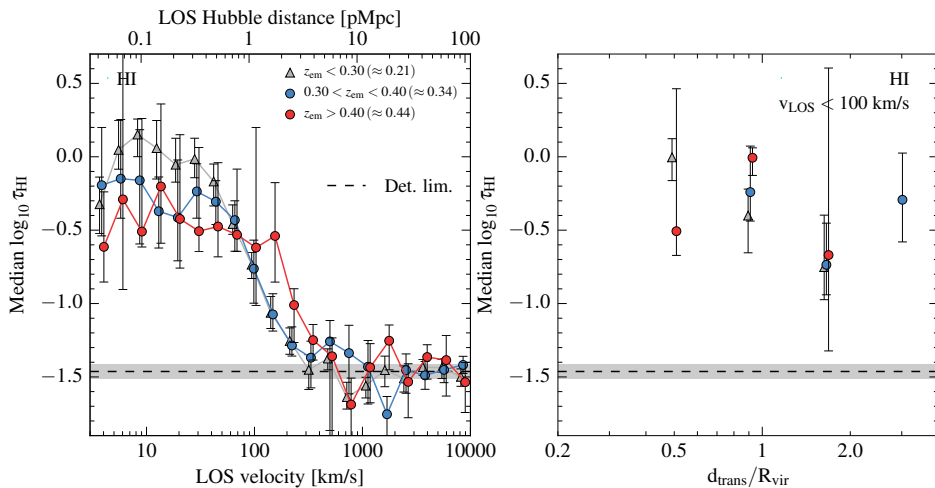**Figure 5.12:** As Fig. 5.11, but showing the dependence on galaxy redshift for the median H I optical depth, with the galaxy sample split into $z_{em} < 0.30$ (grey triangles), $0.30 < z_{em} < 0.40$ (blue circles) and $z_{em} > 0.40$ (red circles). We do not find evidence for significant evolution of the H I optical depth over the range $0.30 < z < 0.48$. Probing evolution down to $z \approx 0$ is difficult, as the typical impact parameter, stellar mass and SFR of the galaxies are lower at $z_{em} < 0.30$ than at $z_{em} > 0.30$.

is also highly sensitive to the ionization state of the gas. It is therefore not straightforward to predict how a certain population of absorbers, in the Universe in general or around galaxies of a given mass, evolves as a function of redshift. Considering only the expansion of the Universe and assuming that we probe gas at a fixed overdensity and temperature across redshifts, we would expect the optical depth to scale with redshift as $\tau_Z \propto n_Z \propto (1+z)^3$ (where n_Z is the ion number density). However, Chen (2012) compared the strength and transverse spatial extent of the H I, Mg II and C IV absorption around galaxies with a similar stellar mass between $z \approx 2.2$ and $z \approx 0$ and found no significant evolution. Furthermore, Wakker & Savage (2009) showed that the incidence of H I and O VI absorbers as a function of the minimum absorption equivalent width does not significantly evolve from $z = 0.5$ to $z = 0$.

Even though the ion redshift ranges covered by COS are relatively small, we explore how the absorption enhancement depends on galaxy redshift. We compare the median $\log_{10} \tau_Z$ as a function of LOS velocity and transverse distance (normalized by R_{vir}) between different subsamples of galaxies selected according to their redshifts. Since the small dynamic range of the C III optical depths complicates an assessment of the absorption signal for galaxy samples smaller than the full sample, we will focus on H I and O VI. In Sections 5.4.3 and 5.4.4, we will focus solely on O VI, and present the results for H I in Appendix 5.C.

Fig. 5.11 shows the median optical depth profiles of O VI for three galaxy redshift samples: $z_{em} < 0.38$ (57 galaxies; grey triangles), $0.38 < z_{em} < 0.56$ (62 galaxies; blue circles) and $z_{em} > 0.56$ (52 galaxies; red circles). For each sample in the left-hand panel and each d_{trans}/R_{vir} bin (which we only show if it contains three or more

galaxies) in the right-hand panel, τ_{lim} is, by construction, estimated from regions that follow the same redshift distribution as the galaxies: as a result, τ_{lim} depends on the typical galaxy redshift of the bin or sample. To enable a straightforward comparison between the different samples, we convert all optical depth values to a common $\tau_{\text{lim}}^{\text{norm}}$, by linearly adding the difference $(\tau_{\text{lim}}^{\text{norm}} - \tau_{\text{lim}})$ to τ_{Z}. We choose $\tau_{\text{lim}}^{\text{norm}}$ to be the highest τ_{lim} (where we take all $d_{\text{trans}}/R_{\text{vir}}$ bins together) of the three samples in the comparison.

As discussed in Section 5.4.1, due to correlations between galaxy properties like redshift and stellar mass, only the samples above the $z_{\text{em}} = 0.38$ redshift cut provide an approximately unbiased comparison between redshift regimes. The $0.38 < z_{\text{em}} < 0.56$ and $z_{\text{em}} > 0.56$ samples have median redshifts of 0.47 and 0.66, respectively, and have similar median impact parameters (≈ 150 pkpc and, in units of the virial radius, $\approx 1.7 R_{\text{vir}}$) and stellar masses ($M_* \approx 10^{9.0}\,\text{M}_\odot$). However, the median SFR of the samples do differ by ≈ 0.4 dex (where we, to calculate the median, consider the SFR upper limits as actual values). Comparing the optical depth profiles of the two samples (see Fig. 5.11), we find no evidence for significant evolution of the O VI optical depth over the redshift range $0.38 < z < 0.74$[16]. Along the LOS direction, the strength and extent of the absorption enhancement with respect to the detection limit are consistent within the error bars, and in the transverse direction, we only find a significant difference between the redshift samples for $1.2 < d_{\text{trans}}/R_{\text{vir}} < 2.2$. Note that the halo circular velocity does scale with redshift as $(1 + z)^{1/2}$ for a fixed halo mass, but that the redshift range is too small for this to have a significant effect on the scale at which the optical depths fall off as a function of v_{LOS}.

We do include the optical depth profile for the $z_{\text{em}} < 0.38$ sample in Fig. 5.11. However, while the galaxies in this sample have a median redshift of 0.29, they also have significantly lower impact parameters (with a median of ≈ 79 pkpc) than the galaxies at $z_{\text{em}} > 0.38$ (with a median of ≈ 150 pkpc), and a median stellar mass that is lower by ≈ 0.5 dex. The median R_{vir}-normalized impact parameter is lower by $\lesssim 0.2$ dex. Hence, the fact that the $z_{\text{em}} < 0.38$ sample shows somewhat lower optical depths for $v_{\text{LOS}} < 100$ km/s and $d_{\text{trans}}/R_{\text{vir}} < 2.2$ cannot be unambiguously explained as evolution of the O VI optical depth with redshift. The reduction at $z < 0.38$ may well be due to the lower stellar masses and SFRs of the galaxies, as we find that the absorption strength is positively correlated with both of these quantities (see Sections 5.4.3 and 5.4.4), thereby also compensating for the increase of the optical depth at smaller impact parameter.

For H I, the median optical depth profiles for three galaxy redshift samples are shown in Fig. 5.12, where we adopt redshift ranges of $z_{\text{em}} < 0.30$ (33 galaxies; grey triangles), $0.30 < z_{\text{em}} < 0.40$ (35 galaxies; blue circles) and $z_{\text{em}} > 0.40$ (38 galaxies; red circles). The two samples above the redshift cut of $z_{\text{em}} > 0.30$ have similar median stellar masses of $M_* \approx 10^{8.9}\,\text{M}_\odot$. However, the median impact parameter and median SFR are still somewhat lower for the $0.30 < z_{\text{em}} < 0.40$ sample (i.e. ≈ 115 pkpc and $SFR \approx 0.1\,\text{M}_\odot\,\text{yr}^{-1}$, respectively) than for the $z_{\text{em}} > 0.40$ sample (≈ 146 pkpc and $SFR \approx 0.2\,\text{M}_\odot\,\text{yr}^{-1}$), where these two differences would affect the absorption signal in opposite ways. Comparing the optical depth profiles for the

---

[16]We have checked that if we divide the $0.38 < z < 0.74$ range up into three instead of two subsamples, we reach the same conclusion.
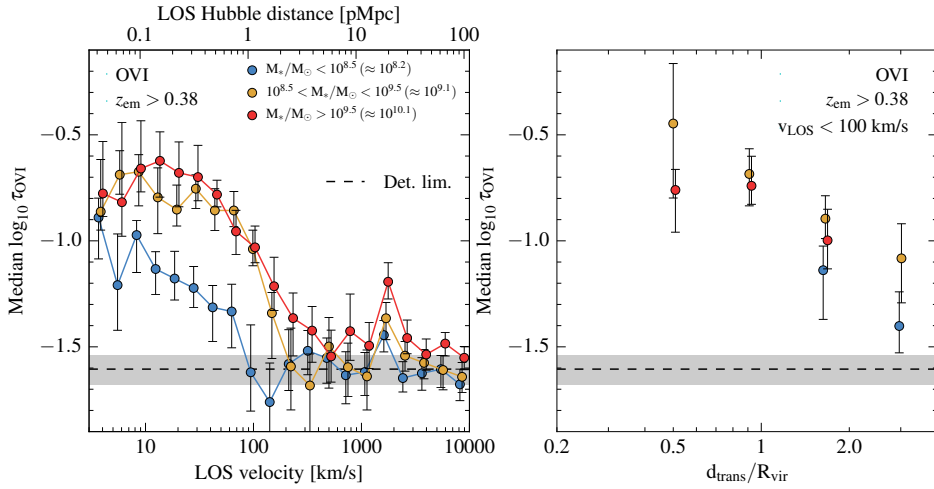
Figure 5.13: The dependence on galaxy stellar mass of the median Ovı optical depth as a function of LOS velocity (left) and normalized transverse distance (using only pixels at $v_{\rm LOS} < 100$ km/s; right). We compare samples of galaxies with $M_* < 10^{8.5}\,\rm M_\odot$ (blue), $10^{8.5} < M_* < 10^{9.5}\,\rm M_\odot$ (yellow) and $M_* > 10^{9.5}\,\rm M_\odot$ (red), with redshifts constrained to $z_{\rm em} > 0.38$. The median stellar mass of each sample is indicated in the legend. The median $\log_{10} \tau_{\rm Ovı}$ values for each mass sample and $d_{\rm trans}/R_{\rm vir}$ bin have been linearly shifted to the same $\tau_{\rm lim}$ (horizontal dashed line). We only show $d_{\rm trans}/R_{\rm vir}$ bins containing at least three galaxies. For clarity, the points are offset horizontally from each other by 0.02 dex and 0.075 dex in the left- and right-hand panels, respectively. The velocity axis shows the absolute LOS Hubble distance at $z = 0.5$. The Ovı absorption signal along the LOS direction is stronger, and more extended, for $M_* > 10^{8.5}\,\rm M_\odot$ galaxies than for $M_* < 10^{8.5}\,\rm M_\odot$ galaxies. Combining the results from the $1.2 < d_{\rm trans}/R_{\rm vir} < 2.2$ and $2.2 < d_{\rm trans}/R_{\rm vir} > 4.0$ bins, we also find a significantly lower Ovı optical depth for $M_* < 10^{8.5}\,\rm M_\odot$ galaxies at fixed $d_{\rm trans}/R_{\rm vir}$. There is, however, no significant difference in the absorption signal between the $10^{8.5} < M_* < 10^{9.5}\,\rm M_\odot$ and $M_* > 10^{9.5}\,\rm M_\odot$ samples, which is likely due to reduced ability of galactic winds to drive out metals into the CGM in higher mass galaxies (as we rule out other explanations: see the text for details).

two samples, we do not find evidence for evolution in the Hı optical depth over the range $0.30 < z < 0.48$.

As expected, a comparison of the Hı optical depth between galaxies at $z_{\rm em} < 0.30$ and at $z_{\rm em} > 0.30$ is even less straightforward. The $z_{\rm em} < 0.30$ sample has a median impact parameter of ≈ 70 pkpc, and a median stellar mass and median SFR that are lower by ≈ 1.0 dex and $\approx 0.5 - 0.8$ dex, respectively, than those of the $z_{\rm em} > 0.30$ samples. Hence, the fact that we find the Hı optical depths at $z < 0.30$ and $z > 0.30$ to be consistent within the error bars is likely because the dependence of the absorption strength on impact parameter compensates for the dependence on stellar mass and SFR.

5.4.3 Dependence on stellar mass

While the extent of the absorption signal along the LOS direction depends on the typical halo circular velocity, and therefore the halo mass, of the galaxies in the

sample, we also expect the strength of the metal absorption to depend on the mass of the galaxies and their host haloes (e.g Rakic et al., 2013; Turner et al., 2017). On the one hand, more massive galaxies have higher metallicities (both in the gas-phase and in stars; e.g. Tremonti et al., 2004; Gallazzi et al., 2005; Zahid et al., 2014a), and a fraction of this metal-enriched gas is released into the CGM, as stellar (or AGN) feedback ejects material from the galactic disc in galactic winds (e.g. Aguirre et al., 2001b; Oppenheimer & Davé, 2006; Shen et al., 2012). On the other hand, the ion abundances as observed in absorption are strongly dependent on the ionization state of the gas. For example, Oppenheimer et al. (2016) showed that the virial temperature ($T_{\rm vir}$) of the halo is a major factor in determining the column density of OvI in the CGM. For galaxies with a luminosity somewhat below L^* ($M_{\rm vir} \lesssim 10^{12.0}\,{\rm M_\odot}$), more massive galaxies exhibit larger CGM column densities of OvI, as their virial temperature is closer to the temperature at which the OvI ion fraction peaks in collisional ionization equilibrium (i.e. $T_{\rm peak} \sim 10^{5.5}$ K). Furthermore, while for haloes with $T_{\rm vir} \ll T_{\rm peak}$ OvI arises predominantly from photoionized gas, their CGM still contains less OvI than that of L^* haloes, as the total mass of oxygen is lower.

In this section, we investigate how the median OvI optical depth as a function of LOS velocity and normalized transverse distance depends on the mass of the galaxies. We divide the galaxy sample into three subsamples of roughly equal size, where the restriction to $z_{\rm em} > 0.38$ ensures that the distribution of galaxies in impact parameter (and redshift) space is approximately uniform. Fig. 5.13 shows the resulting absorption profiles for the three galaxy mass samples, $M_* < 10^{8.5}\,{\rm M_\odot}$ (36 galaxies; blue), $10^{8.5} < M_* < 10^{9.5}\,{\rm M_\odot}$ (47 galaxies; yellow) and $M_* > 10^{9.5}\,{\rm M_\odot}$ (31 galaxies; red), which have median stellar masses of $M_* = 10^{8.2}, 10^{9.1}, 10^{10.1}\,{\rm M_\odot}$, respectively. According to the abundance matching relation from Moster et al. (2013) (assuming $z = 0.5$), these correspond to halo masses of $M_{\rm vir} = 10^{10.8}, 10^{11.2}$ and $10^{11.8}\,{\rm M_\odot}$, and hence halo circular velocities of $v_{\rm circ} = 63, 85$ and 135 km/s. Unavoidably, lower mass galaxies are probed at larger fractions of their virial radius than higher mass galaxies: the three galaxy mass samples correspond to median $d_{\rm trans}/R_{\rm vir}$ values of 2.6, 1.7 and 1.2.

Along the LOS direction (left-hand panel), the optical depths within $v_{\rm LOS} \sim$ 100 km/s are significantly lower for the $M_* < 10^{8.5}\,{\rm M_\odot}$ galaxies than for the higher mass galaxies. Since the three galaxy mass samples exhibit similar impact parameter distributions (due to the $z_{\rm em} > 0.38$ cut), this is a trend at fixed $d_{\rm trans}$. At fixed $d_{\rm trans}/R_{\rm vir}$ (right-hand panel), the OvI optical depths seem consistent between the $M_* < 10^{8.5}\,{\rm M_\odot}$ and $M_* > 10^{8.5}\,{\rm M_\odot}$ mass regimes. However, while the difference is not significant for the $1.2 < d_{\rm trans}/R_{\rm vir} < 2.2$ and $2.2 < d_{\rm trans}/R_{\rm vir} > 4.0$ bins individually, we do find a significant difference for the two bins *combined*. We calculate the confidence level of this difference in a similar way to the confidence level of the absorption enhancement described in Section 5.4.1. For each $d_{\rm trans}/R_{\rm vir}$ bin, we calculate the fraction, $f_{\rm high}^{\rm bin}$, of bootstrap realizations for which $\tau_{Z,{\rm sample1}}^{\rm i} > \tau_{Z,{\rm sample2}}^{\rm i}$, where in this case $\tau_{Z,{\rm sample1}}^{\rm i}$ and $\tau_{Z,{\rm sample2}}^{\rm i}$ refer to the median optical depths of the $M_* < 10^{8.5}\,{\rm M_\odot}$ and $10^{8.5} < M_* < 10^{9.5}\,{\rm M_\odot}$ samples at the ith bootstrap iteration (after linearly shifting them to the same $\tau_{\rm lim}^{\rm i}$). The optical depth for the $M_* < 10^{8.5}\,{\rm M_\odot}$

sample is then lower than for the $10^{8.5} < M_* < 10^{9.5} \, M_\odot$ sample with a confidence level of $1 - 4 f_{\text{high}}^{\text{bin1}} f_{\text{high}}^{\text{bin2}} = 98\%$[17] for the $1.2 < d_{\text{trans}}/R_{\text{vir}} < 2.2$ ('bin1') and $2.2 < d_{\text{trans}}/R_{\text{vir}} > 4.0$ ('bin2') bins combined. Furthermore, the fact that the LOS profile of the $M_* < 10^{8.5} \, M_\odot$ galaxies falls off at a lower LOS velocity is consistent with their lower halo v_{circ}, but can also be partly due to the gas dynamics in the outer halo (i.e. at higher fractions of the virial radius) being less sensitive to peculiar velocities.

In contrast, for the $10^{8.5} < M_* < 10^{9.5} \, M_\odot$ and $M_* > 10^{9.5} \, M_\odot$ samples, the O VI optical depths (in the LOS and transverse directions) agree within the error bars, despite the 1.0 dex difference in median stellar mass and the 0.6 dex difference in corresponding halo mass. This suggests that the O VI optical depth in this mass regime is insensitive to stellar mass, both at fixed d_{trans} and at fixed $d_{\text{trans}}/R_{\text{vir}}$. Even for the three bins at $0.4 < d_{\text{trans}}/R_{\text{vir}} < 2.2$ combined, we find no significant difference between the mass samples. Also, there seems to be no significant difference in the LOS velocity scale at which the LOS profiles fall off, even though the samples have a different median halo v_{circ} (and a different median R_{vir}-normalized impact parameter). We do note, however, that a ≈ 0.2 dex difference in the velocity scale of the drop (corresponding to the difference in the median v_{circ}) is not ruled out considering the size of the error bars[18] at $v_{\text{LOS}} \approx 100 - 300$ km/s.

One possible explanation for the lack of mass dependence of the LOS profiles at $M_* > 10^{8.5} \, M_\odot$ is that the highest mass bin contains galaxies both above and below $M_* \sim 10^{10.5} \, M_\odot$, which corresponds to a halo mass scale of $M_{\text{vir}} \sim 10^{12} \, M_\odot$. Oppenheimer et al. (2016) showed that, while the O VI column density around galaxies with $M_{\text{vir}} < 10^{12} \, M_\odot$ increases with halo mass, the O VI content of $M_{\text{vir}} > 10^{12} \, M_\odot$ haloes decreases with mass, as their higher virial temperatures increasingly suppress the ion fraction of O VI. However, when we recompute the optical depths for the $M_* > 10^{9.5} \, M_\odot$ sample, where we exclude the 6 galaxies with $M_* > 10^{10.5} \, M_\odot$, we find no significant increase. Hence, the lack of mass dependence is not the result of averaging the absorption strength from haloes with a high and low O VI content.

Furthermore, given that the strength of the absorption signal exhibits a positive correlation with galaxy SFR (see Section 5.4.4), we need to confirm that the difference in absorption strength at fixed d_{trans} between galaxies with $M_* < 10^{8.5} \, M_\odot$ and galaxies with $M_* > 10^{8.5} \, M_\odot$ is not solely driven by the different SFR distributions exhibited by the different galaxy mass samples. While the $10^{8.5} < M_* < 10^{9.5} \, M_\odot$ and $M_* > 10^{9.5} \, M_\odot$ samples have median SFRs of $\approx 0.4 \, M_\odot \, \text{yr}^{-1}$ and $\approx 0.7 \, M_\odot \, \text{yr}^{-1}$, respectively, the $M_* < 10^{8.5} \, M_\odot$ sample has a much lower median SFR of $\approx 0.09 \, M_\odot \, \text{yr}^{-1}$. This accounts for at least part of the difference between the absorption strength for $M_* < 10^{8.5} \, M_\odot$ and higher stellar mass. However, we show in Appendix 5.B that both stellar mass (comparing galaxies with $10^{8.0} < M_* < 10^{9.0} \, M_\odot$ and $10^{9.0} < M_* < 10^{10.0} \, M_\odot$) and SFR also independently correlate positively with the strength of the absorption signal along the LOS direction. We demonstrate this by varying one property, while restricting the galaxies to a narrow range

---

[17]We consider a difference with a confidence level > 95% to be significant.

[18]Even though the points respresenting consecutive LOS velocity bins (unlike the transverse distance bins) are not independent from each other, the error bars do reflect the true optical depth confidence intervals, as they are derived by bootstrapping independent chunks of absorption distance.

in the other property.

Another factor that might play a role in the comparison of galaxy mass samples, is the possible occurrence of galaxies in groups. A fraction of the galaxies at low stellar masses will be satellites of more massive galaxies, while at the high-mass end some galaxies will also be part of larger structures, where multiple galaxies are contained within the same group-scale dark matter halo. In both cases, the halo mass inferred from the galaxy stellar mass through abundance matching is not representative of the mass of the group halo. Observations of circumgalactic Ovi in group environments suggest that the Ovi column density (or equivalent width) and covering fraction are lower for groups than for isolated galaxies (e.g. Wakker & Savage, 2009; Pointon et al., 2017). This is likely due to the higher virial temperature of the group-scale halo, which causes less oxygen to reside in Ovi, and more in higher states (Ovi absorption in group environments is generally broad; see e.g. Stocke et al., 2014, 2017).

To assess the importance of this environmental dependence for the results presented in this section, we repeat the comparison of the Ovi absorption signal between different stellar mass samples, using only galaxies without any neighbouring galaxies (within the MUSE FoV) within a LOS velocity difference of $|\Delta v|$ = 300 km/s. To be conservative, we consider all galaxies identified at $z < z_{\rm QSO}$ − not just the ones with the highest-quality redshift assignment, to which we limit our absorption analysis – as potential neighbours. Furthermore, we consider galaxies with all masses, not just the ones with higher masses, as potential neighbours, which makes our approach even more conservative. From low to high stellar mass, this removes 16, 26 and 20 non-isolated galaxies from the samples shown in Fig. 5.13. We find that the Ovi absorption profiles for isolated galaxies, when we split them according to their stellar mass as in Fig. 5.13, are consisted with those for all (isolated and non-isolated) galaxies. Hence, we find that the effects of the group environment do not impact our conclusions about the dependence of the CGM Ovi content on galaxy stellar mass. However, we note that when we split the galaxy sample according to the number of neighbours of each galaxy (irrespective of their stellar mass), we do find significantly lower Ovi absorption around galaxies with three or more neighbours than around galaxies with two or fewer neighbours. We will explore the Ovi content of groups identified in our MUSE fields in more detail in a forthcoming paper.

We conclude that the lack of a galaxy mass dependence in the Ovi absorption signal along the LOS direction for $M_* > 10^{8.5}$ M$_\odot$ galaxies is not due to a significant contribution from $T_{\rm vir} \gg 10^{5.5}$ K haloes to the highest-mass galaxy sample or due to the suppression of Ovi in group environments. It can also not be attributed solely to the dependence of Ovi absorption on SFR. The inferred mass trend is therefore likely related to a reduced efficiency of galactic winds in expelling metals from the disc into the CGM in higher mass galaxies (as the ionization conditions do seem more favourable around higher mass galaxies in this mass regime; Oppenheimer et al., 2016). As a result, the difference in the enrichment level of the CGM between $M_* \sim 10^9$ M$_\odot$ and $M_* \sim 10^{10}$ M$_\odot$ galaxies is smaller – and too small for us to observe a difference in the optical depth – than between $M_* \sim 10^8$ M$_\odot$ and $M_* \sim 10^9$ M$_\odot$ galaxies, even though the metallicity of the galaxy itself does increase with increasing
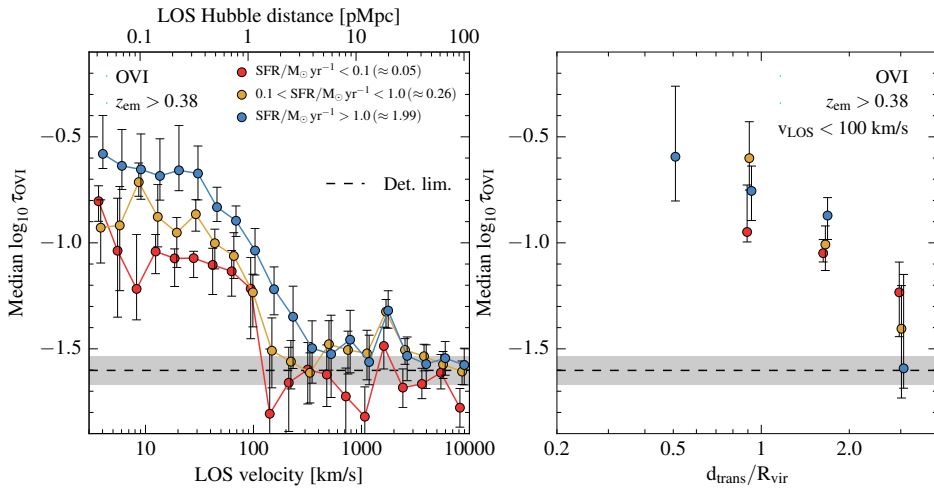
Figure 5.14: As Fig. 5.13, but showing the dependence of the median Ovɪ optical depth on galaxy SFR. We compare samples of galaxies with $SFR < 0.1\,\mathrm{M}_\odot\,\mathrm{yr}^{-1}$ (red), $0.1 < SFR < 1.0\,\mathrm{M}_\odot\,\mathrm{yr}^{-1}$ (yellow) and $SFR > 1.0\,\mathrm{M}_\odot\,\mathrm{yr}^{-1}$ (blue), with redshifts constrained to $z_{\mathrm{em}} > 0.38$. We only consider galaxies for which we could determine the SFR. Along the LOS direction, the Ovɪ optical depths increase within increasing SFR, especially within $v_{\mathrm{LOS}} \approx 100$ km/s. The profiles also fall off at increasingly higher LOS velocities, where the differences are possibly larger than expected based on the halo circular velocities. The SFR dependence is too weak to show an effect across all $d_{\mathrm{trans}}/R_{\mathrm{vir}}$ bins. Only at $1.2 < d_{\mathrm{trans}}/R_{\mathrm{vir}} < 2.2$ or for the results at $0.7 < d_{\mathrm{trans}}/R_{\mathrm{vir}} < 4.0$ combined, is the optical depth lower for the $SFR < 0.1\,\mathrm{M}_\odot\,\mathrm{yr}^{-1}$ sample than for the $SFR > 1.0\,\mathrm{M}_\odot\,\mathrm{yr}^{-1}$ sample, although the difference is barely significant.

stellar mass (see e.g. Tremonti et al., 2004; Zahid et al., 2014a, who probe the relation between stellar mass and gas-phase metallicity down to $M_* \sim 10^{8.5-9}\,\mathrm{M}_\odot$.).

5.4.4 Dependence on (specific) star formation rate

The discovery of a correlation between the Ovɪ column density around a sample of $L \approx L^*$ galaxies and their sSFR by Tumlinson et al. (2011) suggested that there is a connection between the enrichment of the CGM and the star formation activity of the host galaxy. Other studies have also shown that the rate of incidence of Ovɪ and other metal ions is higher around star-forming galaxies than around quiescent ones (e.g. Chen & Mulchaey, 2009; Borthakur et al., 2013; Werk et al., 2013; Bordoloi et al., 2014). Such a connection between the CGM metal content and star formation may arise naturally if stellar feedback is responsible for enriching the CGM by driving metal-enriched galactic winds. However, due to the time delay between the actual star formation event – if star formation is bursty – and the metals reaching distances comparable to the virial radius of the galaxy, and due to fact that metals may remain in the CGM even after the SFR of the host decreases, the correlation between the CGM metal content and the instantaneous SFR is not expected to be tight. Indeed, the simulations of Oppenheimer et al. (2016) suggest that the correlation between sSFR and Ovɪ column density is indirect: passive galaxies reside in
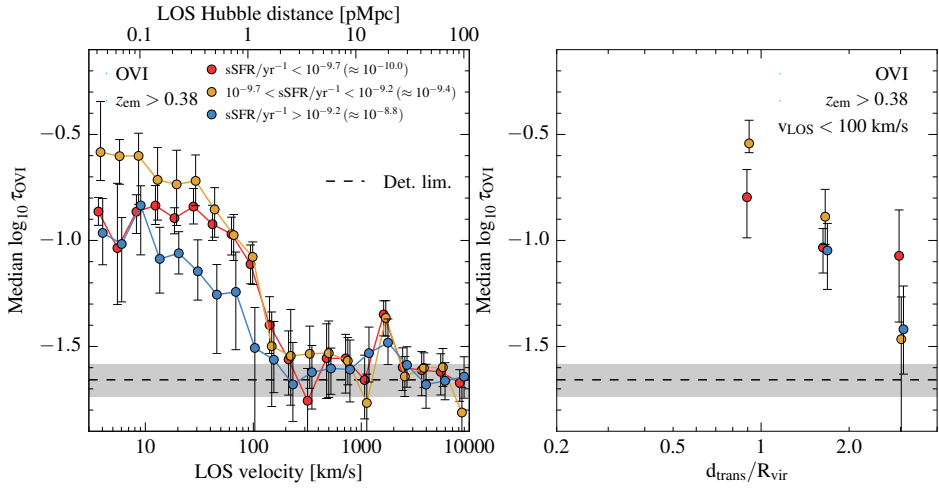
Figure 5.15: As Fig. 5.13, but showing the dependence of the median OVI optical depth on the specific SFR of the galaxies. We compare samples of galaxies with $SFR/M_* < 10^{-9.7}\,\mathrm{yr^{-1}}$ (red), $10^{-9.7} < SFR/M_* < 10^{-9.2}\,\mathrm{yr^{-1}}$ (yellow) and $SFR/M_* > 10^{-9.2}\,\mathrm{yr^{-1}}$ (blue), with redshifts constrained to $z_{\mathrm{em}} > 0.38$. We only consider galaxies for which we could determine the SFR. As a function of LOS velocity, the OVI optical depths for the $SFR/M_* > 10^{-9.2}\,\mathrm{yr^{-1}}$ sample are lower than for the lower sSFR samples, consistent with lower median stellar mass ($M_* = 10^{8.4}\,\mathrm{M_\odot}$). As a function of $d_{\mathrm{trans}}/R_{\mathrm{vir}}$, there is no significant difference between the $SFR/M_* > 10^{-9.2}\,\mathrm{yr^{-1}}$ sample and the lower sSFR samples. However, we find a significantly higher optical depth for the $10^{-9.7} < SFR/M_* < 10^{-9.2}\,\mathrm{yr^{-1}}$ sample than for the $SFR/M_* < 10^{-9.7}\,\mathrm{yr^{-1}}$ sample at $0.7 < d_{\mathrm{trans}}/R_{\mathrm{vir}} < 1.2$ or for the bins at $0.7 < d_{\mathrm{trans}}/R_{\mathrm{vir}} < 4.0$ combined.

haloes with virial temperatures that are too high for Ovi.

In this section, we study the dependence of the Ovi absorption strength on the SFR and sSFR of the galaxies. Our sample contains predominantly star-forming galaxies: only two galaxies at $z_{em} > 0.38$ and within the Ovi redshift range have $SFR/M_* < 10^{-11}$ yr^{-1} (and three have an upper limit below this value). Although we do include these galaxies in the analysis, our assessment of how the CGM Ovi content depends on the star formation activity of the galaxies is mainly focussed on the star-forming population. Fig. 5.14 shows the median Ovi optical depth as a function of LOS velocity and R_{vir}-normalized transverse distance for three galaxy samples divided by SFR: $SFR < 0.1\,M_\odot$ yr^{-1} (21 galaxies; red), $0.1 < SFR < 1.0\,M_\odot$ yr^{-1} (45 galaxies; yellow) and $SFR > 1.0\,M_\odot$ yr^{-1} (30 galaxies; blue). These samples have median SFRs of $SFR = 0.048, 0.26, 2.0\,M_\odot$ yr^{-1}. As before, we only use galaxies with $z_{em} > 0.38$. Furthermore, in this section we only consider galaxies for which we could obtain a reliable estimate of the SFR (as described in Section 5.2.4), excluding those galaxies with only an upper limit on the SFR. However, we have checked that if we do include the galaxies with SFR upper limits, either considering the limits as the actual values or including them all in the lowest SFR sample, the significance of the correlation between absorption strength and SFR slightly decreases (despite the *higher* number of galaxies), but that our conclusions remain unaffected.

Fig. 5.14 shows that along the LOS direction (left-hand panel), the median Ovi optical depths increase (especially within $v_{LOS} \approx 100$ km/s) and fall off at a larger LOS velocity as the SFR of the galaxies increases. However, based on the median stellar masses of $M_* = 10^{8.2}, 10^{8.9}, 10^{9.4}\,M_\odot$ (corresponding to the $SFR < 0.1\,M_\odot$ yr^{-1}, $0.1 < SFR < 1.0\,M_\odot$ yr^{-1} and $SFR > 1.0\,M_\odot$ yr^{-1} samples, respectively), we expect differences of only ≈ 0.1 dex in the halo circular velocity. For the $SFR > 1.0\,M_\odot$ yr^{-1} sample in particular, the velocity scales of the drop and the maximum extent seem to differ by more than 0.1 dex from the other SFR samples.

While the impact parameters of the galaxies in the three samples are similar, the high-SFR galaxies are probed at slightly smaller fractions of their virial radii due to their slightly higher stellar masses. The median d_{trans}/R_{vir} in decreases by ≈ 0.1 dex from the low to intermediate and from intermediate to high SFRs. To confirm that the result in the left-hand panel of Fig. 5.14 is not solely due to the dependence of the Ovi absorption strength on stellar mass and d_{trans}/R_{vir}, we show in Appendix 5.B that, even at fixed stellar mass (and hence fixed d_{trans}/R_{vir}), the absorption strength at small LOS velocities is higher at higher SFR.

However, the SFR dependence is too weak to cause a significant trend when we split the sample up into d_{trans}/R_{vir} bins (right-hand panel of Fig. 5.14). Only for the $1.2 < d_{trans}/R_{vir} < 2.2$ bin, which does contain the highest number of galaxies, is the Ovi optical depth lower for the $SFR < 0.1\,M_\odot$ yr^{-1} sample than for the $SFR > 1.0\,M_\odot$ yr^{-1} sample, although the difference is comparable to the size of the errors. For the three bins at $0.7 < d_{trans}/R_{vir} < 4.0$ combined, we find a confidence level for the difference of 93%, which is just below our significance threshold. The $0.1 < SFR < 1.0\,M_\odot$ yr^{-1} sample is consistent with both of the other samples (for the d_{trans}/R_{vir} bins individually or combined).

Following Werk et al. (2016), we have also computed the Ovi optical depth profiles for three different samples of SFR/d_{trans}^2, which may be a measure of the

amount of ionizing radiation originating from ongoing star formation in the galaxy. We note, however, that this neglects the dependence of the Ovi abundance on the ionization state of the gas. Taking into account the dependence on the ionization parameter, we would expect Ovi to scale with $SFR/d_{trans}^2/\rho$, where ρ is the gas mass density, which decreases as a function of radial distance from the galaxy. Although we do not show it here, we find that the difference between the profiles is somewhat more distinct than for the different SFR samples. Within $v_{LOS} \sim 100$ km/s, the optical depths along the LOS direction increase by ≈ 0.2 dex as the median SFR/d_{trans}^2 of the sample increases by ≈ 1.0 dex, where we do note that the SFR/d_{trans}^2 values probed here ($10^{-6.0} \lesssim SFR/d_{trans}^2 \lesssim 10^{-3.5}$ M$_\odot$ yr^{-1} kpc^{-2}) are much lower than those considered by Werk et al. (2016). While this might hint at a significant impact of local ionizing radiation on the metal ion fractions in the CGM, it is also possible that the correlation between the Ovi absorption strength and SFR/d_{trans}^2 arises from a combination of the positive correlation of absorption strength with SFR and the negative correlation with impact parameter.

Finally, in Fig. 5.15 we show the dependence of the Ovi optical depth on sSFR, which is related to the gas fraction ($= M_{gas}/(M_{gas}+M_*)$, where M_{gas} is the mass of gas in the interstellar medium) of the galaxy. We choose the boundaries of the samples so as to have three samples of roughly equal size: $SFR/M_* < 10^{-9.7}$ yr^{-1} (33 galaxies; red), $10^{-9.7} < SFR/M_* < 10^{-9.2}$ yr^{-1} (31 galaxies; yellow) and $SFR/M_* > 10^{-9.2}$ yr^{-1} (32 galaxies; blue), which have median sSFRs of $SFR/M_* = -10.0, -9.4, -8.8$ yr^{-1}. Along the LOS direction (left-hand panel), the optical depth profile for the $SFR/M_* < 10^{-9.7}$ yr^{-1} sample (median $M_* = 10^{9.5}$ M$_\odot$ and median $SFR = 0.17$ M$_\odot$ yr^{-1}) is similar to the $10^{-9.7} < SFR/M_* < 10^{-9.2}$ yr^{-1} sample (median $M_* = 10^{8.9}$ M$_\odot$ and median $SFR = 0.27$ M$_\odot$ yr^{-1}). These sSFR samples contain predominantly galaxies in the mass regime where the Ovi optical depth is insensitive to stellar mass. Furthermore, the ≈ 2 times higher SFR for the $10^{-9.7} < SFR/M_* < 10^{-9.2}$ yr^{-1} sample may cancel out any mass dependence.

The optical depths for the $SFR/M_* > 10^{-9.2}$ yr^{-1} sample (median $M_* = 10^{8.4}$ M$_\odot$ and median $SFR = 0.85$ M$_\odot$ yr^{-1}) are lower than for the other samples and fall off at a lower LOS velocity. This indicates that the effect of a lower stellar mass more than compensates for the effect of a higher SFR, which is also consistent with the different profile shape. As a function of d_{trans}/R_{vir} (right-hand panel), the sSFR samples show similar Ovi optical depths on the scales where all three samples can be compared ($1.2 < d_{trans}/R_{vir} < 4.0$). Even for the $1.2 < d_{trans}/R_{vir} < 2.2$ and $2.2 < d_{trans}/R_{vir} < 4.0$ bins combined, the differences between the $SFR/M_* > 10^{-9.2}$ yr^{-1} sample and the other samples are not significant. However, at $0.7 < d_{trans}/R_{vir} < 1.2$, where the $SFR/M_* > 10^{-9.2}$ yr^{-1} sample does not have sufficient galaxies, the optical depth is significantly higher for the $10^{-9.7} < SFR/M_* < 10^{-9.2}$ yr^{-1} sample than for the $SFR/M_* < 10^{-9.7}$ yr^{-1} sample. Combining the results from the three bins at $0.7 < d_{trans}/R_{vir} < 4.0$, we find a higher optical depth for the $10^{-9.7} < SFR/M_* < 10^{-9.2}$ yr^{-1} sample at 96% confidence.

5.5   Conclusions

We have studied the H$\textsc{i}$, O$\textsc{vi}$ and C$\textsc{iii}$ abundances in the CGM of 208 galaxies at z_{em} < 0.91, which were blindly selected with MUSE in the fields centred on 15 QSOs – plus one field where we found no galaxies – with high-quality COS quasar spectra. We compiled the sample of galaxies by detecting them through their continuum emission, and measuring their redshifts from their emission lines – mainly Hα, Hβ, O$\textsc{ii}$ and O$\textsc{iii}$ – and, in a few cases, from their absorption lines. For this study, we only selected the galaxies with redshift estimates based on multiple spectral features. Our sample has a median stellar mass of $10^{8.9}$ M$_\odot$ and a median SFR of 0.21 M$_\odot$ yr^{-1}. Hence, the typical galaxy mass is much lower than for other (low- and high-redshift) quasar absorption-line studies. We studied the CGM of the galaxies in absorption by calculating the median pixel optical depth, employing the pixel optical depth method to partially correct for the effects of noise, saturation and contamination, as a function of LOS velocity and transverse distance (up to impact parameters of 300 pkpc or four times the halo virial radius). We investigated the extent of the absorption signal in both of these directions, and explored the dependence of the absorption strength, where we mainly focused on O$\textsc{vi}$, on galaxy redshift, stellar mass, SFR and sSFR. Our main results can be summarized as follows.

1. Along the LOS direction, the median H$\textsc{i}$, O$\textsc{vi}$ and C$\textsc{iii}$ optical depths generally decrease with increasing LOS velocity from the galaxies. The characteristic scale at which the optical depth starts to deviate from the approximately flat trend at small v_{LOS} is v_{drop} = 50 km/s for H$\textsc{i}$ and $v_{drop} \approx$ 80 km/s for O$\textsc{vi}$ and C$\textsc{iii}$.

2. We find a significant enhancement of the H$\textsc{i}$ and O$\textsc{vi}$ absorption, with respect to the detection limit, with > 95% confidence out to LOS velocities of $v_{LOS} \approx$ 260 km/s ($d_{LOS} \approx$ 3.2 pMpc in the case of pure Hubble flow) and $v_{LOS} \approx$ 115 km/s ($d_{LOS} \approx$ 1.3 pMpc), respectively. At small LOS velocities, the median optical depth reaches values up to $\approx$ 1.3 dex above τ_{lim} in the case of H$\textsc{i}$, and up to $\approx$ 0.8 dex above τ_{lim} in the case of O$\textsc{vi}$, where τ_{lim} is the median optical depth far from the galaxies. For C$\textsc{iii}$, we find enhanced absorption with > 68% confidence out to $v_{LOS} \approx$ 115 km/s ($d_{LOS} \approx$ 1.3 pMpc), with the median optical depth reaching values up to $\approx$ 0.2 dex above τ_{lim} (Fig. 5.9, left-hand panels).

3. In the direction projected on the sky, the median H$\textsc{i}$, O$\textsc{vi}$ and C$\textsc{iii}$ optical depths decrease as a function of both transverse distance and transverse distance divided by the halo virial radius. A tentative drop in the optical depths profiles, comparable to twice the size of the estimated error on the median optical depth, is seen at $d_{trans} \approx$ 120 pkpc and $d_{trans}/R_{vir} \approx$ 1.2.

4. For H$\textsc{i}$ and O$\textsc{vi}$, the absorption is enhanced with > 95% confidence over the whole transverse distance range probed (i.e. up to d_{trans} = 300 pkpc). For C$\textsc{iii}$, the absorption is enhanced with > 95% confidence out to $d_{trans} \approx$ 120 pkpc.

These scales are ~ 10 times smaller than the extent of the absorption enhancement along the LOS direction, which can be attributed to gas peculiar velocities smearing the absorption signal along the LOS but not in the transverse direction (Fig. 5.9, right-hand panels). When considering transverse distances in units of the halo virial radius, we find the H$_I$ and O$_{VI}$ absorption to be enhanced with > 95% confidence out to d_{trans}/R_{vir} = 4.0. For C$_{III}$, we find a confidence level of > 95% only at $0.7 < d_{trans}/R_{vir}$ = 1.2 (Fig. 5.10).

5. We emphasize that, to enable an approximately unbiased assessment of the dependence of the absorption signal on a particular galaxy property, it is necessary to eliminate any secondary correlations – due to observational bias or with a physical origin – with other galaxy properties as much as possible. This avoids misinterpreting the effects of different galaxy properties on the absorption signal. We find that imposing a minimum galaxy redshift of $z_{em} > 0.38$ (and $z_{em} > 0.30$ in the case of H$_I$) largely removes the correlations of impact parameter, stellar mass and SFR with redshift, and thereby also the correlations of stellar mass and SFR with impact parameter, while still yielding a reasonable sample size (i.e. 73 galaxies for H$_I$, 116 for O$_{VI}$ and 150 for C$_{III}$).

6. Comparing the LOS and transverse absorption profiles for different galaxy samples split according to their redshifts, we find no evidence for significant evolution of the H$_I$ and O$_{VI}$ optical depth over the ranges $0.30 < z < 0.48$ and $0.38 < z < 0.74$, respectively. At lower redshifts, an unbiased comparison is impossible, as the typical impact parameter, stellar mass and SFR of the galaxies in the sample is also significantly lower (Figs. 5.11 and 5.12).

7. We find that the O$_{VI}$ absorption strength as a function of LOS velocity is significantly higher, and falls off at a higher LOS velocity, for galaxies with $M_* > 10^{8.5}\,M_\odot$ than for galaxies with $M_* < 10^{8.5}\,M_\odot$ (Fig. 5.13, left-hand panel). This is a comparison at fixed d_{trans}, as we eliminate the correlation between impact parameter and stellar mass, but the median d_{trans}/R_{vir} does decrease from low to high stellar mass. At fixed d_{trans}/R_{vir}, we also find a significantly lower O$_{VI}$ optical depth for $M_* < 10^{8.5}\,M_\odot$ galaxies than for higher mass galaxies (Fig. 5.13, right-hand panel). In contrast, for galaxies at $M_* > 10^{8.5}\,M_\odot$, the O$_{VI}$ LOS and transverse profiles do not exhibit a clear dependence on stellar mass, which can be explained if the total CGM metal abundance no longer increases with increasing galaxy mass in this mass regime (due to the lower efficiency of galactic winds in driving out metals), as the ionization conditions for O$_{VI}$ do seem more favourable in higher mass galaxies at these mass scales. We have checked that this lack of a stellar mass dependence is not due to the suppression of the O$_{VI}$ abundance in galaxy groups. We have also confirmed that the O$_{VI}$ absorption strength along the LOS direction exhibits positive correlations with both stellar mass and SFR when these are varied independently: hence, any trend of the signal with stellar mass is not solely driven by the correlation with SFR (Fig. 5.18).

8. Using only the galaxies with a reliable estimate of the SFR ($\approx$ 89% of the sample), we find that the median O$_{VI}$ optical depth increases with increasing SFR

and weakly decreases with increasing sSFR, but only when we consider the optical depth as a function of LOS velocity (Figs. 5.14 and 5.15). The SFR dependence is too weak to show an effect accross all $d_{\mathrm{trans}}/R_{\mathrm{vir}}$ bins. The trend of decreasing Ovi optical depth with increasing sSFR is only evident when comparing the $SFR/M_* > 10^{-9.2}\,\mathrm{yr}^{-1}$ sample with the two $SFR/M_* < 10^{-9.2}\,\mathrm{yr}^{-1}$ samples, which is consistent with the fact that the median stellar masses of the samples in these two sSFR regimes are lower and higher than $M_* = 10^{8.5}\,\mathrm{M}_\odot$, respectively. In contrast, for $SFR/M_* < 10^{-9.2}\,\mathrm{yr}^{-1}$, the median Ovi optical depth (weakly) increases with sSFR, but only when considered at fixed $d_{\mathrm{trans}}/R_{\mathrm{vir}}$.

5.A   Optical depth profiles of other metal ions

Fig. 5.16 shows the median pixel optical depth, $\log_{10} \tau_Z$, as a function of LOS velocity for the following ions: Siɪɪ 1260.42 Å$(z < 0.43)$, Cɪɪ 1334.53 Å$(z < 0.35)$, Siɪɪɪ $(z < 0.49)$, Siɪv $(z < 0.29)$, Cɪv $(z < 0.16)$ and Nv $(z < 0.45)$. As described in Section 5.3.2, the optical depths have been corrected for Hɪ contamination and, in the case of a doublet transition, corrected for further contamination by taking the doublet minimum. For Siɪɪ and Cɪɪ, which are multiplets, we only apply the Hɪ contamination correction and show the absorption in the strongest transition.

Only Nv shows a significant absorption enhancement with respect to the detection limit within $v_{\mathrm{LOS}} \sim 100$ km/s, although for the individual points the confidence levels of the enhancement vary from less than 50% to 97%. In the transverse direction (Fig. 5.17), we find an enhancement at 100% confidence for $0.2 < d_{\mathrm{trans}}/R_{\mathrm{vir}} < 0.4$ and at 88% confidence for $0.7 < d_{\mathrm{trans}}/R_{\mathrm{vir}} < 1.2$. For none of the other ions, is the absorption significantly enhanced. Especially in the case of Cɪv, this can be partly attributed to the limited sample size, as Cɪv is only observable with COS at $z < 0.16$.

5.B   Varying the stellar mass and star formation rate independently

We investigate how the Ovi absorption strength as a function of LOS velocity depends on galaxy stellar mass and SFR, when we vary one property independently from the other. The lower-left panel of Fig. 5.18 shows the median Ovi optical depth profile along the LOS direction for a sample of galaxies with $10^{8.0} < M_* < 10^{9.0}\,\mathrm{M}_\odot$ (23 galaxies; blue) and a sample with $10^{9.0} < M_* < 10^{10.0}\,\mathrm{M}_\odot$ (15 galaxies; red), which have all been selected to have a SFR in the range $0.1 < SFR < 1.0\,\mathrm{M}_\odot\,\mathrm{yr}^{-1}$ (as illustrated in the upper-left panel). As in Sections 5.4.3 and 5.4.4, we restrict the galaxy redshifts to $z_{\mathrm{em}} > 0.38$, in order to eliminate any correlation between stellar mass and impact parameter. The median $d_{\mathrm{trans}}/R_{\mathrm{vir}}$ does decrease with increasing stellar mass (from 1.9 to 1.5), but we aim to perform a comparison at fixed d_{trans}, to mimic the investigation of the stellar mass dependence (left-hand panel of Fig. 5.13) in a restricted SFR range. The optical depth profile of the high mass sample reaches up to higher values at small LOS velocities, and falls off at a larger LOS velocity
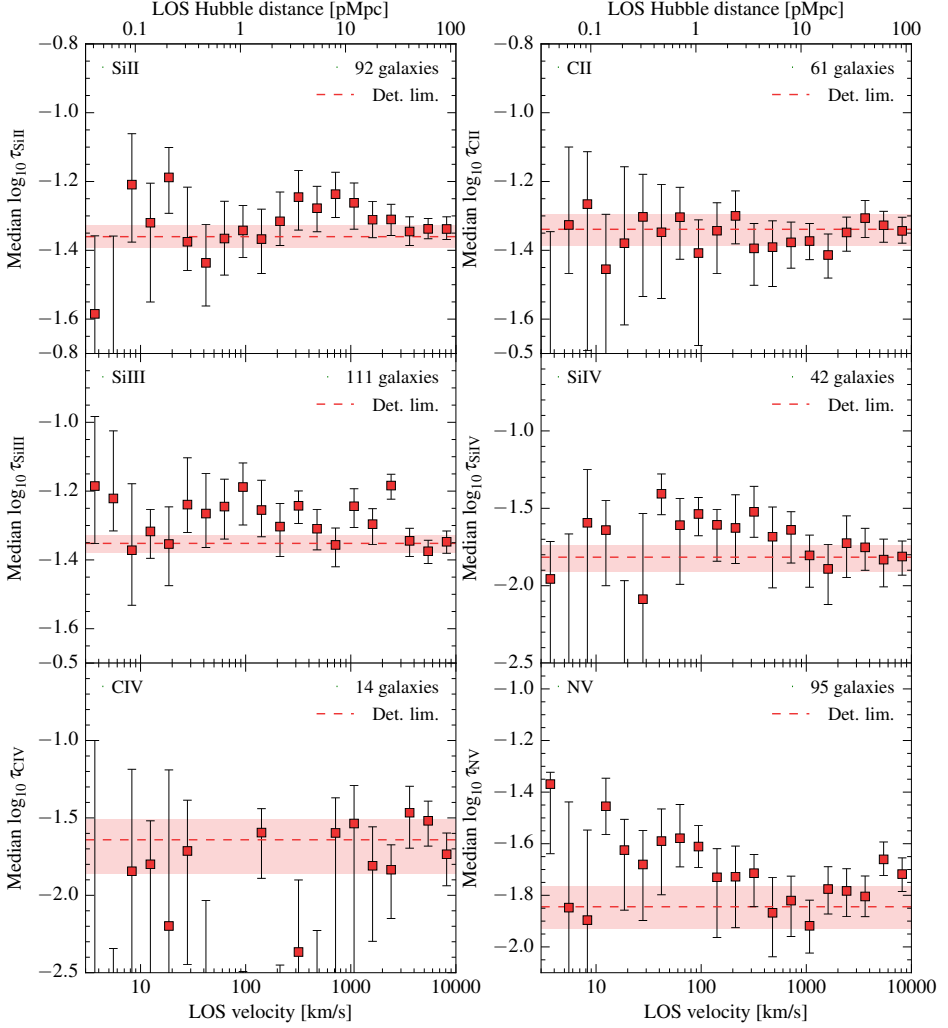
Figure 5.16: The median pixel optical depth of, from top left to bottom right, S$\textsc{ii}$ 1260.42 Å($z < 0.43$), C$\textsc{ii}$ 1334.53 Å($z < 0.35$), S$\textsc{iii}$ ($z < 0.49$), S$\textsc{iv}$ ($z < 0.29$), C$\textsc{iv}$ ($z < 0.16$) and N$\textsc{v}$ ($z < 0.45$) as a function of LOS velocity. The corresponding absolute LOS Hubble distance, assuming $z = 0.5$, is shown at the top. In the top right of each panel, we indicate the number of galaxies contributing to the profile. We do not apply a redshift cut. Only N$\textsc{v}$ shows a significant enhancement of the absorption signal with respect to the detection limit (horizontal dashed line) for $v_{\mathrm{LOS}} \lesssim 100$ km/s. The other ions show no significant absorption enhancement.
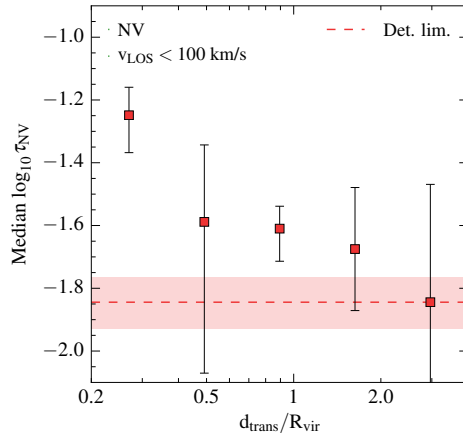
Figure 5.17: The median Nv optical depth as a function of transverse distance normalized by the virial radius. For each $d_{\rm trans}/R_{\rm vir}$ bin, we calculate the median $\log_{10} \tau_{\rm Nv}$ using only pixels at $v_{\rm LOS} < 100$ km/s and we linearly shift the optical depths to the same $\tau_{\rm lim}$ as in the bottom right panel of Fig. 5.16 (horizontal dashed line). We only show $d_{\rm trans}/R_{\rm vir}$ bins containing at least three galaxies. We find an enhancement of the Nv absorption signal at 100% confidence for $0.2 < d_{\rm trans}/R_{\rm vir} < 0.4$ and at 88% confidence for $0.7 < d_{\rm trans}/R_{\rm vir} < 1.2$.

scale, which is consistent with what is expected for more massive haloes. Hence, even at fixed SFR, the optical depth profile exhibits a clear dependence on galaxy stellar mass.

In the right-hand panels of Fig. 5.18, we show a comparison of the median Ovi optical depth profile between galaxies with $0.03 < SFR < 0.3\,{\rm M}_\odot\,{\rm yr}^{-1}$ (20 galaxies; yellow) and galaxies with $0.3 < SFR < 3.0\,{\rm M}_\odot\,{\rm yr}^{-1}$ (20 galaxies; green), which are selected from a narrow range in stellar mass ($10^{8.5} < M_* < 10^{9.5}\,{\rm M}_\odot$). As the two samples exhibit similar impact parameter and stellar mass distributions, the galaxies are also probed at similar fractions of their virial radius (i.e. at similar $d_{\rm trans}/R_{\rm vir}$, where both sample have a median of ≈ 1.7). While the optical depth profiles of both samples fall off at a similar LOS velocity, reflecting the similar halo mass distributions of the two samples, the optical depths at small LOS velocities are significantly higher for the high-SFR sample than for the low-SFR sample. We therefore confirm that the Ovi absorption strength correlates positively with the SFR of the galaxies, even at fixed galaxy stellar mass.

5.C   Dependence of the Hi optical depth on stellar mass and star formation rate

Fig. 5.19 shows how the median Hi optical depth as a function of $v_{\rm LOS}$ and $d_{\rm trans}/R_{\rm vir}$ depends on galaxy stellar mass. As, compared with Ovi, Hi is observable over a smaller redshift range, we split the galaxy sample into two instead of three stellar
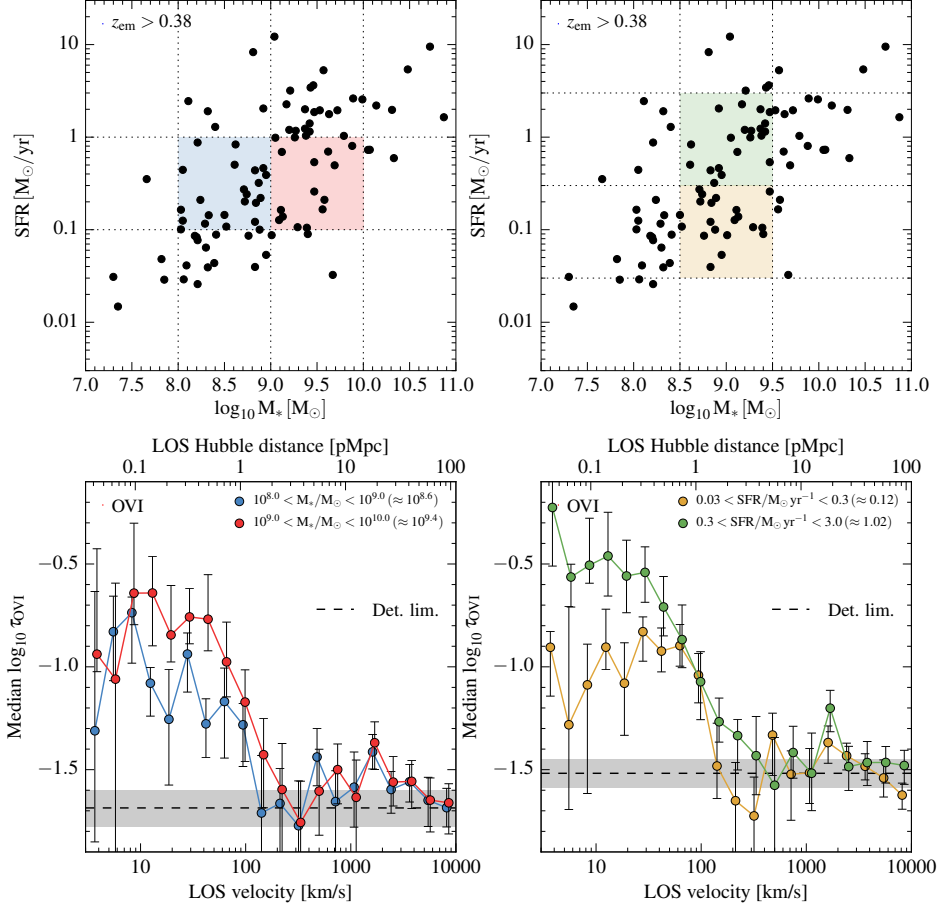
Figure 5.18: The dependence of the median O VI optical depth as a function of LOS velocity on galaxy stellar mass (left-hand panels) and SFR (right-hand panels) for galaxies with $z_{\rm em} > 0.38$. As shown in the upper panels, we select galaxies from a narrow range in SFR when we vary the stellar mass ($10^{8.0} < M_* < 10^{9.0}\,{\rm M_\odot}$: blue; $10^{9.0} < M_* < 10^{10.0}\,{\rm M_\odot}$: red), and we select galaxies from a narrow range in stellar mass when we vary the SFR ($0.03 < SFR < 0.3\,{\rm M_\odot\,yr^{-1}}$: yellow; $0.3 < SFR < 3.0\,{\rm M_\odot\,yr^{-1}}$: green). The legends indicate the median stellar mass and SFR of each sample in the left- and right-hand panels, respectively. In both of the lower panels, the points are offset horizontally from each other by 0.02 dex, and have been linearly shifted to the same $\tau_{\rm lim}$ (horizontal dashed line). The velocity axis indicates the absolute LOS Hubble distance at $z = 0.5$. We conclude that both stellar mass and SFR independently exhibit positive correlations with the O VI absorption strength.
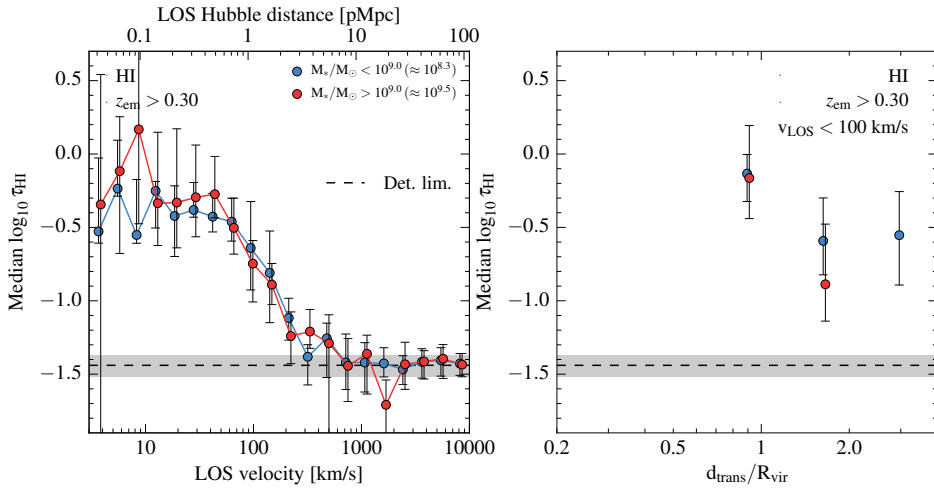
Figure 5.19: The dependence on galaxy stellar mass of the median HI optical depth as a function of LOS velocity (left) and normalized transverse distance (using only pixels at $v_{LOS} < 100$ km/s; right). We compare samples of galaxies with $M_* < 10^{9.0}$ $M_\odot$ (blue) and $M_* > 10^{9.0}$ $M_\odot$ (red), with redshifts constrained to $z_{em} > 0.30$. The median stellar mass of each sample is indicated in the legend. The median $\log_{10} \tau_{OVI}$ values for each sample and d_{trans}/R_{vir} bin have been linearly shifted to the same τ_{lim} (horizontal dashed line). We only show d_{trans}/R_{vir} bins containing at least three galaxies. For clarity, the points are offset horizontally from each other by 0.02 dex and 0.075 dex in the left- and right-hand panels, respectively. The velocity axis shows the absolute LOS Hubble distance at $z = 0.5$. We do not find a significant dependence of the median HI optical depth on stellar mass.
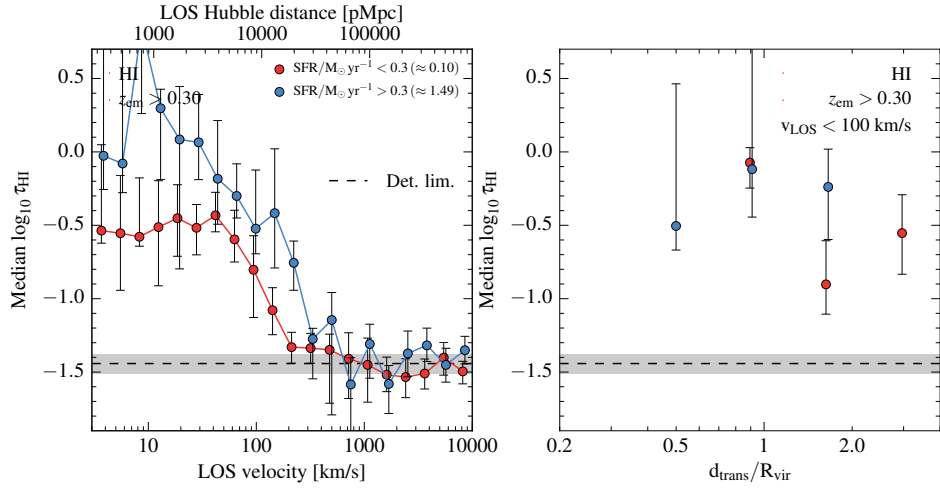
Figure 5.20: As Fig. 5.19, but showing the dependence of the median HI optical depth on galaxy SFR. We compare samples of galaxies with $SFR < 0.3\,M_\odot\,\mathrm{yr}^{-1}$ (red) and $SFR > 0.3\,M_\odot\,\mathrm{yr}^{-1}$ (blue), with redshifts constrained to $z_{em} > 0.30$. We only consider galaxies for which we could determine their SFR. Along the LOS direction, the HI optical depth seems to be significantly higher for the high-SFR sample than for the low-SFR sample. A similar dependence on SFR in the transverse direction is only shown by the $1.2 < d_{trans}/R_{vir} < 2.2$ distance bin.
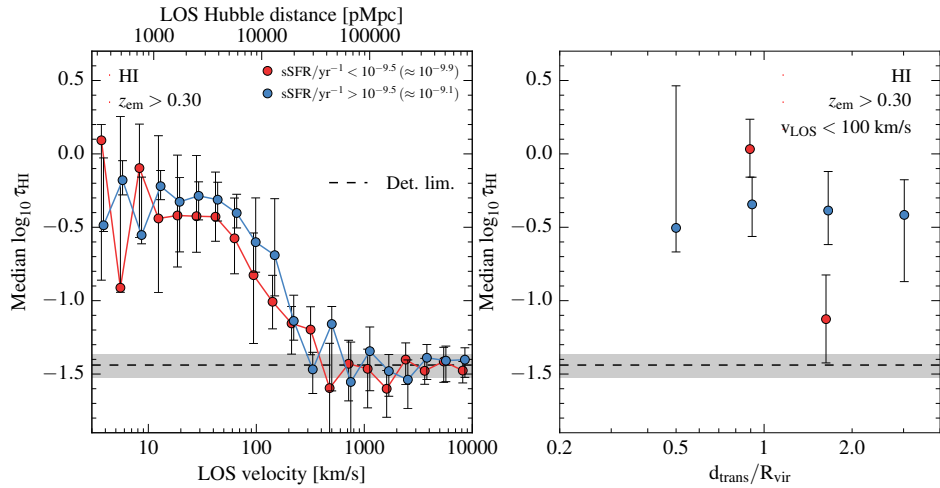

Figure 5.21: As Fig. 5.19, but showing the dependence of the median HI optical depth on the specific SFR of the galaxies. We compare samples of galaxies with $SFR/M_* < 10^{-9.5}\,\mathrm{yr}^{-1}$ (red) and $SFR/M_* > 10^{-9.5}\,\mathrm{yr}^{-1}$ (blue), with redshifts constrained to $z_{em} > 0.30$. We only consider galaxies for which we could determine their SFR. Except for the significant increase of the HI absorption strength with increasing sSFR shown at $1.2 < d_{trans}/R_{vir} < 2.2$, we do not find evidence for a dependence of the absorption signal on sSFR.

mass samples, so as to maintain reasonable sample sizes. We split the sample in the middle of the bins used for Ov$\scriptstyle\rm I$, yielding $M_* < 10^{9.0}\,\mathrm{M}_\odot$ (42 galaxies; blue) and $M_* > 10^{9.0}\,\mathrm{M}_\odot$ (31 galaxies; red). These samples have median stellar masses of $M_* = 10^{8.3}, 10^{9.5}\,\mathrm{M}_\odot$ and median SFRs of $SFR = 0.087, 0.31\,\mathrm{M}_\odot\,\mathrm{yr}^{-1}$.

While the imposed redshift cut of $z_\mathrm{em} > 0.30$ ensures that the samples have similar impact parameter and redshift distributions, lower mass galaxies are typically probed at a higher fraction of their virial radius. The median $d_\mathrm{trans}/R_\mathrm{vir}$ values corresponding to the low- and high-mass samples are 1.7 and 1.1, respectively. However, despite the 1.2 dex difference in median stellar mass and the 0.19 dex difference in median $d_\mathrm{trans}/R_\mathrm{vir}$, we do not find a significant dependence of the H$\scriptstyle\rm I$ absorption signal on stellar mass, neither at fixed v_LOS (left-hand panel) nor at fixed $d_\mathrm{trans}/R_\mathrm{vir}$ (right-hand panel).

Interestingly, we do find a significant dependence of the median H$\scriptstyle\rm I$ optical depth as a function of LOS velocity on SFR. This is shown in Fig. 5.20. We split the total sample in two, creating samples with $SFR < 0.3\,\mathrm{M}_\odot\,\mathrm{yr}^{-1}$ (46 galaxies; red) and $SFR > 0.3\,\mathrm{M}_\odot\,\mathrm{yr}^{-1}$ (22 galaxies; blue), where we only use galaxies for which we could determine the SFR. We find a higher H$\scriptstyle\rm I$ absorption signal out to $v_\mathrm{LOS} \approx 300$ km/s for the high-SFR sample than for the low-SFR sample. The median SFRs of the two samples are $SFR = 0.10, 1.5\,\mathrm{M}_\odot\,\mathrm{yr}^{-1}$ and the median stellar masses ($d_\mathrm{trans}/R_\mathrm{vir}$ values) are $M_* = 10^{8.5}, 10^{9.4}\,\mathrm{M}_\odot$ ($d_\mathrm{trans}/R_\mathrm{vir} = 1.5, 1.1$). In the transverse direction, only the $1.2 < d_\mathrm{trans}/R_\mathrm{vir} < 2.2$ shows a (barely significant) difference between the low- and high-SFR samples.

However, the H$\scriptstyle\rm I$ absorption signal does not exhibit a significant dependence on the specific SFR. This is shown in Fig. 5.21, where we split the total sample into galaxies with $SFR/M_* < 10^{-9.5}\,\mathrm{yr}^{-1}$ (32 galaxies; red) and $SFR/M_* > 10^{-9.5}\,\mathrm{yr}^{-1}$ (36 galaxies; blue). The median sSFRs of the two samples are $SFR/M_* = 10^{-9.9}$, $10^{-9.1}\,\mathrm{yr}^{-1}$. The median stellar mass and SFR of the high-sSFR sample are 0.8 dex lower and 0.4 dex higher, respectively, than those for the low-sSFR sample. At $1.2 < d_\mathrm{trans}/R_\mathrm{vir} < 2.2$, we do find a significant increase of the H$\scriptstyle\rm I$ absorption strength with increasing sSFR, which would be consistent with its dependence on the SFR. However, the median optical depth at $0.7 < d_\mathrm{trans}/R_\mathrm{vir} < 1.2$ suggests (although with a low significance) opposite trend.

The results presented in this section stand in contrast with the clear dependence of the Ov$\scriptstyle\rm I$ optical depth on both SFR *and* stellar mass (at fixed v_LOS and d_trans). For metal ion species, a strong dependence of the CGM abundance on SFR might be interpreted as the result of a connection between the enrichment of the CGM and the star formation activity of the host galaxy, considering that stellar feedback can drive galactic winds. Furthermore, more massive galaxies have had more time to increase the metal content of the CGM. However, for H$\scriptstyle\rm I$, the higher abundance around higher SFR galaxies with a similar stellar mass can also be due an enhanced infalling gas component. Hence, the results for H$\scriptstyle\rm I$ are not in contradiction with such an interpretation of our findings for Ov$\scriptstyle\rm I$.

References

Adelberger, K. L., Shapley, A. E., Steidel, C. C., et al. 2005, ApJ, 629, 636

Aguirre, A., Dow-Hygelund, C., Schaye, J., & Theuns, T. 2008, ApJ, 689, 851

Aguirre, A., Hernquist, L., Schaye, J., et al. 2001a, ApJ, 561, 521

—. 2001b, ApJ, 560, 599

Aguirre, A., Schaye, J., & Theuns, T. 2002, ApJ, 576, 1

Aird, J., et al. 2010, MNRAS, 401, 2531

Alexander, D. M., & Hickox, R. C. 2012, New A Rev., 56, 93

Andrews, B. H., & Martini, P. 2013, ApJ, 765, 140

Arrigoni, M., Trager, S. C., Somerville, R. S., & Gibson, B. K. 2010, MNRAS, 402, 173

Asplund, M., Grevesse, N., Sauval, A. J., & Scott, P. 2009, ARA&A, 47, 481

Bacon, R., et al. 2010, in Proc. SPIE, Vol. 7735, Ground-based and Airborne Instrumentation for Astronomy III, 773508

Bahcall, J. N., & Peebles, P. J. E. 1969, ApJ, 156, L7

Bahcall, J. N., & Spitzer, Jr., L. 1969, ApJ, 156, L63

Bahé, Y. M., & McCarthy, I. G. 2015, MNRAS, 447, 969

Baldry, I. K., Glazebrook, K., Brinkmann, J., et al. 2004, ApJ, 600, 681

Baldry, I. K., et al. 2012, MNRAS, 421, 621

Baldwin, J. A., Phillips, M. M., & Terlevich, R. 1981, PASP, 93, 5

Begelman, M. C., & Cioffi, D. F. 1989, ApJ, 345, L21

Behroozi, P. S., Wechsler, R. H., & Conroy, C. 2013, ApJ, 770, 57

Bertin, E., & Arnouts, S. 1996, A&AS, 117, 393

Birnboim, Y., & Dekel, A. 2003, MNRAS, 345, 349

Bongiorno, A., et al. 2012, MNRAS, 427, 3103

Booth, C. M., & Schaye, J. 2009, MNRAS, 398, 53

Booth, C. M., Schaye, J., Delgado, J. D., & Dalla Vecchia, C. 2012, MNRAS, 420, 1053

Bordoloi, R., et al. 2011, ApJ, 743, 10

—. 2014, ApJ, 796, 136

Borisova, E., et al. 2016, ApJ, 831, 39

Borthakur, S., Heckman, T., Strickland, D., Wild, V., & Schiminovich, D. 2013, ApJ, 768, 18

Bowen, D. V., Blades, J. C., & Pettini, M. 1995, ApJ, 448, 634

Bower, R. G., Schaye, J., Frenk, C. S., et al. 2017, MNRAS, 465, 32

Boyle, B. J., & Terlevich, R. J. 1998, MNRAS, 293, L49

Brinchmann, J., Charlot, S., White, S. D. M., et al. 2004, MNRAS, 351, 1151

Brinchmann, J., Kunth, D., & Durret, F. 2008, A&A, 485, 657

Brooks, A. M., Governato, F., Quinn, T., Brook, C. B., & Wadsley, J. 2009, ApJ, 694, 396

Bruzual, G., & Charlot, S. 2003, MNRAS, 344, 1000

Burchett, J. N., et al. 2016, ApJ, 832, 124

Calura, F., & Menci, N. 2009, MNRAS, 400, 1347

—. 2011, MNRAS, 413, L1

Calzetti, D., Armus, L., Bohlin, R. C., et al. 2000, ApJ, 533, 682

Cardelli, J. A., Clayton, G. C., & Mathis, J. S. 1989, ApJ, 345, 245

Carswell, B., Schaye, J., & Kim, T.-S. 2002, ApJ, 578, 43

Carswell, R. F., Whelan, J. A. J., Smith, M. G., Boksenberg, A., & Tytler, D. 1982, MNRAS, 198, 91

Cattaneo, A., Dekel, A., Faber, S. M., & Guiderdoni, B. 2008, MNRAS, 389, 567

Cen, R., & Chisari, N. E. 2011, ApJ, 731, 11

Cen, R., Miralda-Escudé, J., Ostriker, J. P., & Rauch, M. 1994, ApJ, 437, L9

Chabrier, G. 2003, PASP, 115, 763

Chen, H.-W. 2012, MNRAS, 427, 1238

Chen, H.-W., Helsby, J. E., Gauthier, J.-R., et al. 2010, ApJ, 714, 1521

Chen, H.-W., Lanzetta, K. M., & Webb, J. K. 2001, ApJ, 556, 158

Chen, H.-W., & Mulchaey, J. S. 2009, ApJ, 701, 1219

Choi, Y.-Y., Woo, J.-H., & Park, C. 2009, ApJ, 699, 1679

Ciotti, L., D'Ercole, A., Pellegrini, S., & Renzini, A. 1991, ApJ, 376, 380

Conroy, C., Graves, G. J., & van Dokkum, P. G. 2014, ApJ, 780, 33

Cooksey, K. L., Kao, M. M., Simcoe, R. A., O'Meara, J. M., & Prochaska, J. X. 2013, ApJ, 763, 37

Cowie, L. L., & Songaila, A. 1998, Nature, 394, 44

Cowie, L. L., Songaila, A., Hu, E. M., & Cohen, J. G. 1996, AJ, 112, 839

Crain, R. A., McCarthy, I. G., Frenk, C. S., Theuns, T., & Schaye, J. 2010, MNRAS, 407, 1403

Crain, R. A., McCarthy, I. G., Schaye, J., Theuns, T., & Frenk, C. S. 2013, MNRAS, 432, 3005

Crain, R. A., et al. 2009, MNRAS, 399, 1773

—. 2015, MNRAS, 450, 1937

Creasey, P., Theuns, T., & Bower, R. G. 2015, MNRAS, 446, 2125

Dalla Vecchia, C., & Schaye, J. 2008, MNRAS, 387, 1431

—. 2012, MNRAS, 426, 140

Dall'Aglio, A., Wisotzki, L., & Worseck, G. 2008, A&A, 480, 359

Danforth, C. W., & Shull, J. M. 2005, ApJ, 624, 555

Davé, R., Hernquist, L., Katz, N., & Weinberg, D. H. 1999, ApJ, 511, 521

Davis, M., Efstathiou, G., Frenk, C. S., & White, S. D. M. 1985, ApJ, 292, 371

de La Rosa, I. G., La Barbera, F., Ferreras, I., & de Carvalho, R. R. 2011, MNRAS, 418, L74

Dekel, A., et al. 2009, Nature, 457, 451

Di Matteo, T., Springel, V., & Hernquist, L. 2005, Nature, 433, 604

Dolag, K., Borgani, S., Murante, G., & Springel, V. 2009, MNRAS, 399, 497

Dubois, Y., Volonteri, M., Silk, J., et al. 2015, MNRAS, 452, 1502

Durier, F., & Dalla Vecchia, C. 2012, MNRAS, 419, 465

Elbaz, D., Jahnke, K., Pantin, E., Le Borgne, D., & Letawe, G. 2009, A&A, 507, 1359

Ellison, S. L., Songaila, A., Schaye, J., & Pettini, M. 2000, AJ, 120, 1175

Faucher-Giguère, C.-A., Lidz, A., Zaldarriaga, M., & Hernquist, L. 2009, ApJ, 703, 1416

Fontanot, F., De Lucia, G., Monaco, P., Somerville, R. S., & Santini, P. 2009, MNRAS, 397, 1776

Ford, A. B., Oppenheimer, B. D., Davé, R., et al. 2013, MNRAS, 432, 89

Ford, A. B., et al. 2016, MNRAS, 459, 1745

Furlong, M., et al. 2015, MNRAS, 450, 4486

—. 2017, MNRAS, 465, 722

Gabor, J. M., & Bournaud, F. 2013, MNRAS, 434, 606

Gallazzi, A., Charlot, S., Brinchmann, J., White, S. D. M., & Tremonti, C. A. 2005, MNRAS, 362, 41

Gargiulo, I. D., et al. 2015, MNRAS, 446, 3820

Gonçalves, T. S., Steidel, C. C., & Pettini, M. 2008, ApJ, 676, 816

Green, J. C., et al. 2012, ApJ, 744, 60

Greene, J. E., & Ho, L. C. 2007, ApJ, 667, 131

Guimarães, R., Petitjean, P., Rollinde, E., et al. 2007, MNRAS, 377, 657

Gunn, J. E., & Gott, III, J. R. 1972, ApJ, 176, 1

Gunn, J. E., & Peterson, B. A. 1965, ApJ, 142, 1633

Haardt, F., & Madau, P. 2001, in Clusters of Galaxies and the High Redshift Universe Observed in X-rays, ed. D. M. Neumann & J. T. V. Tran

Haardt, F., & Madau, P. 2012, ApJ, 746, 125

Haas, M. R., Schaye, J., Booth, C. M., et al. 2013, MNRAS, 435, 2931

Haiman, Z., Ciotti, L., & Ostriker, J. P. 2004, ApJ, 606, 763

Haiman, Z., & Hui, L. 2001, ApJ, 547, 27

Häring, N., & Rix, H.-W. 2004, ApJ, 604, L89

Hasinger, G., Miyaji, T., & Schmidt, M. 2005, A&A, 441, 417

Haywood, M., Di Matteo, P., Lehnert, M. D., Katz, D., & Gómez, A. 2013, A&A, 560, A109

Heckman, T. M., Kauffmann, G., Brinchmann, J., et al. 2004, ApJ, 613, 109

Herenz, E. C., & Wisotzki, L. 2017, A&A, 602, A111

Hickox, R. C., Mullaney, J. R., Alexander, D. M., et al. 2014, ApJ, 782, 9

Hinton, S. R., Davis, T. M., Lidman, C., Glazebrook, K., & Lewis, G. F. 2016, Astronomy and Computing, 15, 61

Hopkins, P. F. 2013, MNRAS, 428, 2840

Hopkins, P. F., Kereš, D., Oñorbe, J., et al. 2014, MNRAS, 445, 581

Hopkins, P. F., & Quataert, E. 2010, MNRAS, 407, 1529

Hummels, C. B., Bryan, G. L., Smith, B. D., & Turk, M. J. 2013, MNRAS, 430, 1548

Johansson, J., Thomas, D., & Maraston, C. 2012, MNRAS, 421, 1908

Johnson, S. D., Chen, H.-W., & Mulchaey, J. S. 2015, MNRAS, 449, 3263

Kauffmann, G., & Heckman, T. M. 2009, MNRAS, 397, 135

Kauffmann, G., et al. 2003, MNRAS, 346, 1055

Keel, W. C., et al. 2012, MNRAS, 420, 878

Kennicutt, Jr., R. C. 1998, ApJ, 498, 541

Kennicutt, Jr., R. C., Tamblyn, P., & Congdon, C. E. 1994, ApJ, 435, 22

Kereš, D., Katz, N., Fardal, M., Davé, R., & Weinberg, D. H. 2009, MNRAS, 395, 160

Kereš, D., Katz, N., Weinberg, D. H., & Davé, R. 2005, MNRAS, 363, 2

Kewley, L. J., Dopita, M. A., Sutherland, R. S., Heisler, C. A., & Trevena, J. 2001, ApJ, 556, 121

Kewley, L. J., & Ellison, S. L. 2008, ApJ, 681, 1183

Kewley, L. J., Geller, M. J., & Jansen, R. A. 2004, AJ, 127, 2002

Kirkman, D., & Tytler, D. 2008, MNRAS, 391, 1457

Kollmeier, J. A., et al. 2006, ApJ, 648, 128

Komatsu, E., et al. 2011, ApJS, 192, 18

Kormendy, J., & Ho, L. C. 2013, ARA&A, 51, 511

Kriek, M., van Dokkum, P. G., Labbé, I., et al. 2009, ApJ, 700, 221

Lagos, C. d. P., et al. 2015, MNRAS, 452, 3815

Larson, R. B., Tinsley, B. M., & Caldwell, C. N. 1980, ApJ, 237, 692

Leitner, S. N., & Kravtsov, A. V. 2011, ApJ, 734, 48

Liang, C. J., & Chen, H.-W. 2014, MNRAS, 445, 2061

Lintott, C. J., et al. 2009, MNRAS, 399, 129

Liske, J., & Williger, G. M. 2001, MNRAS, 328, 653

Lopez, S., Ellison, S., D'Odorico, S., & Kim, T.-S. 2007, A&A, 469, 61

Lutz, D., et al. 2008, ApJ, 684, 853

Lynden-Bell, D. 1969, Nature, 223, 690

Mac Low, M.-M., & Ferrara, A. 1999, ApJ, 513, 142

Mac Low, M.-M., & McCray, R. 1988, ApJ, 324, 776

Marconi, A., & Hunt, L. K. 2003, ApJ, 589, L21

Marconi, A., Risaliti, G., Gilli, R., et al. 2004, MNRAS, 351, 169

Marigo, P. 2001, A&A, 370, 194

Martin, D. C., et al. 2007, Nature, 448, 780

Martini, P., & Weinberg, D. H. 2001, ApJ, 547, 12

Mathews, W. G. 1990, ApJ, 354, 468

McAlpine, S., Bower, R. G., Harrison, C. M., et al. 2017, MNRAS, 468, 3395

McAlpine, S., et al. 2016, Astronomy and Computing, 15, 72

McQuinn, M., & Werk, J. K. 2017, ArXiv e-prints, arXiv:1703.03422

Merritt, D., & Ferrarese, L. 2001, MNRAS, 320, L30

Miller, C. J., Nichol, R. C., Gómez, P. L., Hopkins, A. M., & Bernardi, M. 2003, ApJ, 597, 142

Mistani, P. A., et al. 2016, MNRAS, 455, 2323

Mo, H. J., & Mao, S. 2002, MNRAS, 333, 768

Moster, B. P., Naab, T., & White, S. D. M. 2013, MNRAS, 428, 3121

Moustakas, J., Kennicutt, Jr., R. C., Tremonti, C. A., et al. 2010, ApJS, 190, 233

Moustakas, J., et al. 2013, ApJ, 767, 50

Muñoz-Mateos, J. C., Gil de Paz, A., Boissier, S., et al. 2007, ApJ, 658, 1006

Mullaney, J. R., et al. 2012a, MNRAS, 419, 95

—. 2012b, ApJ, 753, L30

Murray, N., Quataert, E., & Thompson, T. A. 2005, ApJ, 618, 569

Muzzin, A., et al. 2013, ApJ, 777, 18

Nagashima, M., Lacey, C. G., Okamoto, T., et al. 2005, MNRAS, 363, L31

Neistein, E., van den Bosch, F. C., & Dekel, A. 2006, MNRAS, 372, 933

Nelson, D., Vogelsberger, M., Genel, S., et al. 2013, MNRAS, 429, 3353

Netzer, H., Lira, P., Trakhtenbrot, B., Shemmer, O., & Cury, I. 2007, ApJ, 671, 1256

Nielsen, N. M., Churchill, C. W., Kacprzak, G. G., & Murphy, M. T. 2013, ApJ, 776, 114

Novak, G. S., Ostriker, J. P., & Ciotti, L. 2011, ApJ, 737, 26

Oppenheimer, B. D., & Davé, R. 2006, MNRAS, 373, 1265

—. 2008, MNRAS, 387, 577

Oppenheimer, B. D., Davé, R., Kereš, D., et al. 2010, MNRAS, 406, 2325

Oppenheimer, B. D., & Schaye, J. 2013a, MNRAS, 434, 1063

—. 2013b, MNRAS, 434, 1043

Oppenheimer, B. D., Segers, M., Schaye, J., Richings, A. J., & Crain, R. A. 2017, ArXiv e-prints, arXiv:1705.07897

Oppenheimer, B. D., et al. 2016, MNRAS, 460, 2157

Osterbrock, D. E., & Ferland, G. J. 2006, Astrophysics of gaseous nebulae and active galactic nuclei (University Science Books)

Parriott, J. R., & Bregman, J. N. 2008, ApJ, 681, 1215

Pasquali, A., Gallazzi, A., & van den Bosch, F. C. 2012, MNRAS, 425, 273

Patel, S. G., et al. 2013, ApJ, 766, 15

Peeples, M. S., Werk, J. K., Tumlinson, J., et al. 2014, ApJ, 786, 54

Peng, Y.-j., & Maiolino, R. 2014, MNRAS, 438, 262

Petitjean, P., & Bergeron, J. 1990, A&A, 231, 309

Pettini, M., Shapley, A. E., Steidel, C. C., et al. 2001, ApJ, 554, 981

Pipino, A., Devriendt, J. E. G., Thomas, D., Silk, J., & Kaviraj, S. 2009, A&A, 505, 1075

Planck Collaboration, et al. 2014, A&A, 571, A16

Pointon, S. K., Nielsen, N. M., Kacprzak, G. G., et al. 2017, ApJ, 844, 23

Portinari, L., Chiosi, C., & Bressan, A. 1998, A&A, 334, 505

Prochaska, J. X., Weiner, B., Chen, H.-W., Mulchaey, J., & Cooksey, K. 2011, ApJ, 740, 91

Prochaska, J. X., et al. 2013, ApJ, 776, 136

Putman, M. E., et al. 2009, in ArXiv Astrophysics e-prints, Vol. 2010, astro2010: The Astronomy and Astrophysics Decadal Survey, 241

Rahmati, A., & Schaye, J. 2014, MNRAS, 438, 529

Rahmati, A., Schaye, J., Bower, R. G., et al. 2015, MNRAS, 452, 2034

Rahmati, A., Schaye, J., Crain, R. A., et al. 2016, MNRAS, 459, 310

Rakic, O., Schaye, J., Steidel, C. C., et al. 2013, MNRAS, 433, 3103

Rakic, O., Schaye, J., Steidel, C. C., & Rudie, G. C. 2012, ApJ, 751, 94

Ramírez, I., Allende Prieto, C., & Lambert, D. L. 2013, ApJ, 764, 78

Rees, M. J., & Ostriker, J. P. 1977, MNRAS, 179, 541

Renzini, A. 2006, ARA&A, 44, 141

Richings, A. J., & Schaye, J. 2016, MNRAS, 458, 270

Roberts, M. S. 1963, ARA&A, 1, 149

Rollinde, E., Srianand, R., Theuns, T., Petitjean, P., & Chand, H. 2005, MNRAS, 361, 1015

Rosas-Guevara, Y. M., et al. 2015, MNRAS, 454, 1038

Rubin, K. H. R., Prochaska, J. X., Koo, D. C., et al. 2014, ApJ, 794, 156

Rudie, G. C., et al. 2012, ApJ, 750, 67

Salpeter, E. E. 1955, ApJ, 121, 161

—. 1964, ApJ, 140, 796

Salviander, S., & Shields, G. A. 2013, ApJ, 764, 80

Sánchez, S. F., et al. 2014, A&A, 563, A49

Sancisi, R., Fraternali, F., Oosterloo, T., & van der Hulst, T. 2008, A&A Rev., 15, 189

Sandage, A. 1986, A&A, 161, 89

Santini, P., et al. 2012, A&A, 540, A109

Savage, B. D., Kim, T.-S., Wakker, B. P., et al. 2014, ApJS, 212, 8

Savage, B. D., Lehner, N., & Narayanan, A. 2011, ApJ, 743, 180

Sawala, T., et al. 2015, MNRAS, 448, 2941

Sazonov, S. Y., Ostriker, J. P., & Sunyaev, R. A. 2004, MNRAS, 347, 144

Schaller, M., Dalla Vecchia, C., Schaye, J., et al. 2015a, MNRAS, 454, 2277

Schaller, M., et al. 2015b, MNRAS, 451, 1247

Schawinski, K., Koss, M., Berney, S., & Sartori, L. F. 2015, MNRAS, 451, 2517

Schaye, J. 2001, ApJ, 559, 507

—. 2004, ApJ, 609, 667

Schaye, J., Aguirre, A., Kim, T.-S., et al. 2003, ApJ, 596, 768

Schaye, J., & Dalla Vecchia, C. 2008, MNRAS, 383, 1210

Schaye, J., Rauch, M., Sargent, W. L. W., & Kim, T.-S. 2000, ApJ, 541, L1

Schaye, J., et al. 2010, MNRAS, 402, 1536

—. 2015, MNRAS, 446, 521

Schiavon, R. P. 2007, ApJS, 171, 146

Schirber, M., Miralda-Escudé, J., & McDonald, P. 2004, ApJ, 610, 105

Schirmer, M., Diaz, R., Holhjem, K., Levenson, N. A., & Winge, C. 2013, ApJ, 763, 60

Schirmer, M., et al. 2016, MNRAS, 463, 1554

Scott, J., Bechtold, J., Dobrzycki, A., & Kulkarni, V. P. 2000, ApJS, 130, 67

Segers, M. C., Crain, R. A., Schaye, J., et al. 2016, MNRAS, 456, 1235

Shankar, F., Crocce, M., Miralda-Escudé, J., Fosalba, P., & Weinberg, D. H. 2010, ApJ, 718, 231

Shen, S., Madau, P., Aguirre, A., et al. 2012, ApJ, 760, 50

Shen, S., Madau, P., Guedes, J., et al. 2013, ApJ, 765, 89

Shen, Y., Greene, J. E., Strauss, M. A., Richards, G. T., & Schneider, D. P. 2008, ApJ, 680, 169

Shen, Y., et al. 2007, AJ, 133, 2222

Silk, J. 1977, ApJ, 211, 638

Silverman, J. D., et al. 2008, ApJ, 679, 118

Songaila, A. 1998, AJ, 115, 2184

Spergel, D. N., et al. 2007, ApJS, 170, 377

Springel, V. 2005, MNRAS, 364, 1105

Springel, V., & Hernquist, L. 2002, MNRAS, 333, 649

Springel, V., White, S. D. M., Tormen, G., & Kauffmann, G. 2001, MNRAS, 328, 726

Steidel, C. C., Erb, D. K., Shapley, A. E., et al. 2010, ApJ, 717, 289

Steidel, C. C., & Sargent, W. L. W. 1992, ApJS, 80, 1

Stocke, J. T., Keeney, B. A., Danforth, C. W., et al. 2017, ApJ, 838, 37

Stocke, J. T., Penton, S. V., Danforth, C. W., et al. 2006, ApJ, 641, 217

Stocke, J. T., et al. 2014, ApJ, 791, 128

Su, M., Slatyer, T. R., & Finkbeiner, D. P. 2010, ApJ, 724, 1044

Sun, M., et al. 2015, ApJ, 802, 14

Suresh, J., Rubin, K. H. R., Kannan, R., et al. 2017, MNRAS, 465, 2966

Sutherland, R. S., & Dopita, M. A. 1993, ApJS, 88, 253

Syphers, D., & Shull, J. M. 2014, ApJ, 784, 42

Taylor, P., & Kobayashi, C. 2015, MNRAS, 448, 1835

Thielemann, F.-K., et al. 2003, in From Twilight to Highlight: The Physics of Supernovae, ed. W. Hillebrandt & B. Leibundgut, 331

Thom, C., & Chen, H.-W. 2008, ApJS, 179, 37

Thomas, D., Maraston, C., Schawinski, K., Sarzi, M., & Silk, J. 2010, MNRAS, 404, 1775

Trager, S. C., Faber, S. M., Worthey, G., & González, J. J. 2000, AJ, 120, 165

Trager, S. C., & Somerville, R. S. 2009, MNRAS, 395, 608

Trayford, J. W., et al. 2015, MNRAS, 452, 2879

Tremonti, C. A., et al. 2004, ApJ, 613, 898

Tripp, T. M., Sembach, K. R., Bowen, D. V., et al. 2008, ApJS, 177, 39

Tumlinson, J., & Fang, T. 2005, ApJ, 623, L97

Tumlinson, J., et al. 2011, Science, 334, 948

—. 2013, ApJ, 777, 59

Turner, M. L., Schaye, J., Crain, R. A., et al. 2017, MNRAS, 471, 690

Turner, M. L., Schaye, J., Steidel, C. C., Rudie, G. C., & Strom, A. L. 2014, MN-RAS, 445, 794

—. 2015, MNRAS, 450, 2067

Ueda, Y., Akiyama, M., Ohta, K., & Miyaji, T. 2003, ApJ, 598, 886

van de Voort, F., & Schaye, J. 2012, MNRAS, 423, 2991

van de Voort, F., Schaye, J., Booth, C. M., & Dalla Vecchia, C. 2011a, MNRAS, 415, 2782

van de Voort, F., Schaye, J., Booth, C. M., Haas, M. R., & Dalla Vecchia, C. 2011b, MNRAS, 414, 2458

Vogelsberger, M., et al. 2014, MNRAS, 444, 1518

Voit, G. M., & Donahue, M. 2011, ApJ, 738, L24

Wakker, B. P., Hernandez, A. K., French, D. M., et al. 2015, ApJ, 814, 40

Wakker, B. P., & Savage, B. D. 2009, ApJS, 182, 378

Weaver, R., McCray, R., Castor, J., Shapiro, P., & Moore, R. 1977, ApJ, 218, 377

Weilbacher, P. M., Streicher, O., Urrutia, T., et al. 2012, in Proc. SPIE, Vol. 8451, Software and Cyberinfrastructure for Astronomy II, 84510B

Weiner, B. J., et al. 2009, ApJ, 692, 187

Werk, J. K., Prochaska, J. X., Thom, C., et al. 2013, ApJS, 204, 17

Werk, J. K., et al. 2016, ApJ, 833, 54

Wiersma, R. P. C., Schaye, J., Dalla Vecchia, C., et al. 2010, MNRAS, 409, 132

Wiersma, R. P. C., Schaye, J., & Smith, B. D. 2009a, MNRAS, 393, 99

Wiersma, R. P. C., Schaye, J., & Theuns, T. 2011, MNRAS, 415, 353

Wiersma, R. P. C., Schaye, J., Theuns, T., Dalla Vecchia, C., & Tornatore, L. 2009b, MNRAS, 399, 574

Woosley, S. E., Heger, A., & Weaver, T. A. 2002, Reviews of Modern Physics, 74, 1015

Woosley, S. E., & Weaver, T. A. 1995, ApJS, 101, 181

Yates, R. M., Henriques, B., Thomas, P. A., et al. 2013, MNRAS, 435, 3500

Yu, Q., & Tremaine, S. 2002, MNRAS, 335, 965

Zahid, H. J., Dima, G. I., Kudritzki, R.-P., et al. 2014a, ApJ, 791, 130

Zahid, H. J., Torrey, P., Vogelsberger, M., et al. 2014b, Ap&SS, 349, 873

Zaritsky, D., Kennicutt, Jr., R. C., & Huchra, J. P. 1994, ApJ, 420, 87

Zubovas, K., King, A. R., & Nayakshin, S. 2011, MNRAS, 415, L21

Samenvatting

Sterrenstelsels zijn systemen bestaande uit gas, stof, sterren en donkere materie, die gebonden zijn door de zwaartekracht. We kunnen sterrenstelsels waarnemen en bestuderen doordat het gas, het stof en de sterren (die zijn opgebouwd uit 'normale', baryonische materie) licht uitzenden. De donkere materie is alleen gevoelig voor zwaartekracht en is daarom niet direct waarneembaar. Deze materie vormt echter wel het grootste deel van de materie in het universum. Donkere materie is geordend in een web van filamentachtige structuren (het kosmisch web) en vormt de ruggengraat van het zichtbare heelal. Baryonische materie voelt de aantrekking van de donkere materie en concentreert zich daarom voornamelijk in de dichtste delen van het kosmisch web, op de knooppunten van de filamenten die we 'halo's' noemen. Omdat de baryonische materie, in tegenstelling tot de donkere materie, wel elektromagnetische interacties kan ondergaan, kan deze materie extra energie kwijtraken in de vorm van straling (licht) en samentrekken tot structuren die veel kleiner zijn dan de halo's van donkere materie. Op deze manier kunnen objecten als sterren, planeten en sterrenstelsels worden gevormd.

De baryoncyclus

De vorming en evolutie van sterrenstelsels is een intensief samenspel tussen sterrenstelsels en hun omgeving. De ruimte tussen sterrenstelsels noemen we het 'intergalactisch medium' (IGM) en het deel van deze ruimte in de directe nabijheid van individuele sterrenstelsels het 'circumgalactisch medium' (CGM). Het IGM is een belangrijke bron van gas, waardoor sterrenstelsels kunnen groeien en sterren kunnen vormen. De aantrekkende werking van de zwaartekracht zorgt ervoor dat het gas vanuit het IGM naar binnen stroomt, mits het gas voldoende kan afkoelen (anders blijft het achter in de halo). Sterrenstelsels die voorkomen in groepen of clusters (grote groepen) kunnen ook gas uit andere sterrenstelsels aantrekken, bijvoorbeeld wanneer twee sterrenstelsels samenvoegen ('mergen').

De binnenste delen van sterrenstelsels bestaan uit sterren en het interstellaire medium (ISM) van gas en stof. Wanneer het gas in het ISM lokaal een hoge dichtheid bereikt, kan een gaswolk onder zijn eigen gewicht ineenzakken. We spreken van een nieuwgevormde ster wanneer de gaswolk dusdanig hoge dichtheden bereikt, dat kernfusie mogelijk wordt. De elementen waterstof en helium zijn gevormd in

het vroege heelal – tijdens de oerknal – terwijl zwaardere elementen ('metalen'[19]) voor het overgrote deel gevormd zijn door kernfusiereacties in sterren. Observaties tonen aan dat metalen zowel binnen als buiten sterrenstelsels voorkomen: zowel het ISM als het CGM en IGM zijn verrijkt met 'sterrenstof'. Grootschalige galactische winden zorgen ervoor dat de metalen tot ver buiten sterrenstelsels worden verspreid, tot op afstanden die vele tientallen malen groter zijn dan de grootte van de sterrenstelsels zelf.

De massa van een ster bepaalt welke evolutiestadia de ster doormaakt en hoe snel de evolutie verloopt. Omdat elk evolutiestadium gekenmerkt wordt door specifieke kernfusiereacties, zorgen verschillende soorten sterren voor de aanmaak van verschillende soorten elementenpatronen, die op verschillende tijdschalen in het gas in en rondom sterrenstelsels terechtkomen. Zo leven massive sterren (met een massa van meer dan $8\,M_\odot$, waarbij $M_\odot$ staat voor één zonsmassa) relatief kort – ongeveer 10 miljoen jaar – en ondergaan ze een lange reeks fusiereacties totdat de sterkern volledig uit ijzer bestaat. Dit leidt uiteindelijk tot explosies die we supernovae noemen (in dit geval van 'Type II'), waarbij de kernfusieproducten worden weggeblazen. Massieve sterren produceren voornamelijk α-elementen, elementen die zijn opgebouwd uit heliumkernen ('α-deeltjes'): dit zijn bijvoorbeeld zuurstof, neon, magnesium en silicium.

Lichte en middelzware sterren (met een massa tussen $0.8\,M_\odot$ en $8\,M_\odot$) evolueren een stuk langzamer, op tijdschalen van vele miljoenen tot vele miljarden jaren. De twee belangrijkste mechanismen waarmee deze sterren het omliggende gas verrijken, zijn de sterwinden tijdens de 'asymptotic giant branch'-fase (AGB-fase) en de supernova-explosies (in dit geval van 'Type Ia') die plaatsvinden in dubbelstersystemen. De AGB-fase is het evolutiestadium waarin sterren opzwellen tot rode reuzen en door instabiliteiten in de steratmosfeer grote hoeveelheden gas kwijtraken. Hierbij komen voornamelijk elementen als koolstof en stikstof vrij; deze zijn weliswaar in de kernen van de sterren gemaakt, maar zijn door convectiestromen in de buitenlagen terechtgekomen. De sterkernen die overblijven nadat de atmosferen geheel zijn vervlogen, noemen we witte dwergen. In het geval dat twee witte dwergen samen een dubbelstersysteem vormen en één van beide in toenemende mate massa van de andere aantrekt, kan het systeem exploderen als een Type Ia supernova. Daarbij vindt in korte tijd een reeks kernfusiereacties plaats, zodat een breed scala aan elementen vrijkomt. Dit type supernovae is met name een belangrijke bron van ijzer.

Tijdens de levensloop van sterren komt niet alleen met metalen verrijkte materie vrij, maar ook kinetische energie en straling. Daarnaast zijn de actieve kernen van sterrenstelsels ('active galactic nuclei', ofwel AGN) sterke bronnen van energie, die aangedreven worden doordat het gas in de sterrenstelsels wordt aangetrokken door de centrale zwarte gaten. De energie die vrijkomt bij sterevolutie en uit AGN, zorgt voor verhitting van het ISM en zelfs de aandrijving van gasstromen die grote hoeveelheden materie uit sterrenstelsels kunnen verwijderen. Deze processen hebben tot gevolg dat er minder nieuwe sterren gevormd kunnen worden: de verhitting zorgt ervoor dat gaswolken in het ISM minder snel kunnen afkoelen en de galactische winden verwijderen gas dat gebruikt had kunnen worden voor de stervorming.

---

[19]Hoewel de scheikundige definitie anders is, gebruiken we volgens de traditie in de sterrenkunde het woord 'metalen' om alle elementen zwaarder dan helium aan te duiden.

Hetzelfde kan gebeuren met het gas dat zich nog in de halo bevindt, waar de verhitting of verwijdering van het gas voorkomt dat het naar het sterrenstelsel toestroomt. De verrijking met metalen zorgt er echter voor dat het gas binnen en buiten sterrenstelsels juist sneller afkoelt. Dit heeft te maken met de grote aantallen gebonden elektronen en de daardoor vele beschikbare excitatieniveaus, die nodig zijn om een gas te laten afkoelen. Al deze processen hebben hun oorsprong in de sterrenstelsels zelf, maar zijn van invloed op de verdere evolutie van deze sterrenstelsels. We noemen dergelijke processen 'feedbackprocessen'. De verrijking van het gas met metalen is bijvoorbeeld zogenaamde 'chemische feedback'. De termen 'stellaire feedback' en 'AGN-feedback' verwijzen naar de energetische feedback van respectievelijk sterevolutie (sterwinden en supernovae) en AGN. Deze twee processen zijn belangrijk voor het reguleren van de stervorming in sterrenstelsels.

Het IGM en CGM vormen een belangrijk reservoir waarmee sterrenstelsels materie uitwisselen. Aan de ene kant bevat het nieuwe 'brandstof' voor stervorming en aan de andere kant ontvangt het gas dat door galactische winden is uitgestoten. Onderzoek naar het IGM – en vooral naar het CGM – kan daarom informatie verschaffen over hoe de evolutie van sterrenstelsels verloopt en hoe efficiënt feedback daarbij is. Het gas in het IGM en CGM is over het algemeen diffuus (met dichtheden van 10^{-5} tot 10^{-3} waterstofatomen per kubieke centimeter) en heeft een hoge temperatuur (tussen de tienduizend en miljoen graden Kelvin) en verkeert daardoor overwegend in geïoniseerde toestand. Afhankelijk van de dichtheid en temperatuur kunnen de ionen van de verschillenden elementen in verschillende verhoudingen voorkomen. Daarnaast is ook de intensiteit van de aanwezige ioniserende straling van invloed op de ionisatietoestand van het gas. Dergelijke straling komt van buiten het sterrenstelsel in kwestie – van het veld van UV-straling dat overal aanwezig is – maar kan ook komen van de sterpopulatie of AGN in het sterrenstelsel zelf. Vooral de foto-ioniserende straling van AGN kan de ionisatietoestand sterk beïnvloeden.

Onderzoeksmethoden

In dit proefschrift bestuderen we sterrenstelsels en hun omgeving door middel van zowel simulaties als observaties. Aan de ene kant kunnen numerieke simulaties voorspellingen doen over processen en grootheden die niet direct waarneembaar zijn, bijvoorbeeld doordat deze veranderen op tijdschalen die vele malen langer zijn dan een mensenleven. Ook maken simulaties het mogelijk om objecten als het ware terug te volgen in de tijd. Een simulatie, waarin we objecten produceren zoals in de waarnemingen, kunnen we namelijk 'terugdraaien' om erachter te komen hoe deze objecten er waarschijnlijk op een eerder moment hebben uitgezien. Op deze manier kunnen simulaties ons helpen bij de interpretatie van de waarnemingen. Aan de andere kant geven simulaties ons de kans om numerieke 'experimenten' uit te voeren. Door twee simulaties te draaien, waarbij een bepaald fysisch proces in de ene is ingeschakeld en in de andere is uitgeschakeld, kunnen we onderzoeken wat de rol is van dit proces in, bijvoorbeeld, de vorming van sterrenstelsels.

De simulaties die we in dit proefschrift gebruiken zijn kosmologische simulaties. Deze bootsen een representatief stuk van het universum na door de inhoud –

donkere materie, gas en sterren – op te delen in massa- of volume-elementjes (in ons geval in massa-elementjes van ongeveer een miljoen $M_\odot$) en te kijken naar hoe de inhoud zich ontwikkelt over een bepaalde tijdsperiode. De interacties tussen de elementjes volgen daarbij de wetten van de zwaartekracht en de hydrodynamica (in het geval van het gas). Omdat de grootte van de massa- of volume-elementjes de resolutie van de simulatie bepaalt, zijn er fysische processen die plaatsvinden op een schaal – bijvoorbeeld op atomaire schaal – die kleiner is dan de resolutie, maar die toch van invloed zijn op de evolutie van het sterrenstelsel als geheel en het medium daarbuiten. Voorbeelden hiervan zijn het afkoelen van gaswolken door het uitzenden van straling en het ontstaan van individuele sterren en hun verdere evolutie tot bijvoorbeeld supernovae. Ook het ontstaan van zwarte gaten en het aandrijven van AGN-feedback kunnen door de beperkte resolutie niet direct op basis van alleen natuurwetten worden gesimuleerd. Het is daarom gebruikelijk om dergelijke processen op de schaal van de resolutie-elementjes van de simulatie te implementeren, op zo'n manier dat het effect van de processen op grotere schaal voldoet aan de verwachtingen of directe observaties. Daarbij kunnen bepaalde aspecten, zoals de intensiteit en tijdsduur van een proces, direct aan de lokale eigenschappen (bijvoorbeeld de dichtheid en temperatuur) van de resolutie-elementjes worden gekoppeld.

Om realistische voorspellingen over de vorming van sterrenstelsels te kunnen doen, is het belangrijk dat de eigenschappen van de sterrenstelsels (en het omliggende medium) in de simulaties overeenkomen met de observaties. In de kosmologische simulaties die we in dit proefschrift gebruiken, de EAGLE-simulaties (waarbij 'EAGLE' staat voor de *Evolution and Assembly of GaLaxies and their Environments*), zijn belangrijke eigenschappen zoals de massa en de grootte van sterrenstelsels in overeenstemming met de waarnemingen. Bovendien maakt de variatie in de geïmplementeerde fysische processen tussen de verschillende simulaties het mogelijk het effect van bepaalde fysische processen te isoleren. Een belangrijke eigenschap van de EAGLE-simulaties is ook dat de hoeveelheden gas en metalen die de sterren in de simulaties produceren realistisch zijn, als ook de mate waarin deze door de ruimte in en rondom sterrenstelsels worden verspreid.

Naast numerieke simulaties maken we in dit proefschrift ook gebruik van observaties uitgevoerd met de *Multi Unit Spectroscopic Explorer* (MUSE) op de *Very Large Telescope* (VLT) en met de *Cosmic Origins Spectrograph* (COS) aan boord van de *Hubble Space Telescope* (HST). We gebruiken deze observaties om het gas in het CGM van sterrenstelsels op lage roodverschuiving ($z < 1$[20]) te bestuderen. Omdat dit gas zo diffuus is, zendt het over het algemeen te weinig licht uit om het direct te kunnen waarnemen. Daarom gebruiken we het licht van een heldere achtergrondbron – in dit geval een quasar, ook wel *quasi-stellar object* (QSO) genoemd – om het gas rondom de sterrenstelsels op de voorgrond te bestuderen aan de hand hoeveel en op welke golflengten het licht wordt geabsorbeerd. Omdat elk ion van elk element zijn eigen absorptiepatroon in het spectrum van de quasar produceert, kunnen we reconstrueren welke elementen er in het gas aanwezig zijn en wat de temperatuur en dichtheid van het gas is.

---

[20]Ter illustratie, een waarneming doen op roodverschuiving $z = 1$ komt overeen met het bekijken van het heelal op een tijdstip dat het half zo oud was als nu.

Dit proefschrift

In dit proefschrift bestuderen we de metalen in en rondom sterrenstelsels en bekijken we wat deze ons kunnen vertellen over de ontwikkeling van sterrenstelsels en het omliggende medium. Metalen geven aan waar en in welke hoeveelheid het gas dat afkomstig is uit sterren zich bevindt. Daarbij geeft de verhouding waarin de verschillende elementen en hun ionen voorkomen, aan op welke tijdschaal de sterrenstelsels en hun omgeving met sterrenstof zijn verrijkt en in welke ionisatietoestand het gas verkeert.

In **Hoofdstuk 2** gebruiken we de EAGLE-simulaties om te onderzoeken in welke mate het gas afkomstig uit sterren bijdraagt aan de vorming van nieuwe sterren. We noemen dit proces ook wel het recyclen van stermateriaal. Door het recyclingproces hebben sterrenstelsels extra brandstof en kunnen ze dus langer sterren vormen. We laten in dit hoofdstuk zien dat recycling vooral belangrijk is voor sterrenstelsels met een stermassa die vergelijkbaar is met die van de Melkweg (ongeveer $10^{10.5} \, M_\odot$). Voor geïsoleerde of centrale[21] sterrenstelsels met een dergelijke massa komt 35% van de huidige stervorming en 20% van de tot nu toe gevormde stermassa van gerecycled stermateriaal. Voor sterrenstelsels met een lagere of hogere massa liggen deze percentages lager. We laten zien dat dit komt doordat de feedback uit stervorming (op lagere massa) en van AGN (op hogere massa) in deze sterrenstelsels efficiënter is en daarbij de stervorming – en vooral de stervorming uit gerecycled stermateriaal – in toenemende mate onderdrukt. Voor satellietstelsels kunnen de percentuele bijdragen van recycling aan de stervorming en stermassa veel hoger zijn dan voor de centrale sterrenstelsels. Deze sterrenstelsels ontvangen minder makkelijk gas uit het IGM en zijn daarom meer afhankelijk van recycling bij de vorming van nieuwe sterren. Verder presenteren we empirische formules die het mogelijk maken om de bijdragen van gerecycled stermateriaal aan de huidige stervorming en stermassa van sterrenstelsels te schatten op basis van twee waargenomen groootheden, de metalliciteit (de fractie van de gas- of stermassa bestaande uit metalen) en de massaverhouding tussen de α-elementen en ijzer.

De verhouding tussen α-elementen en ijzer (Fe) in de sterren van sterrenstelsels is een veel gemeten grootheid in onderzoeken naar de ontstaansgeschiedenis van massieve, elliptische sterrenstelsels en wordt ook wel aangeduid als $[\alpha/\mathrm{Fe}]_*$. Doordat de α-elementen komen van massieve sterren met een relatief korte levensduur, worden sterren in een sterrenstelsel eerst vooral gevormd van gas dat rijk is aan α-elementen en dat weinig ijzer bevat (dus met een hoge $[\alpha/\mathrm{Fe}]_*$). Naarmate steeds meer lage en middelzware sterren het eindstadium van hun leven bereiken en een deel hiervan explodeert als Type Ia supernovae, komt er steeds meer ijzer vrij. Latere generaties sterren worden daarom in toenemende mate gevormd van gas dat rijk is aan ijzer (dus met een lage $[\alpha/\mathrm{Fe}]_*$). In **Hoofdstuk 3** presenteren we een verklaring voor de observaties van elliptische sterrenstelsels die aantonen dat de $[\alpha/\mathrm{Fe}]_*$ van de sterrenstelsels als geheel groter is wanneer de stermassa en de gemiddelde leeftijd van de sterpopulaties hoger is. We laten zien dat de feedback van AGN kan zorgen voor

---

[21]De term 'centrale sterrenstelsels' verwijst naar sterrenstelsels die de hoogste massa of sterkste gravitationele binding hebben in de groep waarin ze leven. 'Satellietstelsels' verwijst naar alle andere sterrenstelsels in deze groepen.

een dergelijke afhankelijkheid tussen deze grootheden. AGN-feedback is namelijk een mechanisme waardoor de stervorming in (massieve) sterrenstelsels wordt onderdrukt, op zo'n manier dat het eerder effect heeft op sterrenstelsels waarvan de huidige massa hoger is. De onderdrukking van de stervorming voorkomt dat er nog veel nieuwe sterren worden gevormd wanneer het langzaam vrijkomende ijzer in het gas van het ISM terechtkomt. De sterren in elliptische sterrenstelsels met een hogere massa zijn dus niet alleen gemiddeld ouder, maar hebben ook een hogere $[\alpha/\text{Fe}]_*$.

In **Hoofdstuk 4** kijken we naar een andere vorm van AGN-feedback, namelijk het foto-ioniserende effect van de uitgezonden straling op het gas in het CGM van sterrenstelsels. AGN behoren tot de sterkste lichtbronnen in het universum, maar staan niet continu 'aan'. Ze fluctueren met een bepaalde frequentie en levensduur per cyclus, die per object en in de tijd kan variëren. Zo bevat ieder sterrenstelsel waarschijnlijk een potentiële AGN, maar hoeft deze niet op ieder moment actief te zijn. Dit scenario heeft consequenties voor de interpretatie van waarnemingen van het CGM, doordat het foto-ioniserende effect van de AGN-straling ook nadat de AGN al zijn uitdoofd zijn sporen kan nalaten. We laten dit zien door het effect van fluctuerende AGN na te bootsen voor vier sterrenstelsels – met twee verschillende stermassa's ($10^{10}\,\text{M}_\odot$ en $10^{11}\,\text{M}_\odot$) op twee verschillende kosmische tijdstippen ($z = 0.1$ en $z = 3$) – in de EAGLE-simulaties. We tonen aan dat door de ioniserende werking van de AGN-straling en de traag verlopende recombinatie (van de vrijgekomen elektronen met de ionen) die daarop volgt, het CGM-gas voor vele miljoenen jaren in een te hoge ionisatietoestand ('overgeïoniseerd') achterblijft. De kolomdichtheid, het aantal ionen per vierkante centimeter, van Ovi (vijf keer geïoniseerde zuurstof) kan zelfs meer dan tien keer hoger zijn dan in de evenwichtstoestand, vooral in het CGM-gas op korte afstand tot het sterrenstelsel en wanneer de tijd tussen twee fasen van AGN-activiteit kort is. We zien de effecten voor alle vier de sterrenstelsels, dus deze zijn niet beperkt tot sterrenstelsels van één bepaalde massa of tot één tijdsperiode. We voorspellen dat de effecten het CGM-gas in vele sterrenstelsels beïnvloeden, ondanks dat deze op het moment van de observatie niet als sterrenstelsels met actieve AGN worden geclassificeerd.

In **Hoofdstuk 5** presenteren we de resultaten van ons observationele onderzoek dat we hebben uitgevoerd met MUSE. Dit instrument kan het licht van objecten op verschillende golflengten apart waarnemen (een spectrum) en kan dit op een groot aantal punten aan de hemel tegelijk doen. Doordat sterrenstelsels op selectieve golflengten extreem veel licht uitzenden ('lijnemissie'), is MUSE ideaal voor het detecteren van sterrenstelsels en het direct bepalen van hun afstand (roodverschuiving). Ons onderzoek is gericht op de velden rondom 16 heldere quasars die eerder zijn waargenomen met COS en waarvoor spectra beschikbaar zijn. We gebruiken deze spectra om de absorptie te meten die veroorzaakt wordt door het CGM-gas van de sterrenstelsels op de voorgrond – de sterrenstelsels die we hebben gedetecteerd met MUSE. Deze combinatie van data afkomstig van twee instrumenten biedt ons de mogelijkheid om naar de dichtheden van neutraal waterstof (Hi) en verschillende metaalionen in het CGM van 208 sterrenstelsels op $z < 1$ te kijken. De nieuwe verzameling sterrenstelsels bevat door onze detectiemethode sterrenstelsels met een lagere stermassa (met een mediaan van $10^{8.9}\,\text{M}_\odot$) dan in voorgaande onderzoeken en is interessant omdat juist deze sterrenstelsels gezien worden als belangrijke bron-

nen van metalen in het IGM. We meten significante hoeveelheden HI, OVI en CIII (twee keer geïoniseerde koolstof), die afnemen als de afstand tot de sterrenstelsels toeneemt. Ook laten we zien dat er meer OVI aanwezig is rondom sterrenstelsels die een hogere stermassa hebben of waarin meer stervorming plaatsvindt.

Publications

1. **Segers M. C.,** Oppenheimer B. D., Schaye J., Richings A. J., 2017, *Metals in the circumgalactic medium are out of ionization equilibrium due to fluctuating active galactic nuclei*, MNRAS, 471, 1026

2. **Segers M. C.,** Schaye J., Bower R. G., Crain R. A., Schaller M., Theuns T., 2016, *The origin of the α-enhancement of massive galaxies*, MNRAS, 461, L102

3. **Segers M. C.,** Crain R. A., Schaye J., Bower R. G., Furlong M., Schaller M., Theuns T., 2016, *Recycled stellar ejecta as fuel for star formation and implications for the origin of the galaxy mass-metallicity relation*, MNRAS, 456, 1235

4. Oppenheimer B. D., **Segers M. C.,** Schaye J., Richings A. J., Crain R. A., 2017, *Flickering AGN can explain the strong circumgalactic O VI observed by COS-Halos*, submitted to MNRAS

Curriculum Vitae

I was born on the 25th of May, 1990, in Leiden. I was raised in Voorschoten, and most of my school and academic life took place in Leiden. I have always been interested in historical topics, so in high school, which I attended at the 'Stedelijk Gymnasium' in Leiden, I took Latin, Greek and history in addition to the science subjects. I was also considering studying archaeology or classical languages after finishing high school. However, during a school project on black holes, astronomy caught my interest and despite my original plan, I eventually chose to study astronomy. I have never regretted this decision, as for me astronomy combines the best of both worlds: astronomy is, in principle, 'archaeology' of the Universe, but with a great emphasis on physics and mathematics.

In 2008, I started studying astronomy at Leiden University. As the final project of my bachelor's, I investigated the intrinsic shapes of galaxies and their significance for studies using the weak gravitational lensing technique under the supervision of Koen Kuijken. During my master's, I did a research project under the supervision of Joop Schaye where I used numerical simulations to study the role of feedback in fuelling star formation in galaxies with recycled stellar ejecta. This project has been the inspiration for the second chapter of this thesis. For my final project – the master's thesis – I worked with Koen Kuijken to study the dark matter haloes of galaxy groups using weak gravitational lensing. I graduated in 2013, and I was awarded the Lorentz Graduation Prize for theoretical physics.

After going back and forth between observational and simulation projects, I started a PhD in the group of Joop Schaye, where I could combine both to study the formation of galaxies. During my PhD, I worked with state-of-the-art cosmological simulations, but I also had the opportunity to go observing with the MUSE instrument on the Very Large Telescope in Chile. Since the year I arrived at Leiden University, I have been a member of the astronomy education committee, first as a student member and later as a staff member. During my PhD, I supervised two research projects, of a high school summer student and a master student, and I acted as a teaching assistant for a number of astronomy courses. I also answered all kinds of astronomy-related questions as a member of the Sterrewacht public outreach committee. I presented my research at various conferences and workshops in the Netherlands, Chile, France, Germany, Italy and the USA.

I will stay at Leiden University on a short-term research position for a few more months, but in 2018 I will make the switch to industry to work as a data scientist.

Acknowledgements

After 9 years at the Sterrewacht, I would like to thank the many people who I have crossed paths with during my bachelor's, master's and PhD. The nice and friendly atmosphere made me feel welcome from the start and made me enjoy studying and working at the Sterrewacht more and more every year.

I am thankful for the great technical and administrative support offered at the Sterrewacht, but also for the help and guidance on a personal level that I received during my PhD. Xander and Jackie, thank you for your support and words of advice, especially in the last few months.

I would also like to thank the past and current members of my research group, my collaborators, and other people at the Sterrewacht that I have shared fun and memorable moments with. Ben, working with you on the fluctuating AGN project has been fun and inspiring. Rob, thank you for your guidance, during my master's project and after, and for being my go-to person for all my EAGLE questions. Ali, even though we only overlapped during my master's, I always had a great time when we met at conferences. Things are never boring when you are around! Marco, I always enjoyed our discussions where neither one of us wanted to give in. Alex, thanks for always being generous in helping out and answering questions. Marcel, thanks for being a mentor and for offering advice (not only on laptops) in the early days of my PhD. Joki, you are one of the most relaxed people I know and you certainly made group meetings more fun. Allison and Margot, I enjoyed our Dutch lunches, even though the teachers usually outnumbered the students. Mason, Henriette and Jeroen, thank you for an amazing trip to the Faroe Islands and for tolerating a morning person in the two m^2 cabin. Chris, it was great sharing an office with you; I am going to miss the smell of bananas on Monday mornings. Nastasha, thanks for adding another Dutchie to the group and I hope you will continue to be a pro at bouldering. Tiago, I always loved your stories about surreal situations, the one about the hairdresser in Amsterdam being my absolute favourite. Sowgat, thanks for adding another observer to the group and for making group meetings less simulation-heavy. Sylvia and Alvaro, you are such open and welcoming people. I really enjoyed our meet-ups for drinks or barbecue in Voorschoten. Camila, you are my running inspiration! Keep the marathon running going! Lorrie, thanks for being my MUSE oracle and conference travel partner, and for listening to my venting about all kinds of things. I still have happy memories of our weekend in Pisa, despite the tropical temperatures and the mosquito plague! Monica, I'm so happy that we could spent part of our PhD's together in the group. You have an

awesome fashion style, and I really like your positive take on life. I hope to see you and Bernard again soon!

Furthermore, I would like to thank my parents and my brother Bob for their love and support throughout the years. Thank you being there for me and driving me to work in times where I literally could not move. I am also grateful to have had a grandmother who has always been a beacon for me and my family, and who has shown me that you are never to old to have an interest in new things.

Finally, Jelmer, I feel lucky that I met you every day. Thank you for being my support, my rational counterpart and my companion for the past six (nine) years. I am excited to start this new chapter of our lives together.